TIME DOMAIN APPROACH TO STABILITY IN MACHINING OPERATIONS

by

Luke Berglind

A dissertation submitted to the faculty of
The University of North Carolina at Charlotte
in partial fulfillment of the requirements
for the degree of Doctor of Philosophy in
Mechanical Engineering

Charlotte

2015

Approved by:

____
Dr. John Ziegert

____
Dr. Tony Schmitz

____
Dr. Scott Smith

____
Dr. Angela Davies

____
Dr. Scott Kelly

____
Dr. Wesley Williams

ABSTRACT

LUKE BERGLIND. Time domain approach to stability in machining operations. (Under the direction of Dr. JOHN ZIEGERT)

Machine tool chatter is a common occurrence in machining environments which can lead to undesirable part outcomes and can even cause damage to the machine. Chatter is a result of regenerative dynamic forces inherent in the machining process which can cause the system to be either stable or unstable depending on the parameters of the cutting operation and the dynamic characteristics of the machine tool. The study of chatter is a common research topic which aims to characterize the dynamic behavior of machining operations so that chatter can be avoided. In this dissertation, a method is developed to analyze the dynamic behavior of cutting processes in the time domain. This approach allows for the tool point behavior to be determined analytically over a finite number of cutting periods. The analytical expressions describing the tool motion are then incorporated into a matrix solution which is used to determine dynamic stability directly without requiring a full time domain solution. These methods are first developed for an orthogonal turning model, and then expanded for the analysis of low radial immersion milling, low radial immersion milling with variable pitch cutters, average angle approximation milling with non-constant number of teeth in the cut, and full milling with variable cutting force directions.

TABLE OF CONTENTS

LIST OF FIGURES

CHAPTER 1: INTRODUCTION

Dynamic instability, or chatter, is a common occurrence in machining environments which can lead to undesirable part outcomes in terms of part surface and dimensional quality, and can cause damage to the part or cutting tool. Chatter is a result of regenerative dynamic forces inherent in the machining process which can cause the system to be either stable or unstable depending on the parameters of the cutting operation and the dynamic characteristics of the machine tool (Schmitz 2009; Tlusty 1963). One of the primary objectives of research in machine dynamics is to better understand and characterize the dynamic behavior of machining operations so that chatter can be avoided.

The analysis of basic machining operations is based on the two system schematics shown in Figure 1 for turning and milling. In the case of turning, the part, which is assumed to be rigid, rotates as a flexible tool removes material. For milling, the assumed rigid work piece is stationary as a flexible tool rotates and removes material as it sweeps through the cut. The resulting motion of these flexible tools throughout the operation must be investigated in order to determine whether the operation is stable or unstable. The primary difference between the turning and milling operations shown in Figure 1 is in the direction of the cutting force which acts on the tools. For turning operations the cutting tool is stationary relative to the coordinate reference frame (x-direction) and the resulting cutting forces act in a single direction throughout the operation. For milling the cutting edges rotate relative to the coordinate reference frame (x and y directions), causing the force direction to change as the tool angle, ϕ, changes. It is this angle dependent cutting force direction which makes the analysis of milling operations significantly more complex than turning operations.

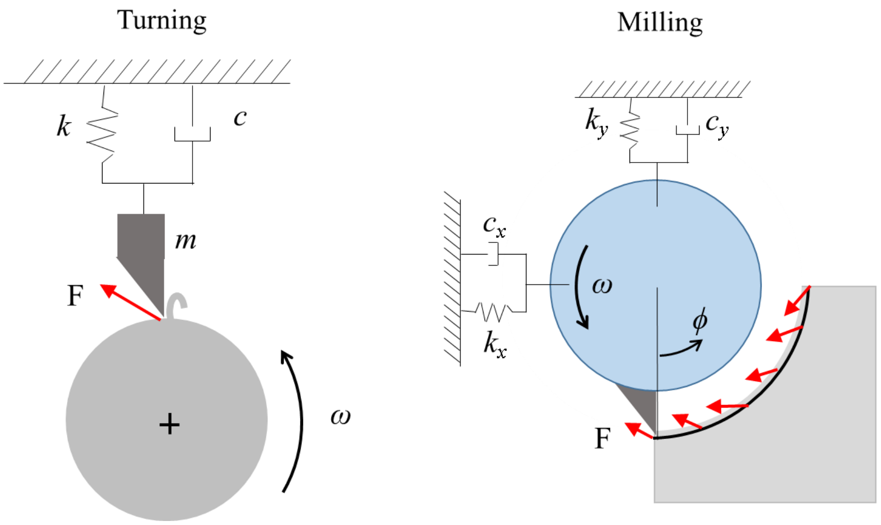

Figure 1: Dynamic systems and cutting forces for turning and milling.

The magnitude of the forces which act on the tools are assumed to be proportional to the area of the chips being formed. In orthogonal cutting (with a rectangular chip profile) this area is determined based on the chip width, b, and the chip thickness, h. The chip width, b, is equal to the depth of cut, or the out of plane dimension of the chip in the model schematics shown in Figure 1. The chip thickness, h, is the dimension of the chip normal the cut surface. If the tool is assumed to be rigid, the area of the chip would be constant for turning, or a repeated periodic shape in milling related to the radial immersion of the cut and the feed per tooth. When tool flexibility is introduced, there are variations in the area of the chip that are a result of the tool vibrations. When the tool first comes into contact with the work piece it experiences a sudden force, or perturbation, which causes it to vibrate. These vibrations leave a wavy imprint on the surface of the work piece which effectively create a variation in the thickness of the chip. When the tool passes over the wavy surface during the next rotation, the variability in the chip thickness results in a variable force which again excites the tool, creating a new wavy surface on the work piece. As the tool repeatedly passes over the wavy surface left behind during each tool pass, regenerative force effects can cause the tool vibrations to become unstable over time. The resulting variability in chip thickness is illustrated in Figure 2 for turning and milling. In this figure the instantaneous chip thickness, h(t), is a function of the normal component of the tool motion in the current pass (x(t) for turning, and $x_N(t)$ and $y_N(t)$ for milling), and the normal component of the tool motion during the previous tool pass (x(t-τ) for turning, and $x_N(t-\tau)$ and $y_N(t-\tau)$ for milling).

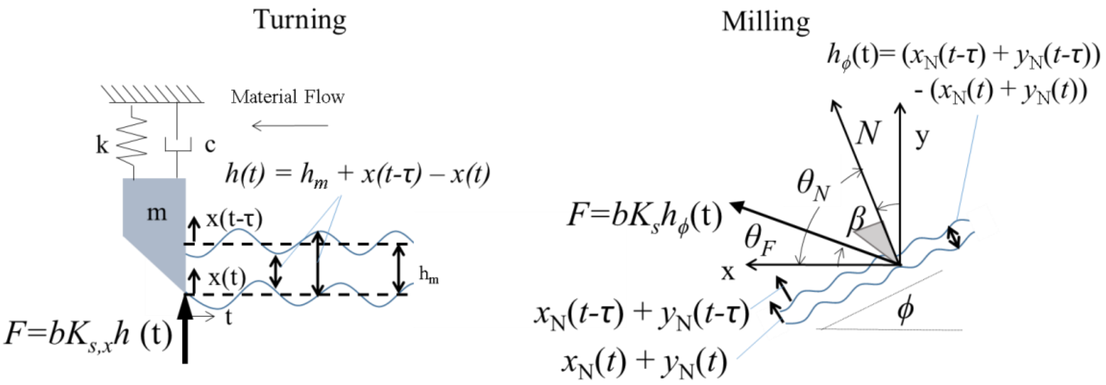

Figure 2: Regenerative forces in turning and milling due to chip thickness variation.

The forces which act on the cutting tool due to variations in the chip thickness are then dependent on the position of the tool at any point in time (x(t), $x_N(t)$ and $y_N(t)$) , and the position of the tool at time t-τ when the tool last passed over the current location (x(t-τ), $x_N(t-\tau)$ and $y_N(t-\tau)$). In Equation 1.1 the resulting differential equations for turning and milling are shown, where the tool point dynamics are modeled as spring mass damper systems, with forcing functions which contain both current time and delayed terms (x_τ and y_τ).

Turning

$$\ddot{x}+\frac{c}{m}\dot{x}+\frac{k}{m}x=\frac{bK_{s,x}}{m}\left(h_m+x_\tau-x\right) \tag{1.1}$$

Milling

$$\begin{aligned} m_x\ddot{x}+c_x\dot{x}+k_x x &= bK_s\cos\left(\theta_F\right)\left(x_\tau\cos\left(\theta_N\right)+y_\tau\sin\left(\theta_N\right)-x\cos\left(\theta_N\right)-y\sin\left(\theta_N\right)\right) \\ m_y\ddot{y}+c_y\dot{y}+k_y y &= bK_s\sin\left(\theta_F\right)\left(x_\tau\cos\left(\theta_N\right)+y_\tau\sin\left(\theta_N\right)-x\cos\left(\theta_N\right)-y\sin\left(\theta_N\right)\right) \end{aligned}$$

The differential equations in Equation 1.1 are known as delay differential equations (DDEs) because the resulting behavior of the system is dependent on both the current states of the system and states of the system at previous points in time. The inclusion of the delay effects in DDEs causes a significant increase in complexity for the analysis of cutting operations compared with other dynamic systems described by ordinary differential equations (ODEs). As such, much research has been devoted to develop effective techniques for evaluating DDEs so that regenerative chatter in machining operations can be better understood, and ultimately avoided in practice.

1.1Background

One of the first successful models for cutting processes was developed by Tobias and Fishwick (Tobias 1958) who attributed regenerative forces in machining processes as the underlining cause of chatter. This model was later modified by Tlusty (Tlusty 1963) who recognized that the chip width and thickness normal to the cut surface were the critical components leading to the regenerative forces. As such, Tlustys' model considers only the normal components of the tool motion, resulting in the DDE model shown in Equation 1.1 for turning. Tlusty furthermore developed a strategy for determining the stability of Equation 1.1 for turning based on the frequency response function (FRF) of the tool and work piece (Tlusty 1963), which is still used reliably for continuous cutting operations such as turning. An example of a stability lobe diagram developed using Tlustys' approach is shown in Figure 3, where the cuts with parameters in the gray regions are predicted to be unstable, and cuts in the white region are stable.

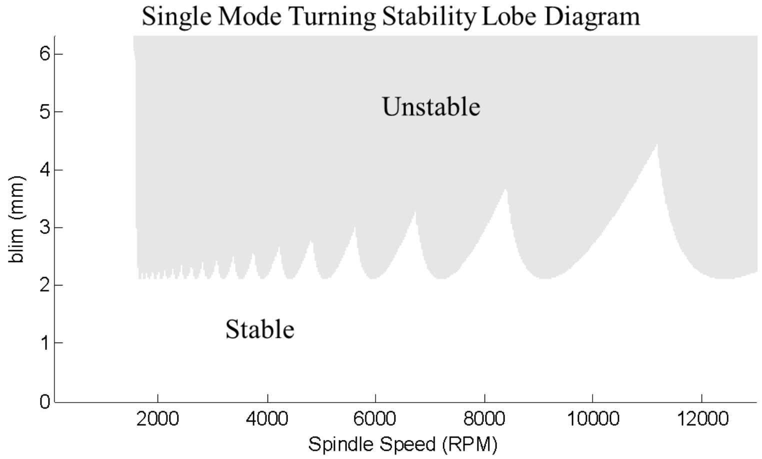

Figure 3: Example of a stability lobe diagram, showing the spindle speeds and depths of cut where the cut is predicted to be stable or unstable.

Tlusty later adapted the analytical stability approach developed for turning to approximate stability in milling (Tlusty 1999).In this approach the angle dependent cutting forces are assumed to act in a single, average direction and additional factors account for this force direction and the effective number of teeth in the cut. Altintas modified the effective force values used in the analytical stability model for milling by considering the average force values over the rotation of the tool instead of using the average angle (Altintas 1995). Altintas' approach uses zeroth order approximation of the cutting forces to determine stability as an eigenvalue problem which has a closed form solution for the stability limit. This method has been expanded to include higher order approximations of the cutting forces to yield higher accuracy in stability predictions (Budak 1998a; Budak 1998b), although these higher order approximations to not allow for the direct calculation of stability limits.

While the analytical stability criteria developed for milling using the system FRF do approximate the stability boundaries in milling, they do not fully capture the nonlinear characteristics of the milling process. Some of these nonlinear effects are the angle dependent cutting force, loss of contact between the tool and the work piece due to large vibrations, and relatively long periods of free vibrations in the case of low radial immersion milling.

The use of numerical simulation is one approach for capturing the nonlinear effects of cutting processes. Tlusty et al used numerical simulation to model the effects of the angle dependent cutting force and the effects of loss of contact between the tool and the work piece (Tlusty 1981) and later expanded the model for milling with variable pitch cutting teeth (Tlusty 1983). Smith et al developed an algorithm to determine the steady state peak to peak forces and displacements in milling over a range of spindle speeds and depths of cut to form stability lobe diagrams with additional information regarding the steady state vibration magnitudes (Smith 1993). Other researchers have used numerical simulation to evaluate the effects of multiple modes, multiple degrees of freedom (Eynian August, 2009; Marsh 1998) and chip formation processes (Gyliene 2013). While numerical simulation is a versatile and effective method for the evaluation of tool point behavior, numerical techniques are computationally expensive, and many individual simulations are needed to characterize the dynamic behavior of a cutting operation over a range of parameters.

Other researchers have sought new analytical approaches to account for some of the nonlinearities in the cutting process. Davies et al developed an approach to evaluate the cutting process for low radial immersion milling by approximating the behavior of the tool while in the cut and coupling these motions with the free vibration periods analytically to determine stability (Davies 2002). Davies' approach was later improved by increasing the accuracy of the tool motion prediction using temporal finite element analysis (TFEA) in (Bayly 2003), which was later generalized for the analysis of higher order systems in (Mann 2010). Insperger and Stepan developed the semi-discretization method (SDM) for the analysis of delayed systems wherein the system is analyzed by discretizing the force input (Insperger 2002; Insperger 2004). Altintas further developed a frequency domain solution by considering multiple harmonics of the tooth passing frequency (Altintas 2008b). More recently, a full discretization method (FDM) has been developed by Ding et al to determine stability of delayed systems (Ding 2010). The FDM is similar to the SDM but has the potential advantage of producing stability limits more efficiently (Ding 2012; Insperger 2010). These analytical methods for evaluating cutting processes account for nonlinearities in the system and improve stability prediction when compared with the methods developed in (Altintas 1995; Tlusty 1963).

In this dissertation, a new approach is developed for the analytical analysis of cutting processes in the time domain which is an alternative approach to the methods developed thus far. This approach is first developed to determine the time response of the cutting tool analytically over a fixed number of tool passes. The methods and equations developed to determine the time response are then used for stability prediction.

CHAPTER 2: SINGLE DEGREE OF FREEDOM TURNING MODEL

Determining the time response of a tool during cutting operations is a more complex process than for other dynamic systems modeled as ODEs due to the regenerative forcing effects inherent in the cutting process. While numerical simulation can be used to evaluate the solutions to DDEs (Tlusty 1981), this approach is computationally expensive and does not lead to an analytical stability criterion. The most common analytical approach, the method of steps (Myshkis 1998), has been employed to solve for the tool response for a single degree of freedom system (Ozoegwu 2012). However, a numerical solution developed for Matlab (Shampine 2001) was eventually used due to the cumbersome nature of the analytical solution.

In this chapter, an alternative approach is developed to analytically evaluate the time response of a single mode tool. In this approach, the time response is composed of a set of curves which are independent of the system delay. These curves are determined analytically and then combined through superposition to form the full time response of the tool. This process developed to evaluate DDEs is described in the following sections.

2.1Model Description

The basic model used to develop the time domain solution is shown in Figure 4. The tool is modeled as a single mode, single degree of freedom spring mass damper system which is flexible in the feed direction of the tool. The forcing function which acts on the tool during the cutting operation is derived by assuming orthogonal cutting conditions, which are illustrated in Figure 5. Under the orthogonal cutting assumption, the tool face is oriented normal to the feed direction, and the magnitude of the cutting force, F, is found as the product of the chip area (area of contact between the tool and the material), and the material cutting force constant, K_s. The dominant cutting forces are assumed to be in the direction of the material flow (F_t), and the feed direction (F_n), which are related to the force magnitude, F, through a cutting force angle, β. As the tool is assumed to be flexible only in the feed direction, only the normal component of the force, F_n, affects tool motions. The cutting force constant, K_s, and the cutting force angle, β, are determined experimentally, and the chip area is calculated as the product of the instantaneous chip thickness, $h(t)$, and the chip width, b.

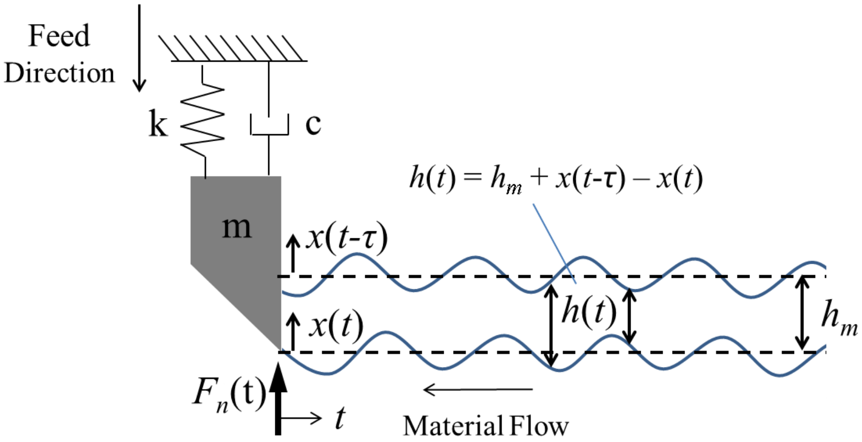

Figure 4: Single mode, single degree of freedom cutting force model, where the cutting force is proportional to the chip width, $h(t)$.

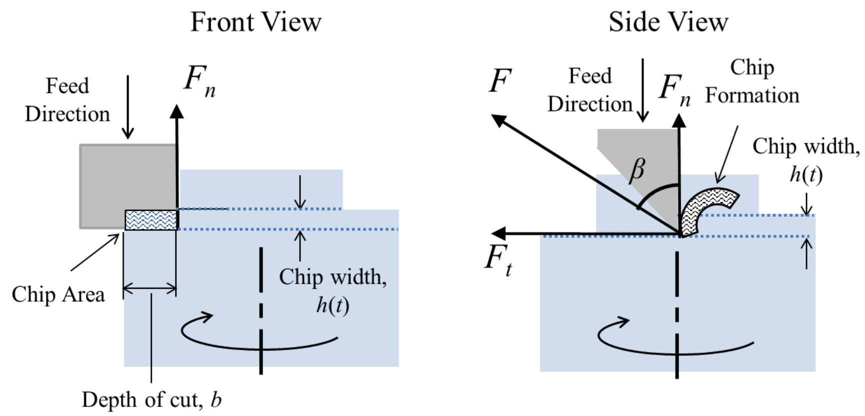

Figure 5: Illustration of cutting forces acting on the tool during orthogonal cutting.

The resulting force acting on the tool varies over time due to variability in the chip area caused by changes in the chip thickness, $h(t)$. The chip width describes the dimension of the chip area in the direction in which the tool is flexible; as such, tool point vibrations change the effective area of the chip, and leave a wavy surface on the part. The resulting value of the chip thickness, $h(t)$, is then a function of the tool position in the current pass, $x(t)$, the tool position in the previous pass, $x(t-\tau)$, and the global feed per revolution, h_m. The resulting expressions describing the force which acts on the tool, F_n, and the instantaneous chip thickness, $h(t)$, are shown in equations 2.1 and 2.2. The resulting differential equation describing the tool point dynamics in turning processes is shown in Equation 2.3.

$$F_n\left(t\right)=K_s\cos\left(\beta\right)bh\left(t\right) \qquad 2.1$$

$$h\left(t\right)=h_m+\mathrm{x(t-}\tau\mathrm{)-x(t)} \qquad 2.2$$

$$\ddot{\mathrm{x}}+\frac{c}{m}\dot{\mathrm{x}}+\frac{k}{m}\mathrm{x}=\frac{bK_s\cos\beta}{m}\left(h_m+\mathrm{x(t-}\tau\mathrm{)-x(t)}\right) \qquad 2.3$$

The inclusion of a time-delay term in equation 2.3 makes it difficult to solve the differential equation analytically to obtain a time domain response of the system. However, if superposition concepts are applied to the system, it is possible to eliminate the time-delay term from the differential equation; thus, an analytical solution is more obtainable. Before discussing the process used to solve equation 2.3 for turning, the general approach used for the solution is illustrated through a relatively simple DDE example of similar form.

2.2General Solution Approach

The time delay term, τ, in equation 2.3 is required to describe the system dynamics because the instantaneous cutting force is dependent on the tool position during the previous revolution. The resulting time delay differential equation (DDE) significantly increases the complexity for an analytical time domain solution. Before delving into the processes used to solve equation 2.3 in particular, we will first discuss the general solution strategies for problems of this type.

The method of steps (Myshkis 1998) is the most common approach to solve DDEs of this form (linear with a single, discrete time delay). This method has been used to develop a time domain solution for turning in (Ozoegwu 2012), however, the solution process proved to be extremely cumbersome after only a few part revolutions, and a Matlab solver, dde23 (Shampine 2001), was employed to simulate the tool behavior over longer periods of time. In this chapter an alternative approach is used to solve equation 2.3 which uses superposition to simplify the solution process. The two solution approaches are compared by examining a relatively simple example DDE shown in Equation 2.4.

$$y' + y\left(t-\tau\right) = 0,\ y\left(0\right) = 1,\ y_0 = 1 \qquad 2.4$$

The method of steps solves DDEs by replacing the delay term, $y(t-\tau)$, with a known function which defines y over the previous time interval, $\left(n-1\right)\tau \le t < n\tau$, starting with an initial function, y_0, defining the position on $-\tau \le t < 0$ to start the solution process. By replacing the delay term with a known function, the DDE is converted into an ordinary differential equation (ODE) that can be solved over discrete time periods. The general solution procedure is shown in Equation 2.5, where the solution over the interval, $n\tau \le t < (n+1)\tau$, is the solution to Equation 2.5 when the position from the previous interval, y_n, is the input. The initial condition at the start of each new interval is equal to the condition of the system at the end of the previous interval. In this way, the total solution is found as a set of individual solutions, each defined over a discrete time interval of length τ. The solution to equation 2.4 using the method of steps with a time delay of $\tau = 0.5$s is shown in Figure 6, where each interval is defined by a single function, y_n(t).

$$\begin{aligned} &y'_{n+1}(t) = -y_n(t),\ n\tau \le t < (n+1)\tau, \\ &y_{n+1}(n\tau) = y_n(n\tau) \end{aligned} \qquad 2.5$$

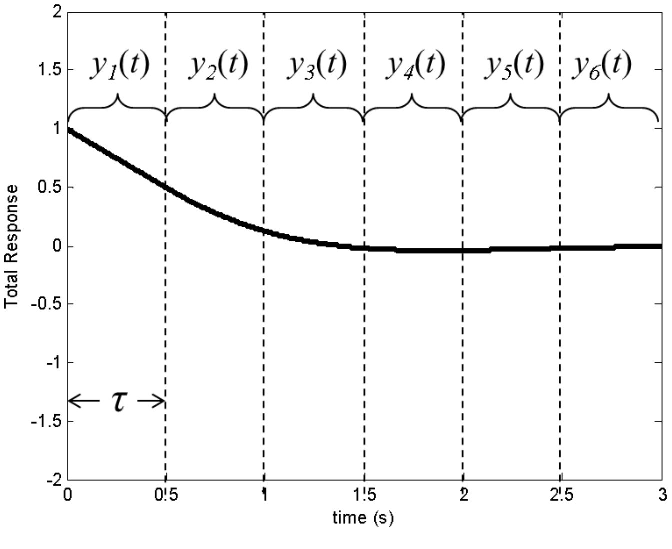

Figure 6: Solution to equation 2.4 using the method of steps with a time delay of $\tau = 0.5$s.

The approach developed in this paper to solve Equation 2.4 is similar to the method of steps in that it converts the single DDE into multiple ODEs. However, rather than having a separate function describing the response over each individual time interval, superposition is used to construct the total response using a set of individual solution curves, called sequential responses. The sequential responses, $y_j(t)$, used to form the solution to Equation 2.4 are found by solving the recursive differential equation shown in Equation 2.6. Note that the sequential responses are defined on a range of zero to infinity, and the initial condition is always zero valued. In Equation 2.7 the first four sequential responses are calculated according to Equation 2.6, starting with the initial function, $y_0=1$. Based on the patterns that emerge from the recursive solutions, the expression for any sequential response for this problem can be calculated directly using Equation 2.8.

$$y_j'(t) = -y_{j-1}(t),\ 0 \le t < \infty,\ y_j(0) = 0 \tag{2.6}$$

$$\begin{array}{lcl} & & y_0 = 1 \\ y_1' = -y_0 = -1 & \rightarrow & y_1 = -t \\ y_2' = -y_1 = t & \rightarrow & y_2 = \dfrac{t^2}{2} \\ y_3' = -y_2 = -\dfrac{t^2}{2} & \rightarrow & y_3 = -\dfrac{t^3}{6} \\ y_4' = -y_3 = \dfrac{t^3}{6} & \rightarrow & y_4 = \dfrac{t^4}{24} \end{array} \tag{2.7}$$

$$y_j = \frac{(-1)^j t^j}{j!} \tag{2.8}$$

The sequential responses described by Equation 2.8 form a set of basis curves which combine through superposition to form the total solution to Equation 2.4. To form the solution to the DDE, each sequential response is added to the total solution at a delayed time, such that the sequential response, y_j, starts at time $t=(j-1)\tau$. The structure of the total solution is defined in Equation 2.9 and a depiction of the process is shown in Figure 7. Note that the value of each sequential response is zero at the time which it is added to the total solution. This is due to the zero initial condition established in Equation 2.6 which prevents discontinuities in the total response (i.e. the conditions at the start of each time interval in the method of steps is already accounted for by the previous sequential responses in the superposition approach).

$$y(t)=\sum_{j=0}^{\infty}\begin{cases}0 & ,t<\tau(j-1)\\ y_j\left(t-\tau(j-1)\right) & ,t\geq\tau(j-1)\end{cases} \tag{2.9}$$

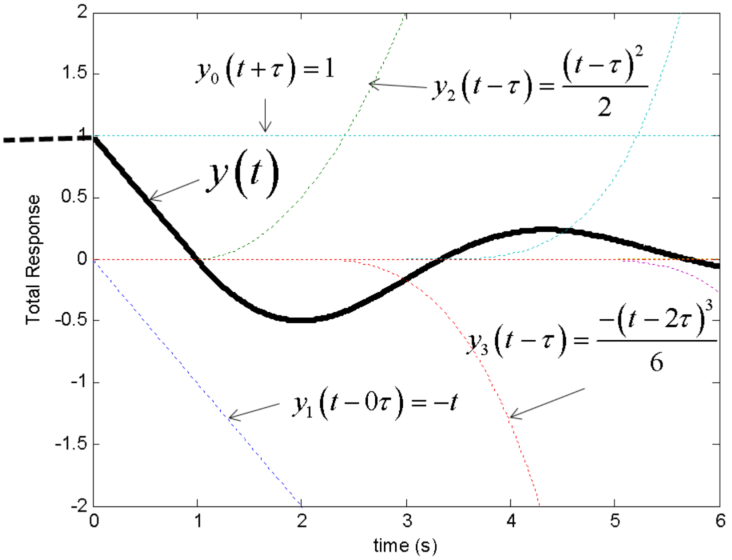

Figure 7: Illustration of how the total solution is constructed using the sequential responses.

It is also interesting to note that as the delay approaches zero, the total response described by Equation 2.8 and 2.9 reduces to Equation 2.10. The resulting summation is the series definition of e^{-t}, which is known to be the solution to $y'+y(t-0)=0$.

$$y(t)=\sum_{j=0}^{\infty}y_j=\sum_{j=0}^{\infty}\frac{(-1)^j t^j}{j!}=e^{-t} \tag{2.10}$$

What is most significant about the superposition approach is that the sequential responses which constitute the total response of the system are independent of the time delay term, τ. As such, for a given system the sequential responses need only be derived once, and the total response can be determined for different values of τ by changing where in time the individual sequential responses are applied. For example, in Figure 8 the solution to equation 2.4 using the superposition approach is shown for four different time delays. Each solution shows significantly different behavior, however, the sequential responses which constitute the total solutions are the same in each. This is in contrast with the method of steps, where the individual functions for each time interval, y_n, must be re-calculated if τ is changed.

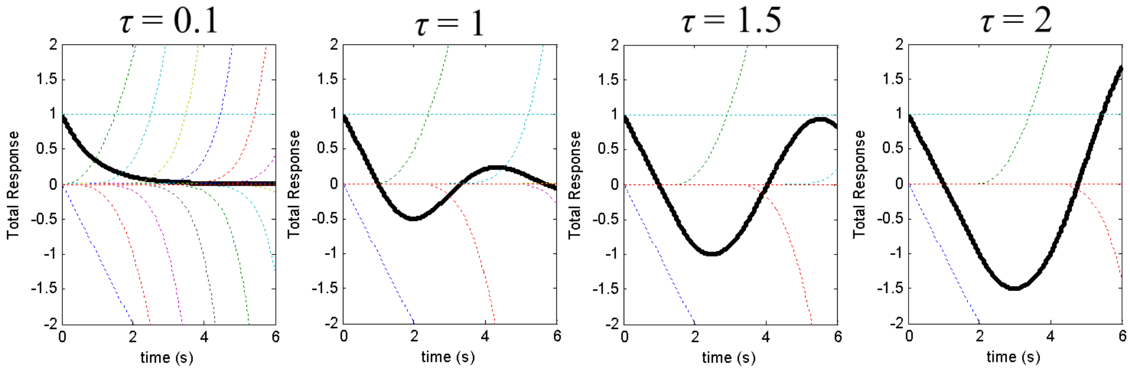

Figure 8: Sequential responses used to solve equation 2.4 for multiple delays, where the sequential responses are the same for each solution.

The general process discussed here to solve linear DDEs with a single discrete time delay is now applied to the more complex turning process. In the following sections, Equation 2.3 is modified to a form in which the superposition approach can be applied, and the resulting sequential responses for turning are derived. These sequential responses are then combined with different time delays to produce the total time response of the tool during the turning process.

2.3DDE Solution for Turning

Before applying the general solution approach described in the previous section to turning, Equation 2.3 must first be modified. Consider now if at any time during the cut we had prior knowledge of the approaching chip shape, including thickness variations created in the previous passes. Figure 9 shows a diagram of this modified view of the system, where the shaded area described by the function $h_{nom}(t)$ is the nominal shape of the approaching chip relative to x=0. This new function, $h_{nom}(t)$, combines all of the information about the approaching chip geometry (h_m and $x(t - \tau)$) into a single function which is dependent only on the current time progression, t. As a result, the time delay term is no longer necessary to describe the shape of the chip and it can be dropped from the equation. The resulting modified differential equation is given in Equation 2.11.

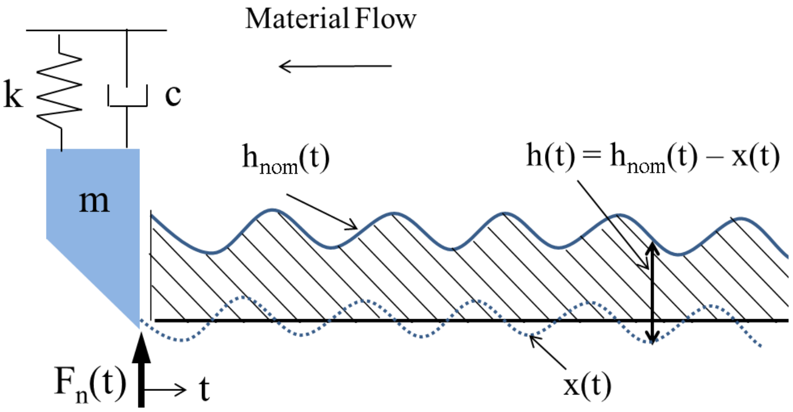

$$F_n(t) = bK_s\cos(\beta)h(t) = bK_s\cos(\beta)(h_{nom}(t) - x(t))$$

Figure 9: Modified view of the approaching chip shape, where all information about the chip is combined into a single function, $h_{nom}(t)$.

$$\ddot{x}+\frac{c}{m}\dot{x}+\frac{k}{m}x=\frac{bR}{m}\left(h_{nom}(t)-x(t)\right), \quad R=K_s\cos\beta \tag{2.11}$$

$$R=K_s\cos\beta \tag{2.12}$$

After moving all x terms to the left side of the equation and simplifying, we are left with a final differential equation, Equation 2.15, describing the dynamic system as the tool passes over the chip profile, $h_{nom}(t)$.

$$\ddot{x}+\frac{c}{m}\dot{x}+\frac{k+bR}{m}x=\frac{bR}{m}h_{nom}(t) \qquad 2.13$$

$$k_p = k + bR \qquad 2.14$$

$$\ddot{x}+\frac{c}{m}\dot{x}+\frac{k_p}{m}x=\frac{bR}{m}h_{nom}(t) \qquad 2.15$$

Equation 2.15 can be solved analytically to obtain the time domain response of the tool, however it requires prior knowledge of the approaching chip shape, $h_{nom}(t)$. This is where superposition comes into play. Consider a diameter turning operation in which the part is initially cylindrical, as shown in Figure 10. As the tool feeds into the cut with a constant feed rate, the initial thickness of the chip is zero when the tool first makes contact, and the chip thickness increases linearly during the first part rotation. After the first rotation is complete, at time $t = \tau$, the nominal thickness of the chip is equal to the feed per revolution, and becomes constant because the slope of the tool motion is nominally canceled out by the slope of the material left behind in the previous rotation.

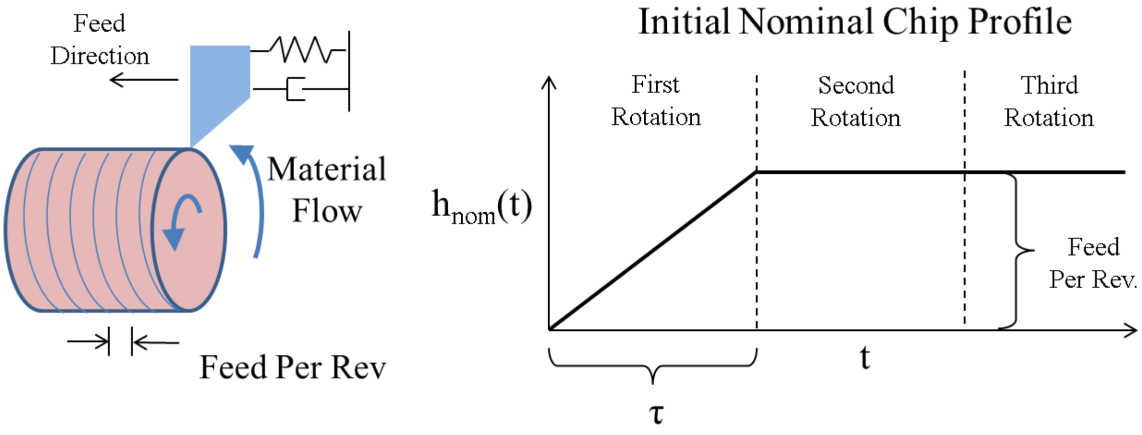

Figure 10: Nominal chip thickness profile for a diameter turning operation with an initially flat face.

The input function plot, $h_{nom}(t)$, in Figure 10 represents the nominal shape of the chip for a turning operation assuming a rigid tool tip. Although there is compliance in the system, this plot serves as a starting point for the superposition analysis. The first application of superposition is to address the slope discontinuity in $h_{nom}(t)$ at $t = \tau$. This is done by combining two ramp input functions; one positive ramp function starting at t = 0 $\left(h_{nom}(t) = \frac{f_{rev}}{\tau}t\right)$, and one negative ramp function with equal slope starting at $t = \tau$ $\left(h_{nom}(t) = -\frac{f_{rev}}{\tau}t\right)$. Through superposition, these two functions form the nominal chip shape, with a positive slope from $0<t<\tau$ and a constant value for $t>\tau$ (see Figure 11(left)). Similarly, the total response of the tool tip can be obtained by combining the tool response to the positive ramp input starting at t = 0 and the tool response to the negative ramp input starting at $t = \tau$ (see Figure 11(right)).

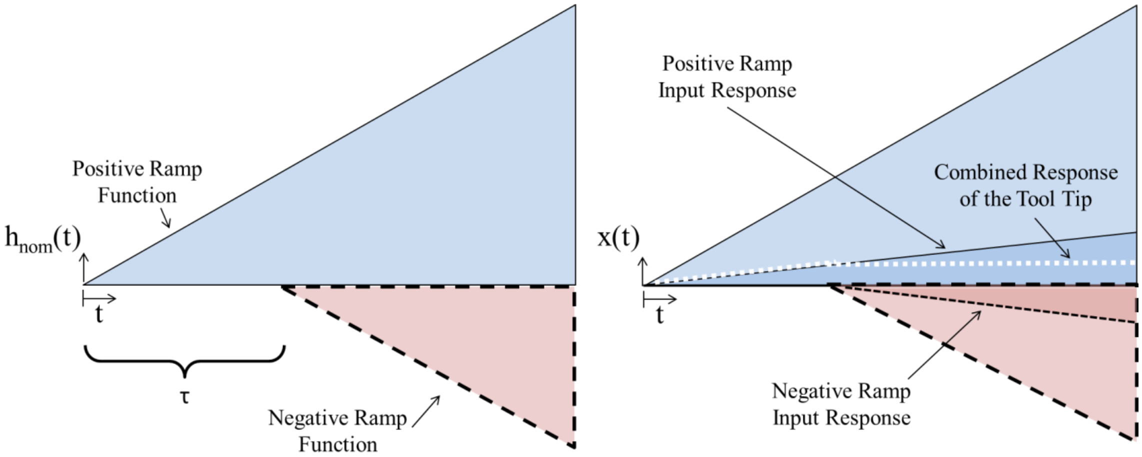

Figure 11: Use of superposition to form the discontinuous nominal chip shape by combining two continuous ramp functions (left), and illustration of how the responses of the two ramp functions individually combine to obtain the global response.

The system response shown in Figure 11 would represent the motion of the tool if the tool point deflections in the previous pass had no effect on the motion of the tool in the current pass (i.e. if this were a broaching operation with a nominal chip thickness profile described in Figure 10). In reality, the motion of the tool in the previous pass will have a residual effect on the current tool pass. For example, during the first rotation, the deflection of the tool leaves behind additional material that is not yet accounted for during the second rotation. Fortunately, the profile of this additional material left behind during the first rotation is known to be x(t).

This leads to the primary application of superposition, where the dynamic response of the system during the second rotation can be determined by combining the response of the negative ramp function in Figure 11 with the response to the additional material profile "left behind" in the first rotation. In Figure 12 the material left behind in the first rotation, $x_1(t)$, is superimposed at the start of the second rotation and labeled as $h_{nom,2}(t)$. It is labeled as $h_{nom,2}(t)$ because this additional material is now considered to be part of the nominal chip profile as the tool begins the second rotation. The effect that this additional material will have on the tool motion can be found by inputting $h_{nom,2}(t)$ into Equation 2.15 and solving for $x_2(t)$. Superposition is then used, combining the initial ramp response, $x_1(t)$ (starting at $t=0$), the negative ramp response, $- x_1(t)$ (starting at $t=\tau$), and the response to the material left behind during the first rotation, $x_2(t)$ (starting at $t=\tau$), to obtain the total tool response for the first two rotations, x(t) for $0 < t < 2\tau$.

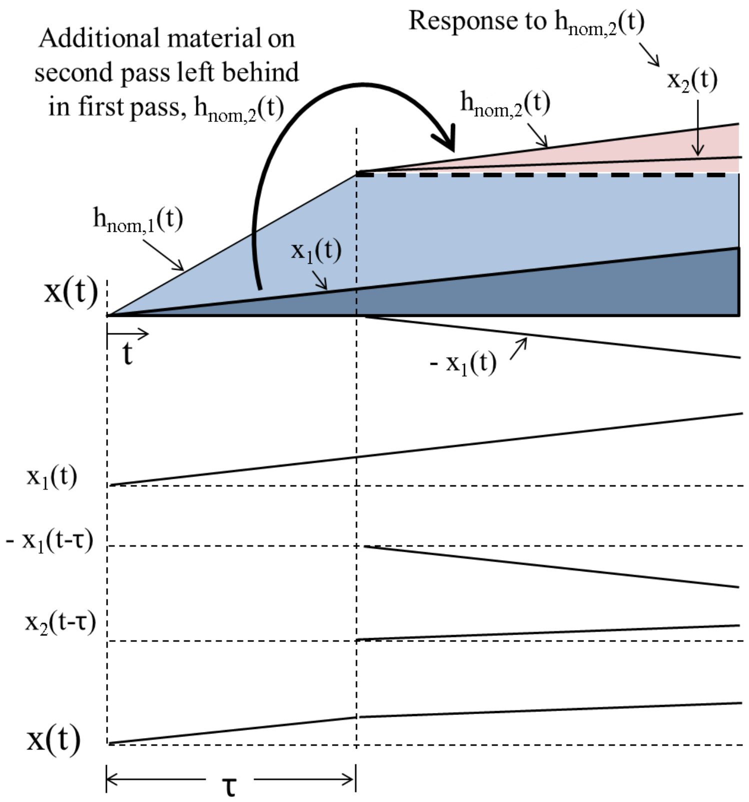

Figure 12: Superposition used to find the total response of the tool as the combination of the initial positive and negative ramp functions, $x_1(t)$ and $– x_1(t)$, and the response to the material left behind after the first pass, $x_2(t)$.

From an analytical point of view, the use of superposition to find the total response of the system during the second rotation can be justified by the fact that the solution to a linear ODE with multiple input functions can be obtained by solving the system response for each input individually, and then combining the individual responses. This is illustrated in Equation 2.16 where the tool response during the second rotation is calculated based on the known chip profile. The approaching chip profile can be described as a combination of the negative ramp function used to define the initial nominal chip profile, $-h_{nom,1}(t)$, plus the material that was left behind in the first rotation, $h_{nom,2}(t) = x_1(t)$. The total response during the second rotation can then be found by calculating the response to $-h_{nom,1}(t)$, which is known to be $-x_1(t)$, with the additional response to the material left behind in the first rotation, $x_2(t)$.

$$\text{A)}\qquad \ddot{x}+\frac{c}{m}\dot{x}+\frac{k_p}{m}x=\frac{bR}{m}\left(h_{nom,2}(t)-h_{nom,1}(t)\right)\ \rightarrow\ x_2(t)-x_1(t)$$

$$=$$

$$\text{B)}\qquad \ddot{x}+\frac{c}{m}\dot{x}+\frac{k_p}{m}x=\frac{bR}{m}h_{nom,2}(t)\ \rightarrow\ x_2(t) \qquad 2.16$$

$$-$$

$$\text{C)}\qquad \ddot{x}+\frac{c}{m}\dot{x}+\frac{k_p}{m}x=\frac{bR}{m}h_{nom,1}(t)\ \rightarrow\ x_1(t)$$

The resulting response during the second rotation, $x_2(t) - x_1(t)$, are combined with the response during the first equation, $x_1(t)$, starting at $t = \tau$ to obtain the total tool point response for the first two rotations.

For the third rotation the same process is followed, except the inputs to Equation 2.16 A are $h_{nom,3}(t)$- $h_{nom,2}(t)$, where $h_{nom,3}(t) = x_2(t)$, and $h_{nom,2}(t) = x_1(t)$. The resulting responses of the tool during the third rotation, $x_3(t) - x_2(t)$, are combined and applied to the total response of the system starting at $t = 2\tau$.

As the number of rotations increases, the process is repeated, where the subsequent responses, $x_j(t)$ and $-x_{j-1}(t)$, are applied to the total response of the system starting at $t = (j-1)\tau$. The resulting time domain response for the turning operation shown in Figure 10 is given in Equation 2.17, where N is the total number of part rotations, and $x_j(t)$ is the j^th^ response to the initial ramp input function.

$$x(t)=x_1(t)+\sum_{j=2}^{N}\begin{cases}0 & ,t<(j-1)\tau\\ x_j\left(t-(j-1)\tau\right)-x_{j-1}\left(t-(j-1)\tau\right) & ,t\geq(j-1)\tau\end{cases} \qquad 2.17$$

It can be seen from Equation 2.17 that the entire time domain response for the turning operation can be obtained by adding and subtracting a set of individual dynamic responses (x_1, x_2, x_3, etc.). These sequential responses all stem from some initial “excitation event” that occurs as a result of the initial nominal chip shape. For example, in the turning operation described in Figure 10, there are two locations on the initial nominal chip profile where abrupt changes in the slope result in tool tip excitation. These slope discontinuities occur at the start of the two ramp functions which define the initial nominal chip profile (at $t=0$ and $t=\tau$). After the initial excitations, the tool will repeatedly pass over the material profile left behind in the previous pass, and the tool motion response to the material profile left behind one rotation prior will then become the chip profile that will be encountered in the next rotation. In this way, the residual effects of the initial “excitation events” will propagate with each new rotation.

2.4Sequential Response Solutions

The sequential responses used in the superposition method are found by taking repeated tool passes over the same section of material, starting with an initial ramp material profile. This concept is illustrated in Figure 13, where in the first pass, the tool passes a ramp material profile described by $h_{nom,1}(t) = t$ (note that a slope of 1 is used for $h_{nom,1}$ for simplicity, and all responses can be scaled to reflect the actual slope which depends on the feed per revolution and the spindle speed). The resulting motion of the tool during the first pass, $x_1(t)$, is found by solving Equation 2.15 with the input function, $h_{nom,1}(t)$. The first response, $x_1(t)$, has an AC component superimposed on linear component with slope, V_0. During the second pass, the tool will pass over the profile left behind in the first pass, $h_{nom,2}(t) = x_1(t)$, generating the second response, $x_2(t)$. With each successive pass, the output, $x_j(t)$, becomes the input, $h_{nom,j+1}(t)$ to Equation 2.15 for the next pass.

Each time the tool passes over the material section, the linear response of the tool will have a slope that is less than the slope of the material that it is passing over, where slope(x_j) = V_0^j and $V_0 < 1$. As a result, the linear component of the sequential responses will diminish as the number of passes increases. The resulting AC components of the sequential responses will ultimately determine the stability behavior of the system, where the magnitudes of the AC component will either grow or decrease with each successive pass depending on the system parameters.

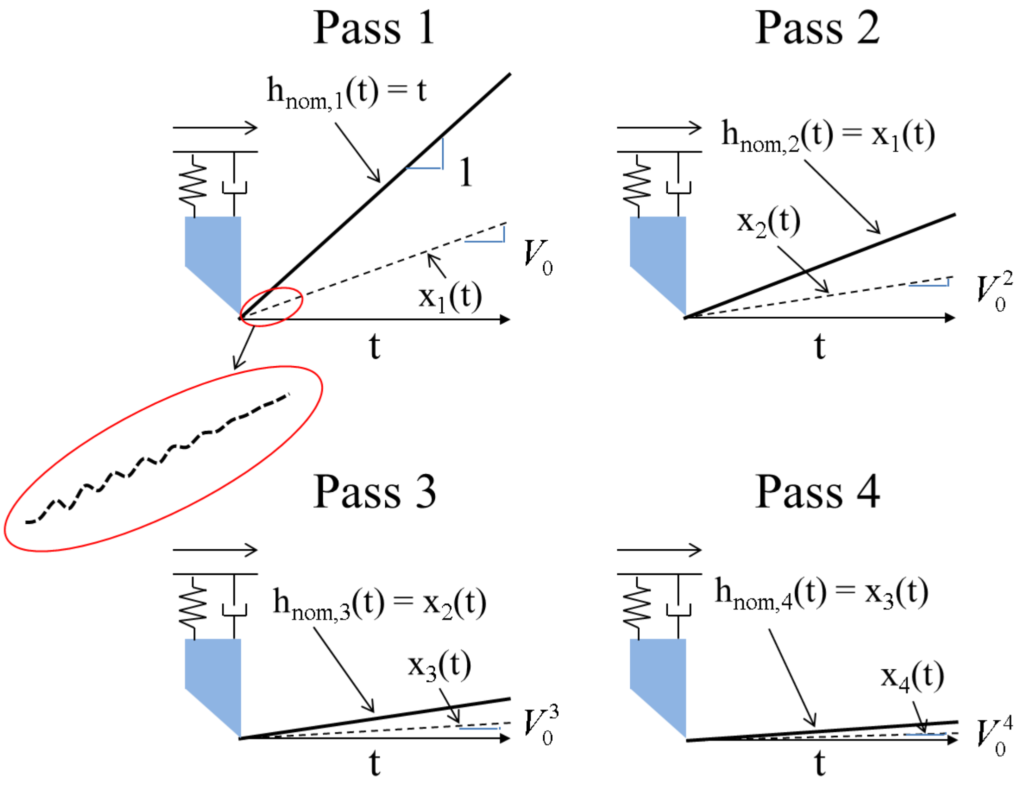

Figure 13: Illustration of the first four sequential responses, where the dynamic response from each pass becomes the input function, h_{nom}, for the next pass.

It is worth noting at this time that a slope of one is used to describe the initial material profile shape for simplicity in the calculations. Because this is a linear system, the sequential responses can be scaled to reflect the appropriate machining conditions.

Also note that the initial conditions for each successive pass will always be zero velocity and zero displacement. When the sequential responses are applied in Equation 2.17, the sequential responses which begin at the start of each new part rotation are simply added to the responses from previous revolutions. The responses from the previous revolutions already account for the conditions of the tool at the instant a new rotation begins. As such, the contribution of the material left behind from the previous sequential response can be added to the total response assuming zero velocity and zero position initial conditions (see Figure 12).

2.4.1 Sequential Response Calculation

The sequential responses are calculated by repeatedly solving Equation 2.18, which is a modified form of Equation 2.15. In Equation 2.18 the h_{nom} term is replaced by x_{j-1} which is the previous sequential response. The initial function (or history function) used to initiate Equation 2.18 is $x_0 = t$ for the ramp input shown in Figure 13.

$$\ddot{x}_j + \frac{c}{m}\dot{x}_j + \frac{k_p}{m}x_j = \frac{bR}{m}x_{j-1}, \quad x_0(t) = t, \; x_j(0) = 0, \; \dot{x}_j(0) = 0 \qquad 2.18$$

Where $k_p = k + bR$, $R = K_s \cos(\beta)$, and b is the depth of cut. The first step is to solve for the first sequential response using the initial input, $x_0(t) = t$, as shown in Equation 2.19.

$$\ddot{x}_1 + \frac{c}{m}\dot{x}_1 + \frac{k_p}{m}x_1 = \frac{bR}{m}t, \qquad x_1(0) = 0, \; \dot{x}_1(0) = 0 \qquad 2.19$$

The particular solution to Equation 2.19 has the form, $x_{p1}(t) = C_1 t + C_2$, which is solved to obtain the steady state solution shown in Equation 2.20. The term, V_0, represents the slope of the linear component of the response (shown in Figure 13), and has the value, $V_0 = \frac{bR}{k_p}$.

$$x_{p1}(t) = C_1 t + C_2 = \frac{bR}{k_p} t - \frac{bRc}{k_p^2} = V_0 \left(t - \frac{c}{k_p} \right) \qquad 2.20$$

The complementary solution to Equation 2.19 has the form:

$$x_{c1}(t) = e^{-At} \left(W_{1,a} \sin(\omega_p t) + W_{1,b} \cos(\omega_p t) \right) \qquad 2.21$$

Where *A* is the exponential decay term calculated using Equation 2.22, and ω_p is the damped natural frequency of the system during the cut (when the effective system stiffness is k_p.) and is calculated using Equation 2.23 or 2.24.

$$A = \zeta \sqrt{\frac{k}{m}} = \frac{c}{2m} \ , \ \zeta = \frac{c}{2\sqrt{km}} \qquad 2.22$$

$$\omega_p = \sqrt{\frac{k_p}{m} \left(1 - \zeta_p^2 \right)} \ , \quad \zeta_p = \frac{c}{2\sqrt{k_p m}} \qquad 2.23$$

$$\omega_p = \sqrt{\frac{k_p}{m} - A^2} \qquad 2.24$$

Combining x_{p1} and x_{c1} and solving for $W_{1,a}$ and $W_{1,a}$ based on the initial conditions, we obtain the first response to the input ramp function, $x_1(t)$, shown in Equation 2.25. The total response and the AC component of $x_1(t)$ is shown in Figure 14. Note the parameters used in the current exercise to find the first sequential responses in Figure 14 through Figure 16 are listed in Table 1.

$$x_1(t) = V_0 \left(e^{-At} \left(\frac{1}{\omega_p} \left(\frac{cA}{k_p} - 1 \right) \sin(\omega_p t) + \frac{c}{k_p} \cos(\omega_p t) \right) + t - \frac{c}{k_p} \right) \qquad 2.25$$

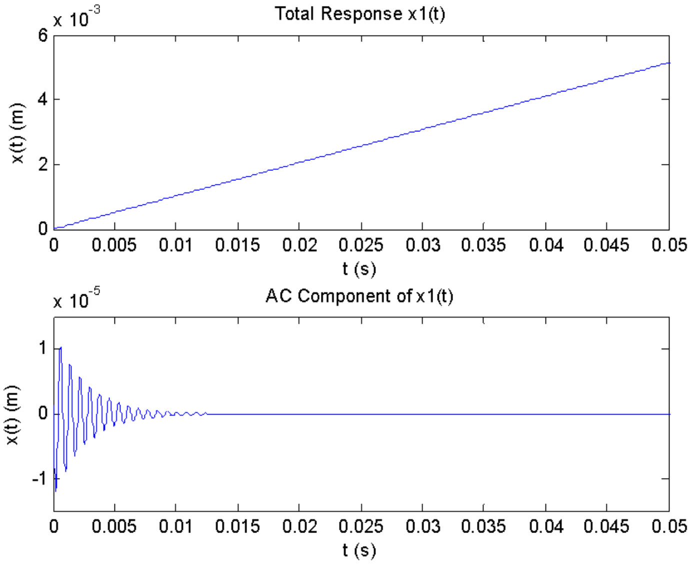

Figure 14: First tool tip response, x_1(t), to the initial ramp input function.

$$G = \frac{1}{\omega_p}\left(\frac{cA}{k_p} - 1\right) = \frac{1}{\omega_p}\left(HA - 1\right),\ \ H = \frac{c}{k_p} \qquad 2.26$$

After replacing the constant terms in Equation 2.25 with G and H (defined in Equation 2.26) the input function to determine the second sequential response becomes, $x_1(t) = V_0\left[e^{-At}\left(G\sin(\omega_p t) + H\cos(\omega_p t)\right) + t - H\right]$, and the ODE is:

$$\ddot{x}_2 + \frac{c}{m}\dot{x}_2 + \frac{k_p}{m}x_2 = \frac{bR}{m}V_0\left[e^{-At}\left(G\sin(\omega_p t) + H\cos(\omega_p t)\right) + t - H\right],\ \ x_2(0) = 0,\ \dot{x}_2(0) = 0 \quad 2.27$$

The solution to Equation 2.27 is rather more cumbersome due to the added complexity of the input function. The responses to the linear and DC components of the input function, seen in sections b and c in Equation 2.28, are found to be x_{p2b} and x_{p2c}. The response to the decaying oscillation portion of the input function, labeled a in Equation 2.28, can be solved for by determining the constant values, W_0, $W_{1,a}$, and $W_{1,b}$, in the particular solution, x_{p2a}. The particular solution to the decaying oscillation portion of the input function was derived under the assumption that the frequency of the response will have the same frequency as the input, and that there will be a phase shift of –π/2 because the frequency of the input is equal to the damped natural frequency of the system. Note that a detailed derivation of the coefficients of x_{p2a} can be found in APPENDIX A.

$$
\begin{gathered}
\ddot{x}_2+\frac{c}{m}\dot{x}_2+\frac{k_p}{m}x_2=\overbrace{\frac{bR}{m}V_0\left[e^{-At}\left(G\sin(\omega_p t)+H\cos(\omega_p t)\right)\right]}^{a}+\overbrace{\frac{bR}{m}V_0 t}^{b}-\overbrace{\frac{bR}{m}V_0 H}^{c},\\
x_{p2a}=W_0e^{-At}\left[W_{1,a}\,t\sin\left(\omega_p t-\frac{\pi}{2}\right)+W_{1,b}\,t\cos\left(\omega_p t-\frac{\pi}{2}\right)\right],\\
x_{p2b}=V_0^2t-V_0^2H,\\
x_{p2c}=-V_0^2H,\\
x_{c2}=e^{-At}\left[W_{2,a}\sin\left(\omega_p t-\frac{\pi}{2}\right)+W_{2,b}\cos\left(\omega_p t-\frac{\pi}{2}\right)\right]
\end{gathered}
\tag{2.28}
$$

After solving for the three particular solutions (x_{p2a}, x_{p2b}, and x_{p2c}) and solving for W_{2a} and W_{2b} based on the initial conditions, the resulting function for the second sequential response is $x_2(t)$ in equation 2.29 and in Figure 15.

$$
x_2(t)=V_0\left(\frac{bR}{m}\right)e^{-At}\left(\begin{array}{l}
\dfrac{G}{2\omega_p}t\sin\left(\omega_p t-\dfrac{\pi}{2}\right)+\dfrac{H}{2\omega_p}t\cos\left(\omega_p t-\dfrac{\pi}{2}\right)\\
\quad-2H\dfrac{m}{k_p}\sin\left(\omega_p t-\dfrac{\pi}{2}\right)\\
\qquad+\left(\dfrac{G}{2\omega_p{}^2}+\dfrac{m}{\omega_p k_p}(1-2HA)\right)\cos\left(\omega_p t-\dfrac{\pi}{2}\right)
\end{array}\right)+V_0^2\left(t-2H\right)
\tag{2.29}
$$

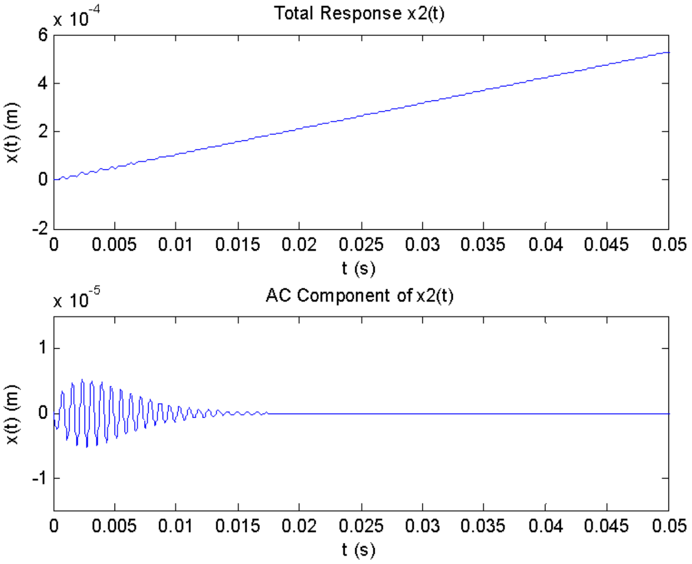

Figure 15: Total response and AC component of $x_2(t)$.

Repeating this process to find the response of the third pass with $h_{nom,3}=x_2(t)$ yields $x_3(t)$ in Equation 2.30 and Figure 16. Note that a detailed explanation of the process used to solve Equation 2.18 is provided in Appendix A.

$$x_3(t)=V_0\left(\frac{bR}{m}\right)^2 e^{-At}\left(\begin{array}{l} \frac{G}{8\omega_p{}^2}t^2\sin\left(\omega_p t-2\frac{\pi}{2}\right)+\frac{H}{8\omega_p{}^2}t^2\cos\left(\omega_p t-2\frac{\pi}{2}\right) \\ -\frac{1}{2\omega_p}\left(\frac{H}{4\omega_p{}^2}+2H\frac{m}{k_p}\right)t\sin\left(\omega_p t-2\frac{\pi}{2}\right) \\ +\frac{1}{2\omega_p}\left(\frac{3G}{4\omega_p{}^2}+\frac{m}{\omega_p k_p}(1-2HA)\right)t\cos\left(\omega_p t-2\frac{\pi}{2}\right) \\ -\left(\frac{1}{2\omega_p}\left(\frac{3G}{4\omega_p{}^2}+\frac{m}{\omega_p k_p}(1-2HA)\right)-\frac{1}{\omega_p}\left(\frac{m}{k_p}\right)^2(1-3HA)\right)\sin\left(\omega_p t-2\frac{\pi}{2}\right) \\ -3H\left(\frac{m}{k_p}\right)^2\cos\left(\omega_p t-2\frac{\pi}{2}\right) \end{array}\right)+V_0^3\left(t-3H\right) \quad 2.30$$

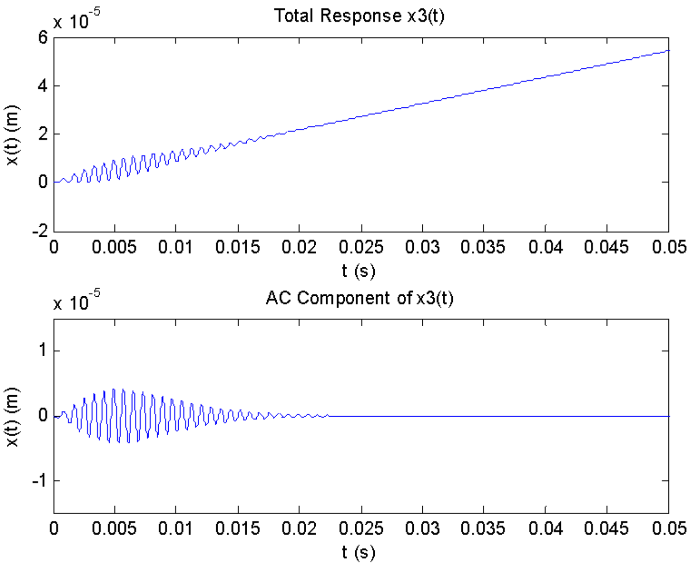

Figure 16: Total response and AC component of x_3(t).

As the number of sequential solutions increases it becomes increasingly difficult (and impractical) to solve them by hand. However, there are several patterns that emerge in the sequential solutions that can be used to develop a general expression for the solutions.

It is apparent from the first three sequential responses (Equations 2.25, 2.29 and 2.30) that the responses are predominately determined by an increasing number of sine and cosine terms which are multiplied by increasing powers of t. The first three responses are again displayed in Equation 2.31, this time with phase shifts within each response such that the G term is always associated with sine, and the H term with cosine.

Looking at Equation 2.31, several patterns emerge in the sequential response solutions as the number of passes increases. First, the linear component of the responses follows the pattern; $x_{j,Lin} = V_0^{\,j}\left(t - jH\right)$, and second, the term in front of the series of sine and cosine terms follows the pattern: $V_0\left(\frac{bR}{m}\right)^{j-1} e^{-At}$.

$$x_1(t) = V_0 e^{-At}\left(G\sin(\omega_p t) + H\cos(\omega_p t)\right) + V_0\left(t - H\right),$$

$$x_2(t) = V_0\left(\frac{bR}{m}\right)e^{-At}\left(\begin{array}{c} \dfrac{G}{2\omega_p}t\sin\left(\omega_p t - \dfrac{\pi}{2}\right) + \dfrac{H}{2\omega_p}t\cos\left(\omega_p t - \dfrac{\pi}{2}\right) \\ +\left(\dfrac{G}{2\omega_p{}^2} + \dfrac{m}{\omega_p k_p}\right)\sin\left(\omega_p t\right) + 2H\dfrac{m}{k_p}\cos\left(\omega_p t\right) \end{array}\right) + V_0^2\left(t - 2H\right),$$

$$x_3(t) = V_0\left(\frac{bR}{m}\right)^2 e^{-At}\left(\begin{array}{c} \dfrac{G}{8\omega_p{}^2}t^2\sin\left(\omega_p t - 2\dfrac{\pi}{2}\right) + \dfrac{H}{8\omega_p{}^2}t^2\cos\left(\omega_p t - 2\dfrac{\pi}{2}\right) \\ +\dfrac{1}{2\omega_p}\left(\dfrac{3G}{4\omega_p{}^2} + \dfrac{m}{\omega_p k_p}\right)t\sin\left(\omega_p t - \dfrac{\pi}{2}\right) + \dfrac{1}{2\omega_p}\left(\dfrac{H}{4\omega_p{}^2} + 2H\dfrac{m}{k_p}\right)t\cos\left(\omega_p t - \dfrac{\pi}{2}\right) \\ +\left(\dfrac{1}{2\omega_p}\left(\dfrac{3G}{4\omega_p{}^2} + \dfrac{m}{\omega_p k_p}\right) - \dfrac{1}{\omega_p}\left(\dfrac{m}{k_p}\right)^2\right)\sin\left(\omega_p t\right) + 3H\left(\dfrac{m}{k_p}\right)^2\cos\left(\omega_p t\right) \end{array}\right) + V_0^3\left(t - 3H\right) \qquad 2.31$$

A third pattern that can be readily observed from Equation 2.31 is the relationship between the power of t and the phase shift which ensures that all sine terms are associated with G, and cosine terms with H. The phase shift for each power of t is equal to the order of t multiplied by negative π/2, and the highest power of t for each solution is j-1 for the jth solution.

The final component of Equation 2.31 to be generalized is the coefficients which appear in in front of the sine and cosine terms. The highest power coefficients can be calculated directly using Equation 2.32 for the sine terms and Equation 2.33 for the cosine terms (See APPENDIX A).

$$W_{1,a} = \frac{G}{(j-1)!(2\omega_p)^{(j-1)}} \qquad 2.32$$

$$W_{1,b} = \frac{H}{(j-1)!(2\omega_p)^{(j-1)}} \qquad 2.33$$

The remaining coefficients are dependent on other coefficients of the same solution and coefficients from the previous solution. In the case of the t^0 terms, the coefficients are dependent on all of the particular solutions of the solution and the initial conditions. The expressions for these coefficients are best expressed in matrix form as described in the next section and in APPENDIX A.

2.4.2 Matrix Form of Sequential Responses

With the components of the sequential responses generalized, it is possible to represent them in matrix form to obtain the time domain response for any number of sequential passes. The generalized matrix solution which produces the tool tip motion as a function of time for each sequential response is shown in Equation 2.34 where each component represents one of the patterns described in the previous section.

$$\mathbf{X}(t) = \begin{bmatrix} x_1(t) \\ x_2(t) \\ \vdots \\ x_N(t) \end{bmatrix} = \mathbf{O}_w \left[\mathbf{W}_G \mathbf{L}_{G,x}(t) + \mathbf{W}_H \mathbf{L}_{H,x}(t) \right] + \mathbf{S}_x(t) \qquad 2.34$$

$\mathbf{S}_x(t)$ is the linear component of the solutions and is calculated in Equation 2.35, where N is the maximum number of part rotations to be modeled.

$$\mathbf{S}_x(t) = \begin{bmatrix} V_0(t-H) \\ V_0^{2}(t-2H) \\ \vdots \\ V_0^{j}(t-jH) \end{bmatrix}_{j=1,2,\dots,N} \qquad 2.35$$

The **W** and **L** matrices piece together the sine and cosine terms with the correct power of t and phase shift (**L**) with the corresponding coefficient (**W**). The G and H subscripts indicate which initial constant the matrices are associated with. The **L** matrices are shown in Equation 2.36, and the **W** matrices in Equation 2.37.

$$\mathbf{L}_{G,x}(t)=\begin{bmatrix} e^{-At}\sin\left(\omega_p t\right) \\ te^{-At}\sin\left(\omega_p t-\frac{\pi}{2}\right) \\ \vdots \\ t^{j-1}e^{-At}\sin\left(\omega_p t-(j-1)\frac{\pi}{2}\right) \end{bmatrix}_{j=1,.,N} ;\ \mathbf{L}_{H,x}(t)=\begin{bmatrix} e^{-At}\cos\left(\omega_p t\right) \\ te^{-At}\cos\left(\omega_p t-\frac{\pi}{2}\right) \\ \vdots \\ t^{j-1}e^{-At}\cos\left(\omega_p t-(j-1)\frac{\pi}{2}\right) \end{bmatrix}_{j=1,.,N} \qquad 2.36$$

$$\mathbf{W}_G=\begin{bmatrix} W_{G1,1} & 0 & 0 & 0 \\ W_{G2,1} & W_{G2,2} & 0 & 0 \\ \vdots & W_{G3,2} & \ddots & 0 \\ W_{G\,j,1} & W_{G\,j,i} & \cdots & W_{G\,j,j} \end{bmatrix}_{j,i=1,.,N} ;\mathbf{W}_H=\begin{bmatrix} W_{H1,1} & 0 & 0 & 0 \\ W_{H2,1} & W_{H2,2} & 0 & 0 \\ \vdots & W_{H3,2} & \ddots & 0 \\ W_{H\,j,1} & W_{H\,j,i} & \cdots & W_{H\,j,j} \end{bmatrix}_{j,i=1,.,N} \qquad 2.37$$

The coefficients of the **W** matrices are calculated based on their position in the matrix. The diagonal terms, which are associated with the highest power of t for the jth sequential response, are calculated using Equation 2.38.

$$W_{G\,j,j}=\frac{G}{(j-1)!(2\omega_p)^{(j-1)}}\ ;\ W_{H\,j,j}=\frac{H}{(j-1)!(2\omega_p)^{(j-1)}} \qquad 2.38$$

The coefficients of the first columns of the **W** matrices, which are associated with the t of zero power, are calculated using Equation 2.39.

$$W_{G\,j,1}=\frac{1}{\omega_p}\left(\mathbf{W}_{G\,j,i+1}-\left(\frac{m}{k_p}\right)^{j-1}\right);\ W_{H\,j,1}=H\ j\left(\frac{m}{k_p}\right)^{j-1} \qquad 2.39$$

The remaining coefficients for the lower triangle of the **W** matrices are dependent on the values of the coefficients of the previous sequential response ($\mathbf{W}_{j-1,i-1}$) and the coefficient of the higher order term of the current sequential response ($\mathbf{W}_{j,i+1}$). The lower triangle coefficients are calculated using Equation 2.40, and the upper triangle coefficients are all zero.

$$W_{G\,j,i}=\frac{1}{2\omega_p\left(i-1\right)}\left[i\left(i-1\right)W_{G\,j,i+1}+W_{G\,j-1,i-1}\right]$$
$$W_{H\,j,i}=\frac{1}{2\omega_p\left(i-1\right)}\left[i\left(i-1\right)W_{H\,j,i+1}+W_{H\,j-1,i-1}\right] \qquad 2.40$$

Finally, the coefficient in front of the oscillating terms is accounted for by **O**$_w$ as shown in Equation 2.41.

$$O_W=\begin{bmatrix} V_0 & 0 & 0 & 0 \\ 0 & V_0\left(\frac{bR}{m}\right) & 0 & 0 \\ 0 & 0 & \ddots & 0 \\ 0 & 0 & 0 & V_0\left(\frac{bR}{m}\right)^{j-1} \end{bmatrix}_{j=1,2,\ldots,N} \qquad 2.41$$

The x subscripts in Equation 2.34 indicate that these are the matrices used to solve for position as a function of time. Matrix forms for the sequential solutions of velocity and acceleration as a function of time are provided in APPENDIX B.

2.5Analytical vs. Numerical Simulations for Turning

The matrix solution provides a structured method for determining the sequential responses, and we can now apply the responses to Equation 2.17 to generate the tool tip motion for the turning operation in Figure 10. In order to compare the results of the analytical model to the numerical simulations, the sequential responses which compose the analytical solution must all be scaled by a factor of RPM**fr*/60, where *fr* is the feed per revolution in meters. As all sequential responses are derived based on an initial input slope of one meter per second, the actual responses must be scaled to reflect the global feed rate of the tool during the simulation, and the global feed rate can be found as RPM**fr*/60. Two examples will be shown, both of which have a depth of cut, b, set at 10% above $b_{lim,crit}$, and the system parameters are shown in Table 1.

Table 1: System parameters for turning examples

k	5E7 N/m
m	0.88 kg
c	663.325 Ns/m (ζ = 0.05)
K_s	2E9 N/m^2
B	70 degrees
Feed per rev	.076 mm (0.003 inch)

In example 1 the operation is simulated at 2000 rpm and in example 2 it is simulated at 12000 rpm. In Figure 17 the two examples are shown on the stability lobe diagram for this system, which predicts that example 1 will be unstable and example 2 will be stable.

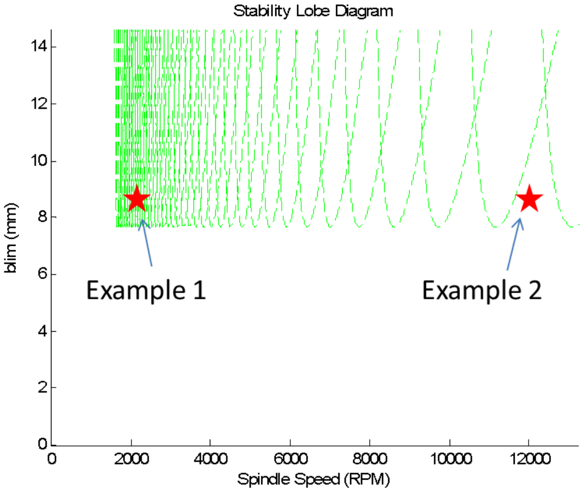

Figure 17: Stability lobe diagram showing the predicted stability for examples 1 and 2.

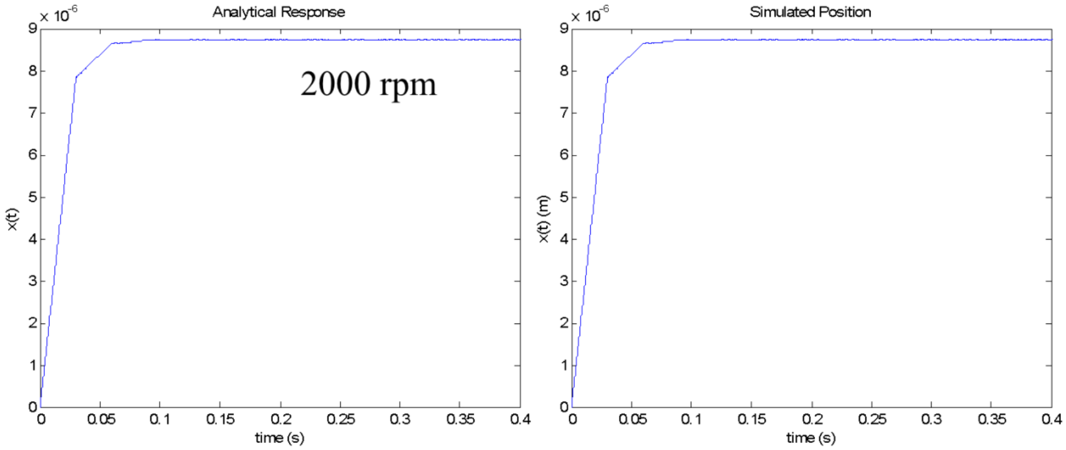

Figure 18: Example 1 positional response of the tool tip generated using analytical model (left) compared with the same response from a numerical simulation (right).

The results from Figure 18 show the positional response from the analytical model and the numerical simulation. The position responses shown here are the tool displacements relative to the nominal position of the tool, which eliminates the global linear feed of the tool during the operation. The results from Figure 18 show that the response from the analytical solution closely matches the response from the numerical simulation. However, the dominance of the linear component of the response makes it difficult to see details of the AC component responses. In Figure 19 the acceleration response is applied using Equation 12.23 in APPENDIX B to eliminate the linear component. Here again, the vibrational component of the tool tip response using the analytical solution matches that of the numerical solution.

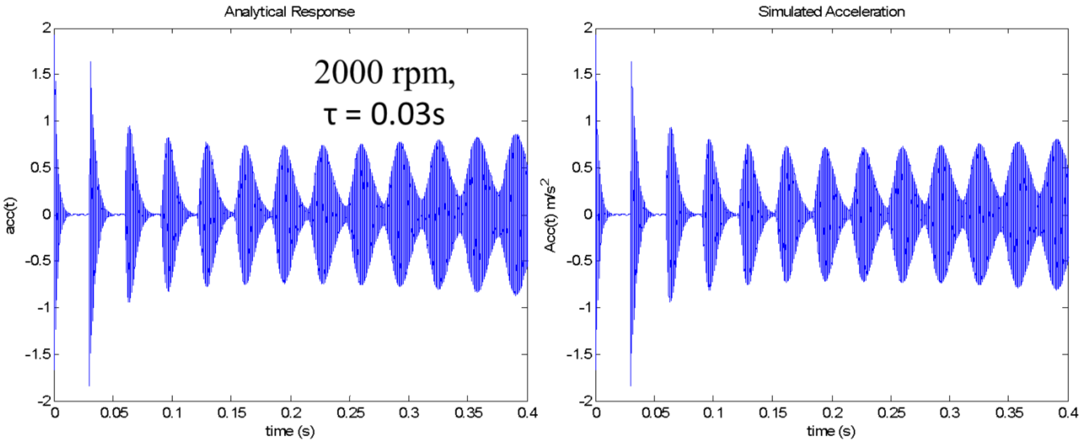

Figure 19: Example 1 acceleration response of the tool tip generated using analytical model (left) compared with the same response from a numerical simulation (right).

The acceleration response of the tool tip for example 2 is shown in Figure 20, which also shows a close agreement between the analytical and numerical solutions. The resulting differences between the accelerations predicted analytically and numerically in Figure 20 are dependent on the time step used for the numerical simulation. In Figure 21, the errors between the two acceleration results are shown as the time step is decreased from 4E-4 seconds (approximately 20 data points per tool period) to 4E-8 seconds (approximately 20,000 data points per tool period). These results show that as the time step is refined, the numerical simulation approaches the results predicted analytically, where the maximum error is reduced from 0.3 to 8E-8 m/s^2 as the time step decreases from 4E-4 to 4E-8 s.

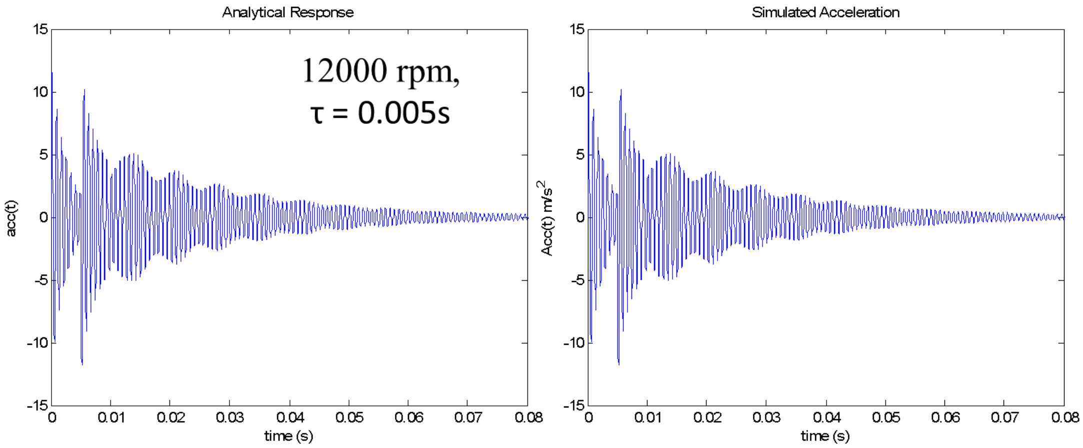

Figure 20: Example 2 acceleration response of the tool tip generated using analytical model (left) compared with the same response from a numerical simulation (right).

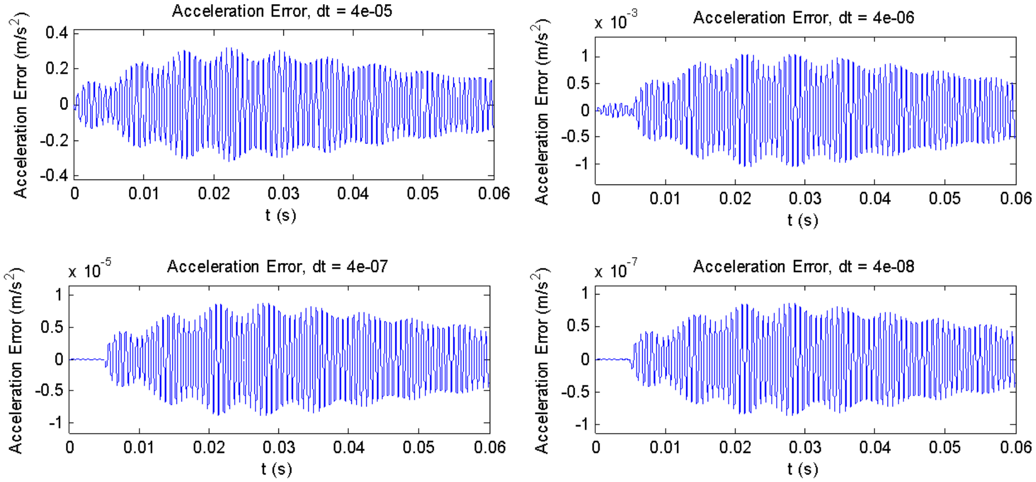

Figure 21: Error in the accelerations predicted analytically and numerically as the time step for the numerical simulation is reduced from 4E-5 s to 4E-8 s for Example 2 results from Figure 20.

The time domain responses for the two examples in Figure 19 and Figure 20 were obtained by applying the sequential responses to Equation 2.17. This process is illustrated in Figure 22, where the individual acceleration components of the sequential responses are plotted along with the total acceleration response for both examples. Because the depth of cut, b, is the same in both examples, the individual acceleration components which combine to generate the total response are the same for both examples (although they have different amplitude scales). As such, the only difference between the two examples is the value of the time delay, τ.

In example 1 τ=0.03s, corresponding to a spindle speed of 2000 RPM, and the individual pulses are spread out far enough in time that there is little interaction between them, and each pulse can be easily observed in the total response. The lack of interaction in example 1 between the individual pulses means that the trend of the total response will likely follow the trend of the individual responses (i.e. if the amplitudes of the individual vibrations grow, so will the total response).

In example 2, τ is much smaller due to higher spindle speed, and the individual vibration pulses have significant overlap. The resulting interactions between the multiple vibration pulses have a cumulative constructive or destructive interference effect, which causes the total response to be stable or unstable depending on the value of τ. In example 2, the cumulative destructive interference between the multiple vibration pulses create a circumstance where the total response has decreasing amplitude with time while the individual acceleration vibrations increase over time.

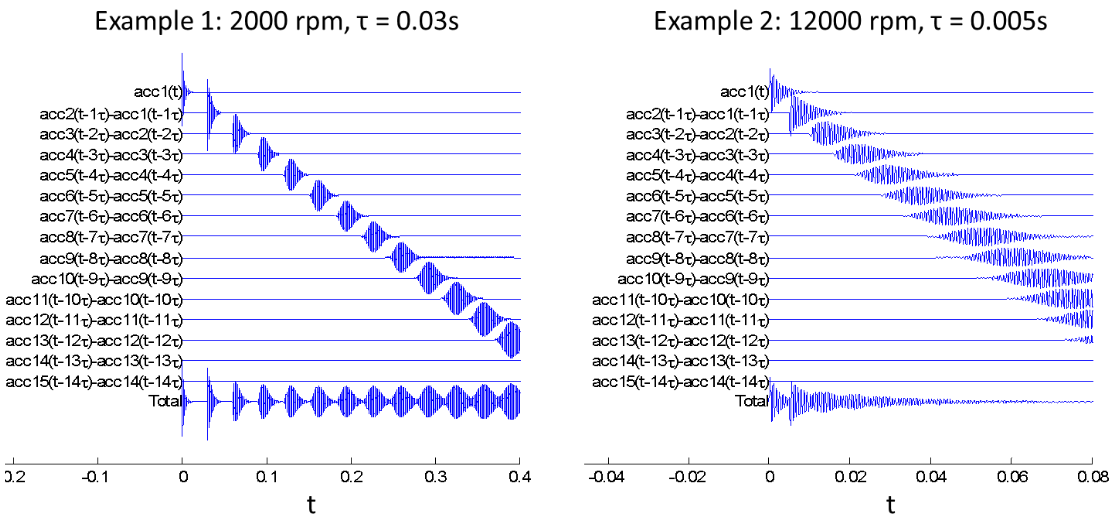

Figure 22: Illustration of how the total tool tip response is generated from the sequential responses.

2.6Stability Analysis Using Sequential Responses

The primary advantage of the analytical solution is that it allows us to directly determine the behavior of the system at any point in time without the use of iterative numerical techniques. This is especially useful for determining the stability of the system. In Figure 23, the AC components of the positional response are shown for the two examples discussed in the previous section. The solid blue lines in Figure 23 represent the full tool tip response for each point in time; however, all of this information is not necessary for determining stability. Nominally, only two data points are required to determine whether the vibration amplitudes grow or decrease over time. In Figure 23, these two data points are amp_1 at t_1 and amp_2 at t_2, and the stability of the system can be predicted depending on whether the vibration amplitude at t_2 is greater than or less than the amplitude at t_1 (note that the strategy used to select t_1 and t_2 to evaluate stability is discussed in the next section). Using this approach it is possible to predict stability of a system for any depth of cut, b, and spindle speed.

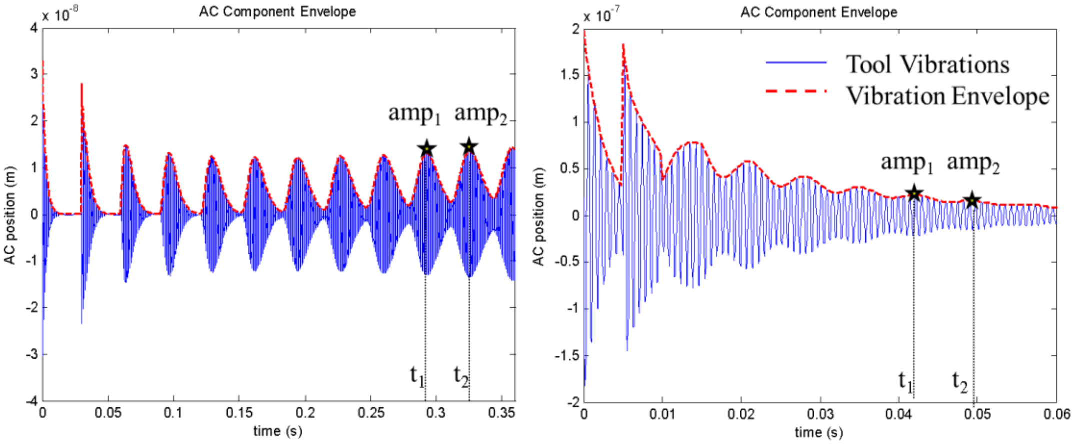

Figure 23: AC component of the tool position with the vibration envelopes for Examples 1 and 2.

The primary objective in determining the stability of the system based on the system parameters is to find the boundary between the stable and unstable regions in the parameter space (spindle speed and depth of cut). This boundary is typically found using the FRF approach which produces multiple “stability lobes” which represents the maximum stable depth of cut as the spindle speed is varied. As the time domain approach and the FRF approach are both used to model the same system, we would expect to find the same limit of stability using either approach.

A program was created to determine how well the stability limit predicted using the time domain approach agrees with the stability lobe diagram predicted using the FRF approach. The program calculates the magnitude of the vibration envelop (see Figure 23) at two points in time over a range of depths of cut, b, at a fixed spindle speed. The difference in the vibration magnitudes is recorded for each value of b, and the limit of stability, b_{lim}, is found as the value of b at which both vibration magnitudes are equal. This process repeats for multiple spindle speeds to produce a stability lobe diagram. The resulting stability lobe diagram for the system described in Table 1 is shown in Figure 24 along with the stability lobe diagram predicted using the frequency response approach.

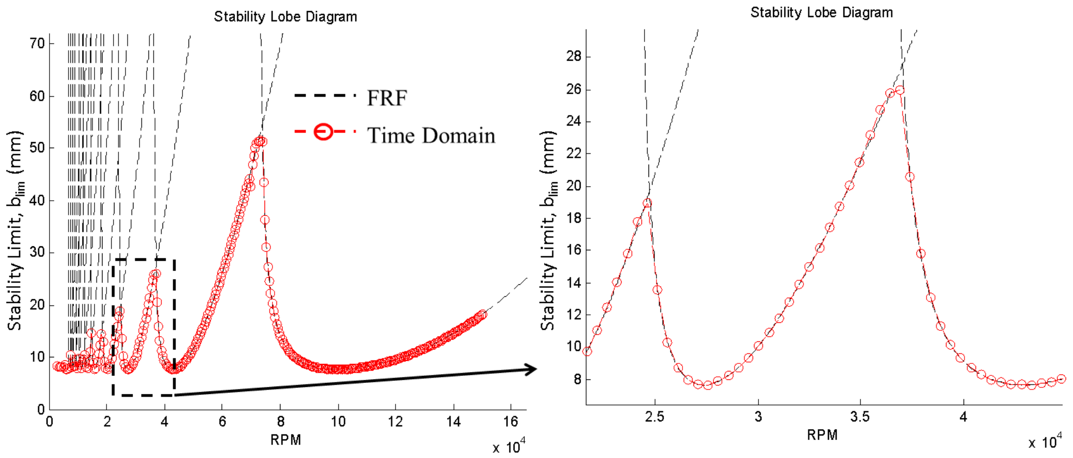

Figure 24: Stability lobe diagram derived using the Frequency Response Function (FRF) and the time domain equations for the system described in Table 1.

Note that the stability lobe diagram is shown here over a range of 3,000 to 150,000 RPM. These spindle speeds are extremely high for turning operations, however, it is convenient to compare the stability predictions of the time domain and frequency response approaches at higher speeds where the higher peaks in the stable regions occur.

2.7Sequential Response Equation Analysis

The equations developed thus far to describe the sequential responses represent the exact solutions for an initial ramp input. This exact form of the sequential responses is capable of generating the time response of the tool analytically, and can be used to generate a stability lobe diagram which matches the stability lobe diagram predicted using the FRF approach. However, the complexity of the exact sequential responses increases as the number of responses increases, and it becomes difficult to perform additional analytical studies based on these equations. As such, it is convenient for analysis purposes to reduce the equations into a more concise, approximate form.

Looking at the W coefficient matrices in equations 2.37 through 2.40, the values of the coefficients decrease by approximately a factor of $1/\omega_p$ as the power of t decreases, where ω_p is the natural damped frequency of the system in rad/s (ω_p is approximately 8000 rad/s in the example in Table 1). This effect can be seen in equation 2.42 where the coefficients of the first five responses are shown in matrix form. In equation 2.42, each row corresponds to the coefficients for one of the sequential responses, and each column corresponds to a specific power of t, such that the coefficients of column 2 are multiplied by $t\sin\left(\omega_p t - \pi/2\right)$, and coefficients from column 4 are multiplied by $t^3\sin\left(\omega_p t - 3\pi/2\right)$, and so on. For each response, the highest power diagonal coefficients are calculated directly using equation 2.38, and the remaining coefficients to the left of the diagonal term are calculated using equations 2.39 and 2.40. Because of the influence of ω_p in equations 2.39 and 2.40, it can be seen that the values of the coefficients are highest for the diagonal terms, and each subsequent term to the left decreases by approximately three orders of magnitude. From this, it can be assumed that the AC component of each response is dominated by the highest order oscillation term if ω_p is large, and each response can be approximated by neglecting the lower order coefficients.

$$\mathbf{W}_{G,Ex} = \begin{bmatrix} -1.25\text{E-}4 & 0 & 0 & 0 & 0 \\ -1.88\text{E-}4 & -4.99\text{E-}1 & 0 & 0 & 0 \\ -2.36\text{E-}4 & -8.76\text{E-}1 & -9.94\text{E+}2 & 0 & 0 \\ -2.75\text{E-}4 & -1.19\text{E+}0 & -1.99\text{E+}3 & -1.32\text{E+}6 & 0 \\ -3.10\text{E-}4 & -1.47\text{E+}0 & -2.93\text{E+}3 & -2.98\text{E+}6 & -1.31\text{E+}9 \end{bmatrix} \qquad 2.42$$

After neglecting all lower triangle terms in the **W** coefficient matrices in equation 2.34, the solution form for the AC component of the sequential responses reduces to equation 2.43. In Figure 25 the AC components from the approximate sequential response solution (equation 2.43) are compared with the exact solutions for the first five responses. The results from this comparison show that there are some differences between the exact and approximate solutions, especially at low values of *t*; however, the majority of the vibration behavior over the duration of the sequential responses is captured in the approximate expression.

$$x_{AC,Approx,j}(t)=V_0\left(\frac{bR}{m}\right)^{j-1}\left(\frac{1}{\omega_p\left(j-1\right)!(2\omega_p)^{j-1}}\right)t^{j-1}e^{-At}\left(G\sin\left(\omega_p t-(j-1)\frac{\pi}{2}\right)+H\cos\left(\omega_p t-(j-1)\frac{\pi}{2}\right)\right) \qquad 2.43$$

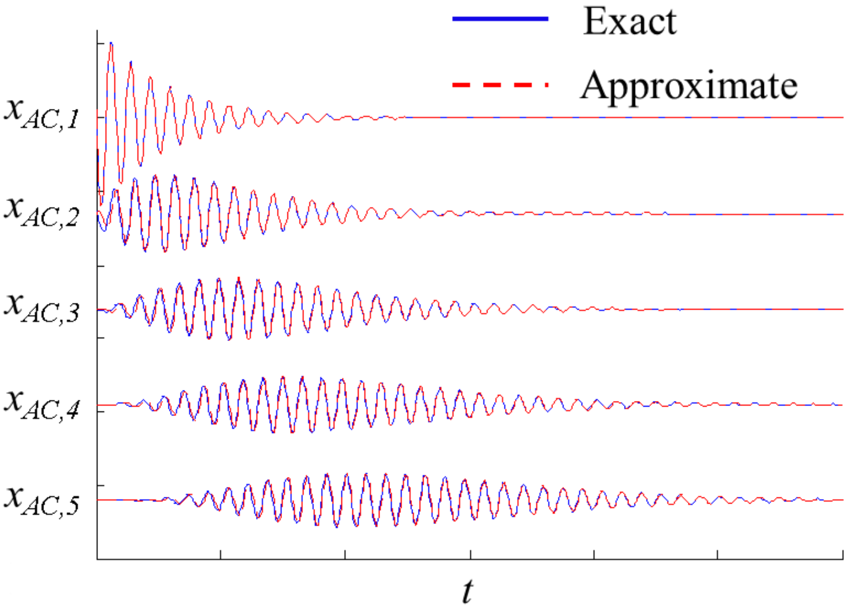

Figure 25: Illustration of the vibrational envelope for the first ten sequential responses.

The approximate form of the sequential responses can be further reduced if the actual magnitude and phase of the responses are not required. This is the case when performing stability analysis, where the objective is to determine whether amplitudes grow or decrease over time. As the global response of the tool is determined by superimposing the individual sequential responses together, the only information required to determine stability are the amplitudes and the phases of the responses relative to each other. As such, all the constant terms in equation 2.43 can be neglected and the Gsin(θ) and Hcos(θ) terms can be combined into a single oscillatory term. The resulting expression describing the relative amplitudes and phases of the sequential responses is provided in equation 2.44. The vibrations in equation 2.44are normalized such that the initial response is a decaying oscillation of an initial magnitude of one, such that $x_{Norm,1}\left(t\right)=e^{\left(i\omega_p-A\right)t}$, and the remaining responses have amplitudes and phases relative to $x_{Norm,1}$.

$$x_{Norm,j}(t)=\frac{1}{\left(j-1\right)!}\left(\frac{bR}{2m\omega_p}\right)^{j-1}t^{j-1}e^{-At}e^{i\left(\omega_p t-\left(j-1\right)\frac{\pi}{2}\right)} \qquad 2.44$$

2.8Stability Analysis

The stability lobe diagram is the primary outcome of stability analysis for machining operations. Shown in Figure 26, the stability lobe diagram shows the stable and unstable regions as a function of the depth of cut, b, and the spindle speed. There are two important features of the stability lobe diagram which will be used to compare the results obtained from the frequency domain approach and the approximate time domain approach using equation 2.44. The first feature is the value of $b_{lim,crit}$, which is the maximum depth of cut at which the operation will be stable at any spindle speed, and the second is b_{lim}, which represents the boundary between the stable and unstable regions, and gives the maximum stable depth of cut at a given spindle speed.

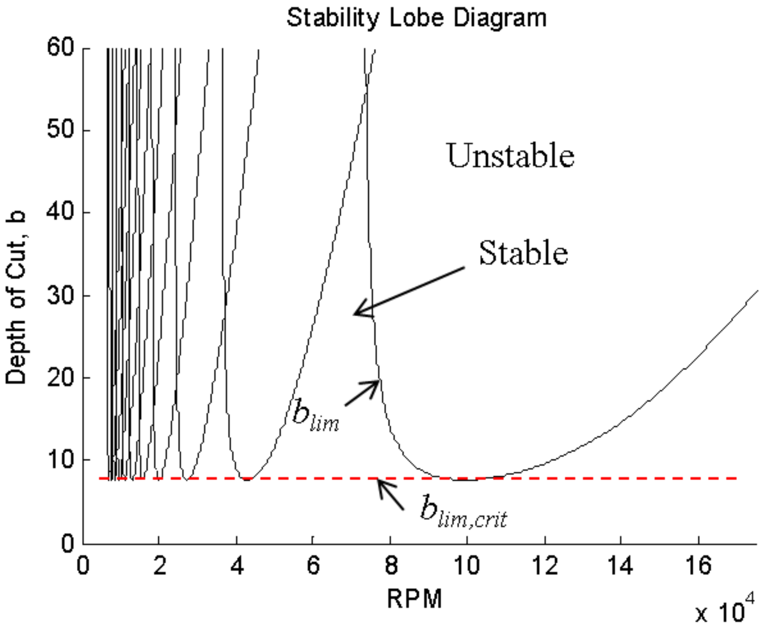

Figure 26: Stability lobe diagram, showing the regions of stability and instability based on the spindle speed and the depth of cut.

2.8.1Calculation of $b_{lim,crit}$

An approach to determine a value of $b_{lim,crit}$ based on the time domain equations can be found by observing the behavior of the sequential responses as the value of b is varied. In Figure 27, the first ten sequential responses are plotted using the equation 2.44 for two different values of *b*. It can be seen from both sets of responses that each individual response contains a pulse of vibration that is the result of excitation from the previous vibration pulse, starting with the initial decaying oscillation. With each successive pass the pulses widen out and the location of the maximum amplitude shifts later in time. The primary difference between the two sets of responses in Figure 27 is that the vibration magnitudes decrease when *b* is less than $b_{lim,crit}$, and increase with each successive pass when *b* is greater than $b_{lim,crit}$. As the growth rate of the sequential response amplitudes depends on the value of b, the strategy for finding $b_{lim,crit}$ is to determine the value of b at which the maximum amplitudes of subsequent vibration pulses neither increase or decrease as the number of responses increases. As the total response of the tool is a combination of the sequential responses, it can be assumed that if the sequential response amplitudes diminish to zero, than the total response must also diminish over time (stable condition). Furthermore, if the sequential responses grow over time, than there is a potential that the total response will also grow (unstable condition).

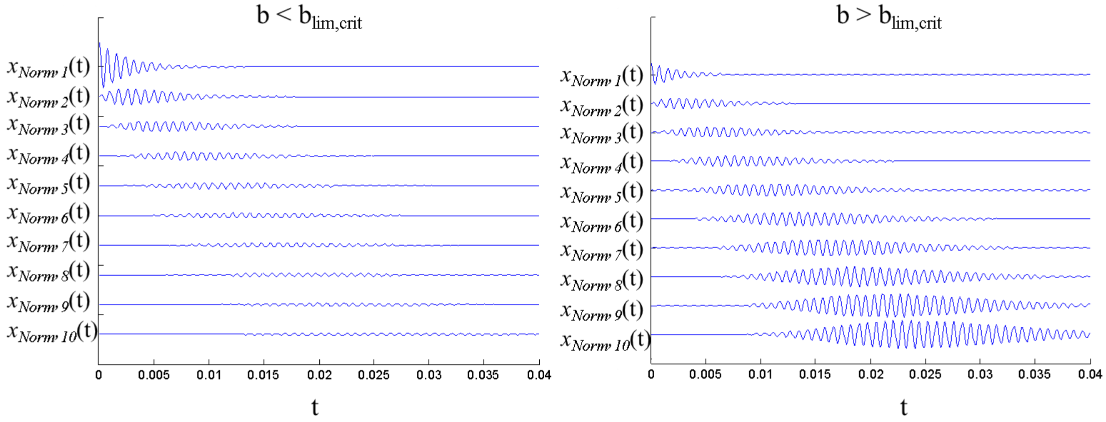

Figure 27: First ten sequential responses when b<$b_{lim,crit}$ (left) and when b>$b_{lim,crit}$ (right) approximated using equation 2.44.

In order to determine the behavior of the sequential response amplitudes, it is convenient to use the absolute value form of Equation 2.44 which describes the oscillation envelopes of the sequential responses (see Equation 2.45). The vibration envelopes of the first ten sequential responses are plotted in Figure 28, where the same amplitude trends can be observed depending on the value of b.

$$x_{Env,j}(t)=\frac{1}{(j-1)!}\left(\frac{bR}{2m\omega_p}\right)^{j-1}t^{j-1}e^{-At} \qquad 2.45$$

From Figure 28 it can be observed that there is a regular spacing in the time at which the maximum amplitudes occur from one response to the next. By differentiating equation 2.45 and setting the result equal to zero, it can be determined that the maximum amplitude of the jth response occurs at time, $t = \frac{(j-1)}{A}$ (see APPENDIX C for derivation). The time of the maximum amplitude can then be substituted into equation 2.45 to determine the maximum amplitude of the jth response, as shown in equation 2.46.

$$x_{Env,max,j} = \frac{1}{(j-1)!}\left(\frac{bR}{2m\omega_p}\right)^{j-1}\left(\frac{j-1}{A}\right)^{j-1} e^{-(j-1)} \qquad 2.46$$

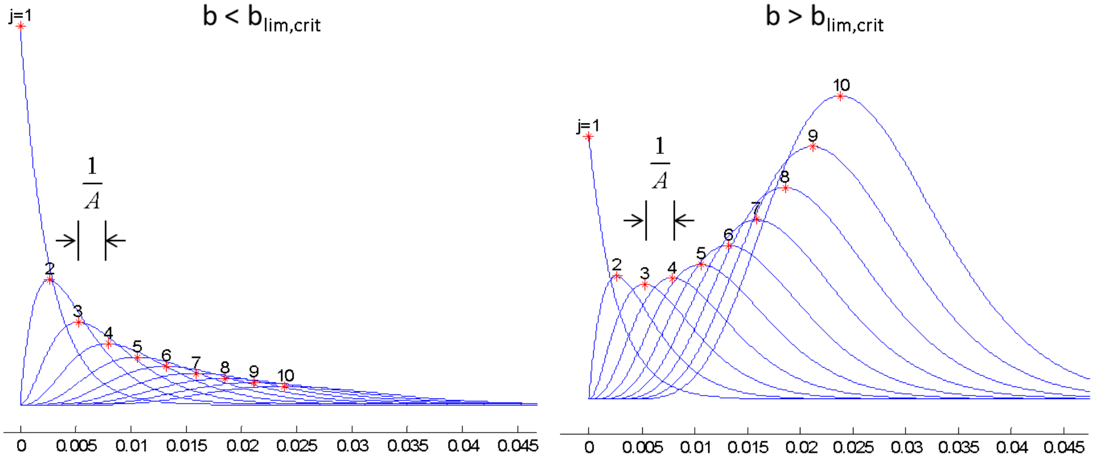

Figure 28: Illustration of how the maximum amplitudes of the vibrational envelope either decrease or increase which each subsequent pass depending on the value of b.

$b_{lim,crit}$ is calculated as the value of b at which the maximum amplitudes from two subsequent responses are equal as the number of responses goes to infinity, as shown in equation 2.47.

$$b_{lim,crit} \text{ when } x_{Env,max,j} = x_{Env,max,j+1} \text{ as } j \to \infty \qquad 2.47$$

To evaluate this expression, equation 2.46 is used and two subsequent maximum amplitudes are set to be equal, as shown in Equation 2.48.

$$\left(\frac{1}{(j-1)!}\right)\left(\frac{bR}{2m\omega_p}\right)^{j-1}\left(\frac{j-1}{A}\right)^{j-1} e^{-(j-1)} = \left(\frac{1}{(j)!}\right)\left(\frac{bR}{2m\omega_p}\right)^{j}\left(\frac{j}{A}\right)^{j} e^{-(j)} \qquad 2.48$$

After evaluating equation 2.48 as *j* goes to infinity, the expression for b reduces to Equation 2.49.

$$b = \frac{2Am\omega_p}{R} \qquad 2.49$$

After applying the identities, $\omega_p = \sqrt{\frac{k}{m} + \frac{bR}{m} - \zeta^2 \frac{k}{m}}$, $A = \zeta\sqrt{\frac{k}{m}}$, and $R = K_s \cos\beta$, and solving for *b*, the resulting expression for $b_{lim,crit}$, which satisfies equation 2.48 is:

$$b_{lim,crit} = \frac{2k\zeta}{K_s \cos\beta}(\zeta + 1) \qquad 2.50$$

The expression for $b_{lim,crit}$ in equation 2.50 derived from the sequential response equations is the same expression for $b_{lim,crit}$ derived from the frequency response approach. Note that a detailed derivation of $b_{lim,crit}$ using both approaches is provided in APPENDIX C.

2.8.2 Calculation of b_{lim}

The calculation of $b_{lim,crit}$ in the previous section can be achieved by examining the amplitudes of the individual sequential responses as the number of responses increases. The determination of b_{lim} is more involved because we are now interested in the behavior of the total response as a function of the spindle speed. The behavior of the total response can be approximated by applying the normalized sequential response functions in equation 2.44 to equation 2.51.

$$x_{Norm,Total}(t) = \sum_{j=1}^{N} \begin{cases} 0 & ,t < (j-1)\tau \\ x_{Norm,j}\left(t - (j-1)\tau\right) & ,t \geq (j-1)\tau \end{cases} \qquad 2.51$$

Equation 2.51 is a simplification of equation 2.17 which describes the exact tool response for the "double ramp" turning model developed previously. Equation 2.51 neglects the second "negative ramp" input and only considers how the sequential responses resulting from the initial ramp function interact over time. Since the effect of both ramp inputs is the same, the stability behavior resulting from one of the ramp inputs will be the same as for the combination of the two inputs which start at different points in time. For example, since the total response is determined by the effects of two initial excitation events, such that $x_{tot}(t) = C\left(e^{Bt} - e^{B(t-\tau)}\right) = Ce^{Bt}\left(1 - e^{-B\tau}\right)$, then the stability behavior, determined by the sign of B, of the total system is equal to the stability behavior of the individual components as long as $\tau \neq 0$.

The strategy for determining b_{lim} is to calculate the amplitude of the total response according to equation 2.51 at two points in time, and find the value of b at which the two amplitudes are equal. The first thing to consider is how to select the two points in time which will be used during the analysis. From Figure 23, it can be seen that the total response has a wavy oscillation envelope which can lead to errors in the global stability determination if the two points in time are not selected appropriately. The strategy employed here is to select two points in time which correspond to the maximum amplitude locations of two subsequent sequential responses. This concept is illustrated in Figure 29, where the times selected to evaluate the system, t_a and t_b, correspond to the peak amplitudes of the fifth and sixth sequential responses. The times used to evaluate stability can be calculated using Equation 2.52, where N_{Eval} is the number response used to find the peak time, t_a ($N_{Eval} = 5$ in Figure 29). Although times t_a and t_b are not guaranteed to be the local peak locations of the full solution, this approximation strategy does show to be effective when comparing stability limit predictions with stability limits predicted using other techniques (see Figure 30).

$$t_a = \left(N_{Eval} - 1\right)\left(\tau + \frac{1}{A}\right);\ t_b = \left(N_{Eval}\right)\left(\tau + \frac{1}{A}\right) \qquad 2.52$$

t_a and t_b represent the global times at which the total vibration amplitudes are sampled. In order to construct all of the individual responses according to equation 2.51, each individual sequential response must be evaluated at a local time, defined as $t_{a,j}$ and $t_{b,j}$, in equation 2.53 which corresponds to the global times, t_a and t_b, for each individual response. After evaluating all of the sequential responses using equation 2.53, we are left with two vectors describing the relative magnitudes and phases of the sequential responses at t_a and t_b. The magnitude of the total response at times t_a and t_b can then be determined as the absolute value of the vector summation of all of the individual responses, as shown in equation 2.54. The general process used to determine stability based on the depth of cut, b, and the spindle speed is depicted in Figure 29.

$$\begin{aligned} \vec{x}_{a,j}\left(t_{a,j}\right) &= \overbrace{\frac{1}{(j-1)!}\left(\frac{bR}{2m\omega_p}\right)^{j-1} t_{a,j}^{\ j-1} e^{-At_{a,j}}}^{Magnitude}\, e^{i\overbrace{\left(\omega_p t_{a.j} - (j-1)\frac{\pi}{2}\right)}^{Phase\ Angle}};\ t_{a,j} = t_a - \left(j-1\right)\tau \\ \vec{x}_{b,j}\left(t_{a,j}\right) &= \frac{1}{(j-1)!}\left(\frac{bR}{2m\omega_p}\right)^{j-1} t_{b,j}^{\ j-1} e^{-At_{b,j}}\, e^{i\left(\omega_p t_{b.j} - (j-1)\frac{\pi}{2}\right)};\ t_{b,j} = t_b - \left(j-1\right)\tau \end{aligned} \qquad 2.53$$

$$\begin{gathered} \vec{X}_a = \sum \vec{x}_a;\ \vec{X}_b = \sum \vec{x}_b \\ \text{find } b \text{ such that } \left\|\vec{X}_a\right\| = \left\|\vec{X}_b\right\| \end{gathered} \qquad 2.54$$

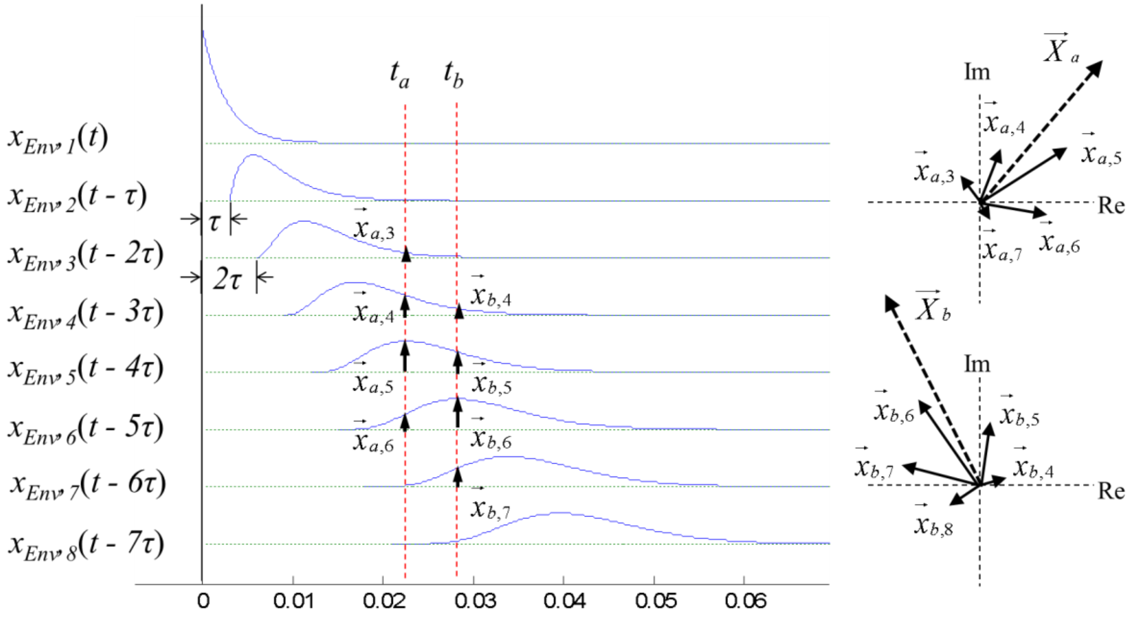

Figure 29: Depiction of the multiple impulses which are active at two points in time.

The process depicted in Figure 29 is used for multiple values of RPM (or τ) to generate a stability lobe diagram based on the approximate time domain equations shown in equation 2.44. In Figure 30 the stability lobe diagram generated by evaluating the two points in time associated with the maximum amplitudes of the 10th and 11th pulses is compared with the stability lobes generated from the frequency response function and the complete time domain solution. These results show that the stability lobe diagram produced using the complete time domain solution is closely aligned with the FRF lobes, while there is a small shift to the right for the stability lobes produced using the approximate solution. While there are some discrepancies, it is clear from Figure 30 that the approximate sequential response equations can be used to effectively approximate stability behavior in a significantly more concise solution form.

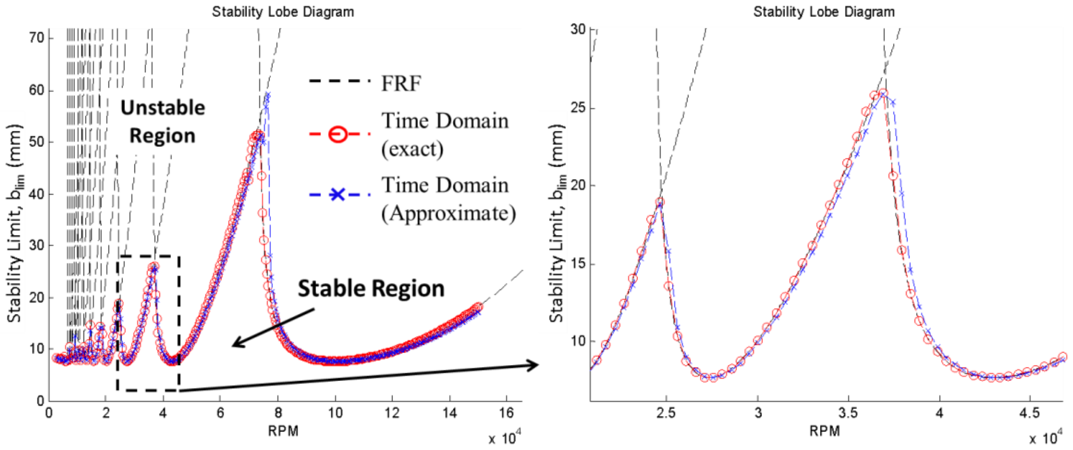

Figure 30: Comparison of stability lobe diagrams generated using the FRF approach, the complete time domain solutions, and the approximate time domain solutions.

2.9Conclusions

In this chapter the sequential response approach for solving DDEs was developed to solve for the time response of a tool analytically. This method is a convenient approach because the sequential responses are independent of the time delay term, so they need only be calculated once for a given depth of cut, b. It was shown through example that the time responses predicted analytically match those found through numerical simulation and that the global stability behavior exhibited by the analytical solutions match those predicted using frequency domain methods.

In the following chapters the basic concepts developed in this chapter for a single mode turning model are expanded to incorporate multiple modes and different machining operations.

CHAPTER 3: EXPANDING TO MULTIPLE MODES

An analytical time domain model is developed to predict the motion of a multi-mode cutting tool during orthogonal turning operations. This model is an extension of a single mode model that finds the solution to the governing delay differential equation (DDE) as a combination of constituent curves (sequential responses) which are independent of the delay term, τ. In the current model, the delay independent constituent curves are found through a recursive state-space solution wherein the individual modal displacements are determined for each sequential response. In this chapter, the solution process is described in detail for a 2 mode system and the resulting analytical time responses are compared with numerical simulations.

3.1Turning Model

$$\ddot{\mathrm{x}}+\frac{c}{m}\dot{\mathrm{x}}+\frac{k}{m}\mathrm{x}=\frac{bK_{s,x}}{m}\left(\mathrm{x(t\text{-}}\tau\mathrm{)\text{-}x(t)}\right) \qquad 3.1$$

A time-domain solution for turning is developed in which the total solution of the delay differential equation (DDE), shown in Equation 3.1, is composed of a fixed set of curves which combine together through superposition. These constituent curves, referred to as sequential responses in the previous chapter, are determined by recursively solving the ordinary differential equation shown in Equation 3.2.

$$\ddot{\mathrm{x}}_j+\frac{c}{m}\dot{\mathrm{x}}_j+\frac{k+bK_{s,x}}{m}\mathrm{x}_j=\frac{bK_{s,x}}{m}x_{j-1}\ ,\quad x_0(t)=x_{init.}\left(t\right),\ \ x_j(0)=0,\ \ \dot{x}_j(0)=0 \qquad 3.2$$

Where m is the modal mass, c is the damping coefficient, k is the stiffness, b is the depth of cut (for orthogonal turning), $K_{s,x}$ is the material cutting force coefficient in the x-direction, x_j is the current tool point position, x_{j-1} is the solution of the previous sequential response, and $x_{init.}$ is the initial input function from which the recursive solutions progress. The sequential responses derived in Equation 3.2 are independent of the delay term, τ, however the delay term is accounted for when the total solution is composed according to Equation 3.3.

$$x(t)=\sum_{j=1}^{N}\begin{cases} 0 & , \; t<(j-1)\tau \\ x_j\big(t-(j-1)\tau\big) & , \; t\geq(j-1)\tau \end{cases} \tag{3.3}$$

For single mode systems, the sequential responses can be iteratively solved directly using Equation 3.2 as was done in the previous chapter. For multiple modes, however, intermodal dependencies due to the forcing function require a state space solution. That is, because the total motion of the tool contains components of each individual mode, the instantaneous chip thickness, and thus the force applied to each mode is dependent on the motions of every mode.

Take for example the two DOF linear, orthogonal turning model shown in Figure 31. Through modal analysis, the total position of the tool can be determined as the summation of the two modal mass positions, assuming that the eigenvector matrix is normalized to x_1, such that, $x_1 = q_1 + q_2$. Although the free response of the system can be determined by analyzing the two decoupled modal systems independently, the inclusion of the forcing term, F(t), which is dependent on the position of both modes according to Equation 3.4 causes the modal system to be recoupled when the tool is in the cut.

$$\begin{aligned} \mathrm{F}(\mathrm{t}) &= b\mathrm{K}_{\mathrm{s,x}}\left(\mathrm{h}_{\mathrm{m}}+\mathrm{x}_1(\mathrm{t}-\tau)-\ \mathrm{x}_1(\mathrm{t})\right) \\ &= b\mathrm{K}_{\mathrm{s,x}}\left(\mathrm{h}_{\mathrm{m}}+\left(\mathrm{q}_1(\mathrm{t}-\tau)+\mathrm{q}_2(\mathrm{t}-\tau)\right)-\left(\mathrm{q}_1(\mathrm{t})+\mathrm{q}_2(\mathrm{t})\right)\right) \end{aligned} \qquad 3.4$$

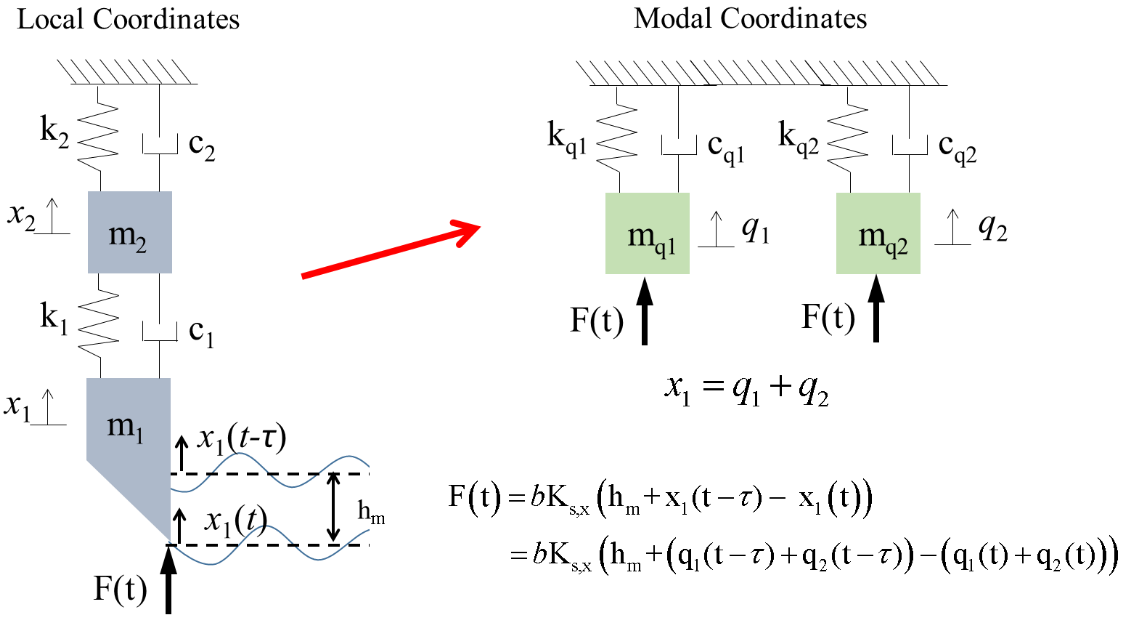

Figure 31: Two degree of freedom turning model local and modal representation, where the force applied to the two independent modal systems is proportional to the position of the tool point, x_1.

The resulting system of equations for the two modes in Figure 31 is shown in Equation 3.5. The approach for solving this system of linear delay differential equations (DDEs) is the same approach used to determine the sequential responses for the single DOF system in Equation 3.2.

$$\begin{aligned} m_{q1}\ddot{q}_1 + c_{q1}\dot{q}_1 + k_{q1}q_1 &= bK_{s,x}\left(\overbrace{q_1(t-\tau)+q_2(t-\tau)}^{\mathrm{x}_1(t-\tau)}\overbrace{-q_1(t)-q_2(t)}^{-\mathrm{x}_1(t)}\right) \\ m_{q2}\ddot{q}_2 + c_{q2}\dot{q}_2 + k_{q2}q_2 &= bK_{s,x}\left(q_1(t-\tau)+q_2(t-\tau)-q_1(t)-q_2(t)\right) \end{aligned} \qquad 3.5$$

The system of equations is evaluated by first putting them in a recursive form from which the subsequent sequential responses can be calculated. This is done by separating all of the terms by placing all current time terms (t) on the left side of the equation, and all delayed terms (t-τ) on the right side. The resulting recursive expression used to determine the sequential responses for the two degree of freedom system is shown in Equation 3.6, where the subscript, j, indicates the jth sequential response. Note that in Equation 3.6 the subscript for x_1 is omitted, and the new *x* subscripts indicate the motion of the tool for each response. In the recursive solutions, the initial conditions are zero for the initial velocities and displacements $\left(q_{1,j}(0)=q_{2,j}(0)=\dot{q}_{1,j}(0)=\dot{q}_{2,j}(0)=0\right)$ except for the initial response $(q_{1,1}(0)=q_{1,init},\ q_{2,1}(0)=q_{2,init},\ \ \dot{q}_{1,1}(0)=\dot{q}_{1,init},\ \dot{q}_{2,1}(0)=\dot{q}_{2,init})$ which are defined by the user, and the history function describing the initial shape of the surface is defined as $x_0 = x_{init}(t)$.

$$
\begin{gathered}
m_{q1}\ddot{q}_{1,j}+c_{q1}\dot{q}_{1,j}+k_{q1}q_{1,j}+bK_{s,x}q_{1,j}+bK_{s,x}q_{2,j}=bK_{s,x}x_{j-1}\\
m_{q2}\ddot{q}_{2,j}+c_{q2}\dot{q}_{2,j}+k_{q2}q_{2,j}+bK_{s,x}q_{1,j}+bK_{s,x}q_{2,j}=bK_{s,x}x_{j-1}\\
q_{1,j}(0)=q_{2,j}(0)=\dot{q}_{1,j}(0)=\dot{q}_{2,j}(0)=0,\\
q_{1,1}(0)=q_{1,init},\ q_{2,1}(0)=q_{2,init},\\
\dot{q}_{1,1}(0)=\dot{q}_{1,init},\ \dot{q}_{2,1}(0)=\dot{q}_{2,init},\\
x_0=x_{init}(t),\ \ x_j=\sum_{n=1}^{N}q_{n,j}=q_{1,j}+q_{2,j}
\end{gathered}
\tag{3.6}
$$

After modifying the system of equations by separating the current time and delay terms in Equation 3.6, the system equations are recoupled due to the presence of all modal positions in each equation. To solve for the coupled modal positions, and thus the sequential responses, x_j, a state space solution is used to again decouple the modified system. The state variable, *r*, is defined in terms of the modal positions and velocities in Equation 3.7, and the matrix form of the state space equations is shown in Equation 3.8

$$\begin{aligned}
r_1 &= q_1; & \dot{r}_1 &= r_2 \\
r_2 &= \dot{q}_1; & \dot{r}_2 &= \frac{1}{m_{q1}}\left(-c_{1q}r_2 - k_{q1}r_1 - bK_{s,x}r_1 - bK_{s,x}r_3\right) + \frac{bK_{s,x}}{m_{q1}}x_{j-1} \\
r_3 &= q_2; & \dot{r}_3 &= r_4 \\
r_4 &= \dot{q}_2; & \dot{r}_4 &= \frac{1}{m_{q2}}\left(-c_{q2}r_4 - k_{q2}r_3 - bK_{s,x}r_1 - bK_{s,x}r_3\right) + \frac{bK_{s,x}}{m_{q2}}x_{j-1}
\end{aligned} \tag{3.7}$$

$$\begin{Bmatrix} \dot{r}_1 \\ \dot{r}_2 \\ \dot{r}_3 \\ \dot{r}_4 \end{Bmatrix} = \begin{bmatrix} 0 & 1 & 0 & 0 \\ -\left(k_{q1}+bK_{s,x}\right)/m_{q1} & -c_{q1}/m_{q1} & -bK_{s,x}/m_{q1} & 0 \\ 0 & 0 & 0 & 1 \\ -bK_{s,x}/m_{q2} & 0 & -\left(k_{q2}+bK_{s,x}\right)/m_{q2} & -c_{q2}/m_{q2} \end{bmatrix} \begin{Bmatrix} r_1 \\ r_2 \\ r_3 \\ r_4 \end{Bmatrix} + \begin{Bmatrix} 0 \\ bK_{s,x}/m_{q1} \\ 0 \\ bK_{s,x}/m_{q2} \end{Bmatrix} x_{j-1}$$

$$\{\dot{R}\} = [A]\{R\} + \{F\}\,x_{j-1} \tag{3.8}$$

The state space system in Equation 3.8 is decoupled by substituting $A = VDV^{-1}$, where V is the matrix of eigenvectors of A, and D is a diagonal matrix of the eigenvalues of A. After pre-multiplying both sides by V^{-1}, and substituting the variables, $W = V^{-1}R$, and $G = V^{-1}F\,x_{j-1}$, the system of equations becomes:

$$\{\dot{W}\} = [D]\{W\} + \{G\} \tag{3.9}$$

The decoupled system of equations in Equation 3.9 can now be used to solve for ***W***, which is then converted back to modal coordinates to ultimately determine the motion of the tool for each sequential response.

Before discussing the solutions to Equation 3.9, consider the general process used to determine the sequential responses for the 2 mode system. In Figure 32 the iterative solution described in Equation 3.6 is shown in relation to Equations 3.8 and 3.9. During each iteration, the function describing the previous sequential response is applied to the forcing vector, ***F***, in Equation 3.8, which is then transformed to the forcing vector, ***G***, in the decoupled system in Equation 3.9. Once the decoupled variables, ***W***, are solved for based on the forcing vector, ***G***, the solutions are transformed back to obtain the solutions for the state variables, ***R***. The resulting state variable solutions for the modal displacements are then combined to determine the total tool displacement for that iteration , x_j. This process repeats, where in each iteration the sequential response, x_j, becomes the input, x_{j-1}, to determine the next sequential response.

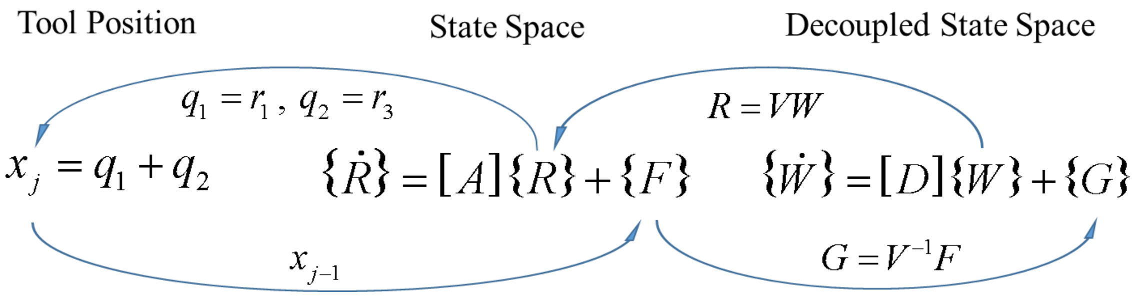

Figure 32: Diagram showing the recursive solution process used to find the sequential responses for multiple modes, where a new function, x_j, is found during each iteration which is dependent on the previous function, x_{j-1}.

3.2Solutions for Decoupled State Variables

The decoupled state space variables, w_n, are found by solving the first order differential equation shown in Equation 3.10 based on the input function, g_n. The solution form for w_n is dependent on the form of the of the input function, g_n, which has the same form as the previous sequential response function, x_{j-1}(although the coefficients will change while transforming from x_{j-1} to ***F*** to ***G***).

$$\dot{w}_n = \lambda_n w_n + g_n \qquad 3.10$$

Let us start by finding the solution to the first sequential response when the initial function (or history function) is zero, $x_{init}(t) = 0$, the initial modal displacements are zero, and the initial modal velocities are one $\left(r_1(0) = r_3(0) = 0,\ r_2(0) = r_4(0) = 1\right)$. Note that in this example the DC force component caused by the constant feed per revolution, h_m, is neglected, and the initial modal velocities serve as the initial system perturbation. During this first response the input function, ***G***, is zero, so the decoupled state solutions are found as the complementary solutions satisfying the initial conditions. After transforming the initial conditions, $W(0)=V^{-1}R(0)$, the decoupled state solutions for the first response are calculated using Equation 3.11.

$$w_n = a_{w,n,0}\, e^{t\lambda_n},\ a_{w,n,0} = w_n(0) \qquad 3.11$$

Once the decoupled state variables are known, they are converted back to the initial state variables, $R=VW$, and the actual tool point position is found as $x_{j=1}(t)=r_1(t)+r_3(t)$. In this two mode example, the function describing the tool motion for the first response has the form shown in Equation 3.12.

$$x_1 = a_{x,1,0}e^{\lambda_1 t} + a_{x,2,0}e^{\lambda_2 t} + a_{x,3,0}e^{\lambda_3 t} + a_{x,4,0}e^{\lambda_4 t} \qquad 3.12$$

During the second sequential response, the forcing terms in the decoupled system of equations are obtained from the previous sequential response, resulting in the system of first order equations shown in Equation 3.13.

$$\dot{w}_n = \lambda_n w_n + \overbrace{a_{gn,1,0}e^{\lambda_1 t} + a_{\mathrm{gn},2,0}e^{\lambda_2 t} + a_{\mathrm{gn},3,0}e^{\lambda_3 t} + a_{\mathrm{gn},4,0}e^{\lambda_4 t}}^{g_n} = \lambda_n w_n + \sum_{u=1}^{2N} a_{\mathrm{gn,u},0}e^{\lambda_u t} \qquad 3.13$$

The solutions to Equation 3.13 are found as a combination of the particular solutions from each individual forcing term, and the complementary solution based on the initial conditions (note that all initial conditions are zero for all sequential responses except for the first). The solution process for the particular solutions depends on the forcing term being applied, which is associated with the eigenvalue λ_u, to a particular decoupled state variable, which is associated with the eigenvalue λ_n. Take for example the solution to w_1

shown in Equation 3.14. When the eigenvalue in the forcing term is **not** equal to the eigenvalue of the decoupled state variable (n ≠ u), the resulting particular solution has the same form as the forcing function. However, if the two eigenvalues are the same (n = u), the particular solution form cannot be the same as the forcing function because the forcing function has the same form as the complementary solution. As such, an additional term with an increase in degree t is added to the particular solution when n=u as shown for $w_{1,1}$ in Equation 3.14.

$$\begin{gathered}
\dot{w}_{1,1} = \lambda_1 w_{1,1} + a_{g1,1,0} e^{\lambda_1 t} \rightarrow w_{1,1} = \left(a_{w1,1,0} + a_{w1,1,1} t\right) e^{\lambda_1 t} \\
\dot{w}_{1,2} = \lambda_1 w_{1,2} + a_{\mathrm{g}1,2,0} e^{\lambda_2 t} \rightarrow w_{1,2} = a_{w1,2,0} e^{\lambda_2 t} \\
\dot{w}_{1,3} = \lambda_1 w_{1,3} + a_{\mathrm{g}1,3,0} e^{\lambda_3 t} \rightarrow w_{1,3} = a_{w1,3,0} e^{\lambda_3 t} \\
\dot{w}_{1,4} = \lambda_1 w_{1,4} + a_{\mathrm{g}1,4,0} e^{\lambda_4 t} \rightarrow w_{1,4} = a_{w1,4,0} e^{\lambda_4 t} \\
w_1 = \sum_{u=1}^{2N\mathrm{mode}} w_{1,\mathrm{u}}
\end{gathered} \tag{3.14}$$

Once determined, the decoupled state variables are again converted back to *x*, and the resulting function describing the second sequential response has the form shown in Equation 3.15. The second sequential response now contains polynomials of degree 1 due to the particular solutions for *w* when n=u. In the following sequential response, these polynomials are applied in the forcing function, and the resulting solutions will contain polynomials with an increase in degree of one (due to the particular solutions when n=u). With each subsequent response the resulting solution polynomials increase by one degree so that the solution form for the j$^{\text{th}}$ response has the form shown in Equation 3.16, where the subscript *v* indicates polynomial coefficient of degree *v*.

$$x_2 = \left(a_{x,1,0} + a_{x,1,1} t\right) e^{\lambda_1 t} + \left(a_{x,2,0} + a_{x,2,1} t\right) e^{\lambda_2 t} + \left(a_{x,3,0} + a_{x,3,1} t\right) e^{\lambda_3 t} + \left(a_{x,4,0} + a_{x,4,1} t\right) e^{\lambda_4 t} \tag{3.15}$$

$$x_j = \sum_{n=1}^{2N}\left(a_{x,\mathrm{n},0} + a_{x,\mathrm{n},1}t + a_{x,\mathrm{n},2}t^2 + \ldots + a_{x,\mathrm{n},\mathrm{j}-1}t^{j-1}\right)e^{\lambda_n t} = \sum_{n=1}^{2N}\left(\sum_{v=0}^{j-1} a_{x,\mathrm{n},v}t^v\right)e^{\lambda_n t} \qquad 3.16$$

The solution coefficients are found by solving the first order differential equation in Equation 3.10 when the forcing function, g, is a polynomial with known coefficients, a_g, multiplied by an exponential term, $e^{\lambda_u t}$. The solution coefficients, a_w, are calculated directly based on the input coefficients using Equation 3.17, and then converted back to r where like terms are combined to determine the sequential response coefficients, a_x. Note that a detailed explanation of Equation 3.17 can be found in Appendix D.

$$\begin{gathered}
\dot{w}_{\mathrm{n,u}} = \lambda_n w_{\mathrm{n,u}} + \left(a_{gn,\mathrm{u},0} + a_{gn,\mathrm{u},1}t + a_{gn,\mathrm{u},2}t^2 + \ldots + a_{gn,\mathrm{u},\mathrm{j}-1}t^{j-1}\right)e^{\lambda_u t} \\
w_{\mathrm{n,u}} = \left(a_{wn,\mathrm{u},0} + a_{wn,\mathrm{u},1}t + a_{wn,\mathrm{u},2}t^2 + \ldots + a_{wn,\mathrm{u},j-1}t^{j-1}\right)e^{\lambda_u t} \\
a_{wn,\mathrm{u},\mathrm{v}+1} = \frac{a_{gn,\mathrm{u,v}}}{v+1};\ n = u \\
a_{wn,\mathrm{u,v}} = \frac{a_{gn,\mathrm{u,v}} - (v+1)\,a_{wn,\mathrm{u},\mathrm{v}+1}}{\lambda_u - \lambda_n};\ n \neq u
\end{gathered} \qquad 3.17$$

3.3Example Solution

The solution process described in the previous section is applied to a two mode system having the system modal parameters shown in Table 2. The example system is evaluated at a depth of cut of 3mm and at a spindle speed of 8000 RPM in the first example, and 6000 RPM in the second. In both examples the initial modal positions are zero and the initial modal velocities are 1 m/s, and the cutting force constant in the x direction is, $K_{s,x}$ = $6.84\text{x}10^8$ N/m^2. Not that in these examples the initial velocity conditions serve as the initial perturbation event instead of the double ramp approach used in the previous chapter. The stability lobe diagram of the system is shown in Figure 33, where the conditions are in the stable region for example 1, and in the unstable region in example 2.

Table 2: Modal Parameters for Example System

	k_q (N/m)	m_q (kg)	c_q (N-s/m)
Mode 1	1x10^7	0.88	400
Mode 2	4x10^7	1.2	300

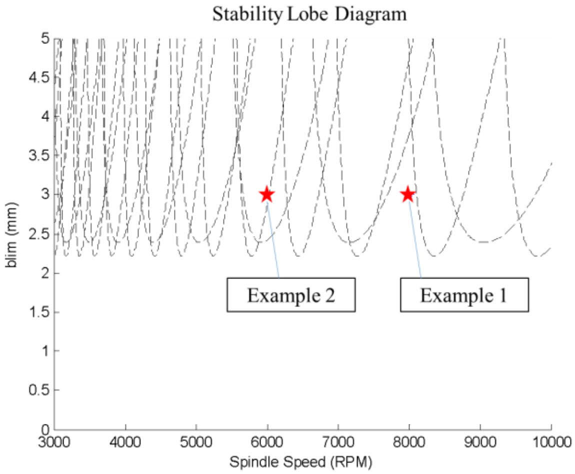

Figure 33: Stability Love Diagrams found using Tlusty's approach for the for the two mode example system with parameters shown in Table 2, where the spindle speeds and depth of cut for the two examples are labeled.

A Matlab program is used to solve for the coefficients of the sequential response solutions and to construct the total tool point response for the two examples. Within the program, the state transition matrices are first determined based on the modal parameters, and the solution process illustrated in Figure 32 is used to find solutions for the sequential responses. For each response, the solution coefficients are found base on the transformed coefficients from the previous response according to Equation 3.17. Finally, the individual sequential response solutions are combed to form the total tool point response according to Equation 3.3. The total tool point response for the first 12 rotations for example 1, and the first 8 rotations for example 2 are shown in Figure 34.

The long term tool behavior in the two examples agree with the predictions of the stability lobe diagram (stable for example 1 and unstable for example 2). The two examples have differing spindle speeds but have the same depth of cut, as such, the sequential responses which form the total solutions are the same (the sequential responses are independent of the delay, but dependent on the depth of cut, *b*, due to the forcing vector, **F**, in Equation 3.8). This is illustrated in Figure 35 which shows the sequential responses plotted with delays according to Equation 3.3 which are then combined to form the total solution. It can be seen from these two examples that despite having the same set of sequential responses, the total long term behavior of the system is determined by the cumulative constructive and destructive interferences between the sequential responses at different delay periods.

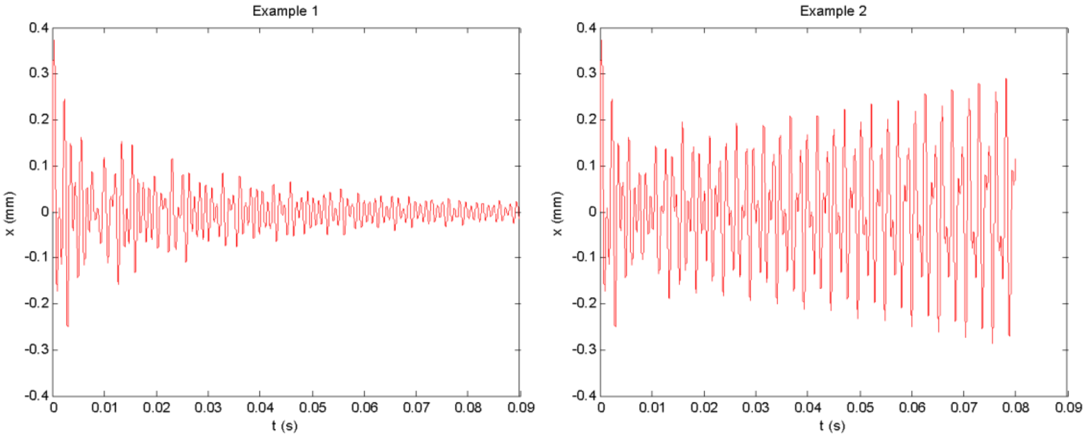

Figure 34: Total tool point response for the first 12 part rotations for Example 1, and the first 8 part rotations for Example 2.

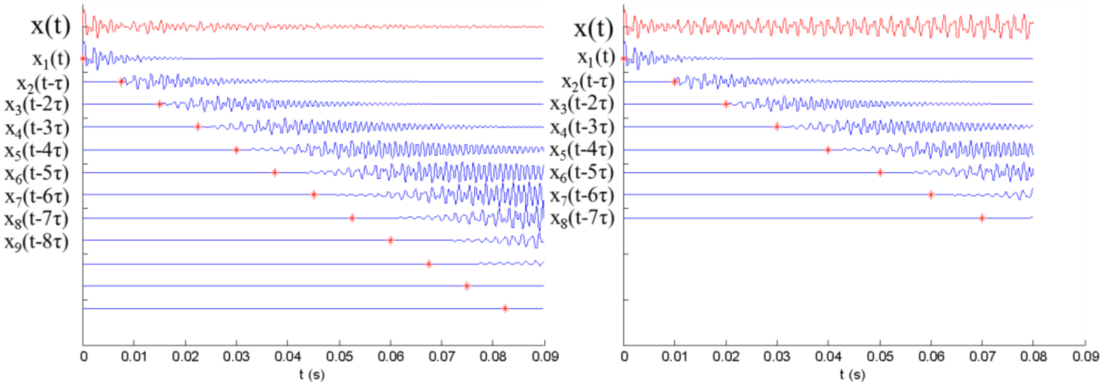

Figure 35: Plots of the sequential responses which are shifted in time to compose the total tool point response according to Equation *3.3*

3.4Numerical Simulation Comparison

The analytical solutions based on the sequential response approach for multiple modes are compared with numerical simulations for the conditions of example 2 in Figure 34. Euler integration is used in the simulations to numerically evaluate the modal displacements based on the delay differential equation in Equation 3.1. The analytical solution is compared with the numerical solution evaluated a time steps from 5x10^{-5} to 2.5x10^{-6} seconds, which corresponds to a range of 21 to 425 points per oscillation of the highest frequency mode. The resulting error plots in Figure 36 show that the error between the two solutions decreases as the time step in the numerical simulation is decreased. The decrease in the error as the time step is refined can be seen in Figure 37, which shows the maximum error decreasing as the number of points used in the numerical simulation increases.

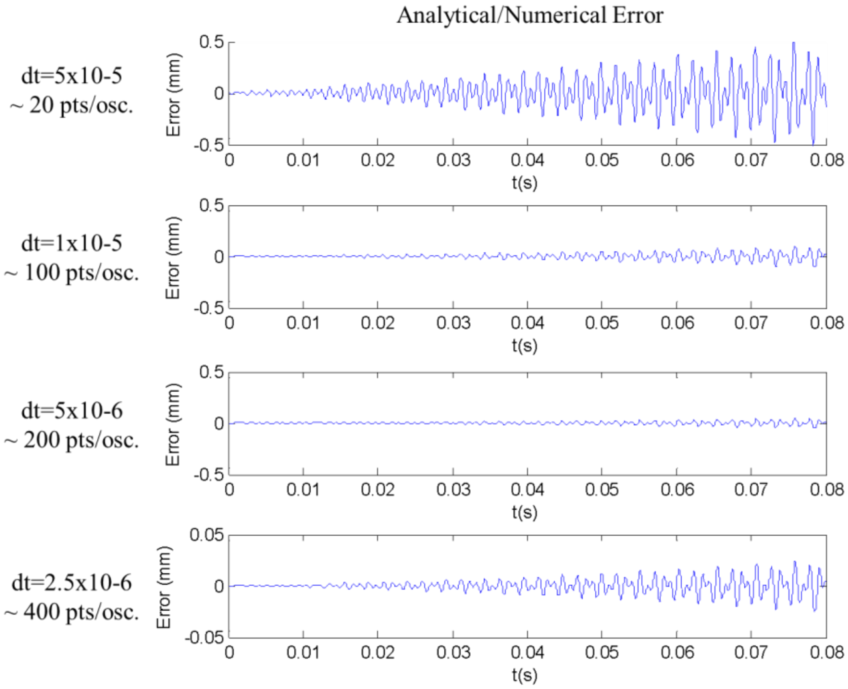

Figure 36: Error plots comparing the tool responses obtained using the analytical sequential response approach and numerical simulations.

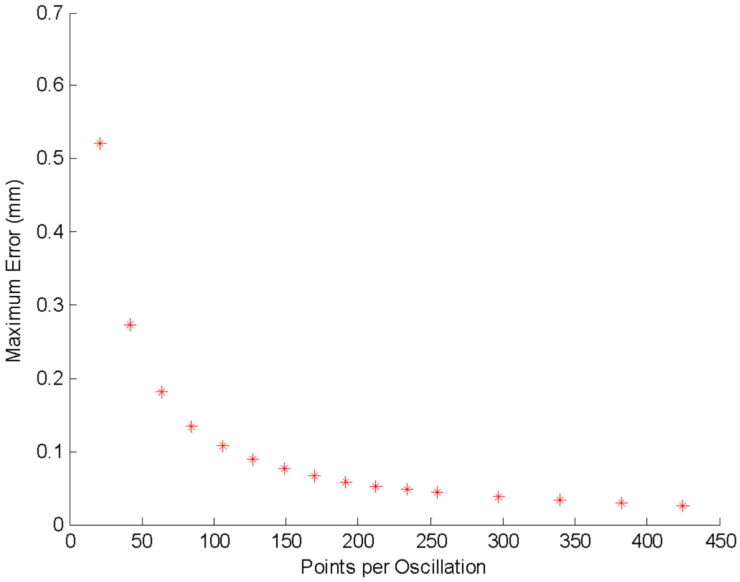

Figure 37: Plot of the maximum error between the numerical and analytical results for example 2 as the time step is refined.

3.5Conclusions

The ability to analytically predict the time response of a tool with multiple modes greatly expands the potential applications of the methods developed in this dissertation. Moving forward, the equations and processes developed in this chapter are incorporated into a matrix solution which allows for the sequential responses to be determined more effectively. However, first, the analytical predictions made thus far in this dissertation are tested experimentally to verify that the predictions are representative of the physical process.

CHAPTER 4: EXPERIMENTAL VERIFICATION

Experimental tests are conducted to verify that the tool motions predicted in the analytical solution for orthogonal turning developed in this work can be observed experimentally. The experiment is set up to create a single mode cutting tool, however, due to additional significant modes which appear in physical measurements of the system, the multiple mode solution is used for comparison.

The general experimental setup is shown in Figure 38 and a picture of the actual setup is shown in Figure 39. The main component of the experiment setup is a monolithic leaf type flexure machined from Aluminum 6061. The flexure is mounted to the machine axis and is designed to be most flexible in the z direction. To create an orthogonal turning operation, the cutting tool is mounted to the flexure tool holder orthogonal to the z axis, and a tubular work-piece (also Aluminum 6061) with a known wall thickness is machined. The use of a tubular work-piece guarantees that chips being formed have a rectangular profile with a constant depth of cut (equal to the wall thickness) and a variable thickness in the z direction.

The objective of the experiments is to measure the motion of the tool after it is perturbed while engaged in the work-piece. According to the regenerative chatter theory on which the analytical solution is based, the tool will be repeatedly excited by the wavy surface that the tool left behind during the previous part revolution. During the experiments, the tool is initially excited by striking the back end of the tool holder with an impact hammer (PCB 086C04). Force data from the hammer impact is used in post processing to obtain the initial states of the tool after the hammer strike for use in the analytical solution and for FRF measurements while the tool is in the work piece. The resulting motion of the tool is measured using a capacitance gage (Lion Precision C5-D W/LEMO). The capacitance gage is mounted to the machine z axis along with the base of the flexure and measures the relative z displacement of the tool.

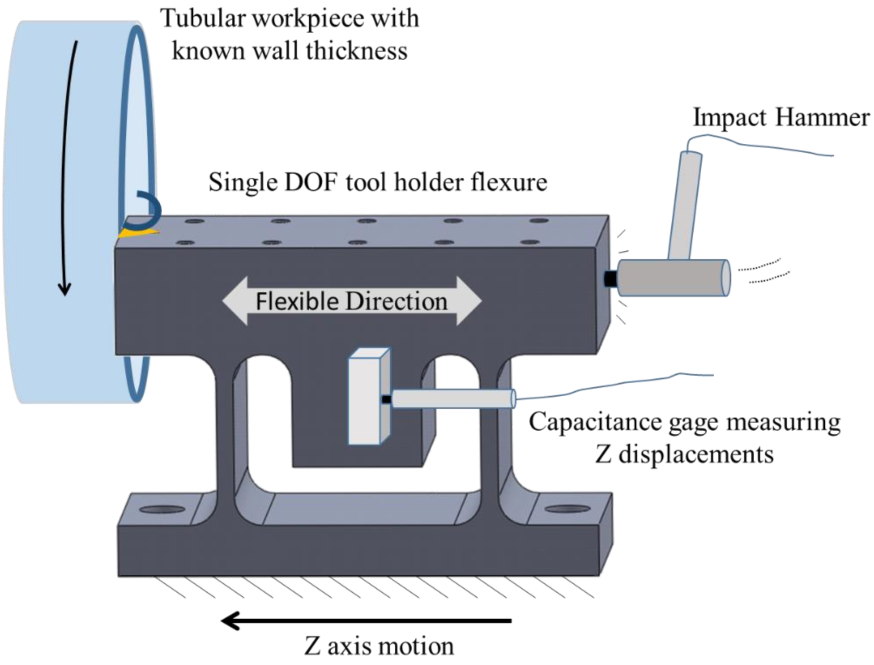

Figure 38: General experimental setup, using a flexure tool holder to machine a tubular work-piece.

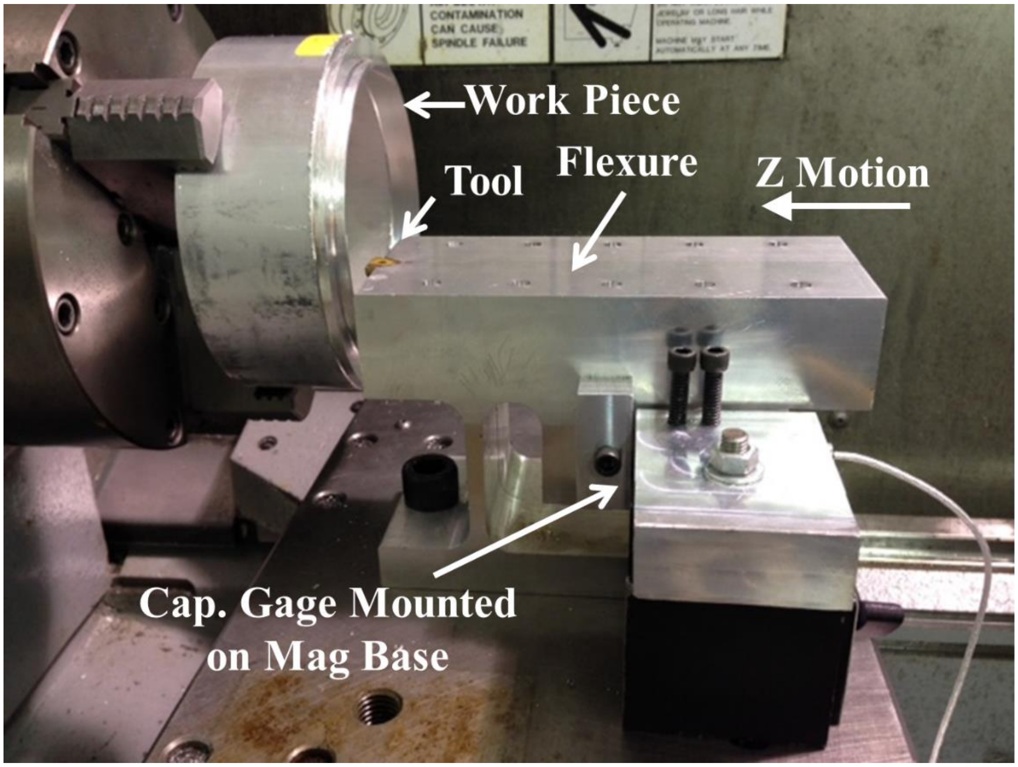

Figure 39: Picture of experimental setup.

Before each experiment the work piece is pre-machined to have a constant wall thickness which is then measured. Prior to the start of the test, the flexure is struck multiple times with the impact hammer and displacement measurements are taken with the capacitance gage. These impact measurements are used to obtain the FRF of the system while the tool is free. After the free FRF measurements are taken the tool feeds into the rotating work-piece at a constant feed rate. Once fully in the cut, the tool holder is again struck multiple times and the tool displacements are measured. Striking the tool with the impact hammer while in the cut has two primary purposes for the experiment; first, the measurement of the perturbation force is used to determine the conditions of the system after the strike for use in the analytical model, second, it is used for a cutting FRF measurement that provides direct information on the amount of process damping present while the tool is cutting. After the tests the force and displacement data are processed and the analytical solution is compared with the experimental results. Further details of each of these steps is provided in the following sections.

4.1Flexure Modal Testing

The aluminum flexure for these experiments was designed to be most flexible in the z direction (feed direction). FRF measurements are taken for the flexure structure in all three directions, where the x y and z directions are shown with respect to the flexure in Figure 40. The FRF measurements are found using tap tests using a PCB 086C04 impact hammer and a PCB 352C23 accelerometer and the resulting FRF measurements were generated using TXF software. Five measurements were taken, three direct FRFs in the x y and z directions (FRF_{XX}, FRF_{YY} and FRF_{ZZ}), and two cross FRFs (FRF_{XZ} and FRF_{YZ}).

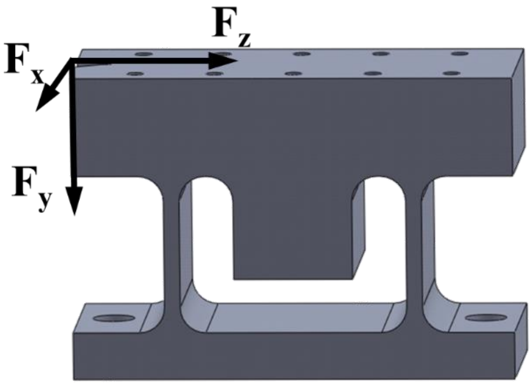

Figure 40: Flexure coordinates for modal tap tests.

The resulting FRF measurements are shown in Figure 41 and the stiffness values and natural frequencies of the most flexible modes from Figure 41 are shown in Table 3. From Figure 41 it can be seen that the most flexible mode occurs at 447 Hz in the z direction and the second most flexible mode occurs at 1358 Hz in the x direction. The flexible mode present in the x direction is likely due to twisting motions in the flexure when forces are applied to the tool point location. However, motions in the x direction are not expected to significantly affect the results of the experiments because motions the x direction do not affect the profile of the chip in orthogonal turning. Furthermore, as discussed in the following section, the cutting forces in the x direction are negligible compared with forces in the z and y directions.

The resulting stiffness values in the y direction (which can affect the chip profile) are 28 times larger than the z direction, and the effective stiffness in the z direction as a result of forces in the x and y directions are 17 and 22 times larger respectively for the most flexible modes. The results from these measurements indicate that the flexure structure designed for these experiments can effectively represent the analytical model, which only considers forces and motions in the z direction.

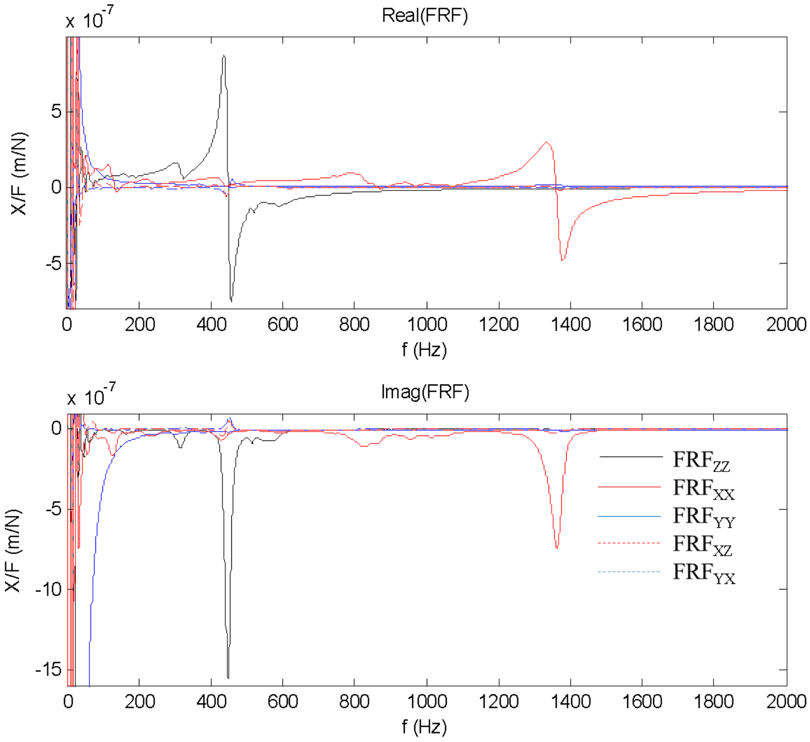

Figure 41: Five frequency response functions for the experiment flexure, where the most flexible mode of the structure is in the Z direction (black).

Table 3: Stiffness and natural frequency of the most flexible modes from Figure 41..

FRF	k (N/m)	f_n (Hz)
FRF_{ZZ}	1.36×10^7	447
FRF_{XX}	4×10^7	1358
FRF_{YY}	38.3×10^7	347
FRF_{XZ}	22.9×10^7	431
FRF_{YZ}	29.9×10^7	451

4.2Cutting Force Tests

Cutting force tests are conducted to determine the cutting force coefficient of the work-piece material (6 inch diameter Aluminum 6061) using the same tool insert used for the position measurement experiments (coated carbide insert with 8° rake angle and 11° relief angle). A diagram of the cutting force test setup is shown in Figure 42. The objective of this test is to determine the magnitude and direction of the cutting forces as the area of the chip changes. Forces are measured using a Kistler 9257B dynamometer which is attached to the machine axes and holds the tool holder.

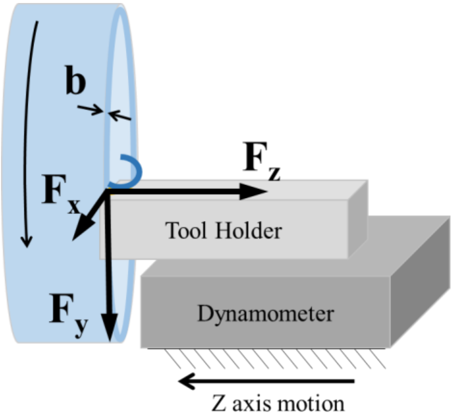

Figure 42: Cutting force experimental setup to measure the cutting forces as the chip area changes.

Three values of chip width, b, are used during the experiments (b=0.025”, 0.041”, and 0.057”), and for each chip width, the tool moves at three feed rates (feed/rev=0.002”, 0.003”, 0.004”), resulting in a total of nine different chip areas. Each of the tests is conducted at 300 and 600 RPM. An example of the force signal collected during one of the tests is shown in Figure 43. During the test the chip width is held constant and the machine is programed to move at three separate feed rates, resulting in three different chip areas.

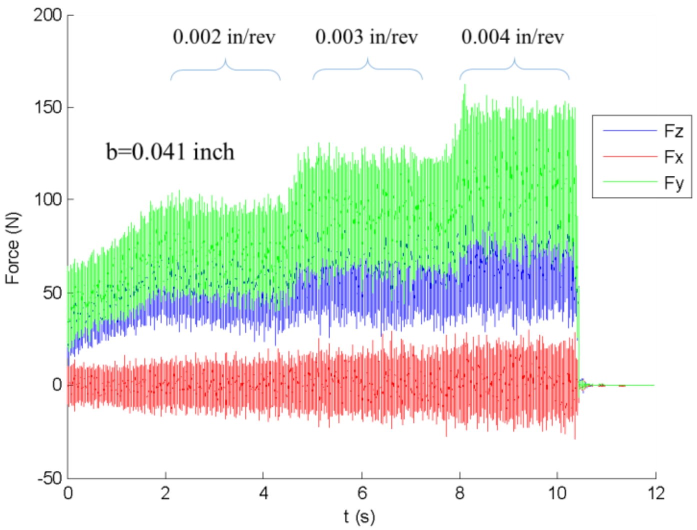

Figure 43: Example of the force measurements obtained from one test, where the chip width, b, is held constant at 0.041 inch, and the chip thickness changes from 0.002” to 0.003” to 0.004” as the feed rate changes with a spindle speed of 300 RPM.

When the cutting force tests are complete, the average cutting forces in the three directions are found over each feed rate range. These average values are then plotted as a function of the chip area, as shown in Figure 44. The mean slope of the average cutting forces are then found to determine the cutting force coefficients in the three directions. The result from the cutting force tests show that the cutting forces are mostly in the y and z directions, while the forces in the x direction are nearly zero for all chip areas (as expected in orthogonal turning). The resulting cutting force coefficients in the y and z directions are $K_{s,y}$=759 N/mm^2 and $K_{s,z}$=468 N/mm^2. The absolute cutting force coefficient is found to be K_s=892 N/mm^2 using $K_s = \sqrt{K_{s,y}^2 + K_{s,z}^2}$, and the cutting force angle is found to be β=58° using $\beta = \tan^{-11}\left(K_{s,y}/K_{s,z}\right)$.

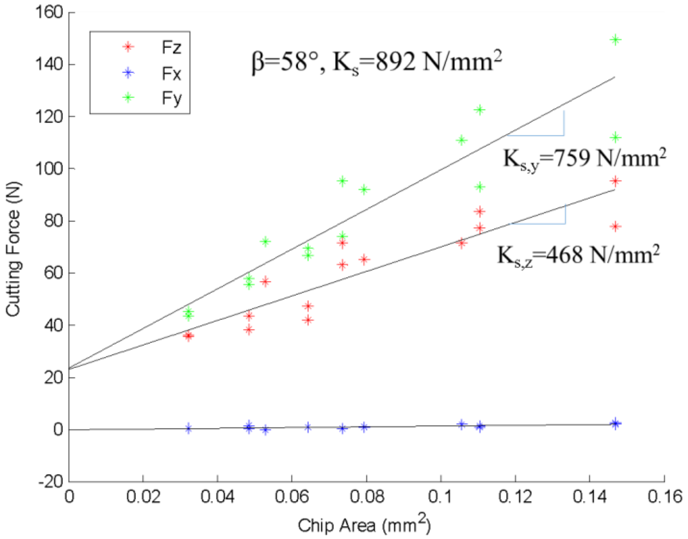

Figure 44: Average cutting force values plotted as a function of the chip area to determine the cutting force coefficient of the material-tool combination.

4.3Free and Cutting FRFs

During the experiments two types of FRF measurements are taken; free FRFs (FRF_F) before the tool enters the cut, and cutting FRFs (FRF_C) taken when the tool is in the cut. The purpose of these FRF measurements is to experimentally determine the modal parameters of the system while in and out of the cut. Before the tool enters the cut the tool is struck multiple times with the impact hammer (approximately five times) and the resulting motions are measured with the capacitance gage (see Figure 38). The process of striking the tool and measuring the displacement is repeated once the tool is in the cut. An example of the force and displacement measurements for a chip width of 0.082 inches, feed rate of 0.003 inch/rev, and 600 RPM is shown in Figure 45. After each strike, the force and displacement data is collected for a time duration equal to the part rotation period for that test (time of 0.1 seconds for the 60 RPM case). The purpose of this time duration is to eliminate regenerative effects that occur after the part completes one full rotation. A detailed view of the tool responses in and out of the cut is shown in Figure 46 for the first 0.035 seconds after a strike.

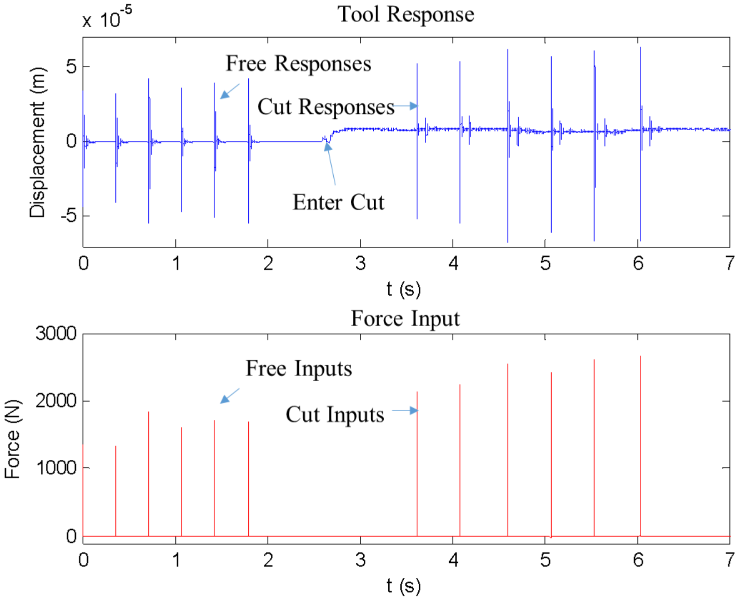

Figure 45: Force and displacement measurements for a chip width of 0.082 inches, feed rate of 0.003 inch/rev, and 600 RPM.

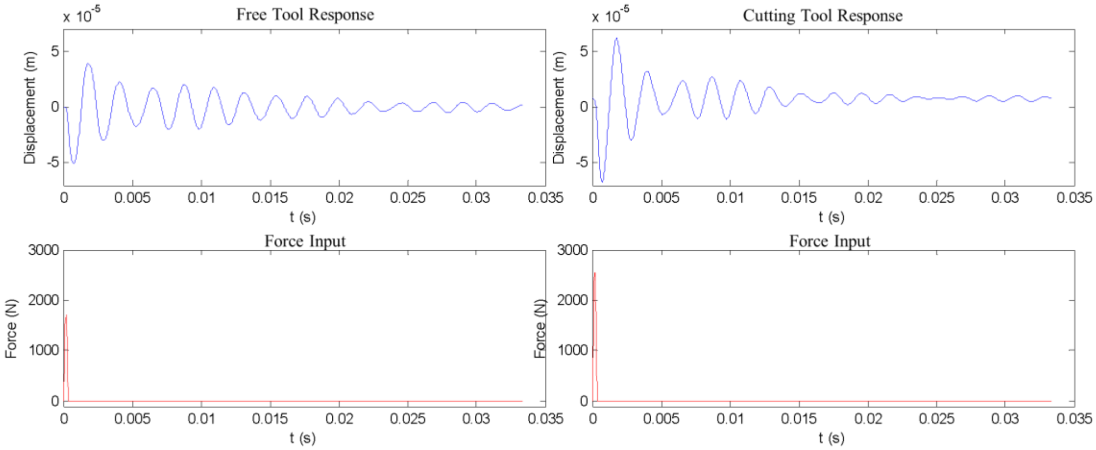

Figure 46: Detailed view of the force input and the tool response when the tool is free (left) and in the cut (right).

The free and cutting FRFs are obtained by dividing the fast Fourier transform (fft in Matlab) of the displacement data by the fft of the force data for each strike. The FRF data is then averaged over all of the free and cutting strikes to obtain FRF_F and FRF_C. Note that all FRFs are corrected to account for phase lag in the sensor signals using the methods developed by Ganguly et al in (Ganguly 2014).

The resulting FRFs for the experiments with a chip width 0.082 inches, and a feed rate of 0.003 in/rev are shown in Figure 49 for a spindle speed of 600 RPM.

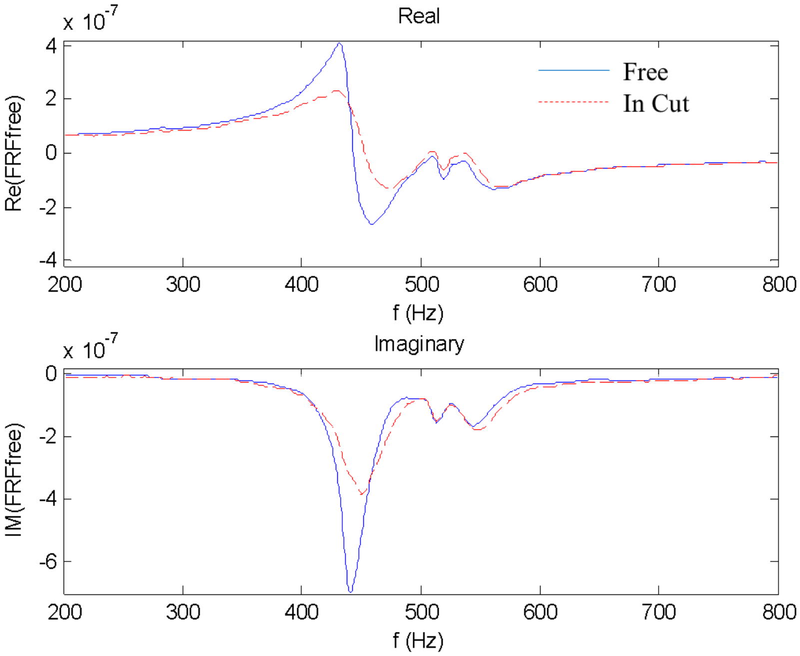

Figure 47: Free and Cut FRFs plotting for b=0.082 inches, feed=0.003 inch/rev, at 600 RPM.

In order to determine the modal parameters to be used in the analytical solution, the peak picking method discussed in (Schmitz 2009) is implemented in a Matlab program and used to calculate the modal mass, stiffness and damping from the FRFs. The resulting modal parameters from this program for the three modes in the free FRF in Figure 47 in order of increasing natural frequency are: m=3, 31 and 11 kg, k= 2.3×10^7, 32.7×10^7 and

12.8 x10^7 N/m, and c= 518, 2005 and 1,779 Ns/m. In Figure 48 the analytical FRF calculated using Equation 4.1 (Schmitz 2009) using the modal parameters found using peak picking are compared with the experimental FRF. From these results, application of the simple peak picking method effectively approximates the modal parameters of the system based on the experimental FRFs.

$$\frac{X}{F}=\sum_{j=1}^{3}\frac{1}{-m_j\omega^2+c_j\omega+k_j} \qquad 4.1$$

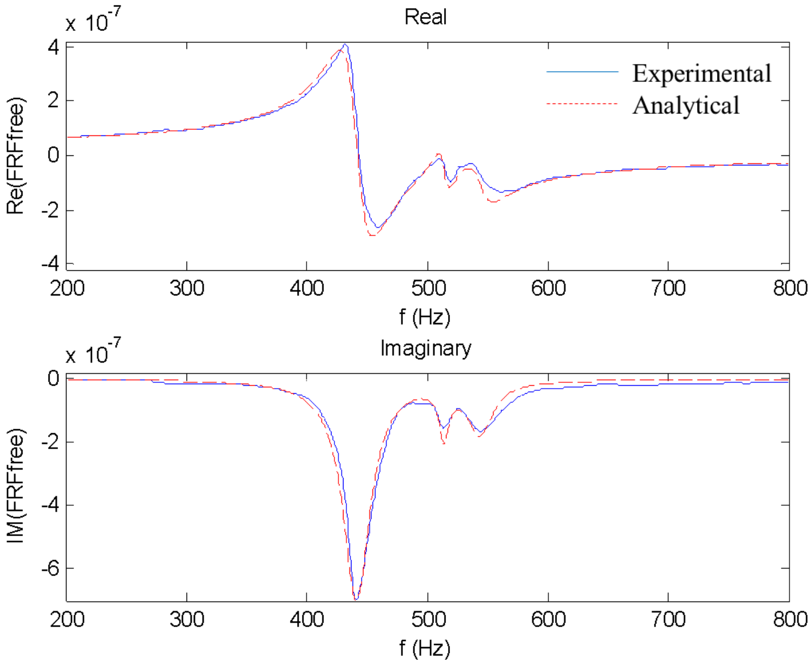

Figure 48: Comparison of the analytical FRF calculated using the modal parameters found using peak picking with the experimental FRF.

4.4Process Damping and Effective Stiffness Considerations

The resulting FRFs for the experiments with a chip width 0.082 inches, and a feed rate of 0.003 in/rev are shown in Figure 49 for spindle speeds of 400, 600 and 1000 RPM. The free FRFs on the left side of Figure 49 are nearly identical for each set of impact tests, as is to be expected because the free system dynamics are not affected by spindle speed.

The resulting Cutting FRFs on the left of Figure 49 do differ depending on the spindle speed. Both sets of FRF measurements show the same basic structure, with the most flexible mode near 440 Hz and two additional modes near 520 and 560 Hz. The most significant difference between the two sets of FRFs is in the magnitudes of the FRFs for the first mode near 440 Hz. While the peak magnitudes of the FRFs are a result of multiple factors, the most likely cause of the decrease in the peak magnitudes in the cut is process damping. The effects of process damping can be seen directly in the cutting FRFs in Figure 49. The peak magnitudes of the 1000 RPM cutting FRF are nearest to those of the free FRFs, and as the spindle speed is decreased, the additional effects of process damping cause the peak magnitudes in the FRFs to decrease.

Process damping is an effect of the machining process which causes an increase in the effective damping in the system which increases as the spindle speed decreases. There are multiple theories as to the cause of process damping, such as an introduction of nonlinear force relations due to changes in tool-chip interactions as the chip wave length decreases (Stepan 2001), or due to the interactions of the tool flank face an the wavy surface of the part (Tlusty 1999). Among these theories, process damping is most commonly attributed tool flank interference, although it is difficult to determine experimentally the precise cause (Taylor 2010). While some have developed analytical models to predict process damping based on tool flank interference (Tunc 2012), a more typical approach is to determine the effects of process damping for a given tool and work piece through experiment. Altintas and Eynian developed an experiment in which the tool vibrations are controlled using a fast servo to negate regenerative effects (vibrations kept in phase) so that additional damping forces could be measured (Altintas 2008a; Eynian 2010). Kurata et al determined new cutting speed dependent stability limits by determining at what cutting speed chatter was suppressd in a constant RPM plunge cut (Kurata 2010). Tyler developed a method to fit an analytical model for process damping stability lobes to experimentally determined stability lobes to determine an effective process damping coefficient (C. 2012).

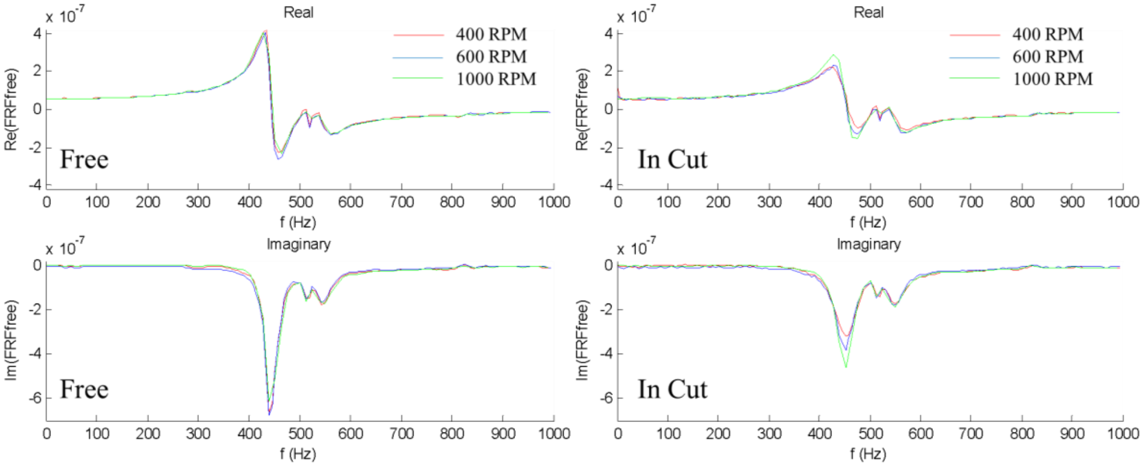

Figure 49: Free and Cut FRFs plotting for b=0.082 inch, feed=0.003 inch/rev, at 400, 600 and 1000 RPM.

While process damping is not a focus of these experiments, the effects of process damping will have a significant effect on the analytical solution, especially with the limited range of spindle speeds typically used in turning. As such, the effects of process damping must be considered to adequately compare the analytical results with the experimental measurements.

As the amount of damping in the system while cutting is known from the in cut FRF tests, the in cut damping coefficient is used in the analytical model. For the current system, the free damping coefficients are only replaced by the cutting damping coefficients for the most flexible mode (from Figure 49, the other stiffer modes are less effected by process damping). The mass and stiffness coefficients from the free FRF remain unchanged as a result of process damping. In Figure 50 the flow of operations is shown to determine the modal parameters that are to be used in the analytical solution to model the turning operation with process damping effects.

The effectiveness of the process damping compensation process in Figure 50 can be seen in the resulting plots in Figure 51. When the damping coefficients are not corrected (Figure 51 left) the errors between the analytical and experimental results are great even after the initial impact, and grow significantly in each part rotation. When process damping effects are included (Figure 51 right) the analytical and experimental motions are much closer even after three part rotations.

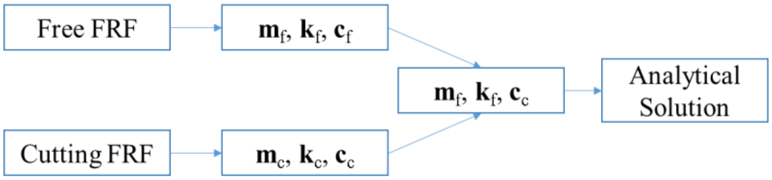

Figure 50: Flow of dynamic parameters used in the analytical solution to model the model the experimental system with process damping effects.

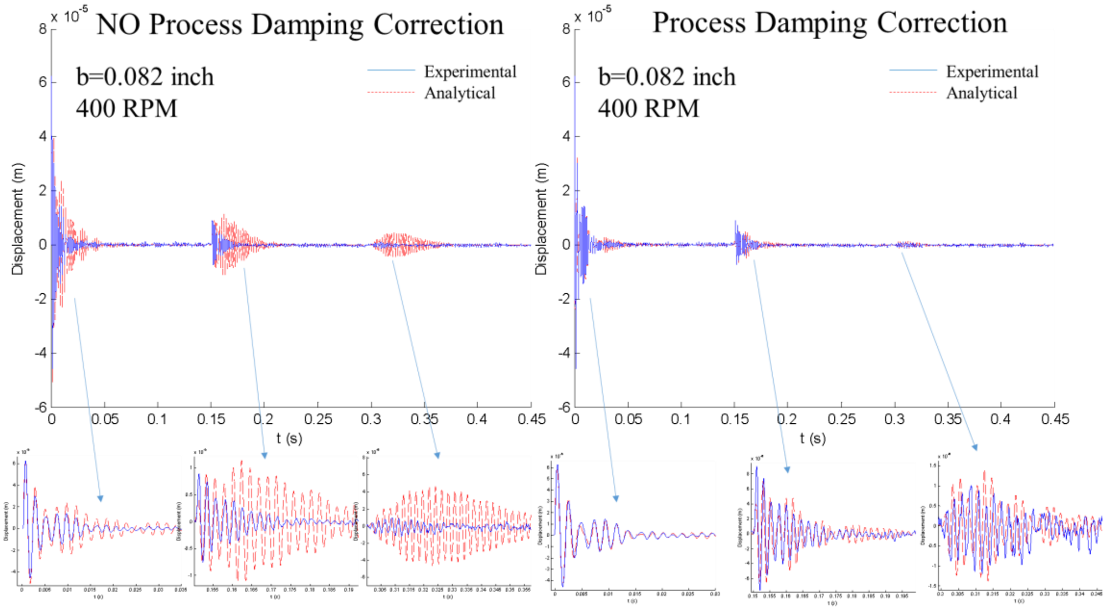

Figure 51: Comparison of experimental and analytical displacement data when process damping is ignored (left) and when process damping is compensated for (right) with b=0.082 inch at 400 RPM.

The differences between the free and cutting FRFs are due in part to the effects of process damping, however, process damping alone does not explain why there is a shift in the natural frequency (in Figure 49 the natural frequency of the first mode is shifted right by 10 Hz). Recall from the single degree of freedom analytical model that the tool stiffness is effectively increased while the tool is in the cut, such that $k_{eff.} = k + bK_s \cos(\beta)$. This increase in effective stiffness can be observed experimentally here as an increase in the natural frequency of the system while the tool is in the cut. Consider the three sets of FRFs plotted (first mode only) in Figure 52 for b=0.035 and 0.082 inch at 1000 RPM. The red and blue FRF plots are the measured FRFs while free and in the cut. The black dashed FRF plot represents a modified version of the free FRF plot, where the modal mass is held constant, the damping coefficient is equal to the cutting damping coefficient, and the stiffness is increased by $bK_s \cos(\beta)$. It can be seen that together the adjustments for damping obtained experimentally, and the adjustments for stiffness obtained analytically account for the differences in the two FRF measurements.

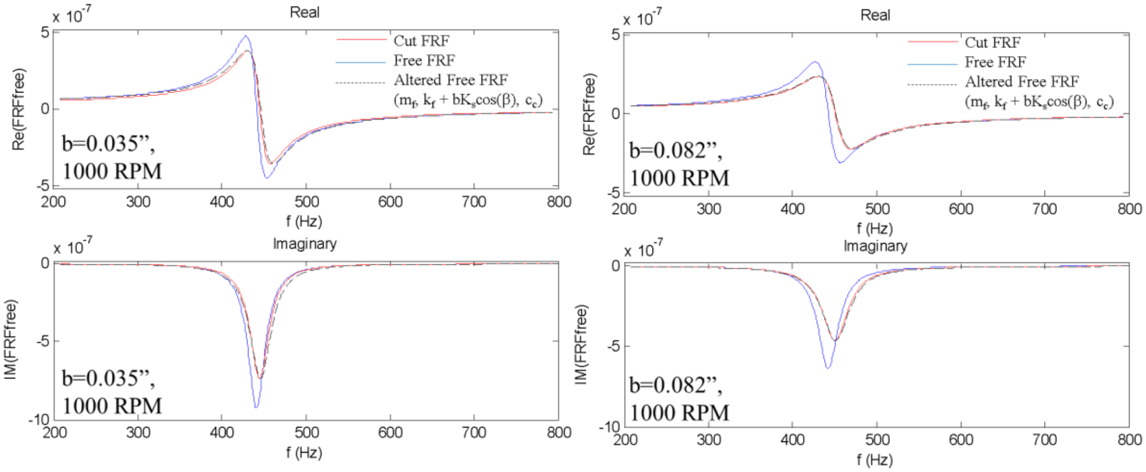

Figure 52: Free and cut FRFs with an additional altered free FRF which makes predicted modifications to the free modal parameters to match the cutting FRF.

4.5Experimental results

The tool displacements measured in the experiments are now compared with analytical solutions. In the analytical solution the process summarized in Figure 50 is used to define the modal parameters, where, in these examples the first three modes are considered. Once the modal parameters are determined, the initial conditions for the analytical solution must be determined to match those of the experiment.

The initial conditions for the analytical solution cannot be determined by simply observing the conditions of the experimental data at any point in time. This is because the analytical solution requires initial conditions for each individual mode in the system, and these cannot be determined based solely on a single position and velocity state provided by the experimental data (i.e. the experimental data only provides the sum of the modal states and not their individual components). The initial modal states are determined by solving for the modal states through numerical simulation. In these simulations, the measured impact force is input and Euler integration is used to simulate the modal states over the duration of the impact. The modal conditions at the end of the impact are then set as initial conditions for the analytical solution. This process is shown in Figure 53 which shows the measured force profile of one impact and the resulting measured motion of the tool (left). In this example the modal system with the measured input force is simulated for 0.0004 seconds assuming that the system is initially at steady state (zero valued initial conditions) and that the vibrations of the tool during the rotation prior to impact are significantly less than the vibrations caused by the hammer impact. The conditions of the individual modes at the end of this period are then set as the initial conditions. The resulting combined initial conditions are shown on the right of Figure 53, where the simulation based initial conditions closely match the measured states at the end of the impact.

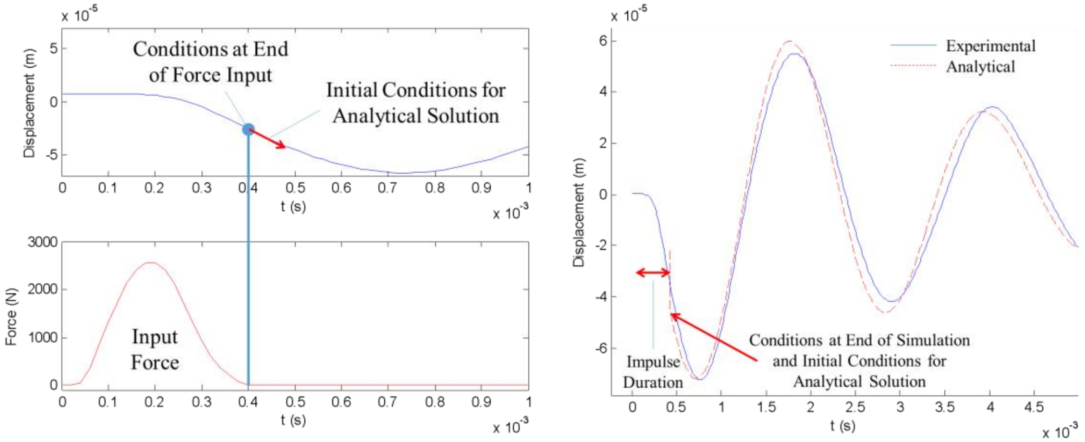

Figure 53: Process used to determine the initial conditions of the tool for the analytical solution based on the input force.

The process of defining the modal parameters based on Figure 50 and the initial conditions based on Figure 53 are automated in a Matlab program, and the resulting analytical solutions are compared with the measured displacements of the tool. In Figure 54 through Figure 56 the solutions are plotted for b=0.035 inch at 1000 RPM, b=0.082 inch at 400 RPM and b=0.082 inch at 1000 RPM. From the full time range plots it can be seen that the general behavior of the analytical solutions closely resemble experimental measurements, where the tool is excited once per revolution and the amplitudes generally decrease. At closer inspection the differences between the two plots are more apparent, where the analytical solutions generally exhibit larger amplitudes. As would be expected, the two plots agree most during the first revolution where the motions are only a result of the initial impact. In these regions the phases of both plots closely match and the shape of the oscillation envelopes also closely match. As the number of rotations increase, the errors between the two plots also increase. This can be attributed in part the cascading effects of the errors, where errors during one rotation lead to errors in the next rotation due to the regenerative forces. Despite the increasing error as the number of revolutions increases, with the exception of the 400 RPM example, all of the plot results show that the frequencies and phases of the predicted in the analytical solution match those determined experimentally.

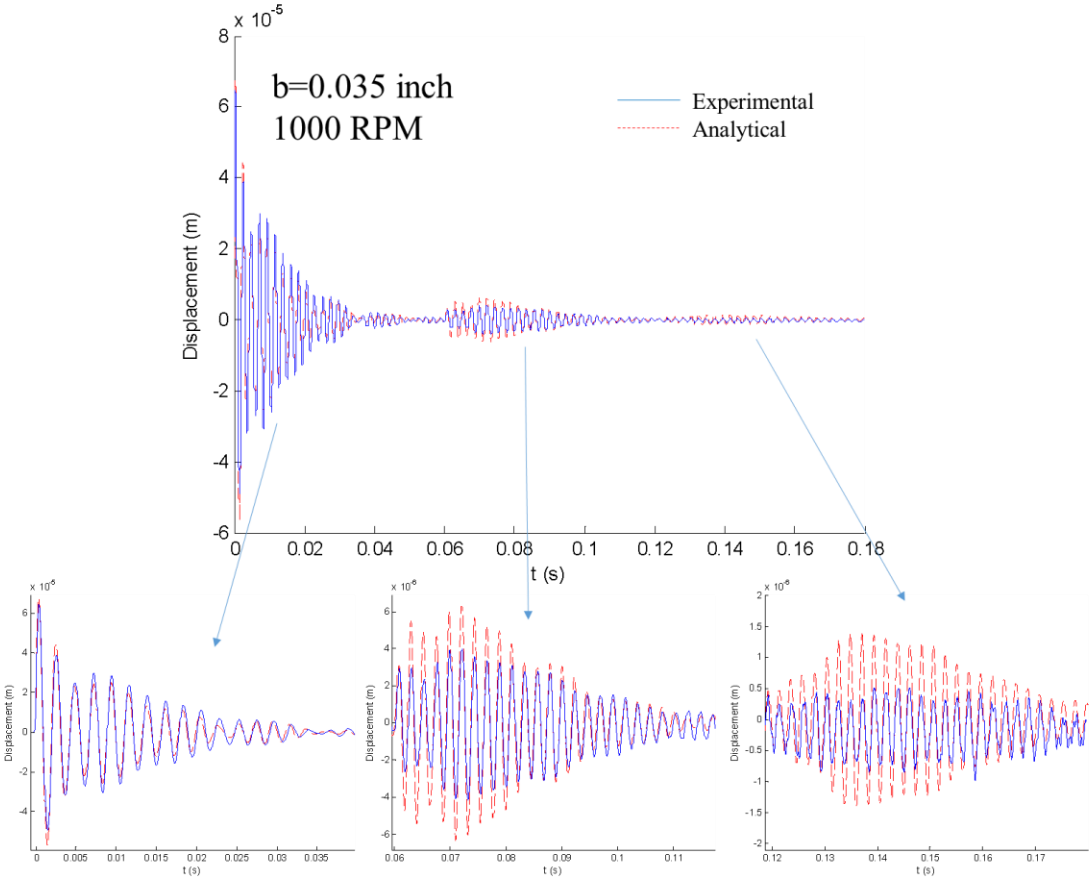

Figure 54: Experimental and analytical displacement data comparison for b=0.035 inch at 1000 RPM.

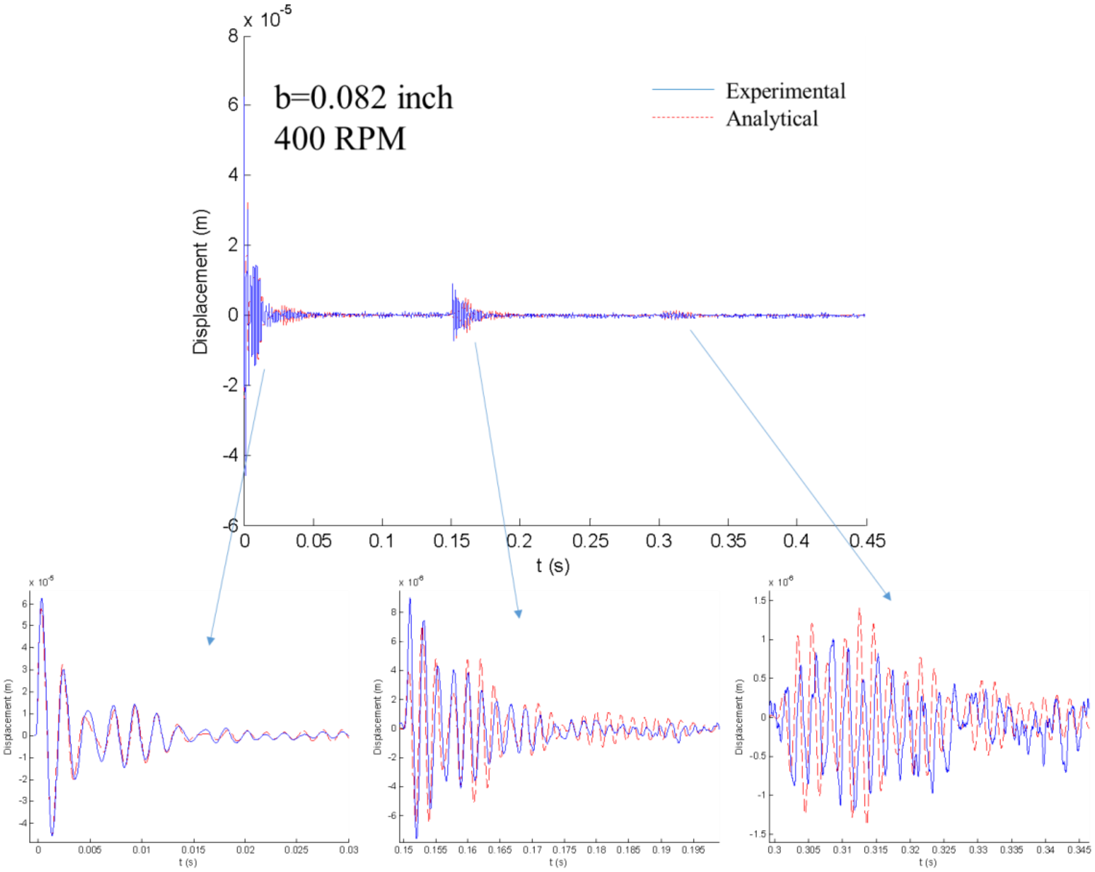

Figure 55: Experimental and analytical displacement data comparison for b=0.082 inch at 400 RPM.

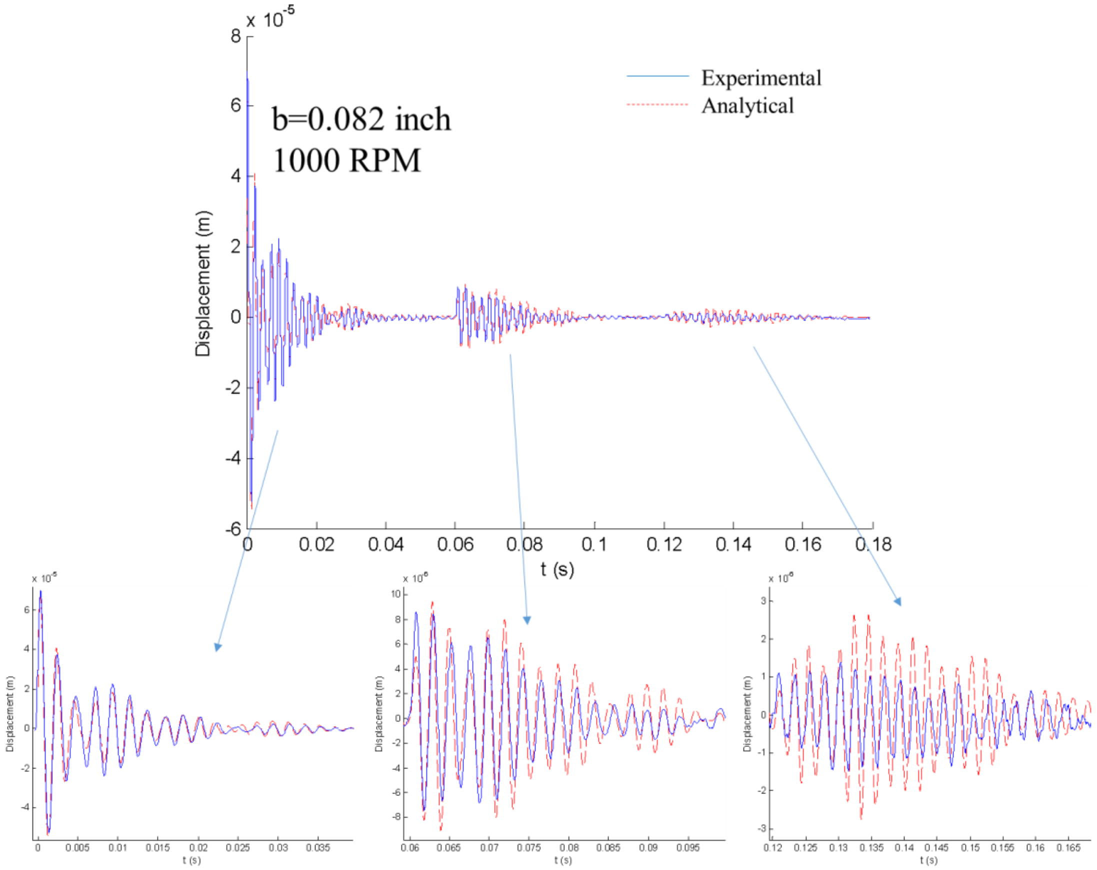

Figure 56: Experimental and analytical displacement data comparison for b=0.082 inch at 1000 RPM.

The results from this experimental study show that the general regenerative characteristics predicted by the analytical model are also observed physically. While the analytically predicted behavior of the tool deviates from the measured behavior as the number of rotations increase, the phase, frequency and general form of the oscillation envelopes closely agree.

CHAPTER 5: MATRIX SOLUTIONS

The analytical framework developed thus far in this dissertation has shown to be effective in determining the time response of a cutting tool in turning when compared with numerical simulation and experimentation. However, one drawback of the approach developed here is that the structure of the solution process becomes quite cumbersome. The objective in this chapter is to simplify the solution process for the sequential responses by generating a single matrix transformation to directly calculate the coefficients of one sequential response based on the coefficients of the previous sequential response. In Chapter 3: the general solution process was developed for multiple modes, which includes four primary steps to go from the coefficients of the previous response, x_{j-1}, to the coefficients of the current response, x_j, as illustrated again in Figure 57. Due to the number of transformations required and the conditional nature of the coefficient calculation process in the decoupled state space form (see Equation 3.17), this solution process becomes rather cumbersome especially as the number of modes increases. As such, a matrix solution is desired which incorporates all of the steps of the solution process into a more concise form, $x_j = \mathbf{Z} x_{j-1}$.

The sequential response transformation matrix, **Z**, is developed by going through the solution process and making the necessary modifications so that all of the coefficients of the various transformations (W coefficients and R coefficients) are expressed in terms of the coefficients of the previous sequential response, x_{j-1}.

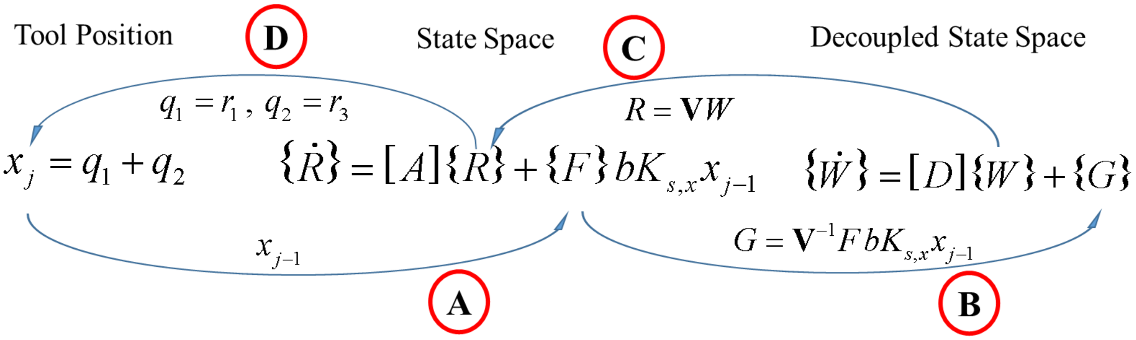

Figure 57: Process used to calculate the coefficients of the sequential responses.

Let us first start by assuming that the coefficients of x_{j-1} are known and systematically go through the solution process. The previous x coefficients are first applied to the forcing function of the state space model (see Figure 57A) as shown in Equation 5.1 , where $x_{1,j-1}$ and $x_{2,j-1}$ are the two modal position from the previous sequential response.

$$\{\dot{R}\} = [A]\{R\} + \{F\} bK_{s,x} x_{j-1} \text{ ,}$$
$$\{F\} bK_{s,x} x_{j-1} = \begin{Bmatrix} 0 \\ 1/m_{q1} \\ 0 \\ 1/m_{q2} \end{Bmatrix} bK_{s,x} \left(x_{1,j-1} + x_{2,j-1} \right) \qquad 5.1$$

The forcing terms in F are then transformed to G in the decoupled system using the transformation matrix V^{-1} (see Figure 57B). In order to represent the new forcing functions, G, in terms of the coefficients of the previous response, a new vector, H, is defined which scales the coefficients of x_{j-1} according to the transformation , $V^{-1}F$, as shown in Equation 5.2.

$$\{\dot{W}\} = [D]\{W\} + \{G\},\ \{G\} = \mathbf{V}^{-1} F\, bK_{s,x} x_{j-1} \text{ ,} H = \mathbf{V}^{-1} F$$
$$G = H\, bK_{s,x} x_{j-1} \qquad 5.2$$

The resulting decoupled system can now be expressed in terms of the coefficients of the previous sequential response as shown in Equation 5.3:

$$\{\dot{W}\} = [D]\{W\} + H\,bK_{s,x}x_{j-1}$$

$$\begin{bmatrix} \dot{w}_1 \\ \dot{w}_2 \\ \dot{w}_3 \\ \dot{w}_4 \end{bmatrix} = \begin{bmatrix} \lambda_1 & & & \\ & \lambda_2 & & \\ & & \lambda_3 & \\ & & & \lambda_4 \end{bmatrix} \begin{bmatrix} w_1 \\ w_2 \\ w_3 \\ w_4 \end{bmatrix} + \begin{bmatrix} h_1 \\ h_2 \\ h_3 \\ h_4 \end{bmatrix} bK_{s,x}x_{j-1} \tag{5.3}$$

Equation 5.3 is the stage of the process in which new coefficients are calculated based on the solutions to the decoupled first order differential equations. Take for example the solutions to w_1. The general form of x_{j-1} is shown in Equation 5.4, so if we take the maximum order of the polynomials to be 2, the solution to w_1 is found by solving Equation 5.5. The solution to Equation 5.5 is described in the previous chapter when the forcing terms are a_g using Equation 3.17. However, in Equation 3.17 when n≠u the solution coefficients ($a_{g,\lambda,n}$) are dependent on the higher order solution coefficients ($a_{g,\lambda,n+1}$). Here, Equation 3.17 is modified so that the solution coefficients are dependent only on the forcing coefficients, a_x, as shown in Equation 5.6 (See Appendix F for derivation of Equation 5.6).

$$\begin{aligned} x_{j-1} = {} & \left(a_{x,\lambda1,0} + a_{x,\lambda1,1}t + \ldots + a_{x,\lambda1,\mathrm{j}-1}t^{j-1}\right)\mathrm{e}^{\lambda_1 t} + \left(a_{x,\lambda2,0} + a_{x,\lambda2,1}t + \ldots + a_{x,\lambda2,\mathrm{j}-1}t^{j-1}\right)\mathrm{e}^{\lambda_2 t} \\ & + \left(a_{x,\lambda3,0} + a_{x,\lambda3,1}t + \ldots + a_{x,\lambda3,\mathrm{j}-1}t^{j-1}\right)\mathrm{e}^{\lambda_3 t} + \left(a_{x,\lambda4,0} + a_{x,\lambda4,1}t + \ldots + a_{x,\lambda4,\mathrm{j}-1}t^{j-1}\right)\mathrm{e}^{\lambda_4 t} \end{aligned} \tag{5.4}$$

$$\begin{aligned} \dot{w}_1 = {} & \lambda_1 w_1 + bK_{s,x}h_1\Big[\left(a_{x,\lambda1,0} + a_{x,\lambda1,1}t + a_{x,\lambda1,2}t^2\right)\mathrm{e}^{\lambda_1 t} + \left(a_{x,\lambda2,0} + a_{x,\lambda2,1}t + a_{x,\lambda2,2}t^2\right)\mathrm{e}^{\lambda_2 t} \\ & + \left(a_{x,\lambda3,0} + a_{x,\lambda3,1}t + a_{x,\lambda3,2}t^2\right)\mathrm{e}^{\lambda_3 t} + \left(a_{x,\lambda4,0} + a_{x,\lambda4,1}t + a_{x,\lambda4,2}t^2\right)\mathrm{e}^{\lambda_4 t}\Big] \end{aligned} \tag{5.5}$$

$$\begin{aligned} a_{wn,\lambda\,\mathrm{u},\mathrm{v}+1} &= bK_{s,x}h_n\frac{a_{\mathrm{x},\lambda\,\mathrm{u},\mathrm{v}}}{v+1};\ n = u \\ a_{wn,\lambda\,\mathrm{u},\mathrm{v}} &= bK_{s,x}h_n\sum_{v_x=v}^{V}\frac{(-1)^{(v+v_x)}\left(v_x\right)!\,a_{x,\lambda\,\mathrm{u},\mathrm{v}_x}}{(v)!\left(\lambda_u - \lambda_n\right)^{(1+v_g-v)}};\ n \neq u \end{aligned} \tag{5.6}$$

The solutions to the w_1 coefficients based on Equation 5.6 are applied in matrix form in Equation 5.7. Here, the transformation matrix, Y_1, is used to solve for the coefficients of w_1 based on the coefficients of x, where the vectors A_{w1} and A_x represent the coefficients of the combined polynomial and exponential basis.

$$A_{w1} = \mathbf{Y}_1 A_x \, bK_{s,x} h_1$$

$$\begin{bmatrix} a_{\mathrm{w}1,\lambda 1,0} \\ a_{\mathrm{w}1,\lambda 1,1} \\ a_{\mathrm{w}1,\lambda 1,2} \\ a_{\mathrm{w}1,\lambda 2,0} \\ a_{\mathrm{w}1,\lambda 2,1} \\ a_{\mathrm{w}1,\lambda 2,2} \\ a_{\mathrm{w}1,\lambda 3,0} \\ a_{\mathrm{w}1,\lambda 3,1} \\ a_{\mathrm{w}1,\lambda 3,2} \\ a_{\mathrm{w}1,\lambda 4,0} \\ a_{\mathrm{w}1,\lambda 4,1} \\ a_{\mathrm{w}1,\lambda 4,2} \end{bmatrix} = \begin{bmatrix} \overbrace{\begin{matrix} 0 & 0 & 0 \\ \frac{1}{1} & 0 & 0 \\ 0 & \frac{1}{2} & 0 \end{matrix}}^{\mathbf{Y}_{1,\lambda 1}} & \overbrace{\begin{matrix} \frac{-1}{\lambda_2-\lambda_1} & \frac{1}{(\lambda_2-\lambda_1)^2} & \frac{-2}{(\lambda_2-\lambda_1)^3} \end{matrix}}^{\mathbf{Y}_{IC1,\lambda 2}} & \overbrace{\begin{matrix} \frac{-1}{\lambda_3-\lambda_1} & \frac{1}{(\lambda_3-\lambda_1)^2} & \frac{-2}{(\lambda_3-\lambda_1)^3} \end{matrix}}^{\mathbf{Y}_{IC1,\lambda 3}} & \overbrace{\begin{matrix} \frac{-1}{\lambda_4-\lambda_1} & \frac{1}{(\lambda_4-\lambda_1)^2} & \frac{-2}{(\lambda_4-\lambda_1)^3} \end{matrix}}^{\mathbf{Y}_{IC1,\lambda 4}} \\ & \overbrace{\begin{matrix} \frac{1}{\lambda_2-\lambda_1} & \frac{-1}{(\lambda_2-\lambda_1)^2} & \frac{2}{(\lambda_2-\lambda_1)^3} \\ 0 & \frac{1}{\lambda_2-\lambda_1} & \frac{-2}{(\lambda_2-\lambda_1)^2} \\ 0 & 0 & \frac{1}{\lambda_2-\lambda_1} \end{matrix}}^{\mathbf{Y}_{1,\lambda 2}} & & \\ & & \overbrace{\begin{matrix} \frac{1}{\lambda_3-\lambda_1} & \frac{-1}{(\lambda_3-\lambda_1)^2} & \frac{2}{(\lambda_3-\lambda_1)^3} \\ 0 & \frac{1}{\lambda_3-\lambda_1} & \frac{-2}{(\lambda_3-\lambda_1)^2} \\ 0 & 0 & \frac{1}{\lambda_3-\lambda_1} \end{matrix}}^{\mathbf{Y}_{1,\lambda 3}} & \\ & & & \overbrace{\begin{matrix} \frac{1}{\lambda_4-\lambda_1} & \frac{-1}{(\lambda_4-\lambda_1)^2} & \frac{2}{(\lambda_4-\lambda_1)^3} \\ 0 & \frac{1}{\lambda_4-\lambda_1} & \frac{-2}{(\lambda_4-\lambda_1)^2} \\ 0 & 0 & \frac{1}{\lambda_4-\lambda_1} \end{matrix}}^{\mathbf{Y}_{1,\lambda 4}} \end{bmatrix} \begin{bmatrix} a_{x,\lambda 1,0} \\ a_{x,\lambda 1,1} \\ a_{x,\lambda 1,2} \\ a_{x,\lambda 2,0} \\ a_{x,\lambda 2,1} \\ a_{x,\lambda 2,2} \\ a_{x,\lambda 3,0} \\ a_{x,\lambda 3,1} \\ a_{x,\lambda 3,2} \\ a_{x,\lambda 4,0} \\ a_{x,\lambda 4,1} \\ a_{x,\lambda 4,2} \end{bmatrix} bK_{s,x} h_1 \qquad 5.7$$

The diagonal block elements of Equation 5.7 , $\mathrm{Y}_{1,\lambda u}$, represent the particular solutions to w_1 based on the input coefficients associated with λ_u. The particular solution transformation blocks, $\mathrm{Y}_{n,\lambda u}$, can be generated for all of the w solutions using Equation 5.8 . As it is known that the maximum degree of the solution polynomials increases by one in each sequential response, the total size of the $\mathrm{Y}_{n,\lambda u}$ matrices should be JxJ, where J is the total number of sequential responses being generated (so the transformation matrix in Equation 5.7 is applicable to the first three sequential responses). The size of the total transformation matrix solving for the w_1 coefficients is $2JN_{\mathrm{mode}} \times 2JN_{\mathrm{mode}}$, where there are $2N_{\mathrm{mode}}$ state variables.

The block elements in the first row of Equation 5.7, $\mathrm{Y}_{\mathrm{IC}1,\lambda u}$, represent the complementary solution to Equation 5.5. Recall that the sequential responses are calculated assuming zero valued initial conditions, so the total solution must be equal to zero at t=0. As such, the complementary solution must offset the initial displacements associated with the particular solutions, which, in this system are equal to the sum of all coefficients of degree zero ($a_{w1,\lambda u,0}$). Notice that the $Y_{IC1,\lambda u}$ blocks are the negative values of the first rows of the $Y_{1\lambda u}$ blocks. The complementary solution blocks can be generated for the w coefficients solutions using Equation 5.9.

$$\mathbf{Y}_{\mathrm{n},\lambda\,\mathrm{u}} = \begin{bmatrix} 0 & 0 & 0 & \cdots & 0 \\ 1/1 & 0 & 0 & \cdots & 0 \\ 0 & 1/2 & 0 & \ddots & 0 \\ 0 & 0 & \ddots & \cdots & 0 \\ 0 & 0 & 0 & \dfrac{1}{J-1} & 0 \end{bmatrix}_{J\times J} \quad ; n = u$$

$$\mathbf{Y}_{\mathrm{n},\lambda\,\mathrm{u}} = \begin{bmatrix} \dfrac{1}{\lambda_u-\lambda_n} & -\dfrac{1}{(\lambda_u-\lambda_n)^2} & \dfrac{2}{(\lambda_u-\lambda_n)^3} & \cdots & \vdots \\ 0 & \dfrac{1}{\lambda_u-\lambda_n} & -\dfrac{2}{(\lambda_u-\lambda_n)^2} & \cdots & \dfrac{(-1)^{(v+v_x)}(v_x)!}{(v)!(\lambda_u-\lambda_n)^{(1+v_x-v)}} \\ 0 & 0 & \dfrac{1}{\lambda_u-\lambda_n} & \ddots & \vdots \\ \vdots & \vdots & \cdots & \cdots & \vdots \\ 0 & 0 & 0 & \cdots & \dfrac{1}{\lambda_u-\lambda_n} \end{bmatrix}_{J\times J} \quad ; n \neq u \qquad 5.8$$

$$\mathbf{Y}_{\mathrm{ICn},\lambda\,\mathrm{u}} = 0 \;\; ; n = u$$

$$\mathbf{Y}_{\mathrm{ICn},\lambda\,\mathrm{u}} = \begin{bmatrix} \dfrac{-1}{\lambda_u-\lambda_n} & \dfrac{1}{(\lambda_u-\lambda_n)^2} & \dfrac{-2}{(\lambda_u-\lambda_n)^3} & \cdots & \dfrac{-(-1)^{(v_x)}(v_x)!}{(\lambda_u-\lambda_n)^{(1+v_x)}} \\ 0 & 0 & 0 & \cdots & \\ 0 & 0 & 0 & \ddots & \vdots \\ \vdots & \vdots & \cdots & \cdots & \vdots \\ 0 & 0 & 0 & \cdots & 0 \end{bmatrix}_{J\times J} \quad ; n \neq u \qquad 5.9$$

The general solutions to all of the w coefficients are found based on the x coefficients of the previous response using Equation 5.10. Note that in Equation 5.10 the Y_{ICn} blocks correspond to the row n of the Y_n matrices.

$$\mathbf{A}_{wn} = \mathbf{Y}_n \mathbf{A}_x bK_{s,x} h_n$$

$$\mathbf{Y}_1 = \begin{bmatrix} \mathbf{Y}_{1,\lambda 1} & \mathbf{Y}_{\mathrm{IC}1,\lambda 2} & \mathbf{Y}_{\mathrm{IC}1,\lambda 3} & \mathbf{Y}_{\mathrm{IC}1,\lambda 4} \\ & \mathbf{Y}_{1,\lambda 2} & & \\ & & \mathbf{Y}_{1,\lambda 3} & \\ & & & \mathbf{Y}_{1,\lambda 4} \end{bmatrix}, \mathbf{Y}_2 = \begin{bmatrix} \mathbf{Y}_{2,\lambda 1} & & & \\ \mathbf{Y}_{\mathrm{IC}2,\lambda 1} & \mathbf{Y}_{2,\lambda 2} & \mathbf{Y}_{\mathrm{IC}2,\lambda 1} & \mathbf{Y}_{\mathrm{IC}2,\lambda 1} \\ & & \mathbf{Y}_{2,\lambda 3} & \\ & & & \mathbf{Y}_{2,\lambda 4} \end{bmatrix} \quad 5.10$$

$$\mathbf{Y}_3 = \begin{bmatrix} \mathbf{Y}_{3,\lambda 1} & & & \\ & \mathbf{Y}_{3,\lambda 2} & & \\ \mathbf{Y}_{\mathrm{IC}3,\lambda 1} & \mathbf{Y}_{\mathrm{IC}3,\lambda 2} & \mathbf{Y}_{3,\lambda 3} & \mathbf{Y}_{\mathrm{IC}3,\lambda 4} \\ & & & \mathbf{Y}_{3,\lambda 4} \end{bmatrix}, \mathbf{Y}_4 = \begin{bmatrix} \mathbf{Y}_{4,\lambda 1} & & & \\ & \mathbf{Y}_{4,\lambda 2} & & \\ & & \mathbf{Y}_{4,\lambda 3} & \\ \mathbf{Y}_{\mathrm{IC}4,\lambda 1} & \mathbf{Y}_{\mathrm{IC}4,\lambda 2} & \mathbf{Y}_{\mathrm{IC}4,\lambda 3} & \mathbf{Y}_{4,\lambda 4} \end{bmatrix}$$

Where $\mathbf{Y_n}$ has the size $2JN_{\mathrm{mode}} \times 2JN_{\mathrm{mode}}$.

The next step in the solution process is to transform the W solutions back to the state space variables, R, using the transformation matrix V, as shown in Figure 57C. Recall that the R variables are the state space representations of the modal positions and velocities, as shown in Equation 5.11.

$$R = \mathbf{V}W = \begin{bmatrix} r_1 \\ r_2 \\ r_3 \\ r_4 \end{bmatrix} = \begin{bmatrix} x_1 \\ vel_1 \\ x_2 \\ vel_2 \end{bmatrix} = \begin{bmatrix} v_{1,1} & v_{1,2} & v_{1,3} & v_{1,4} \\ v_{2,1} & v_{2,2} & v_{2,3} & v_{2,4} \\ v_{3,1} & v_{3,2} & v_{3,3} & v_{3,4} \\ v_{4,1} & v_{4,2} & v_{4,3} & v_{4,4} \end{bmatrix} \begin{bmatrix} w_1 \\ w_2 \\ w_3 \\ w_4 \end{bmatrix} \quad 5.11$$

Since we are only concerned with the modal position values, x, Equation 5.11 can be reduced by considering only the odd rows of matrix V which correspond to the modal positions. The modified transformation is shown in Equation 5.12 in both the variable form and the corresponding coefficient form. In the coefficient form the coefficients, A_x, from the W solutions are replaced by A_x^{j-1} to indicate that these variables are from the previous sequential response.

$$X = \mathbf{V}_{odd}W,\ \begin{Bmatrix} x_1 \\ x_2 \end{Bmatrix} = \begin{bmatrix} v_{1,1} & v_{1,2} & v_{1,3} & v_{1,4} \\ v_{3,1} & v_{3,2} & v_{3,3} & v_{3,4} \end{bmatrix} \begin{Bmatrix} w_1 \\ w_2 \\ w_3 \\ w_4 \end{Bmatrix}$$

$$\mathbf{A}_X^j = \mathbf{V}_{odd}\mathbf{A}_W,\ \begin{Bmatrix} \mathbf{A}_{x1}^j \\ \mathbf{A}_{x2}^j \end{Bmatrix} = \begin{bmatrix} v_{1,1} & v_{1,2} & v_{1,3} & v_{1,4} \\ v_{3,1} & v_{3,2} & v_{3,3} & v_{3,4} \end{bmatrix} \begin{Bmatrix} \mathbf{Y}_1\mathbf{A}_x^{j-1}bK_{s,x}h_1 \\ \mathbf{Y}_2\mathbf{A}_x^{j-1}bK_{s,x}h_2 \\ \mathbf{Y}_3\mathbf{A}_x^{j-1}bK_{s,x}h_3 \\ \mathbf{Y}_4\mathbf{A}_x^{j-1}bK_{s,x}h_4 \end{Bmatrix} \quad 5.12$$

The transformation from the w coefficients to the coefficients of the first modal position, x_1, is carried out in Equation 5.13 where values $v_{1,n}$ correspond to the first row in the matrix $\mathbf{V}_{odd}$ associated with the first modal position (note that for the second modal position values of $v_{3,n}$ are used). The resulting transformation matrix, Z_1, defined by Equation 5.14, directly relates the coefficients of the previous sequential response to the coefficients of the first mode of the current sequential response.

$$\begin{aligned} \mathbf{A}_{x1}^j &= v_{1,1}\mathbf{Y}_1\mathbf{A}_x^{j-1}bK_{s,x}h_1 + v_{1,2}\mathbf{Y}_2\mathbf{A}_x^{j-1}bK_{s,x}h_2 + v_{1,3}\mathbf{Y}_3\mathbf{A}_x^{j-1}bK_{s,x}h_3 + v_{1,4}\mathbf{Y}_4\mathbf{A}_x^{j-1}bK_{s,x}h_4 \\ &= bK_{s,x}\left(v_{1,1}h_1\mathbf{Y}_1 + v_{1,2}h_2\mathbf{Y}_2 + v_{1,3}h_3\mathbf{Y}_3 + v_{1,4}h_4\mathbf{Y}_4\right)\mathbf{A}_x^{j-1} \\ &= Z_1\mathbf{A}_x^{j-1} \end{aligned} \quad 5.13$$

$$Z_{1,2} = bK_{s,x}\sum_{n=1}^{2N_{\text{mode}}} v_{(1,2),\text{n}}h_n\mathbf{Y}_n \quad 5.14$$

Once the Z transformation matrices are obtained the individual modal positions can be directly determined based on the previous sequential response solution using Equation 5.15.

$$\begin{aligned} \mathbf{A}_{x1}^j &= Z_1\mathbf{A}_x^{j-1} \\ \mathbf{A}_{x2}^j &= Z_2\mathbf{A}_x^{j-1} \end{aligned} \quad 5.15$$

As the coefficients of the total solution are a combination of the components of the individual modal solutions $\left(\mathbf{A}_x^j = \mathbf{A}_{x1}^j + \mathbf{A}_{x2}^j\right)$, Equation 5.15 can be combined to form Equation 5.16, or the total solution can be determined directly using Equation 5.17.

$$\begin{bmatrix} \mathbf{A}_{x1}^j \\ \mathbf{A}_{x2}^j \end{bmatrix} = \begin{bmatrix} Z_1 & Z_1 \\ Z_2 & Z_2 \end{bmatrix} \begin{bmatrix} \mathbf{A}_{x1}^{j-1} \\ \mathbf{A}_{x2}^{j-1} \end{bmatrix} \qquad 5.16$$

$$\mathbf{A}_x^j = Z_{seq} \mathbf{A}_x^{j-1}, \text{ } where \text{ } Z_{seq} = Z_1 + Z_2 \qquad 5.17$$

Equations 5.16 and 5.17 allow for the sequential response solutions to be obtained directly through the Z transformation matrices, where the input coefficient vectors, $\mathbf{A}_x^{j-1}$, are the solution coefficients from the previous sequential response. Two forms of the transformation matrices are provided in Equations 5.16 and 5.17 because each one is more advantageous depending on the application. For determining sequential responses, Equation 5.17 is better because the total solution is determined directly without concern for the motions of the individual modes. However, moving forward, the transition matrices developed here will be applied for stability analysis where the states of the individual modes are required within the solution process (see next chapter). As such, Equation 5.16 is needed to “keep track” of the modes individually.

5.1Matrix Dimensions for Z

It is well known that delay differential equations have solutions in infinite dimensional space (Stepan 1989). The solution process developed here determines the exact solution in finite dimensional space over a finite period of time, assuming the initial input function is finite dimensional. If the solution is continued over an infinite period of time, the solution will be infinite dimensional.

The sequential responses discussed in this paper each begin at the start of a new period in the solution process, where the period length is equal to the delay term, τ. Each time a new sequential response is found there is an increase in dimensionality relative to the dimensionality of the previous sequential response due to the solution process when u=n in Equation 5.6. The total solution of the Jth sequential response (for a 2DOF system) is shown in Equation 5.18 as a combined polynomial-exponential basis function with the set of complex coefficients, $\mathbf{A}_x^j$, in Equation 5.19.

The size of the basis function is determined by the total number of delay periods over which the system is to be evaluated, J, (which is equal to the number of sequential responses which must be determined) and the number of modes in the system. Looking at Equation 5.18, there are four sets of polynomials with maximum order, J-1, which each correspond to the eigenvalues of the state transition matrix, **A**, in Equation 3.8. As there are two state variables per mode, the number of dimensions in a solution over J periods with N_{mode} modes is $2JN_{\text{mode}}$, and the size of the transformation matrix $Z_{\text{seq.}}$ is $2JN_{\text{mode}} \times 2JN_{\text{mode}}$.

$$\begin{aligned} x_J = &\left(a_{x,\lambda 1,0} + a_{x,\lambda 1,1}t + \ldots + a_{x,\lambda 1,\mathrm{J}-1}t^{J-1}\right)\mathrm{e}^{\lambda_1 t} + \left(a_{x,\lambda 2,0} + a_{x,\lambda 2,1}t + \ldots + a_{x,\lambda 2,\mathrm{J}-1}t^{J-1}\right)\mathrm{e}^{\lambda_2 t} \\ &+\left(a_{x,\lambda 3,0} + a_{x,\lambda 3,1}t + \ldots + a_{x,\lambda 3,\mathrm{J}-1}t^{J-1}\right)\mathrm{e}^{\lambda_3 t} + \left(a_{x,\lambda 4,0} + a_{x,\lambda 4,1}t + \ldots + a_{x,\lambda 4,\mathrm{J}-1}t^{J-1}\right)\mathrm{e}^{\lambda_4 t} \end{aligned} \tag{5.18}$$

$$\mathbf{A}_x^J = \left\{ \begin{array}{l} a_{x,\lambda 1,0}, a_{x,\lambda 1,1}, \ldots, a_{x,\lambda 1,\mathrm{J}-1}, a_{x,\lambda 2,0}, a_{x,\lambda 2,1}, \ldots, a_{x,\lambda 2,\mathrm{J}-1}, \\ \qquad a_{x,\lambda 3,0}, a_{x,\lambda 3,1}, \ldots, a_{x,\lambda 3,\mathrm{J}-1}, a_{x,\lambda 4,0}, a_{x,\lambda 4,1}, \ldots, a_{x,\lambda 4,\mathrm{J}-1} \end{array} \right\}^J \tag{5.19}$$

Note that the basis function coefficients in Equations 5.18 and 5.19 are fully populated only for the Jth sequential response, and the previous responses have nonzero coefficients for t of order less than or equal to j-1. Starting with the first sequential response, which has nonzero coefficients only for the t of order zero terms, each subsequent response gains nonzero coefficients for t of order j-1 due to the terms under the diagonal of the Y_n matrices.

CHAPTER 6: STABILITY

In the previous chapter a transition matrix, $Z_{seq.}$, was developed to derive the coefficients of the sequential responses based on the coefficients of the previous response. $Z_{seq.}$ incorporates all of the transformations and conditional calculations (Equation 5.6) of the solution process in Figure 57 into a concise form which allows for the first J sequential responses to be found through simple matrix operations. While $Z_{seq.}$ allows for a more direct process when using the sequential response approach, it is not possible to define an analytical stability criterion based on the sequential responses alone. This is because the characteristics (or the coefficients) of the sequential responses individually cannot be used as an indicator of global behavior of the tool. As a result, the transformation matrix, $Z_{seq.}$, cannot not be used alone to determine stability

Take for example the tool response plot in Figure 58, which is composed of the first five sequential responses. The transformation matrix, $Z_{seq.}$, is useful to determine each sequential response based on the previous response, however, this transformation only provides information on the sequential responses but not the global behavior. The global behavior of the tool cannot be observed until the sequential responses are combined according to the delay period τ, as shown at the top of Figure 58, where the functions, y_j, form the total tool motions for each τ period. Note that the variable y is used to describe the total motion of the tool during each j^{th} period, where the variable x_j describes the j^{th} sequential response.

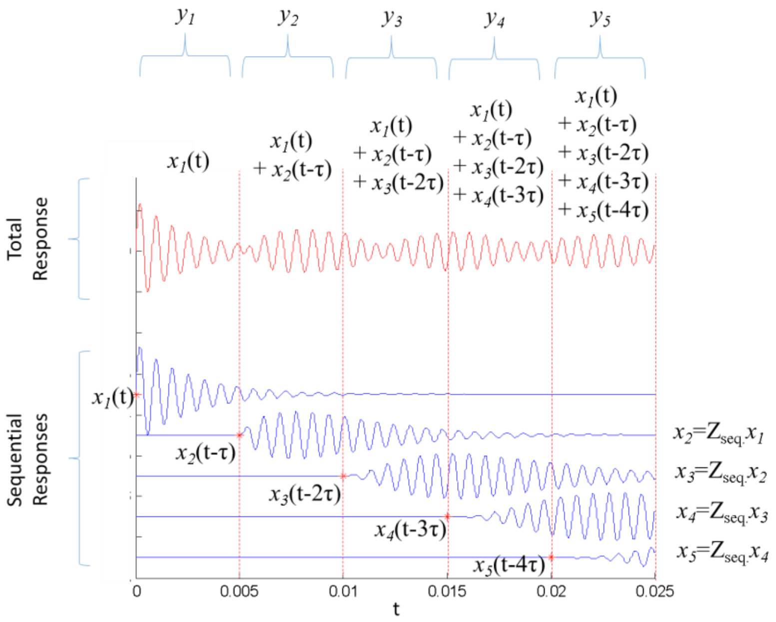

Figure 58: Example tool point response composed of the first five sequential responses, where the functions, y_j, describe the total tool point response during each τ period.

Ultimately it is the functions, y_j, describing the total tool motions during each τ period that are useful in determining the global stability of the system. Furthermore, if a new transition matrix, U, is found which directly relates the total tool motions during one revolution, y_j, to the total tool motions during the previous revolution, y_{j-1}, than a modified version of Floquet theory can be applied to determine stability based on the eigenvalues of U. The modifications to the transition matrix, $Z_{seq.}$, required to obtain the total transition matrix, U, are developed here based on the method of steps.

One difference between the U and $Z_{seq.}$ transition matrices is in the way that the forcing functions are applied to the solution process. In both cases, the transition matrices are used to determine the coefficients of a current function based on the coefficients of a previous function (or forcing function). For $Z_{seq.}$, the forcing coefficients are related to the coefficients of the previous sequential response (see Figure 58), while the forcing coefficients for U (using the method of steps) are related to the coefficients of the total tool motion during the previous period (see Figure 59).

Fortunately, the set of equations relating the forcing function coefficients to the solution coefficients are the same in both cases (see Equation 5.6), so the transformations already established in Z are directly applicable for U. The primary difference for U, however, is that the initial conditions which define the modal states at the beginning of each τ period can no longer be assumed to be zero. According to the method of steps, the initial conditions for each period are equal to the state conditions at the end of the previous period, as shown in Figure 59. As such, the transformation matrix U must contain additional components which define the initial conditions for one period based on the coefficients of the previous period evaluated at time, τ. The resulting matrix U, thus, is dependent on τ, where $Z_{seq.}$ is independent of τ.

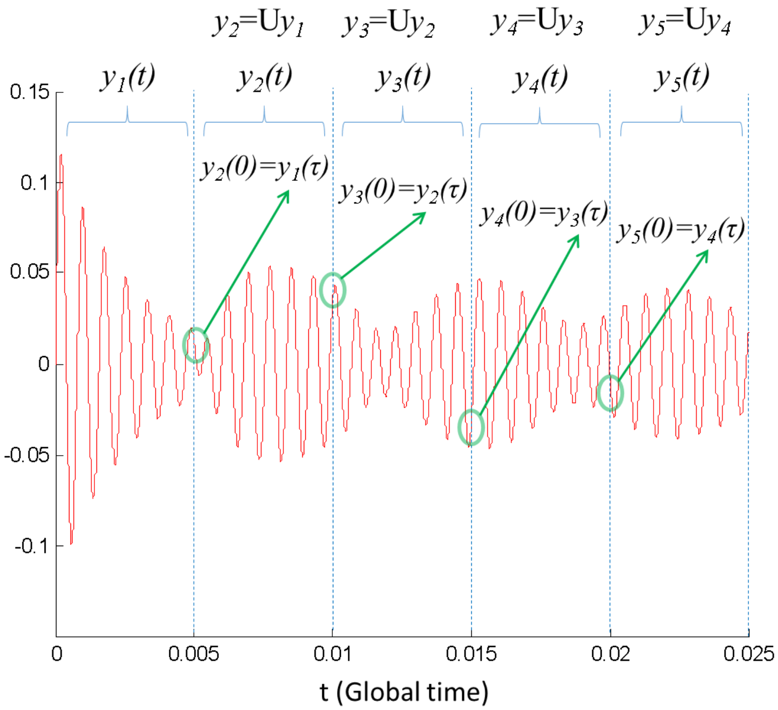

Figure 59: Functions, y_j, describing the total tool position for each τ period which are obtained using the method of steps.

6.1Matrix Dimensions for Stability Analysis

One advantage of the sequential response approach is that the sequential responses can be determined by assuming **zero valued initial conditions** (with the exception of the first response which has defined initial conditions). The assumption of zero initial conditions is significant because the solutions are not dependent on the conditions of each mode independently, so it is not necessary to "keep track" of the motions of each mode individually. This allows us to simply combine the motion of all of the modes by combining the coefficients of $\mathbf{A}_{\mathbf{x1}}$ and $\mathbf{A}_{\mathbf{x2}}$, and the individual transition matrixes, $\mathbf{Z}_{\mathbf{1}}$ and $\mathbf{Z}_{\mathbf{2}}$, to obtain the compact relation, $\mathbf{A}_x^j = Z_{seq.}\mathbf{A}_x^{j-1}$, where the size of $Z_{seq.}$ is $2JN_{\text{mode}} \times 2JN_{\text{mode}}$.

The situation is different when applying the method of steps because the initial conditions of each individual mode must be known in order to solve for the tool response during each period. As a result, the motions of multiple modes can no longer be combined, and it is necessary to maintain the coefficients describing the motion of each mode as separate entities. For this reason, Equation 5.16 is used for stability analysis instead of Equation 5.17, resulting in the transformation matrix, U, with dimensions of $2JN_{\text{mode}}^2 \times 2JN_{\text{mode}}^2$.

The resulting general form of the transformation matrix for the method of steps is shown in Equation 6.1. The Z components of Equation 6.1 solve for the solution coefficients of the current period based on the coefficients of the previous period (just as in Equation 5.16), and the IC_y components are added to relate the initial conditions of the current period to the modal conditions at the end of the previous period.

$$\mathbf{A}_y^j \rightarrow \begin{bmatrix} \mathbf{A}_{y1}^j \\ \mathbf{A}_{y2}^j \end{bmatrix} = \begin{bmatrix} Z_1 + IC_{y1} & Z_1 + IC_{y2} \\ Z_2 + IC_{y1} & Z_2 + IC_{y2} \end{bmatrix} \begin{bmatrix} \mathbf{A}_{y1}^{j-1} \\ \mathbf{A}_{y2}^{j-1} \end{bmatrix} \qquad 6.1$$

CHAPTER 7: TURNING STABILITY

The process for generating the transformation matrix, U, which directly relate the motion of the tool during one rotation and the motion of the tool during the previous rotation for turning is developed in this chapter.

The general form of the functions describing the total motion of the first system mode for the first J part revolutions is shown in Equation 7.1, where all functions for periods prior to J have zero valued coefficients for t of order greater than j-1. In order to apply the method of steps, the transformation matrix U must be able to first determine the initial conditions for each period, then apply those initial conditions to the new solution coefficients.

$$\begin{gathered} y_{\mathrm{J},1}(t)=\left(a_{\mathrm{y}_1,\lambda 1,0}+a_{y_1,\lambda 1,1}t+\ldots+a_{y_1,\lambda 1,\mathrm{J}-1}t^{J-1}\right)\mathrm{e}^{\lambda_1 t}+\left(a_{\mathrm{y}_1,\lambda 2,0}+a_{y_1,\lambda 2,1}t+\ldots+a_{\mathrm{y}_1,\lambda 2,\mathrm{J}-1}t^{J-1}\right)\mathrm{e}^{\lambda_2 t} \\ +\left(a_{\mathrm{y}_1,\lambda 3,0}+a_{\mathrm{y}_1,\lambda 3,1}t+\ldots+a_{\mathrm{y}_1,\lambda 3,\mathrm{J}-1}t^{J-1}\right)\mathrm{e}^{\lambda_3 t}+\left(a_{\mathrm{y}_1,\lambda 4,0}+a_{\mathrm{y}_1,\lambda 4,1}t+\ldots+a_{\mathrm{y}_1,\lambda 4,\mathrm{J}-1}t^{J-1}\right)\mathrm{e}^{\lambda_4 t} \\ y_J=y_{J,1}+y_{J,2} \end{gathered} \qquad 7.1$$

To determine the initial conditions of one period, the function from the previous period must be evaluated at t=τ to determine the modal states at the end of the previous period. A new vector, **Γ** in Equation 7.2, is defined to evaluate the function , $y_{j,n}$, at t=τ. The value of $y_{j,n}$ at t=τ is found by multiplying the vector **Γ** by the coefficient vector, $\mathbf{A}^{\mathrm{j}}_{\mathrm{n}}$, as shown in Equations 7.3 and 7.4.

$$\mathbf{\Gamma}=\left[e^{\lambda_1\tau}\left[1\,\tau\,\tau^2\cdots\tau^{J-1}\right]\ e^{\lambda_2\tau}\left[1\,\tau\,\tau^2\cdots\tau^{J-1}\right]\ e^{\lambda_3\tau}\left[1\,\tau\,\tau^2\cdots\tau^{J-1}\right]\ e^{\lambda_4\tau}\left[1\,\tau\,\tau^2\cdots\tau^{J-1}\right]\right] \qquad 7.2$$

$$y_{j=3,1}(\tau)=\left[e^{\lambda_1\tau}\left[1\,\tau\,\tau^2\right]\;e^{\lambda_2\tau}\left[1\,\tau\,\tau^2\right]\;e^{\lambda_3\tau}\left[1\,\tau\,\tau^2\right]\;e^{\lambda_4\tau}\left[1\,\tau\,\tau^2\right]\right]\begin{bmatrix}a_{\mathrm{y}_1,\lambda 1,0}\\ a_{\mathrm{y}_1,\lambda 1,1}\\ a_{\mathrm{y}_1,\lambda 1,2}\\ a_{\mathrm{y}_1,\lambda 2,0}\\ a_{\mathrm{y}_1,\lambda 2,1}\\ a_{\mathrm{y}_1,\lambda 2,2}\\ a_{\mathrm{y}_1,\lambda 3,0}\\ a_{\mathrm{y}_1,\lambda 3,1}\\ a_{\mathrm{y}_1,\lambda 3,2}\\ a_{\mathrm{y}_1,\lambda 4,0}\\ a_{\mathrm{y}_1,\lambda 4,1}\\ a_{\mathrm{y}_1,\lambda 4,2}\end{bmatrix} \qquad 7.3$$

$$y_{j,1}(\tau)=\mathbf{\Gamma}\mathbf{A}_{y1}^{j} \qquad 7.4$$

The modal velocities at the end of the previous period must also be determined to define the initial conditions of the current period. The first derivative of the position function, $y_{J,1}$ in Equation 7.1, is shown in Equation 7.5. A new vector Ω, defined in Equation 7.6, is created to account for the additional factors resulting from the differentiation process. The resulting velocity of mode n at t=τ can be found based on the **position** coefficient vector, $\mathbf{A}^{\mathrm{j}}{}_{\mathrm{n}}$, in Equation 7.7.

$$\begin{aligned}\dot{y}_{\mathrm{J},1}(t)= &\left(\lambda_1 a_{\mathrm{y}_1,\lambda 1,0}+\left(\lambda_1+\frac{1}{t}\right)a_{y_1,\lambda 1,1}t+\ldots+\left(\lambda_1+\frac{J-1}{t}\right)a_{y_1,\lambda 1,\mathrm{J}-1}t^{J-1}\right)\mathrm{e}^{\lambda_1 t}\\ &+\left(\lambda_2 a_{\mathrm{y}_1,\lambda 2,0}+\left(\lambda_2+\frac{1}{t}\right)a_{\mathrm{y}_1,\lambda 2,1}t+\ldots+\left(\lambda_2+\frac{J-1}{t}\right)a_{\mathrm{y}_1,\lambda 2,\mathrm{J}-1}t^{J-1}\right)\mathrm{e}^{\lambda_2 t}\\ &+\left(\lambda_3 a_{\mathrm{y}_1,\lambda 3,0}+\left(\lambda_3+\frac{1}{t}\right)a_{\mathrm{y}_1,\lambda 3,1}t+\ldots+\left(\lambda_3+\frac{J-1}{t}\right)a_{\mathrm{y}_1,\lambda 3,\mathrm{J}-1}t^{J-1}\right)\mathrm{e}^{\lambda_3 t}\\ &+\left(\lambda_4 a_{\mathrm{y}_1,\lambda 4,0}+\left(\lambda_4+\frac{1}{t}\right)a_{\mathrm{y}_1,\lambda 4,1}t+\ldots+\left(\lambda_4+\frac{J-1}{t}\right)a_{\mathrm{y}_1,\lambda 4,\mathrm{J}-1}t^{J-1}\right)\mathrm{e}^{\lambda_4 t}\end{aligned} \qquad 7.5$$

$$\Omega_n = \left[\lambda_n \;\; \lambda_n + \frac{1}{\tau} \;\; \lambda_n + \frac{2}{\tau} \;\; \cdots \;\; \lambda_n + \frac{(J-1)}{\tau} \right] \qquad 7.6$$

$$\Omega = \left[\Omega_1 \; \Omega_2 \; \Omega_3 \; \Omega_4 \right]$$

$$\dot{y}_{j,1}(\tau) = \Omega \circ \mathbf{\Gamma} \mathbf{A}_{y1}^{j} \qquad 7.7$$

Where ○ is an element-wise vector multiplication.

Equations 7.4 and 7.7 are critical for applying the method of steps to the transformation matrix, U, because they provide a method of determining the states of the system at the end of the previous period based on the coefficients of the previous period in matrix form. In other words, these equations give us "access" to the conditions at the end of the previous period which allow us to determine the initial conditions of the current period within the transformation matrix.

Before these equations can be applied, we must first consider how the coefficients of the current solution are affected by the initial conditions by returning to the general solution process from Figure 57. The initial values of the W functions are found according to Equation 7.8 based on the initial conditions, Y(0).

$$W(0) = \mathbf{V}^{-1} Y(0) = \begin{bmatrix} w_1(0) \\ w_2(0) \\ w_3(0) \\ w_4(0) \end{bmatrix} = \begin{bmatrix} v_{1,1}^{-1} & v_{1,2}^{-1} & v_{1,3}^{-1} & v_{1,4}^{-1} \\ v_{2,1}^{-1} & v_{2,2}^{-1} & v_{2,3}^{-1} & v_{2,4}^{-1} \\ v_{3,1}^{-1} & v_{3,2}^{-1} & v_{3,3}^{-1} & v_{3,4}^{-1} \\ v_{4,1}^{-1} & v_{4,2}^{-1} & v_{4,3}^{-1} & v_{4,4}^{-1} \end{bmatrix} \begin{bmatrix} y_1(0) \\ \dot{y}_1(0) \\ y_2(0) \\ \dot{y}_2(0) \end{bmatrix} \qquad 7.8$$

Expanded in Equation 7.9, the initial conditions for each W function are dependent on all of the modal initial conditions. Recall that the decoupled state space solutions, w_n, contain components associated with all of the eigenvalues, λ, however, the initial conditions only effect the coefficients associated with λ_n. As such, the solutions to Equation 7.9 will be associated with λ_n and t of order zero.

$$\begin{array}{ll}
w_1(0) = v^{-1}_{1,1} y_1(0) + v^{-1}_{1,2} \dot{y}_1(0) + v^{-1}_{1,3} y_2(0) + v^{-1}_{1,4} \dot{y}_2(0) & \rightarrow \; a_{w,\lambda 1,0} \\
\quad \vdots & \\
w_4(0) = v^{-1}_{4,1} y_1(0) + v^{-1}_{4,2} \dot{y}_1(0) + v^{-1}_{4,3} y_2(0) + v^{-1}_{4,4} \dot{y}_2(0) & \rightarrow \; a_{w,\lambda 4,0}
\end{array} \qquad 7.9$$

Once the initial W coefficients are known, they are converted back to Y using Equation 7.10. In Equation 7.11 the position components of Equation 7.10 are expanded, and the eigenvalue components of the solutions are shown.

$$Y(0) = \mathbf{V}W(0) = \begin{bmatrix} y_1(0) \\ \dot{y}_1(0) \\ y_2(0) \\ \dot{y}_2(0) \end{bmatrix} = \begin{bmatrix} v_{1,1} & v_{1,2} & v_{1,3} & v_{1,4} \\ v_{2,1} & v_{2,2} & v_{2,3} & v_{2,4} \\ v_{3,1} & v_{3,2} & v_{3,3} & v_{3,4} \\ v_{4,1} & v_{4,2} & v_{4,3} & v_{4,4} \end{bmatrix} \begin{bmatrix} w_1(0) \\ w_2(0) \\ w_3(0) \\ w_4(0) \end{bmatrix} \qquad 7.10$$

$$\begin{array}{l}
y_1(0) = v_{1,1}\, \overset{a_{w,\lambda 1,0}}{w_1(0)} + v_{1,2}\, \overset{a_{w,\lambda 2,0}}{w_2(0)} + v_{1,3}\, \overset{a_{w,\lambda 3,0}}{w_3(0)} + v_{1,4}\, \overset{a_{w,\lambda 4,0}}{w_4(0)} \\
y_2(0) = v_{3,1} w_1(0) + v_{3,2}\, w_2(0) + v_{3,3}\, w_3(0) + v_{3,4} w_4(0)
\end{array} \qquad 7.11$$

Substituting Equation 7.9 into Equation 7.11 and separating each eigenvalue component, the initial coefficients of the two modes can be calculated using Equation 7.12 based on the initial modal conditions.

$$\begin{array}{ll}
\mathbf{A}_{y1}(0) \rightarrow & \begin{array}{l}
a_{y1,\lambda 1,0} = v_{1,1}\left(v^{-1}_{1,1} y_1(0) + v^{-1}_{1,2} \dot{y}_1(0) + v^{-1}_{1,3} y_2(0) + v^{-1}_{1,4} \dot{y}_2(0)\right) \\
a_{y1,\lambda 2,0} = v_{1,2}\left(v^{-1}_{2,1} y_1(0) + v^{-1}_{2,2} \dot{y}_1(0) + v^{-1}_{2,3} y_2(0) + v^{-1}_{2,4} \dot{y}_2(0)\right) \\
a_{y1,\lambda 3,0} = v_{1,3}\left(v^{-1}_{3,1} y_1(0) + v^{-1}_{3,2} \dot{y}_1(0) + v^{-1}_{3,3} y_2(0) + v^{-1}_{3,4} \dot{y}_2(0)\right) \\
a_{y1,\lambda 4,0} = v_{1,4}\left(v^{-1}_{4,1} y_1(0) + v^{-1}_{4,2} \dot{y}_1(0) + v^{-1}_{4,3} y_2(0) + v^{-1}_{4,4} \dot{y}_2(0)\right)
\end{array} \\
\mathbf{A}_{y2}(0) \rightarrow & \begin{array}{l}
a_{y2,\lambda 1,0} = v_{3,1}\left(v^{-1}_{1,1} y_1(0) + v^{-1}_{1,2} \dot{y}_1(0) + v^{-1}_{1,3} y_2(0) + v^{-1}_{1,4} \dot{y}_2(0)\right) \\
a_{y2,\lambda 2,0} = v_{3,2}\left(v^{-1}_{2,1} y_1(0) + v^{-1}_{2,2} \dot{y}_1(0) + v^{-1}_{2,3} y_2(0) + v^{-1}_{2,4} \dot{y}_2(0)\right) \\
a_{y2,\lambda 3,0} = v_{3,3}\left(v^{-1}_{3,1} y_1(0) + v^{-1}_{3,2} \dot{y}_1(0) + v^{-1}_{3,3} y_2(0) + v^{-1}_{3,4} \dot{y}_2(0)\right) \\
a_{y2,\lambda 4,0} = v_{3,4}\left(v^{-1}_{4,1} y_1(0) + v^{-1}_{4,2} \dot{y}_1(0) + v^{-1}_{4,3} y_2(0) + v^{-1}_{4,4} \dot{y}_2(0)\right)
\end{array}
\end{array} \qquad 7.12$$

Substituting Equations 7.4 and 7.7 into Equation 7.12 and reducing in Equations 7.13 through 7.15, the resulting transformation matrix to determine the initial coefficients of the current solution based on the coefficients of the previous solution, $\mathbf{A}^{j\text{-}1}{}_{y}$, and the delay period, τ, is found as $U_{IC,Reduced}$, in Equation 7.16.

$$
\mathbf{A}^{j}_{y1}(0) \rightarrow
\begin{array}{l}
a_{y1,\lambda 1,0} = v_{1,1}\left(v^{-1}_{1,1}\boldsymbol{\Gamma}\mathbf{A}^{j-1}_{y1} + v^{-1}_{1,2}\boldsymbol{\Omega}\circ\boldsymbol{\Gamma}\mathbf{A}^{j-1}_{y1} + v^{-1}_{1,3}\boldsymbol{\Gamma}\mathbf{A}^{j-1}_{y2} + v^{-1}_{1,4}\boldsymbol{\Omega}\circ\boldsymbol{\Gamma}\mathbf{A}^{j-1}_{y2}\right) \\
a_{y1,\lambda 2,0} = v_{1,2}\left(v^{-1}_{2,1}\boldsymbol{\Gamma}\mathbf{A}^{j-1}_{y1} + v^{-1}_{2,2}\boldsymbol{\Omega}\circ\boldsymbol{\Gamma}\mathbf{A}^{j-1}_{y1} + v^{-1}_{2,3}\boldsymbol{\Gamma}\mathbf{A}^{j-1}_{y2} + v^{-1}_{2,4}\boldsymbol{\Omega}\circ\boldsymbol{\Gamma}\mathbf{A}^{j-1}_{y2}\right) \\
a_{y1,\lambda 3,0} = v_{1,3}\left(v^{-1}_{3,1}\boldsymbol{\Gamma}\mathbf{A}^{j-1}_{y1} + v^{-1}_{3,2}\boldsymbol{\Omega}\circ\boldsymbol{\Gamma}\mathbf{A}^{j-1}_{y1} + v^{-1}_{3,3}\boldsymbol{\Gamma}\mathbf{A}^{j-1}_{y2} + v^{-1}_{3,4}\boldsymbol{\Omega}\circ\boldsymbol{\Gamma}\mathbf{A}^{j-1}_{y2}\right) \\
a_{y1,\lambda 4,0} = v_{1,4}\left(v^{-1}_{4,1}\boldsymbol{\Gamma}\mathbf{A}^{j-1}_{y1} + v^{-1}_{4,2}\boldsymbol{\Omega}\circ\boldsymbol{\Gamma}\mathbf{A}^{j-1}_{y1} + v^{-1}_{4,3}\boldsymbol{\Gamma}\mathbf{A}^{j-1}_{y2} + v^{-1}_{4,4}\boldsymbol{\Omega}\circ\boldsymbol{\Gamma}\mathbf{A}^{j-1}_{y2}\right)
\end{array}
$$

$$
\mathbf{A}^{j}_{y2}(0) \rightarrow
\begin{array}{l}
a_{y2,\lambda 1,0} = v_{3,1}\left(v^{-1}_{1,1}\boldsymbol{\Gamma}\mathbf{A}^{j-1}_{y1} + v^{-1}_{1,2}\boldsymbol{\Omega}\circ\boldsymbol{\Gamma}\mathbf{A}^{j-1}_{y1} + v^{-1}_{1,3}\boldsymbol{\Gamma}\mathbf{A}^{j-1}_{y2} + v^{-1}_{1,4}\boldsymbol{\Omega}\circ\boldsymbol{\Gamma}\mathbf{A}^{j-1}_{y2}\right) \\
a_{y2,\lambda 2,0} = v_{3,2}\left(v^{-1}_{2,1}\boldsymbol{\Gamma}\mathbf{A}^{j-1}_{y1} + v^{-1}_{2,2}\boldsymbol{\Omega}\circ\boldsymbol{\Gamma}\mathbf{A}^{j-1}_{y1} + v^{-1}_{2,3}\boldsymbol{\Gamma}\mathbf{A}^{j-1}_{y2} + v^{-1}_{2,4}\boldsymbol{\Omega}\circ\boldsymbol{\Gamma}\mathbf{A}^{j-1}_{y2}\right) \\
a_{y2,\lambda 3,0} = v_{3,3}\left(v^{-1}_{3,1}\boldsymbol{\Gamma}\mathbf{A}^{j-1}_{y1} + v^{-1}_{3,2}\boldsymbol{\Omega}\circ\boldsymbol{\Gamma}\mathbf{A}^{j-1}_{y1} + v^{-1}_{3,3}\boldsymbol{\Gamma}\mathbf{A}^{j-1}_{y2} + v^{-1}_{3,4}\boldsymbol{\Omega}\circ\boldsymbol{\Gamma}\mathbf{A}^{j-1}_{y2}\right) \\
a_{y2,\lambda 4,0} = v_{3,4}\left(v^{-1}_{4,1}\boldsymbol{\Gamma}\mathbf{A}^{j-1}_{y1} + v^{-1}_{4,2}\boldsymbol{\Omega}\circ\boldsymbol{\Gamma}\mathbf{A}^{j-1}_{y1} + v^{-1}_{4,3}\boldsymbol{\Gamma}\mathbf{A}^{j-1}_{y2} + v^{-1}_{4,4}\boldsymbol{\Omega}\circ\boldsymbol{\Gamma}\mathbf{A}^{j-1}_{y2}\right)
\end{array}
\qquad 7.13
$$

$$
\mathbf{A}^{j}_{y1}(0) \rightarrow
\begin{array}{l}
a_{y1,\lambda 1,0} = v_{1,1}\left[\left[v^{-1}_{1,1} + v^{-1}_{1,2}\boldsymbol{\Omega}\right]\circ\boldsymbol{\Gamma}\ \left[v^{-1}_{1,3} + v^{-1}_{1,4}\boldsymbol{\Omega}\right]\circ\boldsymbol{\Gamma}\right]\begin{bmatrix}\mathbf{A}^{j-1}_{y1}\\ \mathbf{A}^{j-1}_{y2}\end{bmatrix} \\
a_{y1,\lambda 2,0} = v_{1,2}\left[\left[v^{-1}_{2,1} + v^{-1}_{2,2}\boldsymbol{\Omega}\right]\circ\boldsymbol{\Gamma}\ \left[v^{-1}_{2,3} + v^{-1}_{2,4}\boldsymbol{\Omega}\right]\circ\boldsymbol{\Gamma}\right]\begin{bmatrix}\mathbf{A}^{j-1}_{y1}\\ \mathbf{A}^{j-1}_{y2}\end{bmatrix} \\
a_{y1,\lambda 3,0} = v_{1,3}\left[\left[v^{-1}_{3,1} + v^{-1}_{3,2}\boldsymbol{\Omega}\right]\circ\boldsymbol{\Gamma}\ \left[v^{-1}_{3,3} + v^{-1}_{3,4}\boldsymbol{\Omega}\right]\circ\boldsymbol{\Gamma}\right]\begin{bmatrix}\mathbf{A}^{j-1}_{y1}\\ \mathbf{A}^{j-1}_{y2}\end{bmatrix} \\
a_{y1,\lambda 4,0} = v_{1,4}\left[\left[v^{-1}_{4,1} + v^{-1}_{4,2}\boldsymbol{\Omega}\right]\circ\boldsymbol{\Gamma}\ \left[v^{-1}_{4,3} + v^{-1}_{4,4}\boldsymbol{\Omega}\right]\circ\boldsymbol{\Gamma}\right]\begin{bmatrix}\mathbf{A}^{j-1}_{y1}\\ \mathbf{A}^{j-1}_{y2}\end{bmatrix}
\end{array}
$$

$$
\mathbf{A}^{j}_{y2}(0) \rightarrow
\begin{array}{l}
a_{y2,\lambda 1,0} = v_{3,1}\left[\left[v^{-1}_{1,1} + v^{-1}_{1,2}\boldsymbol{\Omega}\right]\circ\boldsymbol{\Gamma}\ \left[v^{-1}_{1,3} + v^{-1}_{1,4}\boldsymbol{\Omega}\right]\circ\boldsymbol{\Gamma}\right]\begin{bmatrix}\mathbf{A}^{j-1}_{y1}\\ \mathbf{A}^{j-1}_{y2}\end{bmatrix} \\
a_{y2,\lambda 2,0} = v_{3,2}\left[\left[v^{-1}_{2,1} + v^{-1}_{2,2}\boldsymbol{\Omega}\right]\circ\boldsymbol{\Gamma}\ \left[v^{-1}_{2,3} + v^{-1}_{2,4}\boldsymbol{\Omega}\right]\circ\boldsymbol{\Gamma}\right]\begin{bmatrix}\mathbf{A}^{j-1}_{y1}\\ \mathbf{A}^{j-1}_{y2}\end{bmatrix} \\
a_{y2,\lambda 3,0} = v_{3,3}\left[\left[v^{-1}_{3,1} + v^{-1}_{3,2}\boldsymbol{\Omega}\right]\circ\boldsymbol{\Gamma}\ \left[v^{-1}_{3,3} + v^{-1}_{3,4}\boldsymbol{\Omega}\right]\circ\boldsymbol{\Gamma}\right]\begin{bmatrix}\mathbf{A}^{j-1}_{y1}\\ \mathbf{A}^{j-1}_{y2}\end{bmatrix} \\
a_{y2,\lambda 4,0} = v_{3,4}\left[\left[v^{-1}_{4,1} + v^{-1}_{4,2}\boldsymbol{\Omega}\right]\circ\boldsymbol{\Gamma}\ \left[v^{-1}_{4,3} + v^{-1}_{4,4}\boldsymbol{\Omega}\right]\circ\boldsymbol{\Gamma}\right]\begin{bmatrix}\mathbf{A}^{j-1}_{y1}\\ \mathbf{A}^{j-1}_{y2}\end{bmatrix}
\end{array}
\qquad 7.14
$$

$$\begin{bmatrix}\mathbf{A}_{y1}^{j}(0)\\ \mathbf{A}_{y2}^{j}(0)\end{bmatrix}\rightarrow\begin{bmatrix}a_{y1,\lambda1,0}\\ a_{y1,\lambda2,0}\\ a_{y1,\lambda3,0}\\ a_{y1,\lambda4,0}\\ a_{y2,\lambda1,0}\\ a_{y2,\lambda2,0}\\ a_{y2,\lambda3,0}\\ a_{y2,\lambda4,0}\end{bmatrix}=\begin{bmatrix}v_{1,1}\left[\left[v_{1,1}^{-1}+v_{1,2}^{-1}\Omega\right]\circ\boldsymbol{\Gamma}\;\left[v_{1,3}^{-1}+v_{1,4}^{-1}\Omega\right]\circ\boldsymbol{\Gamma}\right]\\ v_{1,2}\left[\left[v_{2,1}^{-1}+v_{2,2}^{-1}\Omega\right]\circ\boldsymbol{\Gamma}\;\left[v_{2,3}^{-1}+v_{2,4}^{-1}\Omega\right]\circ\boldsymbol{\Gamma}\right]\\ v_{1,3}\left[\left[v_{3,1}^{-1}+v_{3,2}^{-1}\Omega\right]\circ\boldsymbol{\Gamma}\;\left[v_{3,3}^{-1}+v_{3,4}^{-1}\Omega\right]\circ\boldsymbol{\Gamma}\right]\\ v_{1,4}\left[\left[v_{4,1}^{-1}+v_{4,2}^{-1}\Omega\right]\circ\boldsymbol{\Gamma}\;\left[v_{4,3}^{-1}+v_{4,4}^{-1}\Omega\right]\circ\boldsymbol{\Gamma}\right]\\ v_{3,1}\left[\left[v_{1,1}^{-1}+v_{1,2}^{-1}\Omega\right]\circ\boldsymbol{\Gamma}\;\left[v_{1,3}^{-1}+v_{1,4}^{-1}\Omega\right]\circ\boldsymbol{\Gamma}\right]\\ v_{3,2}\left[\left[v_{2,1}^{-1}+v_{2,2}^{-1}\Omega\right]\circ\boldsymbol{\Gamma}\;\left[v_{2,3}^{-1}+v_{2,4}^{-1}\Omega\right]\circ\boldsymbol{\Gamma}\right]\\ v_{3,3}\left[\left[v_{3,1}^{-1}+v_{3,2}^{-1}\Omega\right]\circ\boldsymbol{\Gamma}\;\left[v_{3,3}^{-1}+v_{3,4}^{-1}\Omega\right]\circ\boldsymbol{\Gamma}\right]\\ v_{3,4}\left[\left[v_{4,1}^{-1}+v_{4,2}^{-1}\Omega\right]\circ\boldsymbol{\Gamma}\;\left[v_{4,3}^{-1}+v_{4,4}^{-1}\Omega\right]\circ\boldsymbol{\Gamma}\right]\end{bmatrix}\begin{bmatrix}\mathbf{A}_{y1}^{j-1}\\ \mathbf{A}_{y2}^{j-1}\end{bmatrix}\qquad 7.15$$

$$\begin{bmatrix}\mathbf{A}_{y1}^{j}(0)\\ \mathbf{A}_{y2}^{j}(0)\end{bmatrix}=U_{IC,\mathrm{Reduced}}\begin{bmatrix}\mathbf{A}_{y1}^{j-1}\\ \mathbf{A}_{y2}^{j-1}\end{bmatrix}\qquad 7.16$$

The components of $U_{\mathrm{IC,Reduced}}$ can be found using Equation 7.17, where $\otimes$ is a Kronecker product. The subscript "Reduced" in $U_{\mathrm{IC,Reduced}}$ is present here because the rows of $U_{\mathrm{IC,Reduced}}$ correspond only to the t of order zero rows of the transition matrix. In the full transition matrix, the rows of $U_{\mathrm{IC,Reduced}}$ are shifted to match the t of order zero terms to form U_{IC}.

$$\begin{gathered}U_{IC,\mathrm{Reduced}}=\begin{bmatrix}U_{IC,1,1}\;U_{IC,1,2}\\ U_{IC,2,1}\;U_{IC,2,2}\end{bmatrix}\\ U_{IC,\mathrm{Reduced},\mathrm{n}_1,\mathrm{n}_2}=\left[\mathbf{V}(2n_1-1,:)^T\circ\mathbf{V}^{-1}(:,2n_2-1)\right]\otimes\boldsymbol{\Gamma}+\left[\mathbf{V}(2n_1-1,:)^T\circ\mathbf{V}^{-1}(:,2n_2)\right]\otimes[\Omega\circ\boldsymbol{\Gamma}]\end{gathered}\qquad 7.17$$

We now have all of the components required to describe the motions of the tool during one period based on the motion of the tool during the previous period. In Equation 7.18, the Z component of the transition matrix (calculated using Equation 5.14) determines the motion of the tool based on the "surface left behind" in the previous period, and the U_{IC} component sets the initial conditions of the current period based on the conditions at the end of the previous period.

$$\begin{bmatrix}\mathbf{A}_{y1}^{j}\\ \mathbf{A}_{y2}^{j}\end{bmatrix}=\begin{bmatrix}Z_1\;Z_1\\ Z_2\;Z_2\end{bmatrix}\begin{bmatrix}\mathbf{A}_{y1}^{j-1}\\ \mathbf{A}_{y2}^{j-1}\end{bmatrix}+U_{IC}\begin{bmatrix}\mathbf{A}_{y1}^{j-1}\\ \mathbf{A}_{y2}^{j-1}\end{bmatrix}\qquad 7.18$$

After combining these two components the total transformation matrix, U_{turn}, is obtained, as shown in Equation 7.19.

$$\begin{bmatrix} \mathbf{A}_{y1}^{j} \\ \mathbf{A}_{y2}^{j} \end{bmatrix} = U_{turn} \begin{bmatrix} \mathbf{A}_{y1}^{j-1} \\ \mathbf{A}_{y2}^{j-1} \end{bmatrix}, \qquad U_{turn} = \begin{bmatrix} Z_1 & Z_1 \\ Z_2 & Z_2 \end{bmatrix} + U_{IC} \tag{7.19}$$

7.1Example

The transition matrix for turning in Equation 7.19 is now compared to numerical simulation results to verify that the tool motions described analytically match numerical results. Euler integration is used in the numerical simulations using a time step which results in approximately 100 iterations per tool oscillation. In both the analytical and numerical simulations, the system parameters shown in Table 4 are used, and the initial conditions at the start of the cutting process are $y(0)=0,\text{and}\,\dot{y}(0)=1m/s$. Two example solutions are plotted using the machining parameters of b=2.5mm at 6000 and 8000 RPM as shown in the stability lobe diagram in Figure 60.

Table 4: System parameters used in the single mode turning examples.

k	1E7 N/m
m	0.88 kg
c	400 Ns/m
K_s	2E9 N/m^2
β	70°

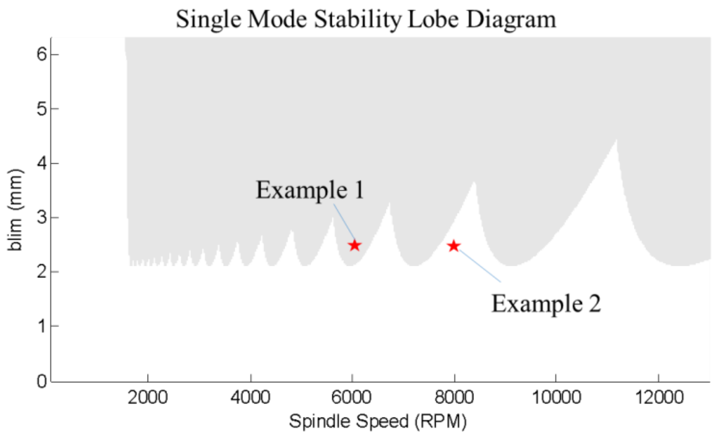

Figure 60: Two time domain examples for a single mode system evaluated at a depth of cut, b=2.5mm at 6000 and 8000 RPM.

The two example solutions are plotted in Figure 61 over 8 part revolutions. These results show that the functions, y_j, match those of the numerical solution over this range. Also, the stability predictions based on the stability lobe diagram in Figure 60 agree with the time domain plots, where example 1 appears to be unstable while example 2 is stable.

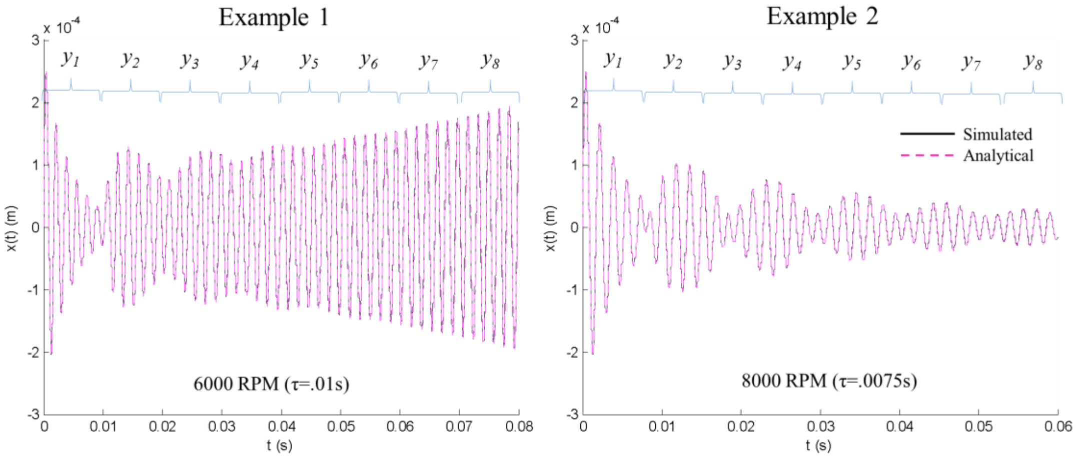

Figure 61: Two time domain examples for a single mode system, where the analytical motions for each period are fount using Equation 7.19. As predicted by the stability lobe diagram, Example 1 is unstable, and Example 2 is stable.

A second set of example solutions is shown for a two mode system using the modal parameters shown in Table 5. The machining parameters shown in the stability lobe diagram in Figure 62 are used for the two examples, with b=3.75mm and spindle speeds of 6000 and 8000 RPM. The same numerical simulation parameters used in the single mode examples are used here.

Table 5: System parameters used in the multi-mode turning examples.

k_1, k_2	1E7, 4E7 N/m
m_1, m_2	0.88, 1.2 kg
c_1, c_2	500, 600 Ns/m
K_s	2E9 N/m^2
β	70°

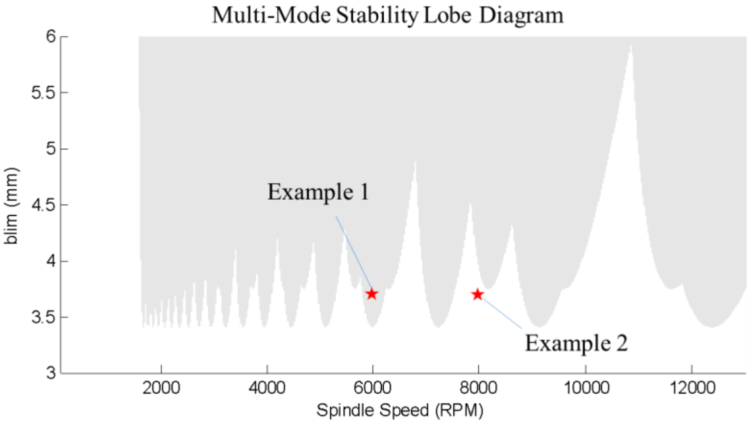

Figure 62: Two time domain examples for a multi-mode system evaluated at a depth of cut, b=3.75mm at 6000 and 8000 RPM.

The resulting time domain plots for the two mode examples are shown in Figure 63. These results also show that the analytical and numerical results agree even though the system dynamics are more complex as a result of the additional mode. The stability characteristics of these plots also agree with the predictions of the stability lobe diagram, where example 1 is unstable and example 2 is stable.

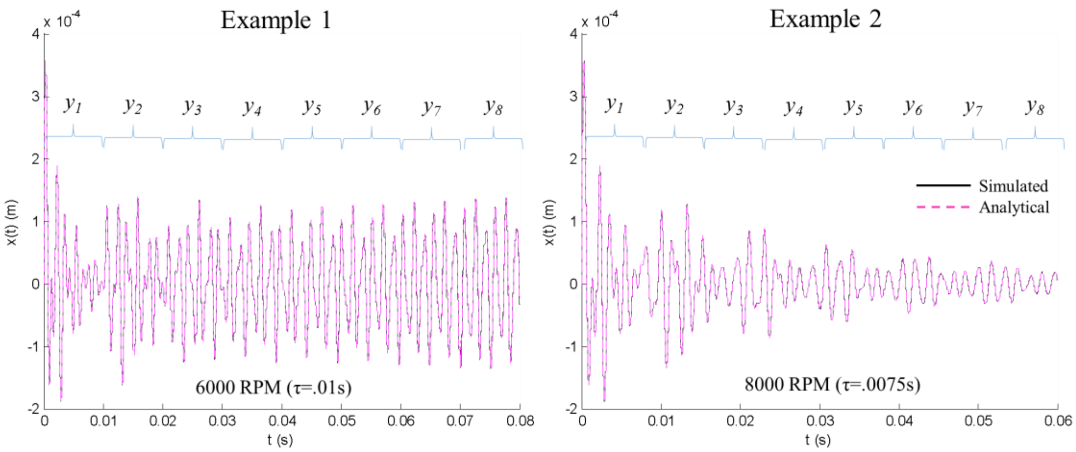

Figure 63: Two time domain examples for a multi-mode system, where the analytical motions for each period are fount using Equation 7.19. As predicted by the stability lobe diagram, Example 1 is unstable, and Example 2 is stable.

7.2Stability Analysis

The ability to describe tool motions analytically during a cutting operation is convenient, however, it is typically more important to be able to determine whether the tool motions will be stable or unstable (chatter) based on the parameters of the machining operation. In this section, the possibility of using characteristics of the transition matrix, U_{turn} in Equation 7.19, to determine stability directly is investigated. Here, a modified version of Floquet theory is used to determine stability based on the eigenvalues of U_{turn}. Floquet theory is used to evaluate the stability of delay systems where the coefficients describing the system at periodic points in time are related through a single transition matrix (U_{turn} Equation 7.19) (Bayly 2003; Insperger 2002; Insperger 2004; Minis 1993). From this theory, the eigenvalues of the transition matrix can be used to indicate the stability of the system, where if the maximum eigenvalue magnitude is less than 1 the system is stable, and if any of the eigenvalue magnitudes are greater than 1, the system is unstable.

The stability lobes generated using Floquet theory are compared with stability lobes generated using numerical simulation in Figure 64 using the system parameters in Table 4. For the simulated stability lobes, time domain simulations are run over 50 revolutions using a time step resulting in approximately 20 iterations per tool oscillation. The simulation is repeated over a range of 30 values of b from 0.01mm to 10mm and 100 spindle speeds from 100 to 13000 RPM, resulting in a total number of 3000 simulations. During each simulation, once per revolution samples are taken of the position of the tool, and the slope of the last two thirds of the absolute values of the sampled positions is found using the "polyfit" command in Matlab. If the slope of these points is greater than zero, it is determined to be unstable, and if the slope is less than zero it is stable.

The analytically determined stability lobes are found by evaluating the eigenvalues of U_{turn} with J=8 part revolutions over 100 values of b from 0.01mm to 10mm and 100 spindle speeds from 100 to 13000 RPM. If the magnitude of any of the eigenvalues is greater than one, the system is unstable, if less than one, the system is stable. Both stability lobe plots are generated in Matlab as contour plots, where the line associated with the value zero over a grid of slope values is plotted for the simulated stability lobes, and the line associated with the value one over a grid of maximum eigenvalue magnitude is plotted for the analytical stability lobes. (Note that the remaining stability lobe plots in this document are plotted using this method)

The resulting stability lobe diagrams are shown in Figure 64. It can be seen in this figure that the stability boundaries closely match at higher spindle speeds, but as the spindle speed is decreased, the analytically determined stability boundary begins to bend upward relative to the simulated stability boundary.

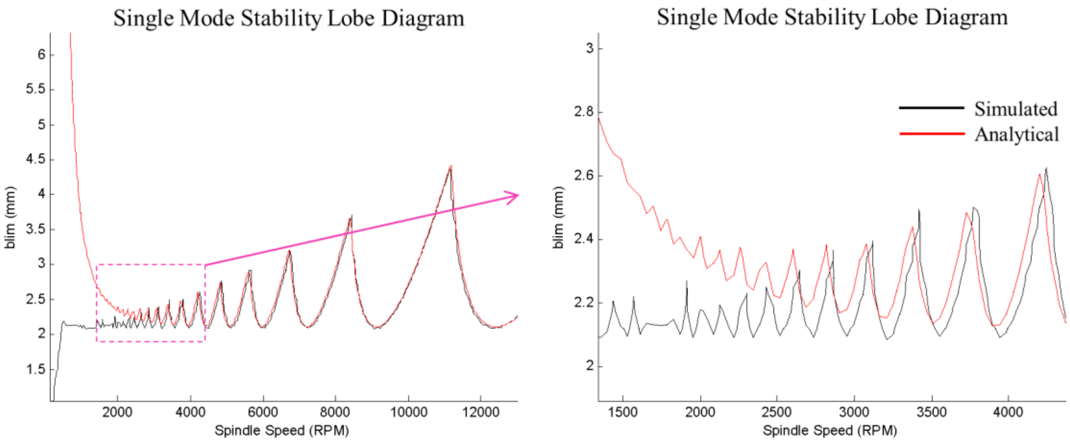

Figure 64: Single Mode stability lobe comparison using numerical simulation with 20 points per oscillation over 50 revolutions, and the analytical stability prediction found by evaluated the eigenvalues of the transition matrix in Equation 7.19 using N_{rev}=8.

The “upward bend” in the analytical stability lobes is a result of the parameter, J, used to produce the transition matrix, U_{turn}. Recall that J is the number of part revolutions (or delay periods) for which the solution to Equation 7.19 is exact. To see how the value of J affects the analytical stability boundary, in Figure 65, the stability lobes are plotted for J=2, 4, 6, and 8 along with the stability boundary generated using Tlusty’s FRF approach. It is clear from this figure that as J is increased, the stability boundaries approach those predicted by Tlusty, and the upward bend occurs at lower spindle speeds. While increasing J produces more accurate results, there is a drawback to increasing J due to the size of the U_{turn} matrix. For example, in this single mode system, if J is increased from 2 to 8, the size of U_{turn} increases from 4x4 to 16x16 (where $size\left(U_{turn}\right)=2N_{rev}N_{\mathrm{mode}}^{2}\times 2N_{rev}N_{\mathrm{mode}}^{2}$).

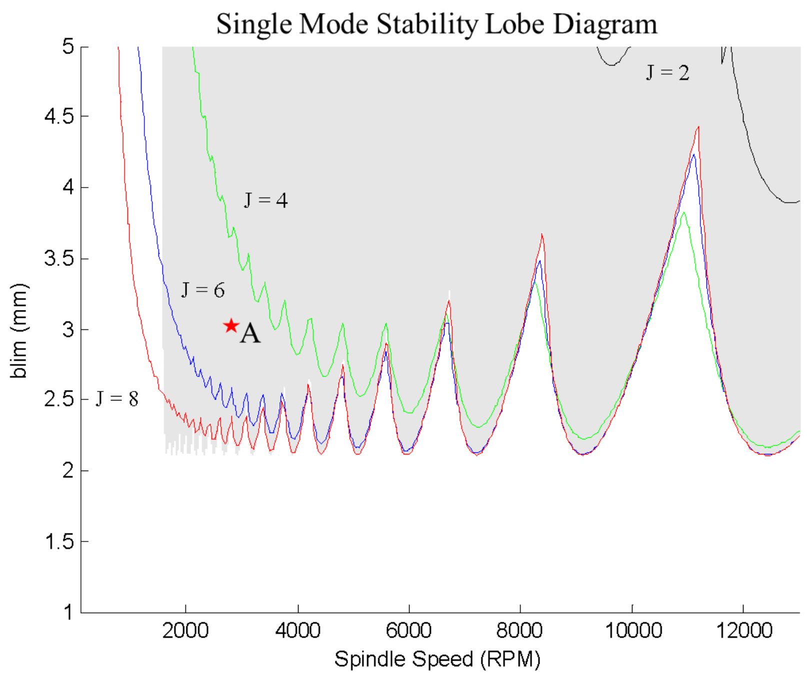

Figure 65: Single mode stability lobe diagram determined analytically using J = 2, 4, 6, and 8 compared with Tlusty's stability lobes (gray).

To better understand how J affects the stability boundary, consider the point A in Figure 65 in between the J=4 and 6 boundaries. Recall that DDEs are inherently infinite dimensional systems. The solution process developed in this dissertation provides an exact, finite dimensional solution to a DDE, however, the solution is only exact over a finite number of delay periods. If a transition matrix generated to be exact for J periods is used to generate the tool response for more than J periods, then all coefficients of the solutions of order greater than J are ignored, and accuracy is lost. For example, in Figure 66 the analytical time responses are shown for 50 revolutions when the transition matrices are limited to J= 4 and 6 using the machining parameters at point A in Figure 65. It is known based on Tlusty's model that the system is unstable at A. When U_{turn} with J=4 is evaluated over 50 revolutions, the time response appears to be stable, while the time response is shown to be unstable if J is increased to 6 (note that both of these results agree with their respective stability boundaries). The takeaway from Figure 65 and Figure 66 is that as the spindle speed decreases (and the delay period increases) higher order terms are required to accurately predict stability in turning, and all of the stability boundaries become more accurate as the spindle speed increases (delay period decreases).

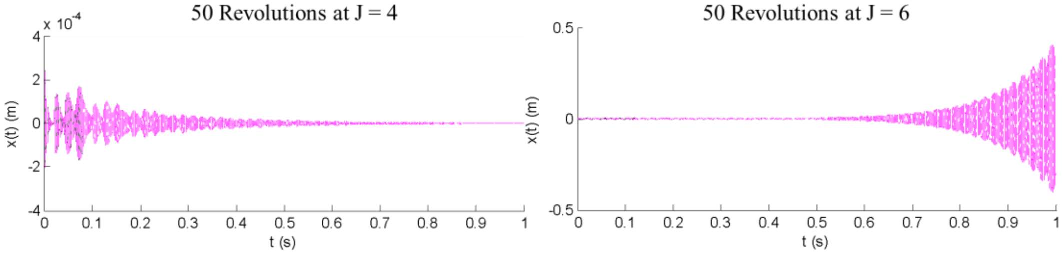

Figure 66: Comparison of analytical solutions at point A in Figure 65 when the transition matrix, U_{turn}, is created as J = 4 and 6 and carried out over 50 revolutions.

The stability boundaries for the two mode system from Table 5 is plotted in Figure 67 for J=2, 4, 6 and 8 along with the stability boundary predicted by Tlusty. The results from Figure 67 show that the application of Floquet theory is effective in predicting stability limits even as more modes are applied to the system. Here again we see that as J is increased, the accuracy of the stability boundaries increases. However, as J is increased for a two mode system, the resulting increase in the size of U_{turn} is more significant, where an increase of J from 2 to 8 causes an increase in the size of U_{turn} from 16x16 to 64x64 (where $size(U_{turn}) = 2JN_{\text{mode}}^2 \times 2JN_{\text{mode}}^2$).

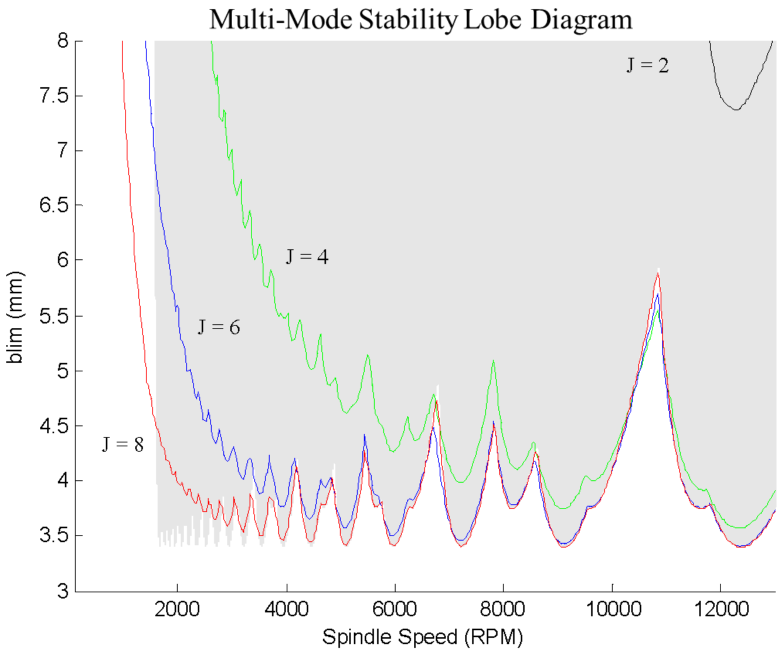

Figure 67: Multi-mode stability lobe diagram determined analytically using J = 2, 4, 6, and 8 compared with Tlusty's stability lobes (gray).

7.3Conclusions

The use of Floquet theory in this chapter to evaluate turning stability based on the transition matrix, U_{turn}, has been shown to be effective at higher spindle speeds, with decreasing accuracy as the spindle speed decreases. As the spindle speed increases, the stability limits approach those predicted using Tlustys' FRF approach. One way to increase the accuracy using the current method at lower spindle speeds is to increase the value of J, and thus the size of U_{turn}, at increased computational expense. It is interesting to note that the upward bends shown in the stability lobes resemble the upward bends known to exist as a result of increased process damping at lower spindle speeds. However, there is no consideration of process damping in the current model so there is no physical link between the upward bends shown here and process damping.

The processes used in this chapter to determine the transition matrix, U_{turn}, and to determine stability analytically have shown to be effective for the most basic cutting operation (turning). In the following chapters, these methods will be expanded for the evaluation of more complex machining operations.

CHAPTER 8: STABILITY IN LOW RADIAL IMMERSION MILLING

Low radial immersion milling (LRIM) is a type of milling operation in which the tool is engaged in the work piece for a relatively short period of time as it rotates.

Classical stability criteria (Altintas 1995; Tlusty 1963) becomes less accurate for LRIM because the tool is only in the work piece for a short period of time, while it vibrates freely for the rest of the time. The introduction of intermittent free vibration periods increases the complexity of the stability prediction process because the system is, in effect, governed by two different dynamic models depending on if the tool is in the cut or not. The result of the free vibrations, noted by Davies et al in (Davies 2002), are additional lobe features that appear in the stability lobe diagram. Davies et al was able to produce these additional lobes by pairing the “free” dynamic system to an “approximate “cutting” dynamic system (Davies 2002). Davies’ process was later improved in (Bayly 2003) by incorporating temporal finite element analysis (TFEA) to better approximate the system dynamics while cutting and Mann et al gained similar results using the Chebyshev collocation method (Butcher 2009; Butcher 2005). Other analytical methods which produce the additional stability lobe features are the multi-frequency solution (Merdol 2004) and the semi-discretization method (Insperger 2002), which has been shown to better match experimental stability results (Gradisek 2005).

The combination of forced vibrations while the tool is in the cut and free vibrations while the tool is out of the cut increases the complexity of this type of milling operation.

However, because the tool is engaged in the work piece for a relatively small angle range in LRIM, the angle dependent cutting force can be more accurately approximated as acting in a single direction (as in turning). This fact makes a “turning model” approximation of the system dynamics more appropriate for LRIM than for higher radial immersion operations, thus, LRIM is the most obvious machining operation to apply the analytical methods developed for turning in the previous chapters.

A general schematic of a LRIM operation with a single tooth cutter is shown in the left side of Figure 68. As the tool rotates, it feeds into the material and makes one cut per revolution. In this simple model it can be seen that the tool is engaged in the work piece for a short period of time and the range of angles which the tool is cutting is relatively small. If it is assumed that the cutting forces can be approximated as acting in a single direction (as done in (Bayly 2003)), than the LRIM operation can be modelled as a modified turning operation, where the tool cuts a protrusion of material once per revolution, as shown in the center of Figure 68. The motion of the tool in this interrupted turning model is shown in Figure 68 right, where the tool makes a new cut at the start of each period, τ, is in the cut for time, t_c, and is freely vibrating for time, t_f. The free and cutting times are determined by the parameter ρ which describes the ratio of time in the cut relative to the tool passing period, τ. t_c and t_f can be calculated using Equation 8.1 (Bayly 2003).

$$t_c = \rho\tau,\ t_f = (1-\rho)\tau \qquad 8.1$$

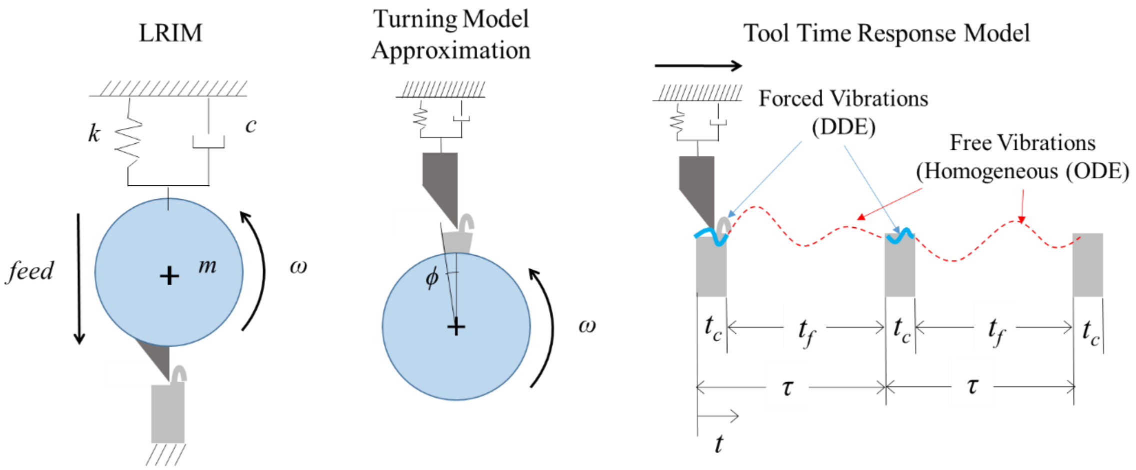

Figure 68: Single tooth low radial immersion model (left), the turning model approximation of LRIM (middle) and the single force direction approximation model (right).

In the previous chapter, Floquet theory was applied to determine the stability of turning operations by evaluating the eigenvalues of the transition matrix, U_{turn}. U_{turn} directly relates the tool motion coefficients of two subsequent periods when the initial conditions of the current period are equal to the conditions at the end of the previous period. For the LRIM case, this same approach is used, however, modifications are needed to account for the free vibrations of the tool.

The presence of the free vibrating periods effectively means that the tool behavior is governed by two separated dynamic systems. During the cutting sections the forces are based on present and past states of the tool (DDE) in Equation 8.2, while there are zero external forces on the tool (ODE) in Equation 8.2 while the tool is freely vibrating (Davies 2002).

$$m\ddot{y}+c\dot{y}+ky=\begin{cases} bK_{s,y}\left(y(t-\tau)-y(t)\right) & 0\le\phi<2\pi\rho \\ 0 & 2\pi\rho\le\phi<2\pi \end{cases};\quad 0\le\phi<2\pi \qquad 8.2$$

The solution to the DDE Equation 8.2 is already known based on the previous cut period coefficients and the initial conditions. The general solution to the DDE in Equation

8.2 is shown in Equation 8.3, where the eigenvalues $\lambda_{\mathrm{f},(1,2)}$ are those of the free vibrating system, and the state solutions based on the initial conditions of the free sections is shown in Equation 8.4 (Bayly 2003).

$$\begin{gathered} y_f(t) = c_1 e^{\lambda_{f,1} t} + c_2 e^{\lambda_{f,2} t} \\ \lambda_{f,(1,2)} = \sqrt{\frac{k}{m}} \pm i \sqrt{\frac{k}{m} + \frac{k}{m}\zeta^2} \end{gathered} \qquad 8.3$$

$$\begin{gathered} \begin{bmatrix} y_f(t) \\ \dot{y}_f(t) \end{bmatrix} = \begin{bmatrix} \dfrac{\lambda_{f,1} e^{\lambda_{f,2} t} - \lambda_{f,2} e^{\lambda_{f,1} t}}{\lambda_{f,1} - \lambda_{f,2}} & \dfrac{e^{\lambda_{f,1} t} - e^{\lambda_{f,2} t}}{\lambda_{f,1} - \lambda_{f,2}} \\ \dfrac{\lambda_{f,1} \lambda_{f,2} e^{\lambda_{f,2} t} - \lambda_{f,1} \lambda_{f,2} e^{\lambda_{f,1} t}}{\lambda_{f,1} - \lambda_{f,2}} & \dfrac{\lambda_{f,1} e^{\lambda_{f,1} t} - \lambda_{f,2} e^{\lambda_{f,2} t}}{\lambda_{f,1} - \lambda_{f,2}} \end{bmatrix} \begin{bmatrix} y_f(0) \\ \dot{y}_f(0) \end{bmatrix} \\ \begin{bmatrix} y_f(t) \\ \dot{y}_f(t) \end{bmatrix} = [D(t)] \begin{bmatrix} y_f(0) \\ \dot{y}_f(0) \end{bmatrix} \end{gathered} \qquad 8.4$$

A schematic of the time response of the tool during LRIM is shown in Figure 69, where the blue sections indicate the tool motion while cutting, and the red dashed sections are when the tool is vibrating freely. It can be seen in this figure that the initial conditions at the beginning of each cutting section are equal to the conditions at the end of the previous free vibration period. Furthermore, the conditions at the beginning of each free vibration section are equal to the condition at the end of the cutting section of the same period. The new transformation matrix for the LRIM case, $\mathrm{U}_{\mathrm{LRIM}}$, must account for both of these “condition transfers” in order to determine the motion during one cutting period based on the motion during the previous cutting period.

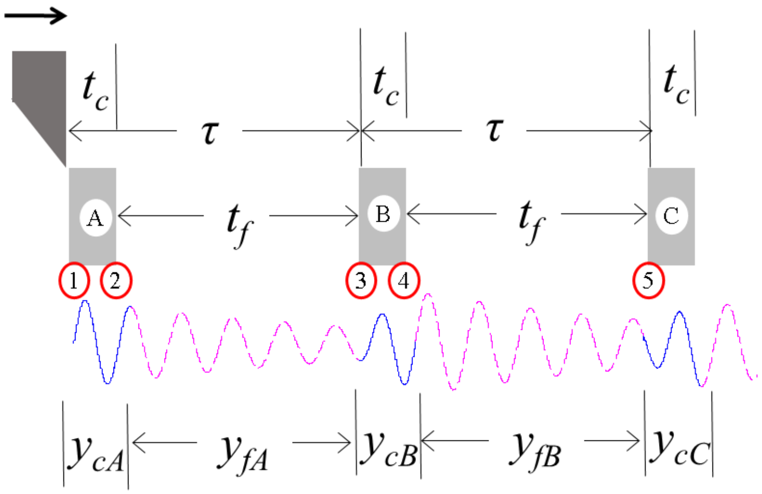

Figure 69: Time response of the tool as it repeatedly enters the cut, where the initial conditions as the tool enters the cut are equal to the conditions at the end of the free vibration period of the previous period.

In Figure 69 the cutting operation is shown over three rotations, cutting at A B and C. Although displayed as three separate material sections, A B and C are actually the same material section shown at three points in time. As such, the wavy surface that the tool encounters when cutting B is the surface left behind after cutting A, and the surface encountered at C was left behind after cutting B, and so on. This repeated interaction between the tool and the surface allows us to apply the same basic procedure to determine the response of the tool as it repeatedly passes over the same material section as was used in turning. The primary difference for LRIM is that the initial conditions of each cut are not equal to the conditions at the end of the previous cut because of the additional free vibrations. Therefore, the initial condition portions of the transition matrix, U_{LRIM}, must account for these additional free vibrations.

Let us start by considering the initial conditions at the start of cut B in Figure 69. The initial conditions of y_{cB} at point 3 are equal to the modal conditions of the free vibrations of, y_{fA}, evaluated at t_f from the start of y_{fA}. The initial conditions of y_{fA} at point

2 are equal to the conditions at the end of cut A, which is equal to y_{cA} evaluated at the cut time, t_c.

The conditions of the first mode at the end of A (point 2) are shown in Equation 8.5 , where the subscripts of Γ and Ω indicate that τ is replaced by tc in Equations 7.2 and 7.6 respectively.

$$\begin{aligned} y_{\mathrm{cA,Mode1}}(t_c) &= \mathbf{\Gamma}_{tc}\mathbf{A}_{ycA,1}^{j} \\ \dot{y}_{cA,\mathrm{Mode1}}(t_c) &= (\Omega_{tc} \circ \mathbf{\Gamma}_{tc})\mathbf{A}_{ycA,1}^{j} \end{aligned} \qquad 8.5$$

The conditions at the end of the free vibration period, at point 3, can be calculated based on the initial conditions at point 2 by expanding Equation 8.4 as shown in Equation 8.6, where D is the 2x2 matrix in Equation 8.4.

$$\begin{aligned} y_{fA,Mode1}(t_f) &= \left(D(t_f)_{Mode1,1,1}\, y_{fA,Mode1}(0) + D(t_f)_{Mode1,1,2}\, \dot{y}_{fA,Mode1}(0)\right) \\ \dot{y}_{fA,Mode1}(t_f) &= \left(D(t_f)_{Mode1,2,1}\, y_{fA,Mode1}(0) + D(t_f)_{Mode1,2,2}\, \dot{y}_{fA,Mode1}(0)\right) \end{aligned} \qquad 8.6$$

Note that the free eigenvalues in Equation 8.4 must correspond to the modal parameters of each individual mode. Recognizing that the conditions of $y_{\mathrm{cA,Mode1}}(t_c)$ are equal to the conditions of $y_{fA,Mode1}(0)$, and that the conditions at $y_{fA,Mode1}(t_f)$ are equal to the initial conditions of cut B at point 3, we can obtain the expression for the initial conditions of $y_{cB,Mode1}(0)$ shown in Equation 8.7

$$\begin{aligned} y_{\mathrm{cB},Mode1}(0) &= \left(D(t_f)_{Mode1,1,1}\mathbf{\Gamma}_{tc} + D(t_f)_{Mode1,1,2}(\Omega_{tc} \circ \mathbf{\Gamma}_{tc})\right)\mathbf{A}_{ycA,1}^{j} \\ \dot{y}_{\mathrm{cB},Mode1}(0) &= \left(D(t_f)_{Mode1,2,1}\mathbf{\Gamma}_{tc} + D(t_f)_{Mode1,2,2}(\Omega_{tc} \circ \mathbf{\Gamma}_{tc})\right)\mathbf{A}_{ycA,1}^{j} \end{aligned} \qquad 8.7$$

In order to account for the free vibrations in matrix form, the derivation of $U_{IC,Reduced}$ is revisited and adjustments are made based in Equation 8.7. Equation 7.12, which is shown again below, gives the zeroth order coefficients of the tool motion solution based on the initial conditions at the beginning of the cut.

$$\mathbf{A}_{y1}(0)\rightarrow\begin{array}{l}a_{y1,\lambda1,0}=v_{1,1}\left(v_{1,1}^{-1}y_1(0)+v_{1,2}^{-1}\dot{y}_1(0)+v_{1,3}^{-1}y_2(0)+v_{1,4}^{-1}\dot{y}_2(0)\right)\\a_{y1,\lambda2,0}=v_{1,2}\left(v_{2,1}^{-1}y_1(0)+v_{2,2}^{-1}\dot{y}_1(0)+v_{2,3}^{-1}y_2(0)+v_{2,4}^{-1}\dot{y}_2(0)\right)\\a_{y1,\lambda3,0}=v_{1,3}\left(v_{3,1}^{-1}y_1(0)+v_{3,2}^{-1}\dot{y}_1(0)+v_{3,3}^{-1}y_2(0)+v_{3,4}^{-1}\dot{y}_2(0)\right)\\a_{y1,\lambda4,0}=v_{1,4}\left(v_{4,1}^{-1}y_1(0)+v_{4,2}^{-1}\dot{y}_1(0)+v_{4,3}^{-1}y_2(0)+v_{4,4}^{-1}\dot{y}_2(0)\right)\end{array}$$

$$\mathbf{A}_{y2}(0)\rightarrow\begin{array}{l}a_{y2,\lambda1,0}=v_{3,1}\left(v_{1,1}^{-1}y_1(0)+v_{1,2}^{-1}\dot{y}_1(0)+v_{1,3}^{-1}y_2(0)+v_{1,4}^{-1}\dot{y}_2(0)\right)\\a_{y2,\lambda2,0}=v_{3,2}\left(v_{2,1}^{-1}y_1(0)+v_{2,2}^{-1}\dot{y}_1(0)+v_{2,3}^{-1}y_2(0)+v_{2,4}^{-1}\dot{y}_2(0)\right)\\a_{y2,\lambda3,0}=v_{3,3}\left(v_{3,1}^{-1}y_1(0)+v_{3,2}^{-1}\dot{y}_1(0)+v_{3,3}^{-1}y_2(0)+v_{3,4}^{-1}\dot{y}_2(0)\right)\\a_{y2,\lambda4,0}=v_{3,4}\left(v_{4,1}^{-1}y_1(0)+v_{4,2}^{-1}\dot{y}_1(0)+v_{4,3}^{-1}y_2(0)+v_{4,4}^{-1}\dot{y}_2(0)\right)\end{array}$$

Substituting Equation 8.7 into this equation and reducting in the same way as was done in Equations 7.13 through 7.16, we obtain a new transition matrix, $U\left(t_c,t_f\right)_{IC,\text{LREM,}}$, to determine the zeroth order coefficients for one cut based on the coefficients of the previous cut when there is a period of free vibration between cuts. The elements of $U\left(t_c,t_f\right)_{IC,\text{LREM,}}$ can be calculated using Equation 8.9, where $\otimes$ is a Kronecker product.

$$\begin{bmatrix}\mathbf{A}_{y1}^{j}(0)\\\mathbf{A}_{y2}^{j}(0)\end{bmatrix}=U\left(t_c,t_f\right)_{IC,\text{LRIM}}\begin{bmatrix}\mathbf{A}_{y1}^{j-1}\\\mathbf{A}_{y2}^{j-1}\end{bmatrix} \qquad 8.8$$

$$\begin{aligned}U\left(t_c,t_f\right)_{IC,\text{LRIM}}&=\begin{bmatrix}U_{IC,1,1}&U_{IC,1,2}\\U_{IC,2,1}&U_{IC,2,2}\end{bmatrix}\\U\left(t_c,t_f\right)_{IC,\text{LRIM},\text{n}_1,\text{n}_2}&=\left[\mathbf{V}\left(2n_1-1,:\right)^T\circ\mathbf{V}^{-1}\left(:,2n_2-1\right)\right]\otimes\left[D\left(t_f\right)_{Mode\,n_2,1,1}\boldsymbol{\Gamma}_{tc}+D\left(t_f\right)_{Mode\,n_2,1,2}\left(\Omega_{tc}\circ\boldsymbol{\Gamma}_{tc}\right)\right]\\&\quad+\left[\mathbf{V}\left(2n_1-1,:\right)^T\circ\mathbf{V}^{-1}\left(:,2n_2\right)\right]\otimes\left[D\left(t_f\right)_{Mode\,n_2,2,1}\boldsymbol{\Gamma}_{tc}+D\left(t_f\right)_{Mode\,n_2,2,2}\left(\Omega_{tc}\circ\boldsymbol{\Gamma}_{tc}\right)\right]\end{aligned} \qquad 8.9$$

Finally, the components of the transition matrix relating the coefficients of one cut based on the coefficients of the previous cut are combined in Equation 8.10 to form $U(t_c,t_f)_{\text{LRIM}}$.

$$\begin{bmatrix}\mathbf{A}_{y1}^{j}\\ \mathbf{A}_{y2}^{j}\end{bmatrix}=U\left(t_c,t_f\right)_{LRIM}\begin{bmatrix}\mathbf{A}_{y1}^{j-1}\\ \mathbf{A}_{y2}^{j-1}\end{bmatrix},$$

$$U\left(t_c,t_f\right)_{LRIM}=\begin{bmatrix}Z_1 & Z_1\\ Z_2 & Z_2\end{bmatrix}+U\left(t_c,t_f\right)_{IC,LRIM} \qquad 8.10$$

8.1Example

The time domain solutions to Equation 8.2 found using Equation 8.10 are now compared with simulated time domain results for the turning approximation model for LRIM shown in Figure 69. For these examples the system parameters shown in Table 6 are used, which are the same parameters used in (Bayly 2003) for the analysis of LRIM using the TFEA approach. Two examples are shown which are plotted in the LRIM stability lobe diagram in Figure 70, having a depth of cut of b=4mm at 5500 and 5850 RPM using ρ=0.1.

Table 6: System parameters used in the LRIM examples (Note these are the same parameters used in Bayly et al, 2003 (Bayly 2003))..

k	2.2E6 N/m
m	2.5859 kg
c	18.1272 Ns/m
K_s cos(β)	2E8 N/m^2

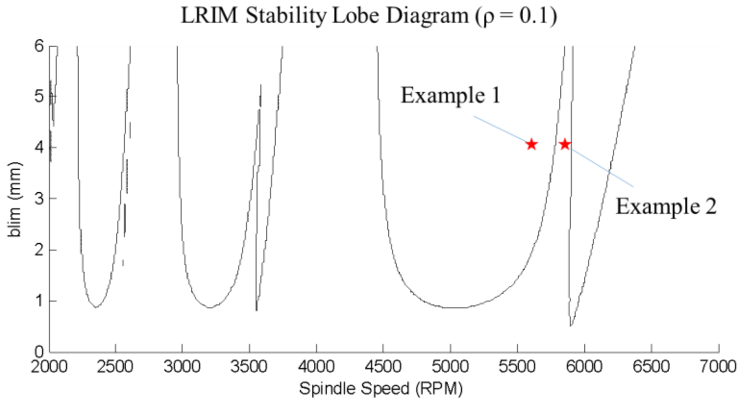

Figure 70: Two time domain examples for a single mode system evaluated at a depth of cut, b=4mm at 5500 and 5850 RPM.

The resulting time domain solutions for the two LRIM examples are shown in Figure 71 when the initial conditions at the start of the cutting process are $y(0)=0$, and $\dot{y}(0)=1m/s$. In Figure 71 the red analytical portions of the solution only represent the motion of the tool while the tool is in the cut since the analytical solution only provides the tool point motions during this time. It can be seen in the first 8 part revolutions that the analytical solutions match the simulated solutions, and at these spindle speeds, the time which the tool is in the cut is significantly shorter than the oscillation period of the tool. By observing the first 8 revolutions, it is difficult to determine the long term stability of the system, however, when plotted over the first 50 revolutions, it is clear that example 1 is unstable while example 2 is stable, as indicated by the stability lobe diagram.

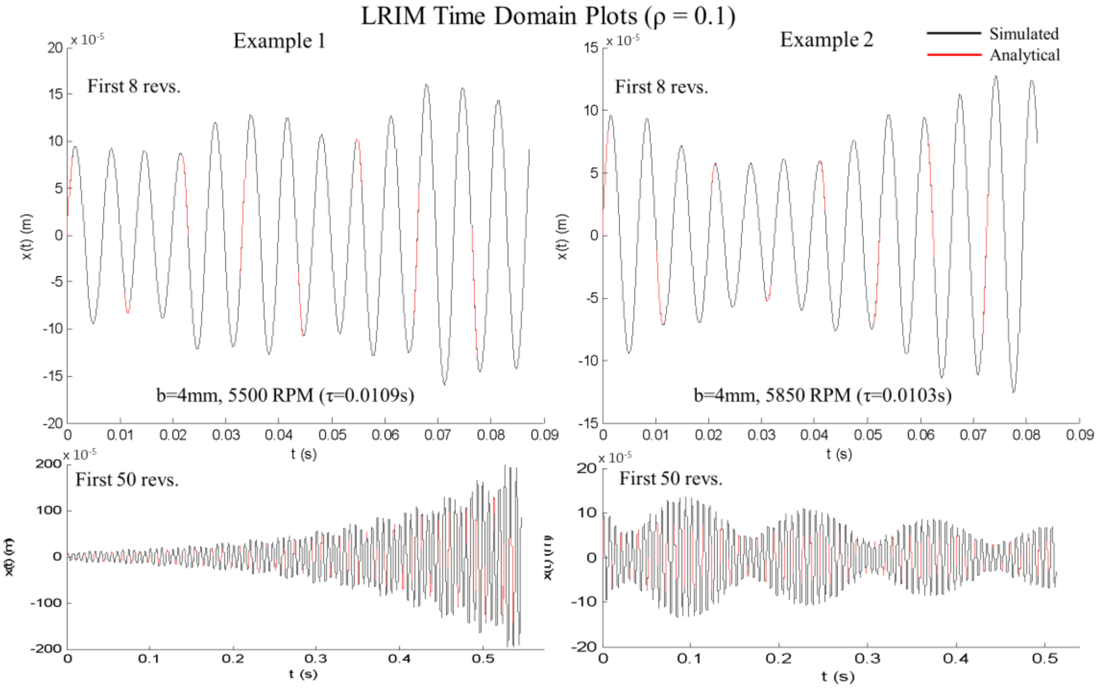

Figure 71: Comparison of the time domain plots for example 1 and 2 with the numerical simulation for the first 8 revolutions (top) and the first 50 revolutions (bottom). Note that the analytical solutions are only plotted during time that the tool is engaged in the cut, and the numerical solutions are plotted over the entire time range..

8.2 Stability

Stability lobe diagrams are produced based on the transition matrix, U_{LRIM}, by determining whether the maximum eigenvalue magnitude is greater than or less than one. The resulting stability lobe diagrams are compared with stability lobes produced through numerical simulation, using the same process used in the turning stability lobes. The resulting stability lobe diagrams are shown in Figure 72 when the time step used for the simulation produces 20 and 100 calculations per tool oscillation. When only 20 points per oscillation are used (as was the case for turning), the two stability lobes are similar, but have significant differences. When the time step is decreased to 100 points per oscillation the simulated stability lobes align more closely to the analytical stability lobes. As the tool is only engaged in the material for a relatively short period of time, a more refined time step is needed for the LRIM simulations to accurately predict the tool motions.

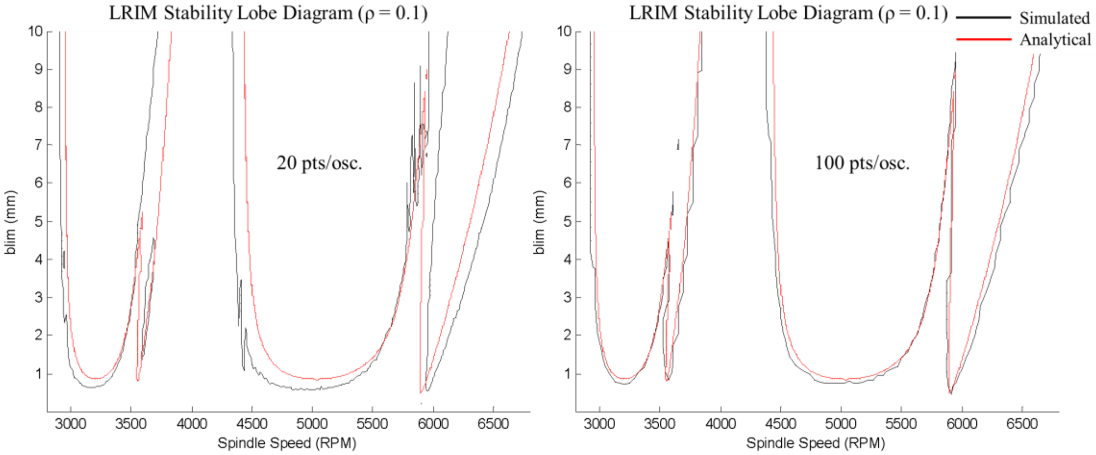

Figure 72: Analytical LRIM stability lobe diagrams using J = 4 compared with numerical simulations using 50 revolutions and approximately 20 points per oscillation (left) and 100 points per oscillation (right) for the simulations.

A significant difference between analytical stability lobes for turning and LRIM is the importance of J on the accuracy of the stability lobes. In Figure 73 the LRIM stability lobes are shown for J=2, 4, 6 and 8. The first observation is that the LRIM lobes do not show the same upward bend that appears in the turning lobes as the spindle speed is decreased. Furthermore, the difference between the stability lobes as J is increased is much less significant for LRIM than it is for turning. In Figure 73 the is a small adjustment in the lobes when J is increased from 2 to 4, but the lobes as J is increased from 4 to 6 to 8 are nearly identical. The difference in the dependence on J for turning and LRIM can be attributed to the fact that the tool is only engaged in the work piece for a short period of time in LRIM. As such, the higher order terms of the solution have a smaller effect on the motion of the tool over the short cutting periods (i.e. the values of the high order polynomial terms are relatively small for small values of t), and the tool motion can be more accurately approximated using fewer terms.

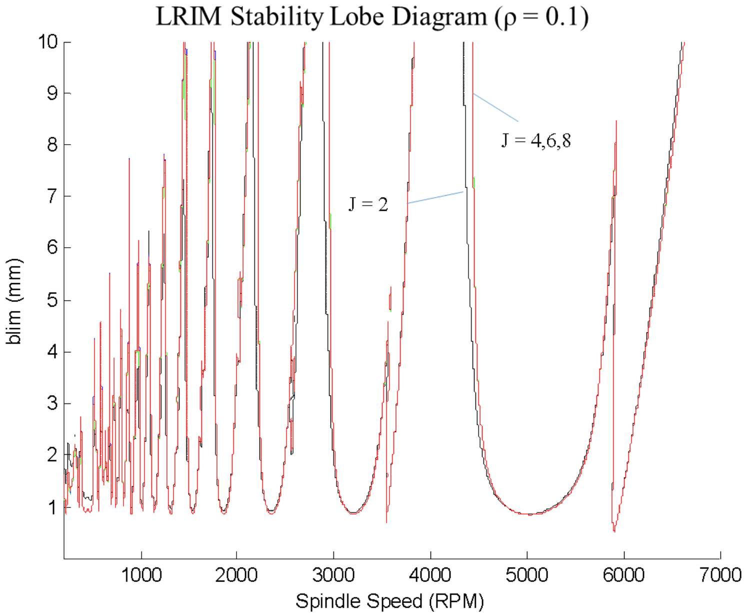

Figure 73: Comparison of analytical LRIM stability lobes using N_{rev} = 2, 4, 6, and 8, where the stability lobes for N_{rev} = 4, 6, and 8 are nearly identical.

The LRIM stability lobes produced using the current analytical approach are now compared with those generated using the TFEA method in (Bayly 2003). For both methods the same model is used (see Figure 68) to approximate the LRIM process and the same system parameters are used for the analysis. In Figure 74 the stability lobes produced using both methods are plotted together for ρ=0.05, 0.1, 0.25 and 0.5. It can be seen in this comparison that the stability lobes are nearly identical using both methods, where the greatest deviation (although small) occurs in the ρ=0.5 plot near 2900 RPM.

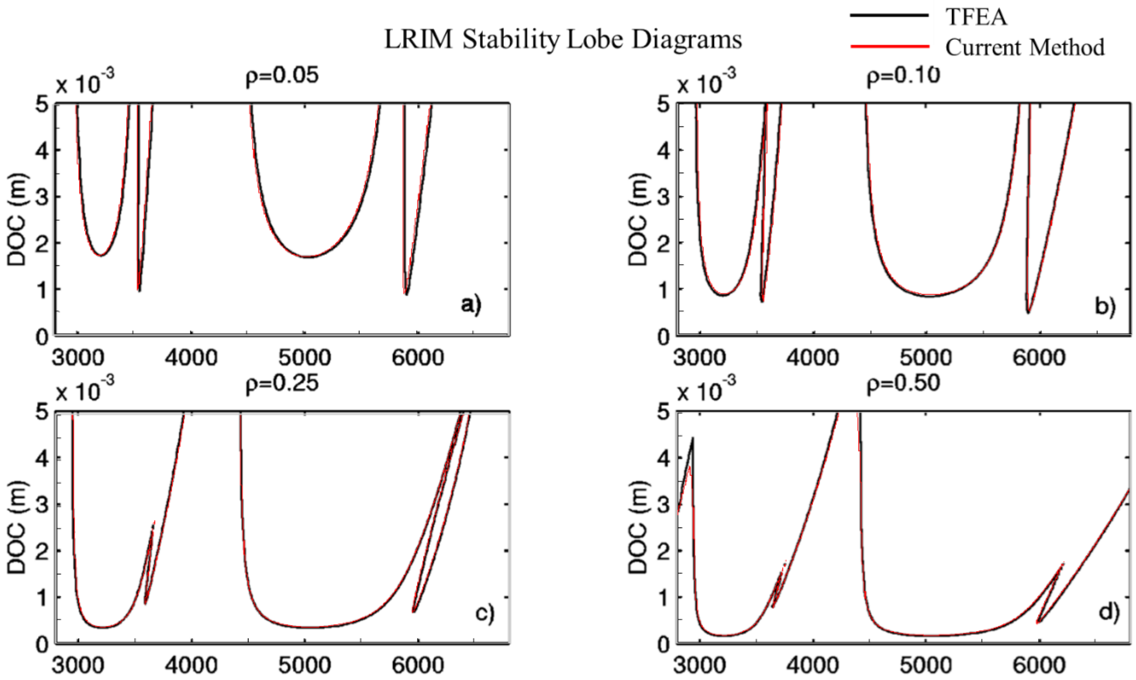

Figure 74: Comparison of the LRIM stability lobes produces using the current approach (red) and the TFEA method for ρ = 0.05, 0.1, 0.25, and 0.5 (TFEA stability lobes from Bayly et al, 2003) (Bayly 2003).

8.3Conclusions

The analytical processes developed in this dissertation have been shown to be effective for modeling intermittent cutting operations, where the time domain results match numerical results, and the stability results match those obtained using TFEA. In the next chapter the matrix solutions for intermittent cutting are used for variable pitch cutting.

CHAPTER 9: LRIM WITH VARIABLE PITCH CUTTERS

The use of variable pitch cutters have been applied in milling applications in order to alter the stability characteristics of equal pitch tool cutters. Researchers have investigated variable pitch as a potential for increasing stability limits by "interrupting" the regenerative processes in the cutting operation (Smith 2010). This work has focused on characterizing the effects of and designing variable pitch and variable helix angle cutters to improve performance (Altintas 1999; Olgac 2006; Sims 2008; Tlusty 1983). The results of this work have shown some increases in the stability limits, or shifts in the ideal spindle speeds.

In this chapter, a model is developed to analyze a variable pitch LRIM cutting process. The LRIM component of this model again allows for the force to be approximated as acting in a single direction. It also allows for the assumption that the tool has a period of free vibrations in between each cut, as is required for the model developed here. Figure 75 illustrates the variable pitch LRIM cutting process model. In this example there are three cutting teeth used which are separated by angles $\phi_{A,B,C}$. The unequal angle spacing between the cutters causes the free vibration period to differ in length after each tooth exits the cut, $t_{fA,B,C}$, while the time that the tooth is in the cut is the same for each cutter, t_c. The free and cutting times can be calculated using Equation 9.1, and the resulting system of ODEs and DDEs describing the system are shown in Equation 9.2. Figure 75 also shows the cutting and free periods for one complete tool revolution, where the material sections labeled A, B and C indicate which tool is cutting.

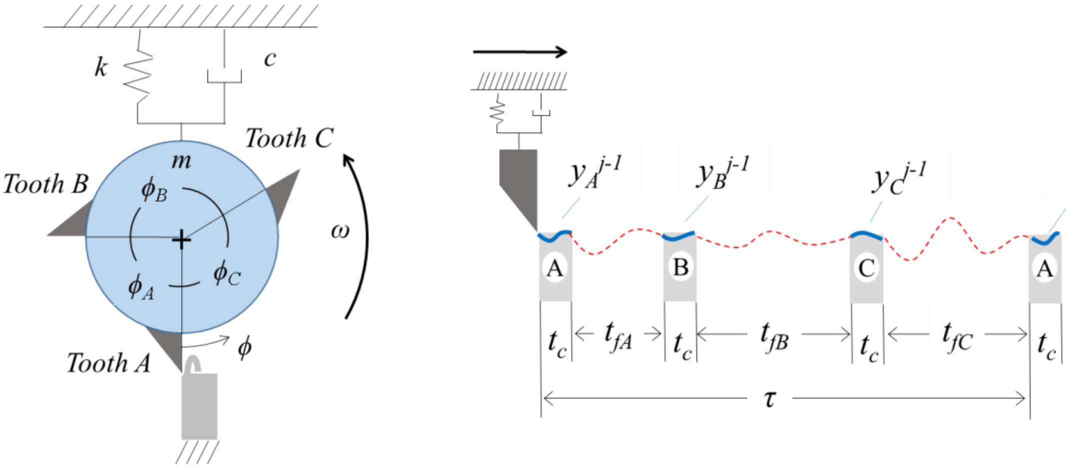

Figure 75: LRIM with variable pitch cutters, where the time in the cut is the same for each tooth, but the free vibration periods vary for each tooth.

$$t_c = \frac{\rho\tau}{N_t} \qquad t_{f\,A,B,C} = \frac{\theta_{A,B,C}\tau}{2\pi} - t_c \tag{9.1}$$

$$m\ddot{y}+c\dot{y}+ky = \begin{cases} bK_{s,y}\left(y\left(t-\left(t_c+t_{fC}\right)\right)-y(t)\right) & 0 \le \phi < \rho 2\pi/N_t \\ 0 & \rho 2\pi/N_t \le \phi < \phi_A \\ bK_{s,y}\left(y\left(t-\left(t_c+t_{fA}\right)\right)-y(t)\right) & \phi_A \le \phi < \phi_A + \rho 2\pi/N_t \\ 0 & \phi_A + \rho 2\pi/N_t \le \phi < \phi_A + \phi_B \\ bK_{s,y}\left(y\left(t-\left(t_c+t_{fB}\right)\right)-y(t)\right) & \phi_A + \phi_B \le \phi < \phi_A + \phi_B + \rho 2\pi/N_t \\ 0 & \phi_A + \phi_B + \rho 2\pi/N_t \le \phi < 2\pi \end{cases} \quad ; \quad 0 \le \phi < 2\pi \tag{9.2}$$

Analysis of the variable pitch system is more complex than the equal pitch (or single tooth) cutters because multiple free vibrations periods and multiple delay periods must be considered. Rather than searching for a direct solution to the DDE with multiple delays in Equation 9.2, we can simply piece together the solution by using the transition matrices already developed for LRIM. The transition matrix for LRIM, U_{LRIM}, determines the tool motions when the tool encounters a surface described by the set of coefficients, $\mathbf{A}^{j-1}$, when the tool was in the previous cut for time, t_c, and vibrating freely for a time, t_f, before reentering the cut. In effect, the times (t_c and t_f) used to construct U_{LRIM} account for the delay period between two consecutive cuts, so in the current three tooth cutter example with three delays in Equation 9.2, three transition matrices (U_{LRIM}) are needed to describe the tool motions going from tooth A to B to C and back to A.

In Equation 9.3 the relations between the tool motions in the three subsequent cuts are shown, where A_{yABC} are the coefficients (for a two mode system) describing the tool motions while each tooth is cutting. The transition matrix, $U(t_c,t_f)_{LRIM}$, relates the coefficients from one cut to the next when the time of the first cut is t_c, and the time of the free vibration in between cuts is t_f. For the LRIM case, this transition matrix need only be derived once because there is a single t_c and single t_f. For variable pitch, this transition matrix must be determined multiple times to account for the multiple free vibration periods.

For example, $U\left(t_c,t_{fA}\right)_{LREM}$ is used to determine $\mathbf{A}_{yB}^{j-1}$ based on $\mathbf{A}_{yA}^{j-1}$, $U\left(t_c,t_{fB}\right)_{LREM}$ is used to determine $\mathbf{A}_{yC}^{j-1}$ based on $\mathbf{A}_{yB}^{j-1}$, and $U\left(t_c,t_{fC}\right)_{LREM}$ is used to determine $\mathbf{A}_{yA}^{j}$ based on $\mathbf{A}_{yC}^{j-1}$. By combining these relations in Equation 9.4, the multiple relations for the multiple free periods are reduced to a single transition matrix, $U_{VarPitch}$, in Equation 9.5 which directly relates the coefficients of $\mathbf{A}_{yA}^{j}$ and $\mathbf{A}_{yA}^{j-1}$. As a result, it is possible to determine the motion of the tool during cut A based solely on the motion of the tool during the previous cut A, where all of the complex behaviors, due to multiple cuts and free vibrations in between two A cuts, are built into the transition matrix, $U_{VarPitch}$.

$$\begin{bmatrix}\mathbf{A}_{yB1}^{j-1}\\ \mathbf{A}_{yB2}^{j-1}\end{bmatrix}=U\left(t_c,t_{fA}\right)_{LRIM}\begin{bmatrix}\mathbf{A}_{yA1}^{j-1}\\ \mathbf{A}_{yA2}^{j-1}\end{bmatrix}$$
$$\begin{bmatrix}\mathbf{A}_{yC1}^{j-1}\\ \mathbf{A}_{yC2}^{j-1}\end{bmatrix}=U\left(t_c,t_{fB}\right)_{LRIM}\begin{bmatrix}\mathbf{A}_{yB1}^{j-1}\\ \mathbf{A}_{yB2}^{j-1}\end{bmatrix} \qquad 9.3$$
$$\begin{bmatrix}\mathbf{A}_{yA1}^{j}\\ \mathbf{A}_{yA2}^{j}\end{bmatrix}=U\left(t_c,t_{fC}\right)_{LRIM}\begin{bmatrix}\mathbf{A}_{yC1}^{j-1}\\ \mathbf{A}_{yC2}^{j-1}\end{bmatrix}$$

$$\begin{bmatrix}\mathbf{A}_{yA1}^{j}\\ \mathbf{A}_{yA2}^{j}\end{bmatrix}=U\left(t_c,t_{fC}\right)_{LRIM}U\left(t_c,t_{fB}\right)_{LRIM}\begin{bmatrix}\mathbf{A}_{yB1}^{j-1}\\ \mathbf{A}_{yB2}^{j-1}\end{bmatrix}$$
$$\begin{bmatrix}\mathbf{A}_{yA1}^{j}\\ \mathbf{A}_{yA2}^{j}\end{bmatrix}=U\left(t_c,t_{fC}\right)_{LRIM}U\left(t_c,t_{fB}\right)_{LRIM}U\left(t_c,t_{fA}\right)_{LRIM}\begin{bmatrix}\mathbf{A}_{yA1}^{j-1}\\ \mathbf{A}_{yA2}^{j-1}\end{bmatrix} \qquad 9.4$$

$$\begin{bmatrix}\mathbf{A}_{yA1}^{j}\\ \mathbf{A}_{yA2}^{j}\end{bmatrix}=U_{VarPitch}\begin{bmatrix}\mathbf{A}_{yA1}^{j-1}\\ \mathbf{A}_{yA2}^{j-1}\end{bmatrix} \qquad 9.5$$
$$U_{VarPitch}=U\left(t_c,t_{fC}\right)_{LRIM}U\left(t_c,t_{fB}\right)_{LRIM}U\left(t_c,t_{fA}\right)_{LRIM}$$

NOTE that the subscripts of A_{yABC} indicate which tooth that is in the cut, however, the basis functions for each are the same because all of the cutting parameters are the same for each tool. In other words, the relationship between cuts A and B in the variable pitch model are the same as the relationship between two subsequent LRIM cuts with equal pitch or a single tooth cutter. This allows us to use the same relationships already established, $U\left(t_c,t_{fB}\right)_{LRIM}$, to relate motions between different cutting teeth. (In other machining setups the basis function between two cut sections can change due to a cutting parameter change, and a different approach must be used to relate the motions between the two sections).

9.1Example

Two example time domain solutions are evaluated and compared with numerical simulations of the variable pitch LRIM model. The system parameters found in Table 7 are used in the examples, and the machining parameters labeled in the stability lobe diagram in Figure 76.

Table 7: System parameters used in the Variable Pitch LRIM examples (Note these are the same parameters used in Bayly et al, 2003 (Bayly 2003))..

k	2.2E6 N/m
m	2.5859 kg
c	18.1272 Ns/m
$K_s \cos(\beta)$	2E8 N/m^2
$\theta_{1,2,3}$	0°, 100°, 250°

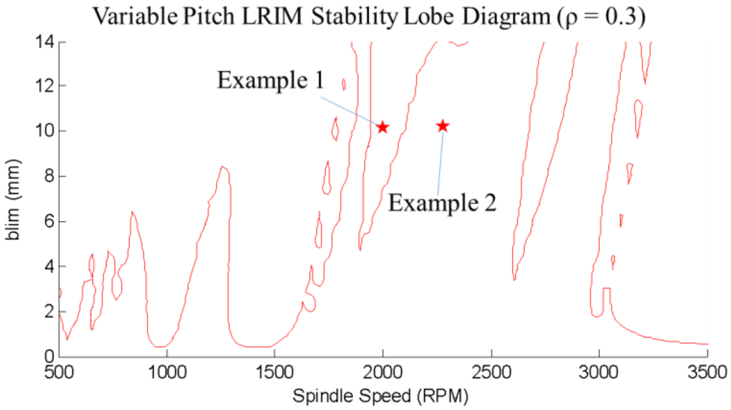

Figure 76: Two time domain examples for variable pitch LRIM milling evaluated at a depth of cut, b=10mm at 2000 and 2500 RPM.

The resulting time domain plots are shown in Figure 77 for the first 6 revolutions. In Figure 77, the simulated results are plotted in two different colors depending on whether the tool is in the cut or not, where the blue sections are when the tool is in the cut, and the black sections are when the tool is freely vibrating. The red analytical sections of Figure 77 are only plotted for when tooth A is in the cut. This is because the transition matrix, $U_{VarPitch}$, need only "keep track" of the motions while only one tooth is in the cut per revolution, and all of the motions between A cuts are accounted for within $U_{VarPitch}$.

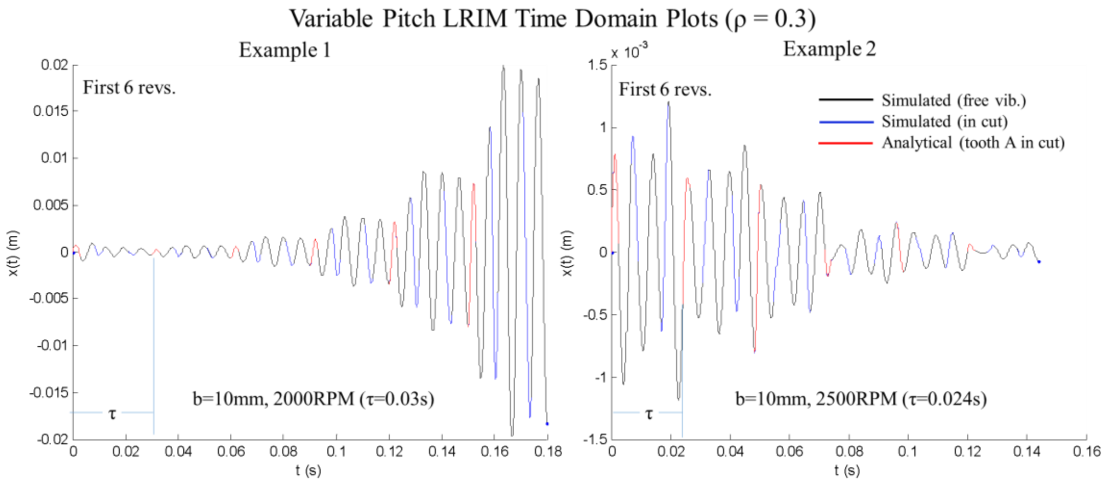

Figure 77: Simulated and analytical time-domain plots for the two variable pitch LRIM examples. The simulated response is shown as black when the tool is out of the cut and blue when the tool is in the cut. The Analytical solution (red) only determines the motion of the tool when tooth A is in the cut and is determined using Equation 9.5

9.2 Stability

Stability lobe diagrams are produced based on the eigenvalues of $U_{VarPitch}$ using the system parameters of Table 7. The stability lobes produced using $U_{VarPitch}$ are compared with simulation based stability lobes in Figure 78. The simulations used for Figure 78 used a time step which produced approximately 300 calculations per tool oscillation, and the same stability criteria developed in the simulated turning stability lobes is used. The results from Figure 78 show that the stability lobes produced analytically and through simulation do closely agree over the range of machining parameters evaluated.

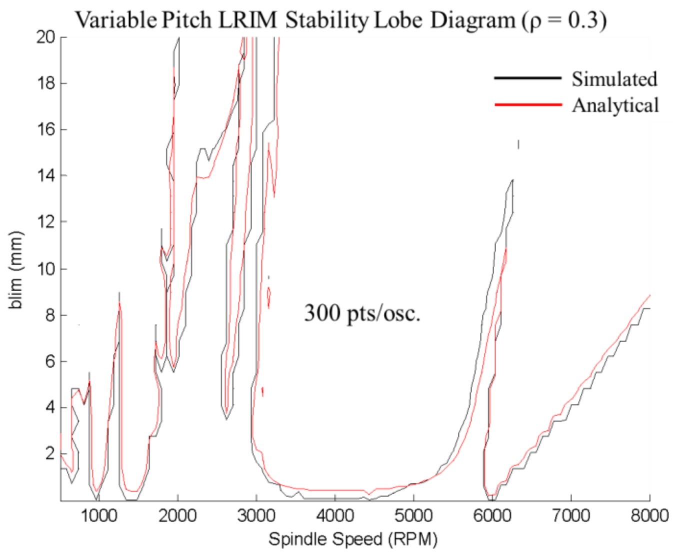

Figure 78: Analytical variable pitch LRIM stability lobe diagram with N_{rev}=4 compared with numerically simulated stability lobes evaluated over 50 revolutions using approximately 300 points per oscillation.

The analytical stability lobes for the variable pitch angles shown in Table 7 are compared with the stability lobes of an equal pitch, three tooth cutter in Figure 79. As expected, the shape of the equal tooth spacing stability lobes resemble those of the LRIM lobes in the previous chapter. The variable pitch lobes show a less ordered structure which agrees more closely with the equal pitch cutter at higher spindle speeds, then deviates as spindle speed decreases. From this example there is no clear advantage to the variable pitch cutter in terms of raising the stability limit, although there are areas of high stability limits which occur at different spindle speed locations when compared with the equal angle cutter. It is possible that a different tooth number and angle combination would result in a more beneficial stability characteristics, however, investigation of the optimum tool arrangement is outside the scope of the current work.

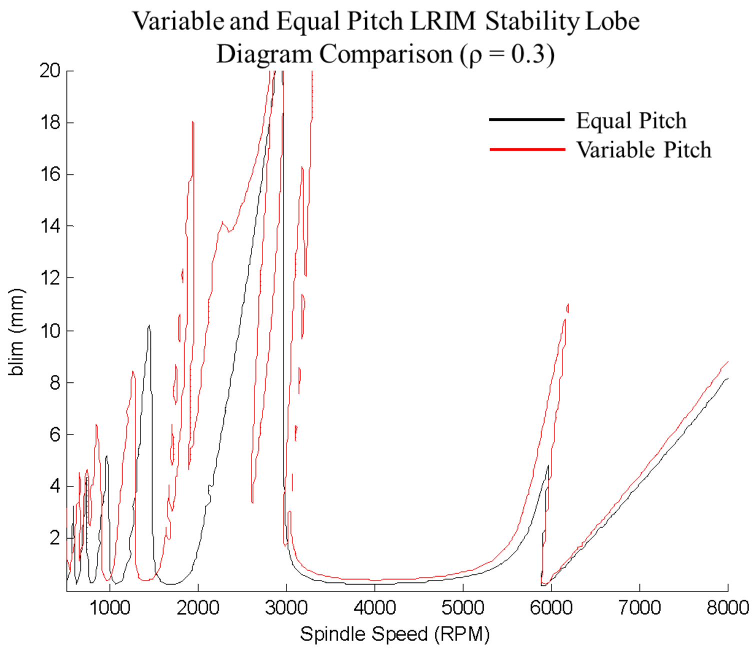

Figure 79: Stability lobe comparison between an equal pitch and variable pitch cutter using the system parameters from Table 7.

9.3Conclusions

It is shown here that application of the matrix solutions for the time-domain and stability analysis of a variable pitch cutting operation match those predicted numerically. The key takeaway from this section, however, is that the solution process developed for LRIM can be applied to systems with increased complexity due to the increased number of time delays (see Equation 9.2). Despite increasing from a single time delay in the previous chapters to three here, the solution process is a simple matter of “piecing together” the multi-delay solution using the same tools developed for single delay systems.

CHAPTER 10: MILLING USING AVERAGE ANGLE APPROXIMATION

At higher radial immersions the single force direction approximation loses accuracy because change in force direction as the tool sweeps around the cut has a more significant effect on the motion of the tool. In this chapter the milling process is approximated using the solution methods developed in this dissertation to model the effects of changing the number of teeth in the cut. Milling operations have been analyzed previously by approximating the variable force direction using the average angle (Tlusty 1999), or average force values (Altintas 1995; Tlusty 1999). In this chapter, the analytical results produced will be compared with the average angle approximation approach. Although only an approximation of the effects of the variable force direction, the average angle approximation provides an additional "machining scenario" that can be used to expand and test the current analytical approach.

Consider the 50% radial immersion diagram using a 6 tooth cutter in Figure 80. In Figure 80A, the dynamic system is oriented to allow motions of a single mode system only in the direction normal to the average cut angle, ϕ_{avg}, surface. The average angle orientation of the dynamic system is a simplification of Tlusty's model, which uses force direction factors to project the cutting force onto two modes oriented in different directions. The average angle simplification shown here projects all of the tool motions in the y-direction (normal to the average cut angle), and if the cutting forces in the y-direction are approximated to be proportional to the motion of the tool in this direction (using the average angle approximation), than the analytical tools developed in the previous chapters can be applied to approximate the tool behavior. The resulting linearized approximation of the milling process is shown in Figure 80B, where the tool forces in the y-direction are proportional to the tool motions in the y-direction.

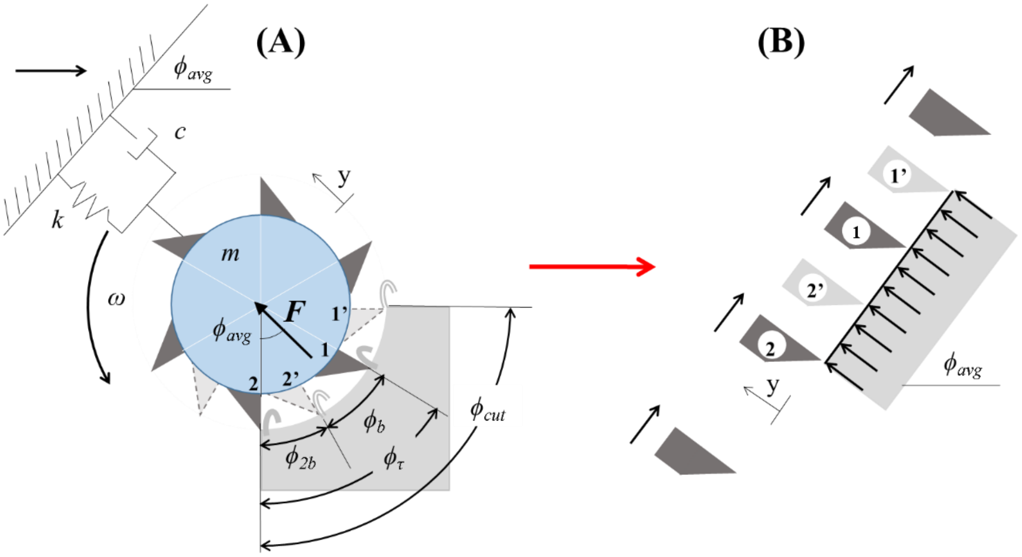

Figure 80: (A) Single DOF milling operation where all motions are normal to the average cut angle direction, and (B) a linear approximation of the milling operation assuming the average angle approximation.

While the system presented in Figure 80 is a significant simplification of Tlusty's average angle approximation model, it allows us to investigate the use of the analytical tools developed in previous chapters to model in detail how the "number of teeth in the cut" affects the behavior of the system. The issue of number of teeth in the cut arises in milling because there are typically multiple cutting teeth on the tool, and depending on the number of teeth and the radial immersion, the number of teeth that are engaged in the work piece can change as the tool rotates. In Tlusty's stability model for milling using the average angle approximation (which is a modification of his turning stability model with an assumed single force direction), the number of teeth in the cut is accounted for by shifting the stability lobe diagram by a factor, N_t*. N_t* represents the average number of teeth in the cut during one rotation of the tool. N_t* can be calculated using Equation 10.1, where N_t is the number of teeth and ϕ_{cut} is the total angle in which the tool is engaged in the cut. The resulting stability limit in this model is found using Equation 10.2, where K_s is the cutting force constant and FRF_{orient} is the oriented FRF which accounts for the force direction factors.

$$N_t^* = \frac{N_t \phi_{cut}}{2\pi} \tag{10.1}$$

$$b_{\lim} = \frac{-1}{2K_s \operatorname{Re}\left[FRF_{orient}\right] N_t^*} \tag{10.2}$$

The analytical model developed in this work provides an opportunity to investigate the effects of the number of teeth in the cut in a more direct way. Rather than assume that the system dynamics can be adequately represented by considering the average number of teeth in the cut, we can explicitly model how the tool behaves when the number of teeth in the cut repeatedly switches from one to two (or two to three etc.) as the tool rotates.

Take for example the six tooth cutter in Figure 80A. As the tool rotates the tooth passing frequency is associated with the angle separation between two adjacent teeth, ϕ_τ. Referring to Figure 80A, each time a tooth enters the cut there is another tooth which is already engaged in the cut (tooth 1 is in the cut when tooth 2 enters the cut). As the tool continues to rotate, both teeth are engaged over an angle range of ϕ_{2b} until tooth 1 exits the cut (in the tooth 1' and 2' positions). After tooth 1 exits the cut, tooth 2 is alone in the cut over the range ϕ_b, until it reaches tooth position 1 and the third tooth enters the cut.

As a result of teeth entering and exiting the cut at different times as the tool rotates through one ϕ_τ period, the system effectively exhibits different dynamic characteristics depending on whether there is one or two teeth engaged in the work piece. To account for these effects, the multiple teeth of the six tooth mill are modeled as a single tooth cutter which passes through regions of b and 2b chip width depending on the number of teeth in the cut, as shown in Figure 81B. Note that the motions of the multiple cutters in Figure 81A can be modeled as a single cutter in Figure 81B because the multiple teeth are assumed to be rigidly attached to the same mill, thus their motions are equal.

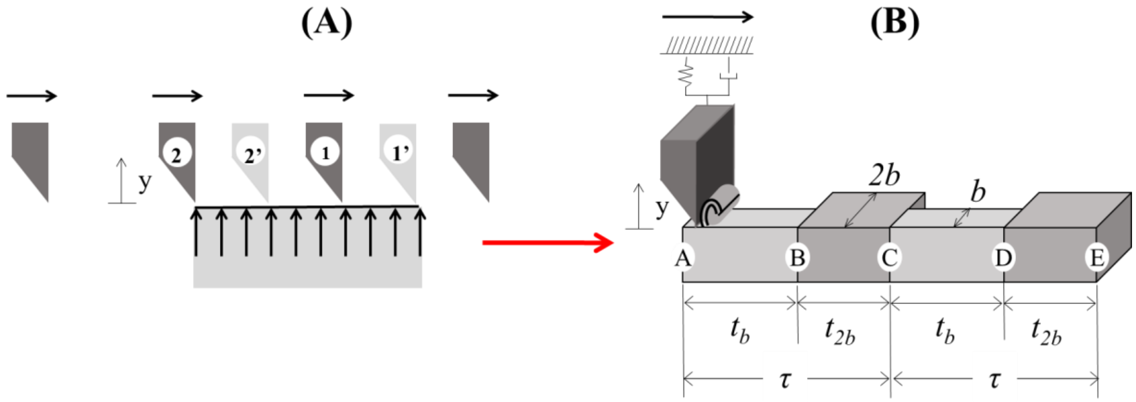

Figure 81: Linear approximation of the milling operation and (B) and the single tool approximation, where the effective chip width alternates between b and 2b.

The DDE describing the tool motions in the model illustrated in Figure 81 is shown in Equation 10.3, where the angles, ϕ_τ, ϕ_b, and ϕ_{2b} are illustrated in Figure 80.

$$m\ddot{y}+c\dot{y}+ky=\begin{cases}2bK_{s,y}\left(y(t-\tau)-y(t)\right) & 0\le\phi<\phi_{2b}\\ bK_{s,y}\left(y(t-\tau)-y(t)\right) & \phi_{2b}\le\phi<\phi_{2b}+\phi_{b}\end{cases};\qquad 0\le\phi<\phi_{\tau} \qquad 10.3$$

In the low radial immersion model discussed previously, the system dynamics were separated into two separate sections depending on whether the tool was in the cut or freely vibrating. A similar circumstance exists in the current model, where the equations of motion differ depending on the effective chip width (b or 2b). As the equations of motion for the tool are dependent on the value of b in the state-space solution, there will be two separate equations of motion (or basis functions) describing the tool motion depending on whether there is one or two teeth in the cut. For example, the motion equations for the b and 2b sections shown in Figure 82 will have the forms shown in Equation 10.4 assuming a single mode system, where the eigenvalues, λ_b and λ_{2b}, are found by applying b and 2b respectively to the state-space solution (see Equation 3.8).

$$\begin{aligned} y_b^J(t) &= \left(a_{\mathrm{b},\lambda_{b,1},0} + a_{\mathrm{b},\lambda_{b,1},1}t + \ldots + a_{\mathrm{b},\lambda_{b,1},\mathrm{J}-1}t^{J-1}\right)\mathrm{e}^{\lambda_{b,1}t} \\ &\quad + \left(a_{\mathrm{b},\lambda_{b,2},0} + a_{\mathrm{b},\lambda_{b,2},1}t + \ldots + a_{\mathrm{b},\lambda_{b,2},\mathrm{J}-1}t^{J-1}\right)\mathrm{e}^{\lambda_{b,2}t} \\ y_{2b}^J(t) &= \left(a_{2\mathrm{b},\lambda_{2b,1},0} + a_{2\mathrm{b},\lambda_{2b,1},1}t + \ldots + a_{2\mathrm{b},\lambda_{2b,1},\mathrm{J}-1}t^{J-1}\right)\mathrm{e}^{\lambda_{2b,1}t} \\ &\quad + \left(a_{2\mathrm{b},\lambda_{2b,2},0} + a_{2\mathrm{b},\lambda_{2b,2},1}t + \ldots + a_{2\mathrm{b},\lambda_{2b,2},\mathrm{J}-1}t^{J-1}\right)\mathrm{e}^{\lambda_{2b,2}t} \end{aligned} \qquad 10.4$$

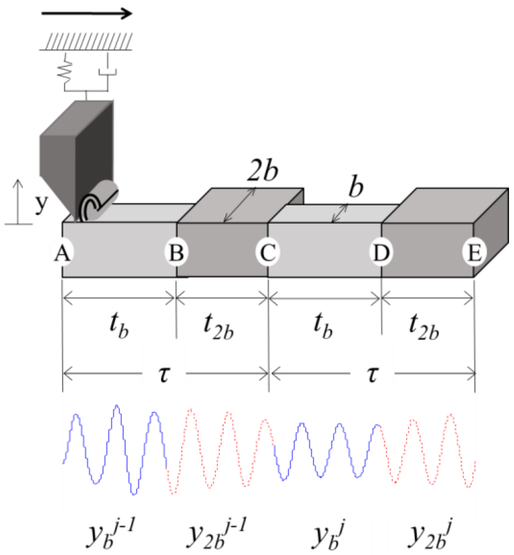

Figure 82: Depiction of the tool motion, where the conditions at the intersections of the b and 2b cut regions are equal.

As the chip width effects the state space solutions which are accounted for in the Z portion of the transition matrixes, a new subscript is added to the Z matrices to describe the state space solutions for each section (Z_b and Z_{2b}). In other words, the Z_b and Z_{2b}

matrices are used to determine the motion of the tool in the b and 2b sections respectively based on the motion of the tool in the b and the 2b sections of the previous period.

The initial conditions at the beginning of each cut region are found as the conditions of the tool at the end of the previous cut region using U_{IC}. As there are two separate state space solutions for the two regions, some extra effort is required to match the conditions at the end of one region to the conditions at the beginning of the next within the U_{IC} matrix. First, the conditions at the end of the previous cut region are found by applying the cut time of the previous region and the eigenvalues of the state space solution of the previous cut region. This determines the modal states at the end of the previous region based on the motion function of the previous region. Second, the states at the end of the previous region must be applied as initial conditions of the current region based on the eigenvector matrix, V, of the current region.

For example, the motion of the tool as it passes between cut regions over two τ cycles is shown in Figure 82. The motion of the tool for y_{2b}^{j} is found as a response to the tool motion during the previous 2b region using $Z_{2b}\mathbf{A}_{2b}^{j-1}$, where $\mathbf{A}_{2b}^{j-1}$ is the set of coefficients describing the motion during the previous 2b region. The motion of y_{2b}^{j} based on initial conditions is found as $U_{IC}\left(t_b,\boldsymbol{\lambda}_b,\mathbf{V}_{2b}\right)\mathbf{A}_{b}^{j}$, where $\mathbf{A}_{b}^{j}$ is the set of coefficients describing the motion during the previous cut region, t_b is the time the tool is engaged in the previous cut region, λ_b, is the set of eigenvalues associated with the b state space solution, and V_{2b} is the eigenvector matrix associated with the 2b state space solution. The resulting equations used to determine the tool motions for both cut regions are shown in Equation 10.5

$$\begin{aligned}\mathbf{A}_{2b}^{j} &= Z_{2b}\mathbf{A}_{2b}^{j-1} + U_{IC}\left(t_b,\boldsymbol{\lambda}_b,\mathbf{V}_{2b}\right)\mathbf{A}_{b}^{j}\\ \mathbf{A}_{b}^{j} &= Z_{b}\mathbf{A}_{b}^{j-1} + U_{IC}\left(t_{2b},\boldsymbol{\lambda}_{2b},\mathbf{V}_{b}\right)\mathbf{A}_{2b}^{j-1}\end{aligned} \qquad 10.5$$

After substituting A_b^j into A_{2b}^j (see Equation 10.6), the transition matrix, $U_{\text{mill,avg,ang}}$, is found directly relating the motions of the tool during one τ period to the motions of the tool during the previous τ period in Equation 10.7.

$$\mathbf{A}_{2b}^{j} = Z_{2b}\mathbf{A}_{2b}^{j-1} + U_{IC}\left(t_b,\boldsymbol{\lambda}_b,\mathbf{V}_{2b}\right)\left(Z_{b}\mathbf{A}_{b}^{j-1} + U_{IC}\left(t_{2b},\boldsymbol{\lambda}_{2b},\mathbf{V}_{b}\right)\mathbf{A}_{2b}^{j-1}\right) \qquad 10.6$$

$$\begin{gathered}\begin{bmatrix}\mathbf{A}_{b}^{j}\\ \mathbf{A}_{2b}^{j}\end{bmatrix} = \begin{bmatrix} Z_b & U_{IC}\left(t_{2b},\boldsymbol{\lambda}_{2b},\mathbf{V}_{b}\right)\\ U_{IC}\left(t_b,\boldsymbol{\lambda}_b,\mathbf{V}_{2b}\right)Z_b & Z_{2b} + U_{IC}\left(t_b,\boldsymbol{\lambda}_b,\mathbf{V}_{2b}\right)U_{IC}\left(t_{2b},\boldsymbol{\lambda}_{2b},\mathbf{V}_{b}\right)\end{bmatrix}\begin{bmatrix}\mathbf{A}_{b}^{j-1}\\ \mathbf{A}_{2b}^{j-1}\end{bmatrix}\\ \begin{bmatrix}\mathbf{A}_{b}^{j}\\ \mathbf{A}_{2b}^{j}\end{bmatrix} = U_{Mill,avg.ang.}\begin{bmatrix}\mathbf{A}_{b}^{j-1}\\ \mathbf{A}_{2b}^{j-1}\end{bmatrix}\end{gathered} \qquad 10.7$$

The reduced form (only degree zero rows) of the U_{IC} matrices in Equation 10.7 can by calculated using Equation 10.8, where $\boldsymbol{\Gamma}_{t_b.\lambda_b}$ and Ω_{λ_b} are found using Equations 10.9 and 10.10,

$$\begin{aligned}U\left(t_b,\boldsymbol{\lambda}_b,\mathbf{V}_{2b}\right)_{IC,\text{Red.}} &= \begin{bmatrix}U\left(t_b,\boldsymbol{\lambda}_b,\mathbf{V}_{2b}\right)_{IC,1,1} & U\left(t_b,\boldsymbol{\lambda}_b,\mathbf{V}_{2b}\right)_{IC,1,2}\\ U\left(t_b,\boldsymbol{\lambda}_b,\mathbf{V}_{2b}\right)_{IC,2,1} & U\left(t_b,\boldsymbol{\lambda}_b,\mathbf{V}_{2b}\right)_{IC,2,2}\end{bmatrix}\\ U\left(t_b,\boldsymbol{\lambda}_b,\mathbf{V}_{2b}\right)_{IC,\text{n}_1,\text{n}_2} &= \left[\mathbf{V}_{2b}\left(2n_1-1,:\right)^T \circ \mathbf{V}_{2b}^{-1}\left(:,2n_2-1\right)\right]\otimes\boldsymbol{\Gamma}_{t_b.\lambda_b}\\ &\quad + \left[\mathbf{V}_{2b}\left(2n_1-1,:\right)^T \circ \mathbf{V}_{2b}^{-1}\left(:,2n_2\right)\right]\otimes\left[\Omega_{\lambda_b}\circ\boldsymbol{\Gamma}_{t_b.\lambda_b}\right]\end{aligned} \qquad 10.8$$

$$\boldsymbol{\Gamma}_{t_b,\lambda_b} = \left[e^{\lambda_{b,1}\tau}\left[1\,t_b\,t_b^2\cdots t_b^{J-1}\right]\; e^{\lambda_{b,2}\tau}\left[1\,t_b\,t_b^2\cdots t_b^{J-1}\right]\right] \qquad 10.9$$

$$\begin{aligned}\Omega_{\lambda_b,n} &= \left[\lambda_{\lambda_b,n}\quad \lambda_{\lambda_b,n}+\frac{1}{\tau}\quad \lambda_{\lambda_b,n}+\frac{2}{\tau}\quad\cdots\quad \lambda_{\lambda_b,n}+\frac{(J-1)}{\tau}\right]\\ \Omega_{\lambda_b} &= \left[\Omega_{\lambda_b,1}\,\Omega_{\lambda_b,2}\right]\end{aligned} \qquad 10.10$$

10.1 Example

The solution to Equation 10.3 using Equation 10.7 is now compared with numerical simulation. The system parameters used for the analysis are shown in Table 9. Two example solutions are shown using spindle speeds of 3,500 and 4,000 RPM both at a depth of cut of 2mm, as shown in the stability lobe diagram in Figure 83 for a six tooth cutter and 50% radial immersion.

Table 8: System parameters used in the single mode average angle approximation milling examples.

k	1E7 N/m
m	0.88 kg
c	400 Ns/m
K_s	2E9 N/m^2
β	70°

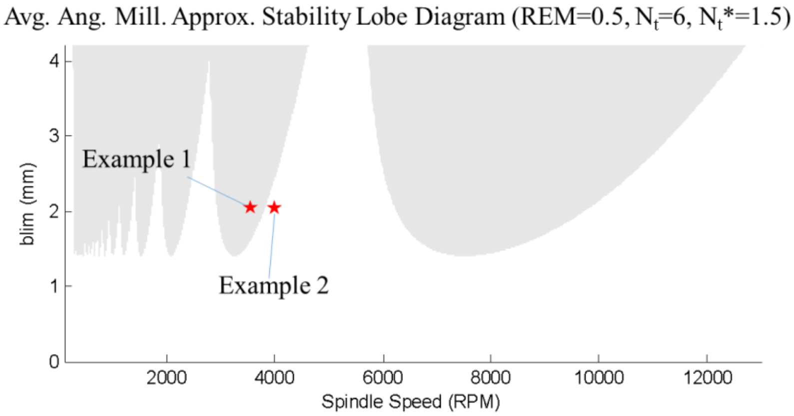

Figure 83: Two time domain examples for average angle milling approximation evaluated at a depth of cut, b=2mm at 4000 and 3500 RPM.

In Figure 84 the two example solutions are compared with the numerically simulated solutions. The analytical solutions are plotted in blue for the regions in which only one tooth is in the cut, and red in the regions where two teeth are in the cut. It can be seen in Figure 84 that the analytical solutions match the numerical solutions, and that the transition matrix, $U_{Mill,Avg.Ang}$, successfully couples the modal conditions as the tool passes between the b and 2b cut sections. The results from Figure 84 also show that the stability behavior predicted in the stability lobe diagram in Figure 83 agree with the behavior of the numerical and analytical solutions.

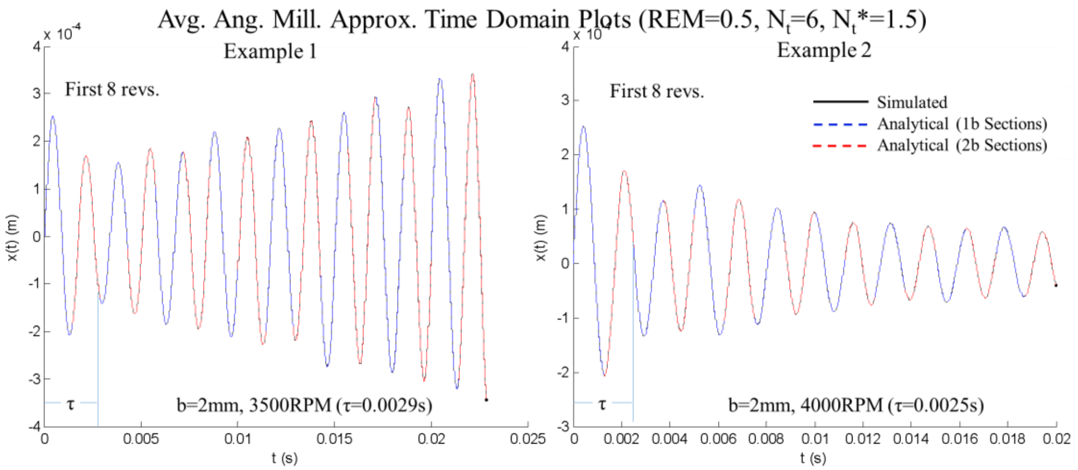

Figure 84: Simulated and analytical time domain plots for the example average angle milling approximations.

Using the relatively high spindle speeds in the solutions shown in Figure 84 it is difficult to observe the effect that changing the number of teeth in the cut has on the behavior of the system. In Figure 85 an additional solution is shown at a depth of cut of 2mm and a spindle speed of 200 RPM. At this slower spindle speed there are more vibrations that occur during each cut section so the difference in behavior as the number of teeth in the cut changes can be more easily seen. When only one tooth is in the cut (blue) the vibration amplitudes during each pass tend to decrease, while the amplitudes increase over time when there are two teeth in the cut due to the doubling of the effective depth of cut.

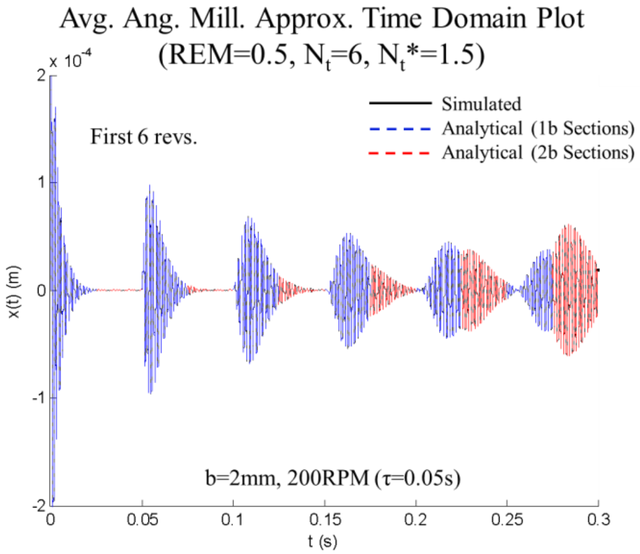

Figure 85: An additional example of average angle milling at a reduced spindle speed, showing the difference in dynamic behavior in the 1b and 2b sections of the cut.

10.2 Stability

The stability lobe diagrams generated by evaluating the eigenvalues of the matrix, $U_{Mill,Avg.Ang}$, in Equation 10.7 are compared with those predicted using Tlusty's average angle approximation approach using Equation 10.2. The three stability lobe diagrams for the six tooth cutter with the system parameters shown in Table 8 for radial immersions of 30, 50 and 70% are shown in Figure 86. The results from Figure 86 show that the predicted stability lobes generated using the current approach match those predicted by Tlusty at higher RPM, where the lobes found using the current approach show the same upward bend observed in the turning stability lobes at lower RPMs.

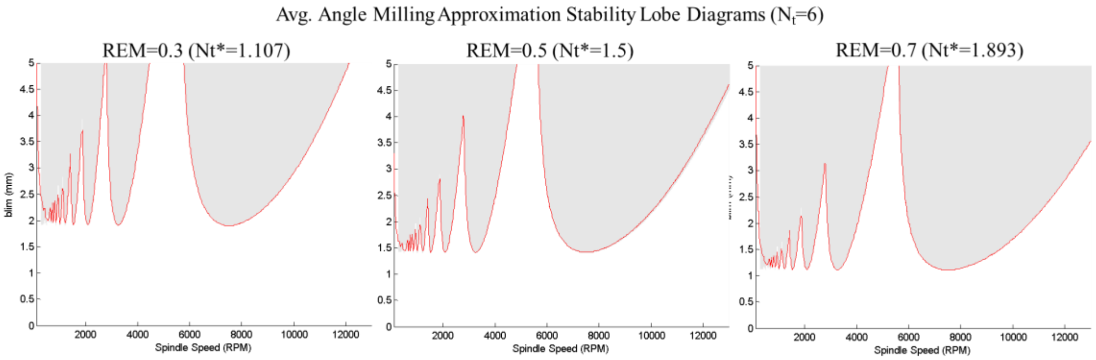

Figure 86: Average angle milling stability lobes at REM = 0.3, 0.5 and 0.7 found by evaluating the eigenvalues of $U_{Mill,avg.ang.}$ (red), compared with Tlusty's stability lobes (gray).

10.3 Conclusions

The degree to which the stability lobes match using both methods is an interesting outcome of this study. The stability lobes generated using the current approach take into account the additional complexity associated with the repeated change in the number of teeth in the cut. In Tlusty's approach, the stability lobes are generated by effectively assuming that a single tooth is constantly engaged in the cut, and then scaling that stability limit by the factor N_t*. In the end, both approaches provide the same effective result in terms of stability.

CHAPTER 11: VARIABLE CUTTING FORCE DIRECTION MILLING

The approaches developed in the previous sections are now applied to approximate tool point motions for milling operations. The method of using different effective dynamic system sections and piecing them together through end and initial conditions is now applied to single tooth milling operations, where the separate dynamic systems to be pieced together account for the changing direction forces acting on the tool as it sweeps through the cut.

In a full milling model, the forces acting on the tool continually change direction as the angle of the cutter rotates through the cut region. A diagram of a single tooth mill is shown in Figure 87 which shows the cutting force, F, acting at an angle β from the surface normal, and the angle θ_F in the fixed X-Y coordinate frame.

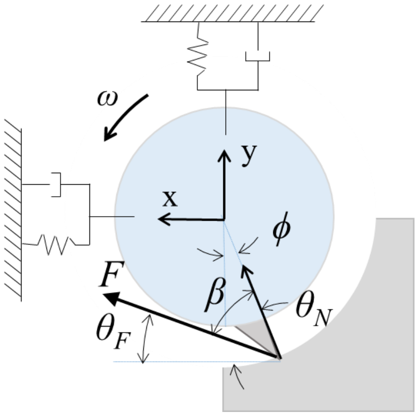

Figure 87: Angle dependent force direction for 2 DOF Milling model.

The magnitude and direction of the angle dependent cutting force, F, are found by expanding the regenerative force model to include the cutting angle, ϕ, and motions in two orthogonal directions. The resulting cutting force model is shown in Figure 88. The magnitude of F is found by multiplying the cutting force constant, K_s, by the instantaneous chip area, bh_ϕ. It is assumed that the chip width, b, is constant, so the only variable component of the chip area, and thus the tool force, is the chip thickness, h_ϕ. The instantaneous chip thickness is found as the thickness of the chip in the direction normal to the cut surface, labeled *N* in Figure 88. In the regenerative force model, the chip thickness is determined by considering the normal components of the tool motion during the current period and the previous period. The normal components of the x and y axes are found using Equation 11.1, where the normal angle, θ_N, is found using Equation 11.2. The resulting instantaneous chip thickness, h_ϕ, and the resulting force projections onto the x and y directions are found using Equation 11.3, where the force angle, θ_F, is found using Equation 11.2.

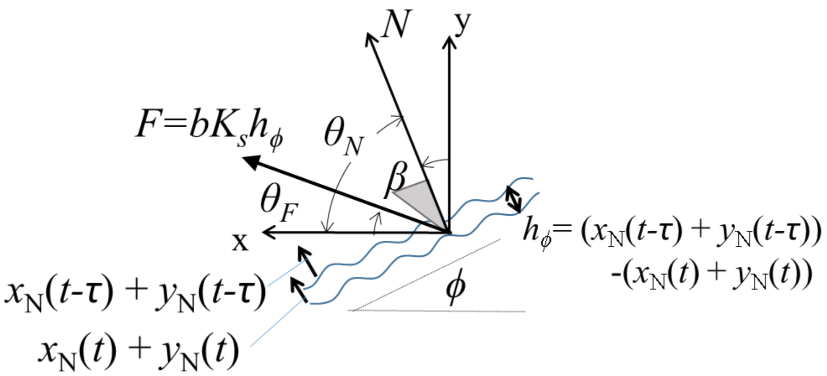

Figure 88: Force diagram for milling where the force magnitudes are proportional to the chip thickness, h_ϕ.

$$\begin{aligned} x_N &= x\cos(\theta_N) \\ y_N &= y\sin(\theta_N) \end{aligned} \qquad 11.1$$

$$\begin{aligned} \theta_N &= \frac{\pi}{2} - \phi \\ \theta_F &= \frac{\pi}{2} - \phi - \beta \end{aligned} \qquad 11.2$$

$$\begin{gathered} h_\phi = \left(x(t-\tau) - x(t)\right)\cos\left(\theta_N\right) + \left(y(t-\tau) - y(t)\right)\sin\left(\theta_N\right) \\ F_x = h_\phi b K_s \cos\left(\theta_F\right) \\ F_y = h_\phi b K_s \sin\left(\theta_F\right) \end{gathered} \qquad 11.3$$

The angle dependent regenerative cutting forces in the x and y directions from Equation 11.3 are applied to the system of equations describing the motions of the tool in the x and y directions in Equation 11.4

$$\begin{aligned} m_x\ddot{x} + c_x\dot{x} + k_x x &= bK_s \cos\left(\theta_F\right)\left(x_\tau \cos\left(\theta_N\right) + y_\tau \sin\left(\theta_N\right) - x\cos\left(\theta_N\right) - y\sin\left(\theta_N\right)\right) \\ m_y\ddot{y} + c_y\dot{y} + k_y y &= bK_{s,} \sin\left(\theta_F\right)\left(x_\tau \cos\left(\theta_N\right) + y_\tau \sin\left(\theta_N\right) - x\cos\left(\theta_N\right) - y\sin\left(\theta_N\right)\right) \end{aligned} \qquad 11.4$$

A state-space solution is used to solve the 2DOF system in Equation 11.4 using the same process used to solve for the tool motions in turning. The first step is to separate the current time and delay terms by bringing all current time terms to the left side of the equation, as shown in Equation 11.5.

$$\begin{aligned} m_x\ddot{x} + c_x\dot{x} + \left(k_x + bK_s\cos\left(\theta_F\right)\cos\left(\theta_N\right)\right)x + \left(bK_s\cos\left(\theta_F\right)\sin\left(\theta_N\right)\right)y &= bK_s\cos\left(\theta_F\right)\left(x_\tau\cos\left(\theta_N\right) + y_\tau\sin\left(\theta_N\right)\right) \\ m_y\ddot{y} + c_y\dot{y} + \left(k_y + bK_s\sin\left(\theta_F\right)\sin\left(\theta_N\right)\right)y + \left(bK_s\sin\left(\theta_F\right)\cos\left(\theta_N\right)\right)x &= bK_{s,}\sin\left(\theta_F\right)\left(x_\tau\cos\left(\theta_N\right) + y_\tau\sin\left(\theta_N\right)\right) \end{aligned} \qquad 11.5$$

Using the state variable, r, the state-space representation of Equation 11.5 is shown in Equation 11.6 and the matrix form of the state-space representation is shown in Equation 11.7.

$$\begin{aligned}
&r_1 = x; \qquad r_2 = \dot{x}; \qquad r_3 = y; \qquad r_4 = \dot{y};\\
&\dot{r}_1 = r_2\\
&\dot{r}_2 = \frac{1}{m_x}\Big(-c_x r_2 - \big(k_x + bK_s\cos(\theta_F)\cos(\theta_N)\big)r_1 - \big(bK_s\cos(\theta_F)\sin(\theta_N)\big)r_3\Big) + \frac{bK_s\cos(\theta_F)}{m_x}\big(x_\tau\cos(\theta_N) + y_\tau\sin(\theta_N)\big)\\
&\dot{r}_3 = r_4\\
&\dot{r}_4 = \frac{1}{m_y}\Big(-c_y r_4 - \big(k_y + bK_s\sin(\theta_F)\sin(\theta_N)\big)r_3 - \big(bK_s\sin(\theta_F)\cos(\theta_N)\big)r_1\Big) + \frac{bK_s\sin(\theta_F)}{m_y}\big(x_\tau\cos(\theta_N) + y_\tau\sin(\theta_N)\big)
\end{aligned} \tag{11.6}$$

$$\begin{Bmatrix}\dot{r}_1\\ \dot{r}_2\\ \dot{r}_3\\ \dot{r}_4\end{Bmatrix} = \begin{bmatrix} 0 & 1 & 0 & 0\\ \frac{-\left(k_x + bK_s\cos(\theta_{F,i})\cos(\theta_{N,i})\right)}{m_x} & \frac{-c_x}{m_x} & \frac{-\left(bK_s\cos(\theta_{F,i})\sin(\theta_{N,i})\right)}{m_x} & 0\\ 0 & 0 & 0 & 1\\ \frac{-\left(bK_s\sin(\theta_{F,i})\cos(\theta_{N,i})\right)}{m_y} & 0 & \frac{-\left(k_y + bK_s\sin(\theta_{F,i})\sin(\theta_{N,i})\right)}{m_y} & \frac{-c_y}{m_y}\end{bmatrix}\begin{Bmatrix}r_1\\ r_2\\ r_3\\ r_4\end{Bmatrix} + \begin{Bmatrix}0\\ \frac{bK_s\cos(\theta_{F,i})}{m_x}\\ 0\\ \frac{bK_s\sin(\theta_{F,i})}{m_y}\end{Bmatrix}\begin{pmatrix}x_\tau\cos(\theta_{N,i})\\ +\,y_\tau\sin(\theta_{N,i})\end{pmatrix} \tag{11.7}$$

$$\{\dot{R}_{\phi i}\} = [A_{\phi i}]\{R_{\phi i}\} + \{F_{\phi i}\}\big(x_{\tau,\phi i}\cos(\theta_{N,i}) + y_\tau(\phi_{av,i})\sin(\theta_{N,i})\big)$$

The process for solving Equation 11.7 is the same process illustrated in Figure 57, although there are some minor modifications required for the transition matrix, Z, to account for the two orthogonal modes (as opposed to multiple modes in the same direction). Recall Equation 5.16 (shown again below) for determining the modal coefficients based on the previous modal coefficients, where $Z_{1,2}$ are defined in Equation 5.14. In the single force direction solution (for the turning model) the total motion of the tool is found as the sum of the modal motions which all act in the same direction. In the milling case, where the modes are orthogonal, the forces are not related to the total motion of the x and y modes due to the sine and cosine terms present in the forcing function ($\{F_{\phi i}\}\big(x_{\tau,\phi i}\cos(\theta_{N,i}) + y_\tau(\phi_{av,i})\sin(\theta_{N,i})\big)$) . These directional scaling factors can be applied to the solution in the final Z transition matrix, $Z_{mill,\phi i}$, as shown in Equation 11.8.

$$\begin{bmatrix}\mathbf{A}_{x1}^{j}\\ \mathbf{A}_{x2}^{j}\end{bmatrix} = \begin{bmatrix}Z_1 & Z_1\\ Z_2 & Z_2\end{bmatrix}\begin{bmatrix}\mathbf{A}_{x1}^{j-1}\\ \mathbf{A}_{x2}^{j-1}\end{bmatrix}$$

$$\begin{Bmatrix} \mathbf{A}_{x,\phi i}^{j} \\ \mathbf{A}_{y,\phi i}^{j} \end{Bmatrix} = \begin{bmatrix} Z_{x,\phi i}\cos\left(\theta_{N,i}\right) & Z_{x,\phi i}\sin\left(\theta_{N,i}\right) \\ Z_{y,\phi i}\cos\left(\theta_{N,i}\right) & Z_{y,\phi i}\sin\left(\theta_{N,i}\right) \end{bmatrix} \begin{Bmatrix} \mathbf{A}_{x,\phi i}^{j-1} \\ \mathbf{A}_{y,\phi i}^{j-1} \end{Bmatrix}$$

$$Z_{mill,\phi i} = \begin{bmatrix} Z_{x,\phi i}\cos\left(\theta_{N,i}\right) & Z_{x,\phi i}\sin\left(\theta_{N,i}\right) \\ Z_{y,\phi i}\cos\left(\theta_{N,i}\right) & Z_{y,\phi i}\sin\left(\theta_{N,i}\right) \end{bmatrix} \qquad 11.8$$

Another more significant difference for the milling solution is the fact that Equation 11.7 can only be used to approximate the motion of the tool assuming a fixed angle, ϕ, where θ_F and θ_N are also fixed, to prevent variable entries in the state space solution. In reality, the terms in matrix A of Equation 11.7 continually change as the angle of the tool changes throughout the cut. However, the solution methods developed thus far (illustrated in Figure 57) are only valid for linear systems in which the terms of matrix A are constant. While this limitation prevents us from determining the motion of the tool exactly as it rotates in the cut, we can approximate the tool motion by discretizing the cut into multiple linearized increments and applying the solution process to each increment individually.

Consider the 50% radial immersion milling operation shown in Figure 89. As the tool rotates in the full milling diagram (top left), the angle of the surface normal, and thus the cutting force, relative to the fixed x and y reference coordinates are continually changing. One way to approximate the effects of this continuous change in force direction is to linearize the system by assuming that all of the cutting forces act in a single average angle associated with the average angle of the cut. This situation, illustrated in Figure 89 with N_{incs}=1, is equivalent to the average angle approximation developed by Tlusty. While the average angle approximation is the simplest way to approximate the milling process, higher accuracy can be achieved by breaking the cut into more linearized increments. As shown in Figure 89 for up to five increments, as the arc of the tool is broken into finer and finer segments, the resulting force model more accurately represents the forces in the full milling diagram.

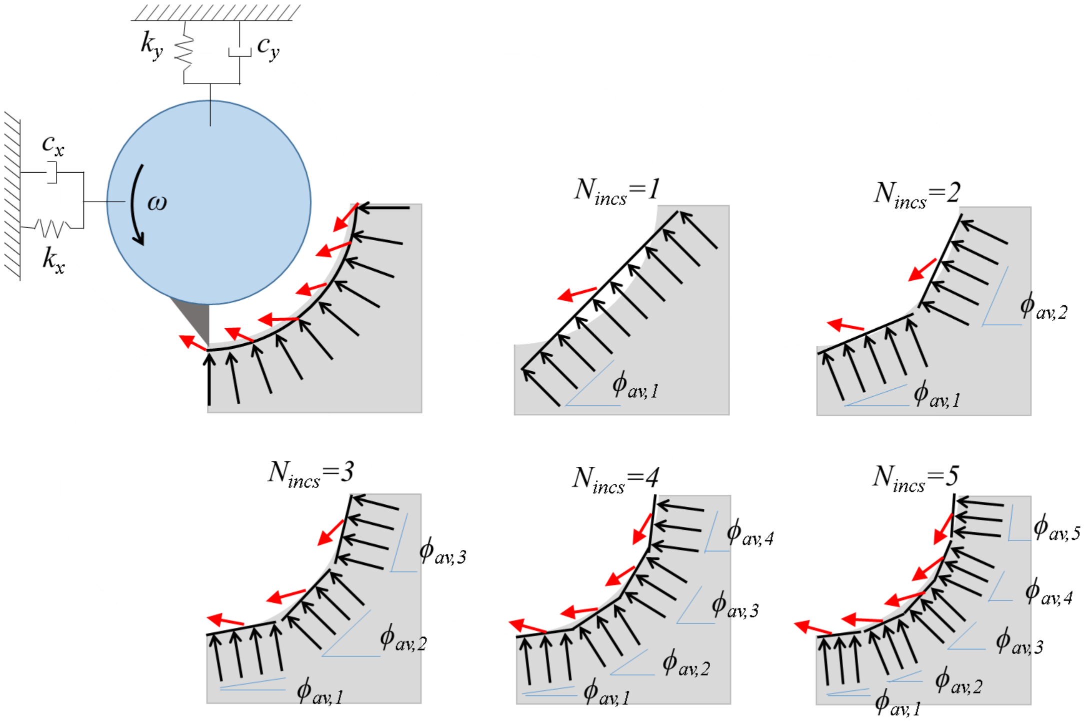

Figure 89: Increasing the number of linear increments used to approximate the effects of changing cutting force direction in milling.

The multiple incremental linear segments in Figure 89 each account for the tool motion while the tool is in the angle range specified by $\phi_{av,i}$, and within that range the surface normal and the cutting force angle are assumed to be constant. As the angle, $\phi_{av,i}$, alters the matrix terms in the state-space solution, each segment will possess a separate basis function with coefficients, $\mathbf{A}^{j}_{x,\phi i}$ and $\mathbf{A}^{j}_{y,\phi i}$. In effect, the system shows different dynamic characteristics from segment to segment similar to how the dynamic characteristics differed depending on whether there is one or two teeth in the cut in the average angle approximation model in the previous chapter. Once the state-space solutions are known for each increment, the end and initial conditions at the points where the segments meet must be tied to determine the tool motion over the entire cut. For discussion purposes, the coefficients describing the motion in the x and y directions are combined to form $\mathbf{A}^{j}_{\mathrm{XY},\phi i}$ as shown in 11.9.

$$\mathbf{A}^{j}_{XY,\phi i} = \begin{bmatrix} \mathbf{A}^{j}_{x,\phi i} \\ \mathbf{A}^{j}_{y,\phi i} \end{bmatrix} \qquad 11.9$$

Consider the 50% radial immersion cut shown in Figure 90 with three linear increments. Starting with the final increment over the range $\phi_{av,3}$, the motion of the tool in this segment is related to the motion of the tool in this segment during the previous revolution by $\mathbf{A}^{j}_{XY,\phi 3} = Z_{mill,\phi 3}\mathbf{A}^{j-1}_{XY,\phi 3}$. The initial conditions of the $\phi_{av,3}$, segment are found as the end conditions of the previous segment using $\mathbf{A}^{j}_{XY,\phi 3} = U_{IC}\left(t_{\phi 2}, \boldsymbol{\lambda}_{\phi 2}, \mathbf{V}_{\phi 3}\right)\mathbf{A}^{j}_{XY,\phi 2}$, where $\mathbf{A}^{j}_{XY,\phi 2}$ are the coefficients of the previous segment, $t_{\phi 2}$ is the time the tool is in the previous segment, $\lambda_{\phi 2}$ are the eigenvalues for the previous segment, and $V_{\phi 3}$ is the eigenvector matrix of the current segment. The total resulting tool motion during the $\phi_{av,3}$ segment is found using Equation 11.10. Moving back increment by increment the tool motions can be determined in this way except for the first increment, $\phi_{av,1}$, where additional information is required to account for the free vibration of the tool as shown in Equation 11.10.

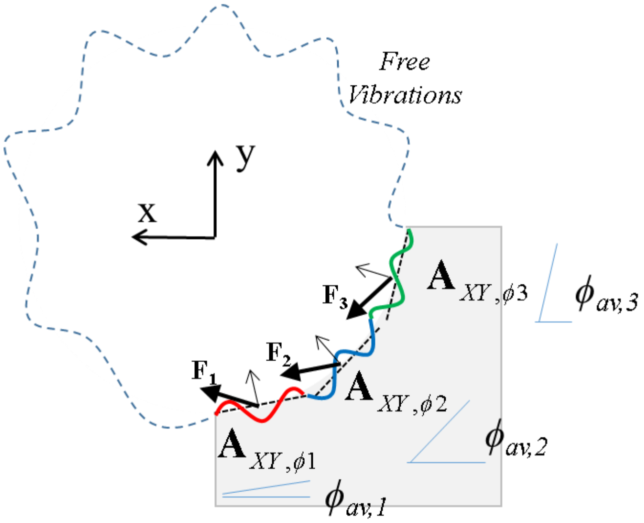

Figure 90: Example milling approximation using three linear increments to model the changing force direction.

$$\begin{aligned}
\mathbf{A}_{XY,\phi 3}^{j} &= Z_{mill,\phi 3}\mathbf{A}_{XY,\phi 3}^{j-1} + U_{IC}\left(t_{\phi 2},\boldsymbol{\lambda}_{\phi 2},\mathbf{V}_{\phi 3}\right)\mathbf{A}_{XY,\phi 2}^{j} \\
\mathbf{A}_{XY,\phi 2}^{j} &= Z_{mill,\phi 2}\mathbf{A}_{XY,\phi 2}^{j-1} + U_{IC}\left(t_{\phi 1},\boldsymbol{\lambda}_{\phi 1},\mathbf{V}_{\phi 2}\right)\mathbf{A}_{XY,\phi 1}^{j} \\
\mathbf{A}_{XY,\phi 1}^{j} &= Z_{mill,\phi 1}\mathbf{A}_{XY,\phi 1}^{j-1} + U_{IC}\left(\mathrm{t}_{free},t_{\phi 3},\boldsymbol{\lambda}_{\phi 3},\mathbf{V}_{\phi 1}\right)\mathbf{A}_{XY,\phi 3}^{j-1}
\end{aligned} \tag{11.10}$$

Substituting components of Equation 11.10 so that the motion in each current increment is defined in terms of the motion during the previous pass, as shown in Equation 11.11, a final transition matrix can be determined relating the motion of the tool during the current previous pass, as shown in Equation 11.12

$$\begin{aligned}
\mathbf{A}_{XY,\phi 1}^{j} &= Z_{mill,\phi 1}\mathbf{A}_{XY,\phi 1}^{j-1} + U_{IC}\left(\mathrm{t}_{free},t_{\phi 3},\boldsymbol{\lambda}_{\phi 3},\mathbf{V}_{\phi 1}\right)\mathbf{A}_{XY,\phi 3}^{j-1} \\
\mathbf{A}_{XY,\phi 2}^{j} &= Z_{mill,\phi 2}\mathbf{A}_{XY,\phi 2}^{j-1} + U_{IC}\left(t_{\phi 1},\boldsymbol{\lambda}_{\phi 1},\mathbf{V}_{\phi 2}\right)\left(Z_{mill,\phi 1}\mathbf{A}_{XY,\phi 1}^{j-1} + U_{IC}\left(\mathrm{t}_{free},t_{\phi 3},\boldsymbol{\lambda}_{\phi 3},\mathbf{V}_{\phi 1}\right)\mathbf{A}_{XY,\phi 3}^{j-1}\right) \\
\mathbf{A}_{XY,\phi 3}^{j} &= Z_{mill,\phi 3}\mathbf{A}_{XY,\phi 3}^{j-1} \\
&\quad + U_{IC}\left(t_{\phi 2},\boldsymbol{\lambda}_{\phi 2},\mathbf{V}_{\phi 3}\right)\left(Z_{mill,\phi 2}\mathbf{A}_{XY,\phi 2}^{j-1} + U_{IC}\left(t_{\phi 1},\boldsymbol{\lambda}_{\phi 1},\mathbf{V}_{\phi 2}\right)\left(Z_{mill,\phi 1}\mathbf{A}_{XY,\phi 1}^{j-1} + U_{IC}\left(\mathrm{t}_{free},t_{\phi 3},\boldsymbol{\lambda}_{\phi 3},\mathbf{V}_{\phi 1}\right)\mathbf{A}_{XY,\phi 3}^{j-1}\right)\right)
\end{aligned} \tag{11.11}$$

$$\begin{Bmatrix} \mathbf{A}_{XY,\phi 1}^{j} \\ \mathbf{A}_{XY,\phi 2}^{j} \\ \mathbf{A}_{XY,\phi 3}^{j} \end{Bmatrix} = \begin{bmatrix} Z_{mill,\phi 1} & 0 & U_{IC,\phi 1} \\ U_{IC,\phi 2}Z_{mill,\phi 1} & Z_{mill,\phi 2} & U_{IC,\phi 2}U_{IC,\phi 1} \\ U_{IC,\phi 3}U_{IC,\phi 2}Z_{mill,\phi 1} & U_{IC,\phi 3}Z_{mill,\phi 2} & Z_{mill,\phi 3}+U_{IC,\phi 3}U_{IC,\phi 2}U_{IC,\phi 1} \end{bmatrix} \begin{Bmatrix} \mathbf{A}_{XY,\phi 1}^{j-1} \\ \mathbf{A}_{XY,\phi 2}^{j-1} \\ \mathbf{A}_{XY,\phi 3}^{j-1} \end{Bmatrix}$$

$$\text{where} \tag{11.12}$$

$$U_{IC,\phi 1} = U_{IC}\left(\mathrm{t}_{free},t_{\phi 3},\boldsymbol{\lambda}_{\phi 3},\mathbf{V}_{\phi 1}\right);\ U_{IC,\phi 2} = U_{IC}\left(t_{\phi 1},\boldsymbol{\lambda}_{\phi 1},\mathbf{V}_{\phi 2}\right);\ U_{IC,\phi 3} = U_{IC}\left(t_{\phi 2},\boldsymbol{\lambda}_{\phi 2},\mathbf{V}_{\phi 3}\right)$$

11.1 Example

The incremented milling solution developed in the previous sections is compared with numerical milling solutions in this section. In these examples the analytical solutions are compared with two types of milling simulations. The first simulation is a full milling simulation in which the cutting force direction changes during each time step based on the instantaneous angle of the tool. ϕ. In the second simulation the cutting force directions are constant over each incremental angle range, directly simulating the incremental analytical solutions. The dynamic parameters used in the examples are provided in Table 9.

Table 9: System parameters used in the multi-mode turning examples.

k_x, k_y	1E7, 5E7 N/m
m_x, m_y	0.88, 1 kg
c_x, c_y	500, 60 Ns/m
K_s	2E9 N/m^2
β	70°

The example solution is performed using a spindle speed of 20,000 RPM at a depth of cut of 7mm and a radial immersion of 100%. Using these dynamic and cutting parameters, the analytical solutions are compared with the numerical solutions as the number of linear increments used in the analytical solutions are increased from one to five over five tool revolutions. The resulting solutions for the x and y motions are shown in Figure 91, where the analytical solutions (red dashed) are only plotted while the tool is in the cut. The results from Figure 91 show firstly that the analytical results regardless of the number of increments do match the incremented numerical solutions. However, the degree to which the analytical solution matches the full milling simulation is highly dependent on the number of increments used. When only a single increment is used there are significant differences between the analytical and numerical solutions, appearing during the first tool revolution. As the number of increments is increased, the analytical solution approaches the full milling simulation, where at N_{incs}=5, there is little visible difference between all three solutions.

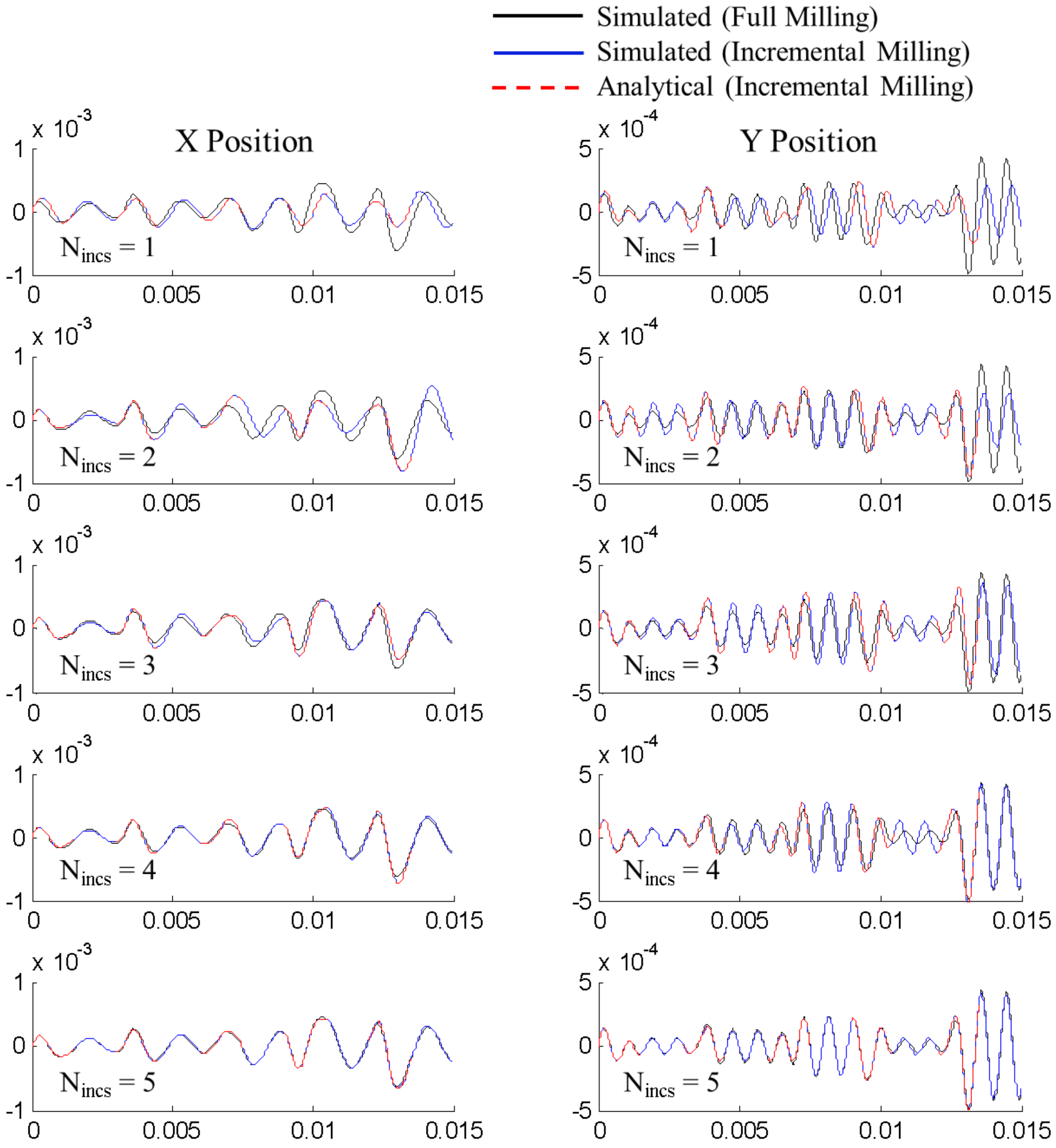

Figure 91: Comparison of the full milling simulation and the incremental milling simulation as the number of linearized increments increases. The analytical plots model the incremental simulations and are plotted only while the tool is in the cut. The parameters used for the simulations are shown in Table 9 with: REM=100%, N_t=1, RPM=20,000, b=7mm.

11.2 Conclusions

The segmented linearization approach to approximate full milling shows that the nonlinear behavior of the tool in milling can be predicted to various degrees of accuracy depending on the number of increments used. While this approach appears to be effective for predicting the time domain behavior of the system, applications of Floquet theory on the transition matrix in Equation 11.12 to predict stability have been unsuccessful. At this time the cause of this issue is unknown and will be a topic of future research.

CHAPTER 12: CONCLUSIONS AND FUTURE WORK

The initial goal of the work presented in this dissertation was to develop a new strategy for analytically solving linear delay differential equations by taking advantage of the fact that the sequential responses can be calculated independently of the time delay period, and can be combined to form the solution. While the sequential response approach has been shown to be effective in determining the time response of a tool with single or multiple modes, this approach alone showed little improvement over numerical approaches for practical applications, where the primary objective for these types of systems is to determine the limits of stability.

However, it was the equations and techniques developed for the sequential response solution approach that provided the ability to expand to a more applicable, matrix solution. By applying the sequential response approach it was possible to analytically determine the behavior of the tool during one period based on the behavior of the tool during the previous period. Combining this approach with the method of steps to determine the initial conditions of each period, it was possible to create a single transition matrix which fully describes the tool behavior from period to period. Once this transition matrix was developed it was possible to apply Floquet theory to directly predict the stability of the system analytically without the need to determine the time response.

Once the tools were in place to predict stability for the most simple machining operation (turning), the process of expanding to more complex machining operations was relatively trivial. The key is to recognize the two basic analytical tools present in all of the applications presented in this dissertation; the Z transition matrices which determine how the tool will respond when it encounters the surface profile left behind during the previous pass, and U_{IC}, which describes the initial conditions of the tool based on its previous motions. By combining these two analytical tools in different ways to effectively "piece together" the machining operations, it was possible to determine the time response and stability of more complex systems.

Moving forward, there is still much research that can be done in this area. Firstly, there is still a need to perform further experimental tests to verify both the time response and stability predictions of the analytical methods developed here. It was shown in this dissertation that the time response predictions closely match those measured experimentally for turning, despite the influence of process damping. However, further tests can be done to experimentally verify the other machining operations studied here. Although process damping was not a focus of this research, it would be possible to use the processes developed in this dissertation to correct for process damping to perform a more thorough characterization of process damping.

Another focus of future work will be on determining why Floquet theory fails to predict stability in the case of full milling while the same transition matrix accurately predicts the time response of the tool.

The final potential focus of future work would be to study more thoroughly the application of the methods developed in this paper for other applications. As the solution process developed here for delayed systems is based on a state-space model, there is no reason that it could not be generalized to accommodate linear DDEs of higher order.

REFERENCES

Altintas, Y., Budak, E.
1995Analytical Prediction of Stability Lobes in Milling. Annals of CIRP 44(1).

Altintas, Y., Engin, S., Budak, E.
1999Analytical Stability Prediction and Desigh of Variable Pitch Cutters. Journal of Manufacturing Science and Engineering 121.

Altintas, Y., Enynian, M., Onozuka, H.
2008aIdentification of Dynamic Cutting Force Coefficients and Chatter Stability with Process Damping. CIRP Annals of Manufacturing Technology 57(1).

Altintas, Y., Stepan, G., Merdol, D., Dombovari, Z.
2008bChatter Stability of Milling in Frequency and Discrete Time Domain. Cirp Journal of Manufacturing Science and Technology 1:35-44.

Bayly, P. V., Halley, J. E., Mann, B. P., Davies, M. A.
2003Stability of Interupted Cutting by Temporal Finite Element Analysis. Journal of Manufacturing Science and Engineering 125(2):220-225.

Budak, E., Altintas, Y.
1998aAnalytical Prediction of Chatter Stability in Milling-Part I: General Formulation. Journal of Dynamic Systems, Measurement and Control 120.

Budak, E., Altintas, Y.
1998bAnalytical Prediction of Chatter Stability in Milling-Part II: Application of the General Formulation to Common Miling Systems. Journal of Dynamic Systems, Measurement and Control 120.

Butcher, E., Mann, B.
2009Delay Differential Equations, Recent Advances and New Directions: Springer US.

Butcher, E. Nindujarla, P., Bueler, E.
2005Stability of Up and Down Milling Using Chebyshev Collocation Method. DETC2005-84880, Long Beach, California, USA, 2005.

C., Tyler.
2012PROCESS DAMPING ANALYTICAL STABILITY ANALYSIS AND VALIDATION, Mechanical Engineering, UNC Charlotte.

Davies, M. A., Pratt, J. R., Dutterer, B., Burns, T. J.
2002Stability Prediction for Low Radial Immersion Milling. Journal of Manufacturing Science and Engineering 124:217-225.

Ding, H., Ding, Y., Zhu, L.

2012On Time-Domain Methods for Milling Stability Analysis. Chinese Science Bulletin 57:4336-4345.

Ding, Y., Zhu, L., Zhang, X., Ding, H.

2010A Full-Discretization Method for Prediction of Milling Stability. International Journal of Machine Tools and Manufacture 50:502-509.

Eynian, M.

2010Chatter Stability of Turning and Milling with Process Damping, Mechanical Engineering, University of British Columbia.

Eynian, M., Altintas, Y.

August, 2009Chatter Stability of General Turning Operations with Process Damping. Journal of Manufacturing Science and Engineering 131:041005-1 through 10.

Ganguly, V., Schmitz, T.

2014Correction for Synchronization Errors in Dynamic Measurements. Proceedings of NAMRI/SME 42.

Gradisek, J., Govekar, E., Grabec, I., Kalveram, M., Weinert, K., Insperger, T., Stepan, G.

2005On Stability Prediction for Low Radial Immersion Milling. Machine Science and Technology 9:117-130.

Gyliene, V., Ostasevicius, V.

2013The Validation of Fe Modeling of Orthogonal Turning Process using Cowper-Symonds Material Behavior Law. Engineering Transactions 61(4):249-263.

Insperger, T.

2010Full-Discretization and Semi-Discretization for Milling Stability Prediction: Some Comments. International Journal of Maching Tools and Manufacture 50:658-662.

Insperger, T., Stepan, G.

2002Semi-Discretization Method for Delayed Systems. International Journal for Numerical Methods in Engineering 55(5):503-518.

Insperger, T., Stepan, G.

2004Updated Semi-Deiscretization Method for Periodic Delay Differential Equations. International Journal for Numerical Methods in Engineering 61:117-141.

Kurata, Y., Merdol, S. D., Altintas, Y. Suzuki, N., Shamoto, E.

2010Chatter Stability in Turning and Milling with in process Identified Process Damping. Journal of Advanced Mechanical Design, Systems, and Manufactuing 4(6).

Mann, B. P., Patel, B. R.

2010Stability of Delay Equations Written as State Space Models. Journal of Sound and Vibraion 16(7-8).

Marsh, E. R., Yantek, D. S., Davies, M. A., Gilsinn, D. E.

1998Simulation and Measurement of Chatter in Diomond Turning. Journal of Manufacturing Science and Engineering 120:230.

Merdol, S. D., Altintas, Y.,

2004Multi Frequency Solution of Chatter Stability for Low Immersion Milling. Journal of Manufacturing Science and Engineering 126:459-466.

Minis, I., Yanushevsky, R.

1993A New Theoretical Approach for Prediction of Machine Tool Chatter in Milling. Journal of Engineering for Industry 115:1-8.

Myshkis, A. D.

1998Differential Equations, Ordinary with Distributed Arguments. *In* Encyclopedia of Mathematics. Pp. 144-147, Vol. 3. Boston: Kluwer Academinc Publishers.

Olgac, N., Sipahi, R.

2006Dynamics and Stability of Variable-pitch Milling. Journal of Vibrations and Control 13(7).

Ozoegwu, C. G., Omenyi, S. N.

2012Time Domain Chatter Stability Comparison of Turning and Milling Processes. International Journal of Multidisciplinary Sciences and Engineering 3(11):25.

Schmitz, T. L., Smith, K. S.

2009Machining Dynamics - Frequency Response to Improved Productivity. New York, NY: Springer.

Shampine, L. F., Thompson, S.

2001Solving DDEs in Matlab. Applied Numerical Mathematics 37:441-458.

Sims, N., Mann, B., Huyanan, S.

2008Analytical prediction of chatter stability for variable pitch and variable helix milling tools. Journal of Sound and Vibraion 317(2-5):664-686.

Smith, S.
2010Fighting Chatter with Nonproportional Spacing. Bluswarf.com.

Smith, S., Tlusty, J.
1993Efficient Simulation Programs for Chatter in Milling. Annals of the CIRP 42(1).

Stepan, G.
1989Retarded Dynamical Systems: Stability and Characteristic Functions: John Wiley and Son., Inc.

Stepan, G.
2001Modelling Nonlinear Regenerative Effects in Metal Cutting. Philosophical Transiactions of the Royal Society of London 359:739-757.

Taylor, C. M., Turner, S., Sims, N.D.
2010Chatter, Process Damping, and Chip Segmentation in Turning: A Signal Processing Approach. Journal of Sound and Vibraion 329(23):4922-4935.

Tlusty, J.
1999Manufacturing Processes and Equipment. Upper Saddle River, New Jersey: Prentice Hall.

Tlusty, J., Ismail, F.
1981Basic Non-linearities in Maching Chatter. Annals of CIRP 30:299-304.

Tlusty, J., Polacek, W.
1963The Stability of Machine Tools Against Self Excited Vibrations. ASME International Research in Productoin Engineering 1:465-474.

Tlusty, J., Zaton, F., Ismail, F.
1983Stability Lobes in Milling. Annals of CIRP 32(1).

Tobias, S. A., Fishwick, W.
1958Theory of Regenerative Machine Tool Chatter. The Engineer 205(199-203).

Tunc, T., Budak, E.
2012Effect of cutting conditions and tool geometry on process damping in machining. INTERNATIONAL JOURNAL OF MACHINE TOOLS AND MANUFACTURE.

APPENDIX A: SEQUENTIAL RESPONSE SOLUTIONS

12.1 Detailed Sequential Response Solutions

This section provides a detailed solution to equation 2.15 when the input function, $h_{nom}(t)$, contains decaying oscillation terms. We will start with the solution to the oscillating input in equation 2.28 (for the calculation of $x_2(t)$). This portion of the ODE and the corresponding particular solution, x_p, are shown in equation 12.1. In order to solve for the constants, W_0, $W_{1,a}$, and $W_{1,b}$, we first take the first two time derivatives of x_{p2}.

$$\begin{aligned} &\ddot{x}+\frac{c}{m}\dot{x}+\frac{k_p}{m}x=\frac{bR}{m}V_0\left[e^{-At}\left(G\sin(\omega_p t)+H\cos(\omega_p t)\right)\right], \\ &x_{p2}=W_0 e^{-At}\left[W_{1,a}\,t\sin\left(\omega_p t-\frac{\pi}{2}\right)+W_{1,b}\,t\cos\left(\omega_p t-\frac{\pi}{2}\right)\right] \end{aligned} \qquad 12.1$$

Using Matlab, the first time derivative is:

$\dot{x}_p =$

```
W0*exp(-A*t)*(-A*t*W1a*sin(wp*t-(pi/2))-A*t*W1b*cos(wp*t-
(pi/2))...
                 +W1a*sin(wp*t-(pi/2))+W1b*cos(wp*t-(pi/2))...
                     +t*W1a*cos(wp*t-(pi/2))*wp-t*W1b*sin(wp*t-
(pi/2))*wp)
```

And the second time derivative is:

$\ddot{x}_p =$

```
-W0*exp(-A*t)*(-A^2*t*W1a*sin(wp*t-(pi/2))-A^2*t*W1b*cos(wp*t-
(pi/2))...
              +2*A*W1a*sin(wp*t-(pi/2))+2*A*W1b*cos(wp*t-(pi/2))...
                 +2*A*t*W1a*cos(wp*t-(pi/2))*wp-2*A*t*W1b*sin(wp*t-
(pi/2))*wp...
                  -2*W1a*cos(wp*t-(pi/2))*wp+2*W1b*sin(wp*t-
(pi/2))*wp...
                  +t*W1a*sin(wp*t-(pi/2))*wp^2+t*W1b*cos(wp*t-
(pi/2))*wp^2)
```

Applying the time derivatives to the left side of the ODE, we obtain:

$\ddot{x}_p+2A\dot{x}_p+\frac{k_p}{m}x_p=$

```
-W0*exp(-A*t)*...
          (-t*(kp/m)*W1a*sin(wp*t-(pi/2))-t*(kp/m)*W1b*cos(wp*t-
(pi/2))...
```

```
                    +A^2*t*W1a*sin(wp*t-(pi/2))+A^2*t*W1b*cos(wp*t-
(pi/2))...
                        -2*wp*W1a*cos(wp*t-(pi/2))+2*wp*W1b*sin(wp*t-
(pi/2))...
                        +t*wp^2*W1a*sin(wp*t-(pi/2))+t*wp^2*W1b*cos(wp*t-
(pi/2)))...
```

Note that c/m is replaced by 2A in the above equation to reduce the number of variables.

After applying the relation, ${\omega_p}^2 + A^2 - \frac{k_p}{m} = 0$, (see equation 2.23) the equation reduces to:

$$\ddot{x}_p + 2A\dot{x}_p + \frac{k_p}{m} x_p = \texttt{W0*exp(-A*t)*(2*W1a*wp*cos(wp*t-pi/2)-2*W1b*wp*sin(wp*t-pi/2))} \qquad 12.2$$

The constants of x_{p2} can now be solved for by equating equation 12.2 to the right side of the ODE in equation 12.1, recognizing that sin(ω_pt-pi/2) = -cos(ω_pt) and so on.

During the next pass, the input function, $h_{nom,3}$(t), will contain oscillating terms described by x_{p2} as well as oscillating terms from the complementary solution, $x_c = e^{-At}\left[W_{2,a}\sin\left(\omega_p t - \frac{\pi}{2}\right) + W_{2,b}\cos\left(\omega_p t - \frac{\pi}{2}\right)\right]$, which takes into account all of the particular solutions and the ICs. The oscillation terms for the input for the following pass (to find x_3) will then be:

$$h_{nom,3,osc} = C_0 e^{-At}\left[C_{1,a}\, t \sin\left(\omega_p t - \frac{\pi}{2}\right) + C_{1,b}\, t \cos\left(\omega_p t - \frac{\pi}{2}\right) + C_{2,a}\sin\left(\omega_p t - \frac{\pi}{2}\right) + C_{2,b}\cos\left(\omega_p t - \frac{\pi}{2}\right)\right] \qquad 12.3$$

And the particular solution to this input will have the form:

$$x_{p,3,osc} = W_0 e^{-At}\left[W_{1,a}\, t^2 \sin\left(\omega_p t - 2\frac{\pi}{2}\right) + W_{1,b}\, t^2 \cos\left(\omega_p t - 2\frac{\pi}{2}\right) + W_{2,a}\, t \sin\omega_p\left(nt - 2\frac{\pi}{2}\right) + W_{2,b}\, t \cos\left(\omega_p t - 2\frac{\pi}{2}\right)\right] \qquad 12.4$$

Again, when $x_3(t)$ is calculated, the complementary solution will add sine and cosine terms which are not multiplied by t. So, as the number of passes increases, the oscillating portion of the responses will contain sine and cosine terms multiplied by increasing orders of t, where the highest order is t^(j-1), and the lowest is t^0, for the response, $x_j(t)$. The primary objective of the sequential response analysis is to find all of the W coefficients to describe the oscillating component of the tool motion during each pass.

We could go on solving the sequential responses individually in this way… Let’s look for patterns in the solution to simplify the process.

Skipping ahead now to the response to the sixth pass, the oscillating portion of the input function has the form:

$$\frac{bR}{m}h_{nom,6,osc}=C_0e^{-At}\left[\begin{array}{l} C_{1,a}t^4\sin\left(\omega_p t-4\frac{\pi}{2}\right) \\ \quad +C_{1,b}t^4\cos\left(\omega_p t-4\frac{\pi}{2}\right) \\ \qquad +C_{2,a}t^3\sin\left(\omega_p t-4\frac{\pi}{2}\right)+C_{2,b}t^3\cos\left(\omega_p t-4\frac{\pi}{2}\right) \\ \qquad\quad +C_{5,a}\sin\left(\omega_p t-4\frac{\pi}{2}\right)+C_{5,b}\cos\left(\omega_p t-4\frac{\pi}{2}\right) \end{array}\right] \tag{12.5}$$

And the particular solution has the form:

$$x_{p,6,osc}=W_0e^{-At}\left[\begin{array}{l} W_{1,a}t^5\sin\left(\omega_p t-5\frac{\pi}{2}\right)+W_{1,b}t^5\cos\left(\omega_p t-5\frac{\pi}{2}\right) \\ \quad +W_{2,a}t^4\sin\left(\omega_p t-5\frac{\pi}{2}\right)+W_{2,b}t^4\cos\left(\omega_p t-5\frac{\pi}{2}\right) \\ \quad\ +W_{5,a}t\sin\left(\omega_p t-5\frac{\pi}{2}\right)+W_{5,b}t\cos\left(\omega_p t-5\frac{\pi}{2}\right) \end{array}\right] \tag{12.6}$$

Differentiating equation 12.6 and applying to the differential equation, we get:

$$\ddot{x}_p+2A\dot{x}_p+\frac{k_p}{m}x_p=\texttt{W0*exp(-A*t)*...} \tag{12.7}$$

```
            (10*wp*W1*t^4*cos(wp*t-5*(pi/2))-10*wp*W2*t^4*sin(wp*t-
    5*(pi/2))...

            +20*W1*t^3*sin(wp*t-5*(pi/2))+20*W2*t^3*cos(wp*t-
5*(pi/2))...
            +8*W3*t^3*wp*cos(wp*t-5*(pi/2))-8*wp*W4*t^3*sin(wp*t-
5*(pi/2))...

            +12*W3*t^2*sin(wp*t-5*(pi/2))+12*W4*t^2*cos(wp*t-
5*(pi/2))...
            +6*W5*t^2*wp*cos(wp*t-5*(pi/2))-6*wp*W6*t^2*sin(wp*t-
5*(pi/2))...

            +6*W5*t*sin(wp*t-5*(pi/2))+6*W6*t*cos(wp*t-5*(pi/2))...
            +4*W7*t*wp*cos(wp*t-5*(pi/2))-4*wp*W8*t*sin(wp*t-
5*(pi/2))...

            +2*W7*sin(wp*t-5*(pi/2))+2*W8*cos(wp*t-5*(pi/2))...
            +2*W9*wp*cos(wp*t-5*(pi/2))-2*wp*W10*sin(wp*t-5*(pi/2)))
```

From equation 12.7 we start to see two patterns emerge; factors of 2, 4, 6, 8, and 10 (2i) appear in the second line for each order of t, and factors of 2, 6, 12, and 20 (i(i+1)) appear on the first line. These patterns continue as the number of passes increases, and from them we can obtain a general form for the evaluated particular solution as shown in equations 12.8 through 12.10.

$$\frac{bR}{m}h_{nom,j}(t)=C_0e^{-At}\sum_{i=1}^{j-1}t^{j-i-1}\left(C_{ia}\sin\left(\omega_pt-(j-2)\frac{\pi}{2}\right)+C_{ib}\cos\left(\omega_pt-(j-2)\frac{\pi}{2}\right)\right) \qquad 12.8$$

General solution

$$x_{p,j}=W_0e^{-At}\sum_{i=1}^{j-1}t^{j-i}\left(W_{ia}\sin\left(\omega_pt-(j-1)\frac{\pi}{2}\right)+W_{ib}\cos\left(\omega_pt-(j-1)\frac{\pi}{2}\right)\right) \qquad 12.9$$

$$\begin{aligned}\ddot{\mathrm{x}}_{p,j}+\frac{c}{m}\dot{\mathrm{x}}_{p,j}+\frac{k_p}{m}\mathrm{x}_{p,j}&=W_0e^{-At}\left(2\omega_p(j-1)t^{j-2}\left(W_{1,a}\cos\left(\omega_pt-(j-1)\frac{\pi}{2}\right)-W_{1,b}\sin\left(\omega_pt-(j-1)\frac{\pi}{2}\right)\right)\right)\\&+W_0e^{-At}\sum_{i=1}^{j-2}t^{j-i-2}\left(\begin{array}{c}(j-i)(j-i-1)\left(W_{i,a}\sin\left(\omega_pt-(j-1)\frac{\pi}{2}\right)+W_{i,b}\cos\left(\omega_pt-(j-1)\frac{\pi}{2}\right)\right)\\+2\omega_p(j-i-1)\left(W_{i+1,a}\cos\left(\omega_pt-(j-1)\frac{\pi}{2}\right)-W_{i+1,b}\sin\left(\omega_pt-(j-1)\frac{\pi}{2}\right)\right)\end{array}\right)\end{aligned} \qquad 12.10$$

Note that equation 12.10 is the result after terms are cancelled based on $\omega_p{}^2 + A^2 - \frac{k_p}{m} = 0$.

It is now a matter of solving for the coefficients in equation 12.9 by equating equation 12.10 to equation 12.8. Keep in mind that the C coefficients in equation 12.8 are the W coefficients from the previous pass.

Here again, we could go on solving for the coefficients individually in this way… Let's look for patterns that can simplify the process.

We will start by looking at the coefficient, W_0. W_0 is simply equal to C_0, where C_0 is equal to W_0 from the previous pass multiplied by bR/m. So as the number of passes increases, W_0 can be determined by the following equation:

$$W_{0,j} = V_0 \left(\frac{bR}{m} \right)^{j-1} \qquad 12.11$$

The V_0 term in equation 12.11 is present because the factor multiplied by the oscillating term after the first pass is V_0 (i.e. V_0 is the initial C_0) (See equation 2.25). In subsequent passes, the W_0 term is repeatedly multiplied by bR/m according to equation 2.15.

W_0 takes care of the effect of the forcing constant which carries through from solution to solution. Moving forward, we can consider the constant terms, C, to be simply equal to the W coefficients from the previous pass.

The next coefficients to be solved for are those associated with the highest order t terms, W_1. Because of the shift in phase from equation 12.8 and equation 12.10, $W_{1,a}$ will be associated with $C_{1,a}$, and $W_{1,b}$ with $C_{1,b}$. Looking at $W_{1,a}$, it is always multiplied by

$2\omega_p(j-1)$ in equation 12.10 so that $W_{1,a} = \frac{C_{1,a}}{2\omega_p(j-1)}$. After the first pass the initial $C_{1,a}$ constant is G (equation 2.27) and as the number of passes increase, $W_{1,a}$ is found by repeatedly applying the equation, $W_{1,a} = \frac{C_{1,a}}{2\omega_p(j-1)}$, as shown in equation 12.12. From the pattern that emerges for W1,a in terms of the initial constant, G, the resulting value of $W_{1,a}$ can be found directly using equation 12.13. The same equation is used to determine the value of $W_{1,b}$, accept that G is replaced by H, as shown in equation 12.14.

$$\begin{aligned} &j=1;\ W_{1,a}=G \\ &j=2;\ W_{1,a}=\frac{G}{2\omega_p} \\ &j=3;\ W_{1,a}=\frac{G}{(2\omega_p)(4\omega_p)} \\ &j=4;\ W_{1,a}=\frac{G}{(2\omega_p)(4\omega_p)(6\omega_p)} \\ &j=5;\ W_{1,a}=\frac{G}{(2\omega_p)(4\omega_p)(6\omega_p)(8\omega_p)} \end{aligned} \tag{12.12}$$

$$W_{1,a} = \frac{G}{(j-1)!(2\omega_p)^{(j-1)}} \tag{12.13}$$

$$W_{1,b} = \frac{H}{(j-1)!(2\omega_p)^{(j-1)}} \tag{12.14}$$

The general solution for the remaining W coefficients becomes more cumbersome because each W term is dependent both on a C term and another W term (i.e. W_2 is dependent on C_2 and W_1). One feature of equation 12.10 which is not easily apparent, but will simplify the generalization process. Each order t set of coefficients, say W_2, has two values, $W_{2,a}$ corresponding to the sine term and $W_{2,b}$ corresponding to the cosine term. The a and b terms of W_2 are always independent of each other, but the $W_{2,a}$ term is dependent on the $W_{1,b}$ term. However, just as the equations for $W_{1,a}$ and $W_{1,b}$ are dependent on either the initial G term or the H term, the cascading solutions for the remaining coefficients also follow two separate independent paths, one always dependent of the initial G term and the other always dependent on the initial H term. For example, $W_{2,a}$ is dependent on $W_{1,a}(G)$ and $C_{2,a}(G)$. So in effect, the W coefficients in equation 12.10 will follow two separate paths which follow the same pattern as the number of W terms increases, and the only difference between the two coefficients at each level of W will depend on the initial values G and H. This can also be seen in equation 2.31 where the first three responses are given with phase shifts at each order of t, such that the G line of coefficients always corresponds to sine, and the H line of coefficients always corresponds to cosine (the non-phase shifting form in equation 12.8 and 12.10 is an artifact of the derivation process).

$$2\omega_p(j-i-1)W_{j,i}+(j-i)(j-i-1)W_{j,i-1}=C_{j,i}$$

$$W_{j,i}=\left(\frac{1}{2\omega_p(j-i-1)}\right)\left(C_{j,i}-(j-i)(j-i-1)W_{j,i-1}\right);\ i=2,3,4,... \qquad 12.15$$

The dependency on the previous solution (j-1) and other coefficients of the same solution (j) creates a cascading effect, where the coefficients for any solution are dependent on the coefficients of all previous solutions. As such, it is convenient to organize all of the coefficients together in matrix form as shown in equation 12.16, where the rows represent all of the coefficients for the jth solution, and the columns represent the order of t that the coefficients correspond to.

$$W = \begin{array}{c|cccc} & i \rightarrow & & & \\ & t^0 & t^1 & t^2 & t^3 \\ j=1 & W_1 & 0 & 0 & 0 \\ j=2 & W_2 & W_1 & 0 & 0 \\ j=3 & W_3 & W_2 & W_1 & 0 \\ j=4 & W_4 & W_3 & W_2 & W_1 \end{array} \qquad 12.16$$

The diagonal W$_1$ terms can be calculated directly using equations 12.13 and 12.14 (there will be two W matrices, one for the G line of coefficients and one for H). The lower triangle terms, excluding the first column, can be calculated by rearranging equation 12.15 , keeping in mind that now i is the column number moving from left to right, and that the C terms are actually the W terms from the row above the solution number being evaluated.

$$\mathbf{W}(j,i) = \frac{1}{2\omega_p(i-1)}\left[i(i-1)\mathbf{W}(j,i+1) + \mathbf{W}(j-1,i-1)\right] \qquad 12.17$$

There is one final thing to consider when constructing the coefficient matrix, W, and that is the calculation of the first column coefficients corresponding to t^0. Looking at equation 12.9, you will notice that the coefficients of the particular solution correspond to t^{j-1} down to t^1. The coefficients corresponding to t^0 come from the complementary solution, $x_{c,j} = e^{-At}\left[W_{j,a}\sin\left(\omega_p t - \frac{\pi}{2}\right) + W_{j,b}\cos\left(\omega_p t - \frac{\pi}{2}\right)\right]$, which must also take into account the linear components of the solution.

The first column coefficients can be calculated using equation 12.18 for the G matrix, and equation 12.19 for the H matrix. They were derived by repeatedly solving the differential equations with zero initial velocity and displacement.

$$\mathbf{W}_G(j,1) = \frac{1}{n}\left(\mathbf{W}_G(j,i+1) - \left(\frac{m}{k_p}\right)^{j-1}\right) \qquad 12.18$$

$$\mathbf{W}_H(j,1) = H\ j\left(\frac{m}{k_p}\right)^{j-1} \qquad 12.19$$

For completeness, the linear components of the sequential response functions can be calculated using Equation 12.20. This pattern can be easily observed in equation 2.31

$$V_0^{\,j}(t - jH) \qquad 12.20$$

In APPENDIX B the derivations discussed in this section will be combined to generate the complete sequential response solutions.

APPENDIX B: SINGLE MODE MATRIX EQUATION

12.2 Single Mode Matrix Equations

Equations of Matrix solution

$$\mathbf{X}(t) = \mathbf{O}_w \left[\mathbf{W}_G \mathbf{L}_{G,x}(t) + \mathbf{W}_H \mathbf{L}_{H,x}(t) \right] + \mathbf{S}_x(t) \qquad 12.21$$

$$\mathbf{V}(t) = \mathbf{O}_w \left[\mathbf{W}_G \mathbf{L}_{G,v}(t) + \mathbf{W}_H \mathbf{L}_{H,v}(t) \right] + \mathbf{S}_v(t) \qquad 12.22$$

$$\mathbf{Acc}(t) = \mathbf{O}_w \left[\mathbf{W}_G \mathbf{L}_{G,a}(t) + \mathbf{W}_H \mathbf{L}_{H,a}(t) \right] \qquad 12.23$$

$$\mathbf{W}_G = \begin{array}{cc} & i \rightarrow \\ \begin{array}{c} j \\ \downarrow \end{array} & \begin{bmatrix} \dfrac{G}{(j-1)!(2\omega_p)^{j-1}} & 0 & \cdots & 0 \\ \dfrac{1}{\omega_p}\left(\mathbf{W}_G(j,i+1) - \left(\dfrac{m}{k_p} \right)^{j-1} \right) & \searrow & \ddots & \vdots \\ \downarrow & \vdots & \searrow & 0 \\ \downarrow & \dfrac{1}{2\omega_p(i-1)}\left[i(i-1)\mathbf{W}_G(j,i+1) + \mathbf{W}_G(j-1,i-1) \right] & \cdots & \searrow \end{bmatrix} \end{array} \qquad 12.24$$

Diagonal terms

$$\mathbf{W}_G(j,j) = \frac{G}{(j-1)!(2\omega_p)^{j-1}} \qquad 12.25$$

First column terms

$$\mathbf{W}_G(j,1) = \frac{1}{\omega_p}\left(\mathbf{W}_G(j,i+1) - \left(\frac{m}{k_p} \right)^{j-1} \right) \qquad 12.26$$

Lower triangle terms

$$\mathbf{W}_G(j,i) = \frac{1}{2\omega_p(i-1)}\left[i(i-1)\mathbf{W}_G(j,i+1) + \mathbf{W}_G(j-1,i-1) \right] \qquad 12.27$$

All upper triangle terms are zero

$$\mathbf{W}_H = \begin{array}{cc} & i \rightarrow \\ \begin{array}{c} j \\ \downarrow \end{array} & \begin{bmatrix} \dfrac{H}{(j-1)!(2\omega_p)^{j-1}} & 0 & \cdots & 0 \\ H\,j\left(\dfrac{m}{k_p}\right)^{j-1} & \searrow & \ddots & \vdots \\ \downarrow & \vdots & \searrow & 0 \\ \downarrow & \dfrac{1}{2\omega_p(i-1)}\left[i(i-1)\mathbf{W}_H(j,i+1)+\mathbf{W}_H(j-1,i-1)\right] & \cdots & \searrow \end{bmatrix} \end{array} \tag{12.28}$$

Diagonal terms

$$\mathbf{W}_H(j,j) = \frac{H}{(j-1)!(2\omega_p)^{j-1}} \tag{12.29}$$

First column terms

$$\mathbf{W}_H(j,1) = H\,j\left(\frac{m}{k_p}\right)^{j-1} \tag{12.30}$$

Lower triangle terms

$$\mathbf{W}_H(j,i) = \frac{1}{2\omega_p(i-1)}\left[i(i-1)\mathbf{W}_H(j,i+1)+\mathbf{W}_H(j-1,i-1)\right] \tag{12.31}$$

All upper triangle terms are zero

$$O_W = \begin{array}{cc} \begin{array}{c} j \\ \downarrow \end{array} & \begin{bmatrix} V_0\left(\dfrac{bR}{m}\right)^{j-1} & 0 & 0 \\ 0 & \searrow & 0 \\ 0 & 0 & \searrow \end{bmatrix} \end{array} \tag{12.32}$$

L vectors for position

$$\mathbf{L}_{G,x}(t) = \begin{array}{cc} \begin{array}{c} j \\ \downarrow \end{array} & \begin{bmatrix} t^{j-1}e^{-At}\sin\left(\omega_p t-(j-1)\dfrac{\pi}{2}\right) \\ \downarrow \\ \downarrow \end{bmatrix} \end{array} \tag{12.33}$$

$$\mathbf{L}_{H,x}(t) = \overset{j}{\downarrow}\begin{bmatrix} t^{j-1}e^{-At}\cos\left(\omega_p t-(j-1)\frac{\pi}{2}\right) \\ \downarrow \\ \downarrow \end{bmatrix} \qquad 12.34$$

The L vectors for velocity are found by differentiating the Lx matrices multiplied by the exponential term, $\mathbf{L}_{G,v}(t)=\frac{d}{dt}\left(\mathbf{L}_{G,x}(t)\right)$, $\mathbf{L}_{H,v}(t)=\frac{d}{dt}\left(\mathbf{L}_{H,x}(t)\right)$.

$$\mathbf{L}_{G,v}(t) = \overset{j}{\downarrow}\begin{bmatrix} t^{j-1}e^{-At}\left[\omega_p\cos\left(\omega_p t-(j-1)\frac{\pi}{2}\right)-A\sin\left(\omega_p t-(j-1)\frac{\pi}{2}\right)\right] \\ +t^{j-2}e^{-At}\left[(j-1)\sin\left(\omega_p t-(j-1)\frac{\pi}{2}\right)\right] \\ \downarrow \\ \downarrow \end{bmatrix} \qquad 12.35$$

$$\mathbf{L}_{H,v}(t) = \overset{j}{\downarrow}\begin{bmatrix} -t^{j-1}e^{-At}\left[\omega_p\sin\left(\omega_p t-(j-1)\frac{\pi}{2}\right)+A\cos\left(\omega_p t-(j-1)\frac{\pi}{2}\right)\right] \\ +t^{j-2}e^{-At}\left[(j-1)\cos\left(\omega_p t-(j-1)\frac{\pi}{2}\right)\right] \\ \downarrow \\ \downarrow \end{bmatrix} \qquad 12.36$$

The L vectors for acceleration are found as, $\mathbf{L}_{G,a}(t)=\frac{d}{dt}\left(e^{-At}\mathbf{L}_{G,v}(t)\right)$, $\mathbf{L}_{H,a}(t)=\frac{d}{dt}\left(e^{-At}\mathbf{L}_{H,v}(t)\right)$.

$$\mathbf{L}_{G,a}(t) = \overset{j}{\downarrow}\begin{bmatrix} t^{j-1}e^{-At}\left[\left(A^2-\omega_p{}^2\right)\sin\left(\omega_p t-(j-1)\frac{\pi}{2}\right)-2A\omega_p\cos\left(\omega_p t-(j-1)\frac{\pi}{2}\right)\right] \\ +t^{j-2}e^{-At}\left(2(j-1)\right)\left[\omega_p\cos\left(\omega_p t-(j-1)\frac{\pi}{2}\right)-A\sin\left(\omega_p t-(j-1)\frac{\pi}{2}\right)\right] \\ -t^{j-3}e^{-At}(j-1)(j-2)\sin\left(\omega_p t-(j-1)\frac{\pi}{2}\right) \\ \downarrow \\ \downarrow \end{bmatrix} \qquad 12.37$$

$$\mathbf{L}_{H,a}(t)=\overset{j}{\downarrow}\begin{bmatrix} t^{j-1}e^{-At}\left[2A\omega_p\sin\left(\omega_p t-(j-1)\frac{\pi}{2}\right)-\left(A^2-\omega_p{}^2\right)\cos\left(\omega_p t-(j-1)\frac{\pi}{2}\right)\right] \\ -t^{j-2}e^{-At}\left(2(j-1)\right)\left[\omega_p\sin\left(\omega_p t-(j-1)\frac{\pi}{2}\right)-A\cos\left(\omega_p t-(j-1)\frac{\pi}{2}\right)\right] \\ +t^{j-3}e^{-At}\left(j-1\right)\left(j-2\right)\cos\left(\omega_p t-(j-1)\frac{\pi}{2}\right) \\ \downarrow \\ \downarrow \end{bmatrix} \qquad 12.38$$

Note that the exponential term, e^{-At}, does not appear on the L matrices because it is pulled out and placed at the front of equations 12.22 and 12.23.

$$\mathbf{S}_x(t)=\overset{j}{\downarrow}\begin{bmatrix} V_0{}^j\left(t-jH\right) \\ \downarrow \\ \downarrow \end{bmatrix} \qquad 12.39$$

$$\mathbf{S}_v(t)=\overset{j}{\downarrow}\begin{bmatrix} V_0{}^j \\ \downarrow \\ \downarrow \end{bmatrix} \qquad 12.40$$

APPENDIX C: CALCULATION OF CRITICAL STAILITY LIMIT

12.3$b_{lim,crit}$, chatter frequency, and maximum amplitude location

12.3.1Location of Maximum Amplitude

The equation describing the oscillation envelope for the j^th^ sequential response is given in equation 12.41

$$f_j(t) = C\left(\frac{1}{\omega_p\left(j-1\right)!(2\omega_p)^{j-1}}\right)V_0\left(\frac{bR}{m}\right)^{j-1} t^{j-1}e^{-At} \qquad 12.41$$

To find the time, t, of the maximum oscillation, we differentiate equation 12.42, where C combines all of the constant terms, and solve for t after setting the derivative equal to zero.

$$f_j(t) = C\,t^{j-1}e^{-At} \qquad 12.42$$

$$\begin{gathered} f_j'(t) = C\left[(j-1)t^{j-2}e^{-At} - At^{j-1}e^{-At}\right] = 0 \\ (j-1)t^{j-2}e^{-At} = At^{j-1}e^{-At} \\ (j-1) = At \\ t = \frac{(j-1)}{A} \end{gathered} \qquad 12.43$$

From equation 12.43, the maximum oscillation amplitude for the j^th^ response occurs at $t = \frac{(j-1)}{A}$, and the value of the maximum amplitude can be calculated using equation 12.44.

$$f_{j,max} = f_j\left(\frac{j-1}{A}\right) = \left(\frac{1}{\omega_p\left(j-1\right)!}\right)V_0\left(\frac{bR}{2m\omega_p}\right)^{j-1}\left(\frac{j-1}{A}\right)^{j-1} e^{-A\left(\frac{j-1}{A}\right)} \qquad 12.44$$

12.3.2Calculation of b$_{lim,crit}$

b$_{lim,crit}$ is calculated as the value of b at which the maximum amplitudes from two subsequent responses are equal as the number of responses goes to infinity as shown in equation 12.45

$$b_{lim,crit} \; when \; f_{j,max} = f_{j+1,max} \; as \; j \to \infty \qquad 12.45$$

To do this, we use equation 12.44 and set two subsequent maximum amplitudes equal to each other, as shown in equation 12.46, and solve for the value of b which satisfies this condition.

$$C\left(\frac{1}{\omega_p\,(j-1)!}\right)V_0\left(\frac{bR}{2m\omega_p}\right)^{j-1}\left(\frac{j-1}{A}\right)^{j-1}e^{-A\left(\frac{j-1}{A}\right)} = C\left(\frac{1}{\omega_p\,(j)!}\right)V_0\left(\frac{bR}{2m\omega_p}\right)^{j}\left(\frac{j}{A}\right)^{j}e^{-A\left(\frac{j}{A}\right)} \qquad 12.46$$

$$\left(\frac{1}{(j-1)!}\right)(j-1)^{j-1}e^{-(j-1)} = \left(\frac{1}{(j)!}\right)\left(\frac{bR}{2Am\omega_p}\right)(j)^{j}e^{-j} \qquad 12.47$$

$$\left(\frac{bR}{2Am\omega_p}\right) = \frac{(j)!}{(j-1)!}\frac{(j-1)^{j-1}}{(j)^{j}}e^{1} \qquad 12.48$$

$$\left(\frac{bR}{2Am\omega_p}\right) = \frac{j}{(j-1)}\left(\frac{j-1}{j}\right)^{j}e^{1} \qquad 12.49$$

The two identities in equation 12.50 are used to eliminate the j term from equation 12.49, resulting in the reduced equation for b in equation 12.52

$$\lim_{j\to\infty}\frac{j}{(j-1)} = 1, \qquad \lim_{j\to\infty}\left(\frac{j-1}{j}\right)^{j} = e^{-1} \qquad 12.50$$

$$\left(\frac{bR}{2Am\omega_p}\right) = 1 \qquad 12.51$$

$$b = \frac{2Am\omega_p}{R} \tag{12.52}$$

The ω_p term in equation 12.52 is a function of b, so we must expand the equation to obtain the final value of $b_{lim,crit}$. As

$$\omega_p = \sqrt{\frac{k}{m} + \frac{bR}{m} - \zeta^2 \frac{k}{m}}, \qquad A = \zeta \sqrt{\frac{k}{m}} \tag{12.53}$$

$$b^2 = \frac{4m^2\left(\zeta^2 \frac{k}{m}\right)\left(\frac{k}{m} + \frac{bR}{m} - \zeta^2 \frac{k}{m}\right)}{R^2} \tag{12.54}$$

$$b^2 - b\frac{4\left(\zeta^2 k\right)}{R} - \frac{4\left(\zeta^2 k^2\right)\left(1-\zeta^2\right)}{R^2} = 0 \tag{12.55}$$

$$\begin{aligned} b &= \frac{1}{2}\left[\frac{4\left(\zeta^2 k\right)}{R} \pm \sqrt{\frac{16\left(\zeta^4 k^2\right)}{R^2} + \frac{16\left(\zeta^2 k^2\right)\left(1-\zeta^2\right)}{R^2}}\right] \\ &= \frac{2k}{R}\left[\left(\zeta^2\right) \pm \sqrt{\left(\zeta^4\right) + \left(\zeta^2\right)\left(1-\zeta^2\right)}\right] \\ &= \frac{2k\zeta}{R}\left[\zeta \pm \sqrt{\left(\zeta^2\right) + \left(1-\zeta^2\right)}\right] \\ &= \frac{2k\zeta}{R}\left(\zeta \pm 1\right) \end{aligned} \tag{12.56}$$

$$R = K_s \cos\beta \tag{12.57}$$

After reducing the expanded equation in equations 12.54 through 12.56, we obtain the final equation for $b_{lim,crit}$ in equation 12.58.

$$b_{lim,crit} = \frac{2k\zeta}{K_s \cos\beta}\left(\zeta + 1\right) \tag{12.58}$$

Equation 12.58 is the value of $b_{lim,crit}$ derived from the time domain solution. In equations 12.59 (Schmitz 2009) through 12.63 the same quantity is derived based on the frequency response solution. The resulting value of $b_{lim,crit}$ is the same from both methods, as seen in equation 12.58 and 12.63.

$$b_{lim,crit} = \frac{-1}{2K_s \cos\beta \min(\mathrm{Re}[FRF])} \quad 12.59$$

$$\mathrm{Re}[FRF] = \frac{1}{k}\left[\frac{1-r^2}{(1-r^2)^2+(2\zeta r)^2}\right], \quad \min(\mathrm{Re}[FRF]) \text{ when } r=\sqrt{1+2\zeta} \quad 12.60$$

$$\begin{aligned} \min(\mathrm{Re}[FRF]) &= \frac{1}{k}\left[\frac{1-1-2\zeta}{(1-1+2\zeta)^2+4\zeta^2(1+2\zeta)}\right] \\ &= \frac{1}{k}\left[\frac{-2\zeta}{(2\zeta)^2+4\zeta^2(1+2\zeta)}\right] \\ &= \frac{-1}{2\zeta k}\left[\frac{1}{1+(1+2\zeta)}\right] \\ &= \frac{-1}{4\zeta k}\left[\frac{1}{1+\zeta}\right] \end{aligned} \quad 12.61$$

$$b_{lim,crit} = \frac{-1}{2K_s \cos\beta \left(\frac{-1}{4\zeta k}\right)\left(\frac{1}{1+\zeta}\right)} \quad 12.62$$

$$b_{lim,crit} = \frac{2k\zeta}{K_s \cos\beta}(1+\zeta) \quad 12.63$$

12.3.3Chatter Frequency at $b_{lim,crit}$

The frequency response solution predicts a chatter frequency when b=blimcrit as:

$$\omega_c = \omega_n(1+\zeta) = \sqrt{\frac{k}{m}}(1+\zeta) \quad 12.64$$

In the time domain solution the tool frequency, ω_p, is determined based on the system parameters and the depth of cut, b. When the cutting frequency, ω_p, is calculated when b=blimcrit, the same chatter frequency is obtained (see equation 12.65).

$$
\begin{aligned}
\omega_p &= \sqrt{\frac{k}{m} + \frac{bR}{m} - \zeta^2 \frac{k}{m}} \\
&= \sqrt{\frac{k}{m} + \frac{R}{m}\frac{2k\zeta\left(1+\zeta\right)}{R} - \zeta^2 \frac{k}{m}} \\
&= \sqrt{\frac{k}{m}}\sqrt{1+2\zeta\left(1+\zeta\right)-\zeta^2} \\
&= \sqrt{\frac{k}{m}}\sqrt{1+2\zeta+\zeta^2} \\
&= \sqrt{\frac{k}{m}}(1+\zeta)
\end{aligned}
\qquad 12.65
$$

APPENDIX D: DDE SOLUTION EXAMPLES

12.4 Additional DDE Solution Examples

The general approach used to solve the delay differential equation describing the dynamics of a machine tool are applied in this section to find the solutions for two more basic DDEs.

$$y' + y(t-\tau) = 0,\ y(0) = 1,\ y_0 = 1 \qquad 12.66$$

$$y'_j = -y_{j-1},\ y_j(0) = 0 \qquad 12.67$$

$$\begin{array}{lcl} & & y_0 = 1 \\ y'_1 = -y_0 = -1 & \rightarrow & y_1 = -t \\ y'_2 = -y_1 = t & \rightarrow & y_2 = \dfrac{t^2}{2} \\ y'_3 = -y_2 = -\dfrac{t^2}{2} & \rightarrow & y_3 = -\dfrac{t^3}{6} \\ y'_4 = -y_3 = \dfrac{t^3}{6} & \rightarrow & y_4 = \dfrac{t^4}{24} \end{array} \qquad 12.68$$

$$y_j = \frac{(-1)^j t^j}{j!} \qquad 12.69$$

$$y(t) = \sum_{j=0}^{\infty} \begin{cases} 0 & ,t < \tau(j-1) \\ y_j\left(t - \tau(j-1)\right) & ,t \geq \tau(j-1) \end{cases} \qquad 12.70$$

$$y(t) = \sum_{j=0}^{\infty} y_j = \sum_{j=0}^{\infty} \frac{(-1)^j t^j}{j!} = e^{-t} \qquad 12.71$$

$$y'' + y(t-\tau) = 0,\ y(0) = 1,\ y_0 = 1 \qquad 12.72$$

$$y_j'' = -y_{j-1}(t) \qquad 12.73$$

$$\begin{aligned} & & y_0 &= 1 \\ y_1'' &= -1 &\rightarrow\quad y_1 &= -\frac{t^2}{2} \\ y_2'' &= \frac{t^2}{2} &\rightarrow\quad y_2 &= \frac{t^4}{24} \\ y_3'' &= -\frac{t^4}{24} &\rightarrow\quad y_3 &= -\frac{t^6}{720} \\ y_4'' &= \frac{t^6}{720} &\rightarrow\quad y_4 &= \frac{t^8}{40320} \end{aligned} \qquad 12.74$$

$$y_j = \frac{(-1)^j t^{2j}}{(2j)!} \qquad 12.75$$

$$y(t) = \sum_{j=0}^{\infty} \begin{cases} 0 & ,t < \tau(j-1) \\ y_j\left(t - \tau(j-1)\right) & ,t \geq \tau(j-1) \end{cases} \qquad 12.76$$

$$y(t) = \sum_{j=0}^{\infty} y_j = \sum_{j=0}^{\infty} \frac{(-1)^j t^{2j}}{(2j)!} = \cos(t) \qquad 12.77$$

APPENDIX E: MULTI-MODE COEFFICIENT SOLUTIONS

12.5 Multi-mode solutions for a_w

The a_w coefficients are solved by applying the forcing term which contains a polynomial multiplied by an exponential to the first order differential equation. An example of the solution process is shown below when the polynomial in the forcing function is of degree 2. In Equation 12.78 the form the of particular solution, $w_{n,u}$, is shown when n≠u.

$$\begin{aligned} \dot{w}_{\mathrm{n,u}} &= \lambda_n w_{\mathrm{n,u}} + \left(a_{gn,\mathrm{u},0} + a_{gn,\mathrm{u},1} t + a_{gn,\mathrm{u},2} t^2\right) e^{\lambda_u t} \\ w_{\mathrm{n,u}} &= \left(a_{wn,\mathrm{u},0} + a_{wn,\mathrm{u},1} t + a_{wn,\mathrm{u},2} t^2\right) e^{\lambda_u t}\ ,\ n \neq u \end{aligned} \qquad 12.78$$

Applying the particular solution form to the differential equation and equating to the forcing term, $\dot{w}_{\mathrm{n,u}} - \lambda_n w_{\mathrm{n,u}} = g_{n,u}$, the following equation is obtained. The coefficients are then calculated by equating the polynomial degree terms and solving based on the forcing coefficients as shown in Equation 12.79. As the degree of the input polynomial increases with each successive response, the solution coefficients, aw, can be calculated directly using 3.17 when n≠u.

$$
\begin{aligned}
&\dot{w}_{\text{n,u}} - \lambda_n w_{\text{n,u}} = g_{n,u} \text{ , n} \neq \text{u} \\
&g_{n,u} = \left(a_{gn,\text{u},0} + a_{gn,\text{u},1} t + a_{gn,\text{u},2} t^2 \right) e^{\lambda_u t} \\
&w_{\text{n,u}} = \left(a_{wn,\text{u},0} + a_{wn,\text{u},1} t + a_{wn,\text{u},2} t^2 \right) e^{\lambda_u t} \\
&\dot{w}_{\text{n,u}} = \lambda_u \left(a_{wn,\text{u},0} + a_{wn,\text{u},1} t + a_{wn,\text{u},2} t^2 \right) e^{\lambda_u t} + \left(a_{wn,\text{u},1} + 2a_{wn,\text{u},2} t \right) e^{\lambda_u t} \\
&t^0 : \left(\lambda_u - \lambda_n \right) a_{wn,\text{u},0} + a_{wn,\text{u},1} = a_{gn,\text{u},0} \rightarrow a_{wn,\text{u},0} = \frac{a_{gn,\text{u},0} - a_{wn,\text{u},1}}{\left(\lambda_u - \lambda_n \right)} \\
&t^1 : \left(\lambda_u - \lambda_n \right) a_{wn,\text{u},1} + 2a_{wn,\text{u},2} = a_{gn,\text{u},1} \rightarrow a_{wn,\text{u},1} = \frac{a_{gn,\text{u},1} - 2a_{wn,\text{u},2}}{\left(\lambda_u - \lambda_n \right)} \\
&t^2 : \left(\lambda_u - \lambda_n \right) a_{wn,\text{u},2} = a_{gn,\text{u},2} \rightarrow a_{wn,\text{u},2} = \frac{a_{gn,\text{u},2}}{\left(\lambda_u - \lambda_n \right)}
\end{aligned}
\tag{12.79}
$$

The solution approach in Equation 12.79 cannot be applied in the case where n=u due to the zero denominator (λ_u-λ_n=0). A solution is obtained in the case where n=u by increasing the degree of the particular solution by one. Applying the modified particular solution as shown in Equation 12.81, a new set of coefficient solutions are obtained, which are shown in Equation 12.81 and can be calculated directly using the formula in Equation 3.17. Note that in the case where n=u, the coefficient, $a_{wn,u,0}$, is determined based on the initial conditions.

$$
\begin{aligned}
&\dot{w}_{\text{n,u}} = \lambda_n w_{\text{n,u}} + \left(a_{gn,\text{u},0} + a_{gn,\text{u},1} t + a_{gn,\text{u},2} t^2 \right) e^{\lambda_u t} \\
&w_{\text{n,u}} = \left(a_{wn,\text{u},0} + a_{wn,\text{u},1} t + a_{wn,\text{u},2} t^2 + a_{wn,\text{u},3} t^3 \right) e^{\lambda_u t} \text{ , } n = u
\end{aligned}
\tag{12.80}
$$

$$
\begin{aligned}
&\dot{w}_{\mathrm{n,u}} - \lambda_n w_{\mathrm{n,u}} = g_{n,u} \text{ , n = u} \\
&g_{n,u} = \left(a_{gn,\mathrm{u},0} + a_{gn,\mathrm{u},1} t + a_{gn,\mathrm{u},2} t^2\right) e^{\lambda_u t} \\
&w_{\mathrm{n,u}} = \left(a_{wn,\mathrm{u},0} + a_{wn,\mathrm{u},1} t + a_{wn,\mathrm{u},2} t^2 + a_{wn,\mathrm{u},3} t^3\right) e^{\lambda_u t} \\
&\dot{w}_{\mathrm{n,u}} = \lambda_u \left(a_{wn,\mathrm{u},0} + a_{wn,\mathrm{u},1} t + a_{wn,\mathrm{u},2} t^2 + a_{wn,\mathrm{u},3} t^3\right) e^{\lambda_u t} + \left(a_{wn,\mathrm{u},1} + 2a_{wn,\mathrm{u},2} t + 3a_{wn,\mathrm{u},3} t^2\right) e^{\lambda_u t} \\
&t^0 : \left(\lambda_u - \lambda_n\right) a_{wn,\mathrm{u},0} + a_{wn,\mathrm{u},1} = a_{gn,\mathrm{u},0} \rightarrow a_{wn,\mathrm{u},1} = a_{gn,\mathrm{u},0} \\
&t^1 : \left(\lambda_u - \lambda_n\right) a_{wn,\mathrm{u},1} + 2a_{wn,\mathrm{u},2} = a_{gn,\mathrm{u},1} \rightarrow a_{wn,\mathrm{u},2} = \frac{a_{gn,\mathrm{u},1}}{2} \\
&t^2 : \left(\lambda_u - \lambda_n\right) a_{wn,\mathrm{u},2} + 3a_{wn,\mathrm{u},3} = a_{gn,\mathrm{u},2} \rightarrow a_{wn,\mathrm{u},3} = \frac{a_{gn,\mathrm{u},2}}{3} \\
&t^3 : \left(\lambda_u - \lambda_n\right) a_{wn,\mathrm{u},3} = 0
\end{aligned}
\tag{12.81}
$$

12.6 Multi-mode matrix coefficient solutions

In the case when n≠u, the w coefficients, $a_{\mathrm{wn,u,v}}$, are dependent on the higher order w coefficients, $a_{\mathrm{wn,u,v+1}}$. Using the higher order w coefficients to calculate the lower order coefficients is convenient when calculating using Equation (1.82), however, it is possible to obtain these values based only on the g coefficients for a matrix solution. Take for example the solutions for w_1 (n=1) and the forcing mode is 2 (u=2) in a 2 mode system when the maximum order of the g coefficients is 3. Equation (1.83) gives the solutions for the w_1 coefficients based on Equation (1.82), and the solutions are given in reduced form in Equation (1.85).

$$
\begin{gathered}
a_{wn,\lambda \mathrm{u,v+1}} = \frac{a_{gn,\lambda \mathrm{u,v}}}{v+1}; \;\; n = u \\
a_{wn,\lambda \mathrm{u,v}} = \frac{a_{gn,\lambda \mathrm{u,v}} - (v+1)\, a_{wn,\lambda \mathrm{u,v+1}}}{\lambda_u - \lambda_n}; \;\; n \neq u
\end{gathered}
\tag{1.82}
$$

$$
\begin{aligned}
g_{1,\lambda 2} &= \left(a_{\mathrm{g}1,\lambda 2,0} + a_{\mathrm{g}1,\lambda 2,1}t + a_{\mathrm{g}1,\lambda 2,2}t^2 + a_{\mathrm{g}1,\lambda 2,3}t^3\right)\mathrm{e}^{\lambda_2 t} \\
w_{1,\lambda 2} &= \left(a_{\mathrm{w}1,\lambda 2,0} + a_{\mathrm{w}1,\lambda 2,1}t + a_{\mathrm{w}1,\lambda 2,2}t^2 + a_{\mathrm{w}1,\lambda 2,3}t^3\right)\mathrm{e}^{\lambda_2 t} \\
a_{w1,\lambda 2,3} &= \frac{a_{g1,\lambda 2,3}}{\lambda_2 - \lambda_1} \\
a_{w1,\lambda 2,2} &= \frac{a_{g1,\lambda 2,2} - 3a_{w1,\lambda 2,3}}{\lambda_2 - \lambda_1} = \frac{a_{g1,\lambda 2,2} - 3\dfrac{a_{g1,\lambda 2,3}}{\lambda_2 - \lambda_1}}{\lambda_2 - \lambda_1} \\
a_{w1,\lambda 2,1} &= \frac{a_{g1,\lambda 2,1} - 2a_{w1,\lambda 2,2}}{\lambda_2 - \lambda_1} = \frac{a_{g1,\lambda 2,1} - 2\dfrac{a_{g1,\lambda 2,2} - 3\dfrac{a_{g1,\lambda 2,3}}{\lambda_2 - \lambda_1}}{\lambda_2 - \lambda_1}}{\lambda_2 - \lambda_1} \\
a_{w1,\lambda 2,0} &= \frac{a_{g1,\lambda 2,0} - a_{w1,\lambda 2,1}}{\lambda_2 - \lambda_1} = \frac{a_{g1,\lambda 2,0} - \dfrac{a_{g1,\lambda 2,1} - 2\dfrac{a_{g1,\lambda 2,2} - 3\dfrac{a_{g1,\lambda 2,3}}{\lambda_2 - \lambda_1}}{\lambda_2 - \lambda_1}}{\lambda_2 - \lambda_1}}{\lambda_2 - \lambda_1}
\end{aligned}
\tag{1.83}
$$

$$
\begin{aligned}
a_{w1,\lambda 2,3} &= \frac{a_{g1,\lambda 2,3}}{\lambda_2 - \lambda_1} \\
a_{w1,\lambda 2,2} &= \frac{a_{g1,\lambda 2,2}}{\lambda_2 - \lambda_1} - \frac{3a_{g1,\lambda 2,3}}{\left(\lambda_2 - \lambda_1\right)^2} \\
a_{w1,\lambda 2,1} &= \frac{a_{g1,\lambda 2,1}}{\lambda_2 - \lambda_1} - \frac{2a_{g1,\lambda 2,2}}{\left(\lambda_2 - \lambda_1\right)^2} + \frac{6a_{g1,\lambda 2,3}}{\left(\lambda_2 - \lambda_1\right)^3} \\
a_{w1,\lambda 2,0} &= \frac{a_{g1,\lambda 2,0}}{\lambda_2 - \lambda_1} - \frac{a_{g1,\lambda 2,1}}{\left(\lambda_2 - \lambda_1\right)^2} + \frac{2a_{g1,\lambda 2,2}}{\left(\lambda_2 - \lambda_1\right)^3} - \frac{6a_{g1,\lambda 2,3}}{\left(\lambda_2 - \lambda_1\right)^4}
\end{aligned}
\tag{1.84}
$$

The generalized w coefficient solutions are given in Equation 5.6, where the subscript v_g indicates the order of the g coefficient, and V is the highest order g coefficient.

$$
\begin{aligned}
a_{wn,\lambda \mathrm{u},\mathrm{v}+1} &= \frac{a_{\mathrm{gn},\lambda \mathrm{u},\mathrm{v}}}{v+1};\ n = u \\
a_{wn,\lambda \mathrm{u},\mathrm{v}} &= \sum_{v_g=v}^{V} \frac{(-1)^{\left(v+v_g\right)}\left(v_g\right)!\, a_{gn,\lambda \mathrm{u},\mathrm{v}_g}}{(v)!\left(\lambda_u - \lambda_n\right)^{\left(1+v_g-v\right)}};\ n \neq u
\end{aligned}
\tag{1.85}
$$